GEOCHRONOLOGY AND CHRONOSTRATIGRAPHY OF THE EOCENE - OLIGOCENE TRANSITION

Thesis submitted for the degree of

Doctor of Philosophy

at the University of Leicester

by

Claudia Diana Sahy BSc

Department of Geology

University of Leicester

2013

GEOCHRONOLOGY AND CHRONOSTRATIGRAPHY OF THE EOCENE - OLIGOCENE TRANSITION

Claudia Diana Sahy

This thesis integrates high-precision (<0.2%, 2σ) $^{206}Pb/^{238}U$ dating of zircons from volcanic tuffs intercalated in key Late Eocene-Oligocene marine and terrestrial sedimentary successions, with high-resolution biostratigraphic and magnetostratigraphic data sets in order to critically examine the accuracy and precision of the numerical age calibration of the Eocene – Oligocene transition (EOT).

Weighted mean $^{206}Pb/^{238}U$ ages from the Italian Umbria-Marche and North American White River Group (WRG) sedimentary successions are 0.4-1.0 Myr younger than legacy $^{40}Ar/^{39}Ar$ biotite and sanidine data from the same tuffs (calibrated relative to Fish Canyon sanidine at 28.201 Ma).

$^{206}Pb/^{238}U$ calibrated age-depth models were used to constrain the age of magnetic reversals between 26.5-36 Ma (C8r-C16n.2n). Interpolated magnetic reversal ages are consistent with relatively constant seafloor spreading rates, and provide a fully integrated and robust chronostratigraphic framework for the EOT, as shown by mutual consistency of chron boundary ages from the Umbria-Marche basin and the WRG between 31-36 Ma. These data effectively eliminate the discrepancies between astronomically tuned and radio-isotopically calibrated time scales of the EOT.

An evaluation of the fidelity of planktonic foraminifer bioevent based chronostratigraphy across the EOT indicates that the last occurrence of hantkeninids and the last common occurrence of Chiloguembelina cubensis which mark the Eocene-Oligocene (34.090 ± 0.074 Ma) and Rupelian – Chattian (28.126 ± 0.175 Ma) boundaries are not time-transgressive across oceanic basins. However, other Oligocene planktonic foraminifer bioevents occur 0.4-0.8 Myr later in the western Tethys than in tropical and subtropical open ocean settings. In the WRG sedimentary succession, the first and last appearance datums of key Late Eocene mammal taxa show diachroneity of ca. 1 Myr over a distance of 400 km.

Long-term aridification recorded by the WRG appears to be time-transgressive, and progressed gradually from west to east, while abrupt Early Oligocene cooling reported from WRG outcrops in NE Nebraska was synchronous with Early Oligocene glaciation of Antarctica.

Acknowledgements:

Firstly, I would like to thank my supervisors, Dan Condon, and Mark Williams, whose enthusiasm, dedication, support, and, when needed, constructive criticism have made this PhD 'journey' an enjoyable and rewarding experience.

Many others have contributed formally or informally to the research presented in this thesis Foremost among these I would like to express my gratitude to Klaudia Kuiper and Frits Hilgen who guided the GTSnext network and offered helpful advice at various stages of this research. The geochronologic and magnetostratigraphic studies of the North American terrestrial record would not have been possible without the generous assistance of Dennis Terry, Joe Hiess, Anne Fischer, Hemmo Abels, and Bill Lukens. Permits to carry out work at Flagstaff Rim and Toadstool Park were kindly provided by Brent Breithaupt of the Bureau of Land Management, Cheyenne, Wyoming, and Carla Loop and Barbara Beasley from the US Forest Service, Nebraska National Forest. Silja Huesing provided training and assistance in the acquisition and interpretation of paleomagnetic data at the University of Utrecht. I gratefully acknowledge the funding provided for this project through European Community's Seventh Framework Programme (FP7/2007-2013) under grant agreement n° [215458].

My colleagues and friends at NIGL have contributed to making the last four years a fulfilling professional and personal experience. I would especially like to thank Nicola Atkinson for her help with the chemical preparation of my samples, and also the suggestions of good books to read in my non-existent spare time, and introducing me to Poppy, Toni Milodowski for his assistance in running the SEM, Laura Bracciali for making working late seem almost like fun, Noah McLean for shedding light on the mysteries of Tripoli and Redux, and Adrian Wood for his help in the mineral separation lab.

Table of contents:

List of figures and tables:

1. Current state of the numerical age calibration of the Eocene - Oligocene transition

Abstract: This chapter examines the numerical age constraints on which the calibration of the Eocene-Oligocene transition is based. The strengths and weaknesses of widely used numerical dating methods (i.e. $^{40}Ar/^{39}Ar$ dating of sanidine and biotite, $^{206}Pb/^{238}U$ dating of zircon, astronomical tuning) are discussed and evaluated. An overview of radio-isotopically calibrated and astronomically tuned age models for the Paleogene is given, and the discrepancies between the results of the two time scale calibration approaches are explored. An analytical program aiming to resolve these discrepancies through high-precision $^{206}Pb/^{238}U$ dating of zircons from volcanic tuffs intercalated in key marine and terrestrial Late Eocene and Oligocene sedimentary successions and the development of high resolution magnetic polarity records is outlined.

1.1. Introduction

The Eocene-Oligocene transition (EOT) represents an abrupt climate shift from the "greenhouse" world of the Late Cretaceous and Early Paleogene, to the "icehouse" world of the Oligocene and Neogene, marking a pivotal step in the development of our modern, glacial climate. Understanding of the driving forces behind global climate dynamics and biotic turnover at the EOT relies on the availability of accurate and precise numerical age constraints supporting the global and regional correlation and integration of marine and terrestrial sedimentary records.

Over the last two decades, the resolving power of the dating methods used to constrain the Paleogene time scale, and implicitly the temporal resolution of Late Eocene – Early Oligocene records has improved considerably, so that questions related to the synchronicity of events preserved in disparate sedimentary successions can now be addressed at the <100 kyr scale. This has been achieved through the development of increasingly stable numerical models for the Earth's insolation quantities as a function of time, and the acquisition of high-quality ocean sediment records via various OPD and IODP expeditions, which led to the development of astrochronologic age models for much of the Paleogene. At the same time, community-based initiatives in the field of radio-isotopic geochronology (i.e., EARTHTIME) resulted in improved accuracy and precision for dates obtained using the $^{40}Ar/^{39}Ar$ and $^{206}Pb/^{238}U$ isotope systems. These efforts led to more robust radio-isotopic age constraints by effectively eliminating systematic biases between the $^{40}Ar/^{39}Ar$ and $^{206}Pb/^{238}U$ systems through the re-evaluation of the age of commonly used $^{40}Ar/^{39}Ar$ mineral standards (Renne et al., 1998, 2010, 2013; Kuiper et al., 2008; Smith et al., 2010; Rivera et al., 2011). However, calibration of legacy Late Eocene - Oligocene $^{40}Ar/^{39}Ar$ data relative to revised neutron fluence monitor ages has revealed discrepancies on the order of 0.5 Myr between astronomically tuned and radio-

isotopically calibrated time scales of the EOT (Hilgen and Kuiper, 2009; Vandenberghe et al., 2012), which I aim to address in this thesis.

Between 2008-2012, a concerted effort to improve the consistency of radio-isotopic and astronomically derived time scales was initiated by the European Earth science community, in the form of the GTSnext Marie Curie Initial Training Network (www.gtsnext.eu). The network brought together researchers from 10 European institutions, working on individual but connected projects aimed at addressing fundamental issues related to the calibration of geological time, and the integration of state-of-the-art high-precision radio-isotopic geochronology, and cyclostratigraphy, with biostratigraphic and magnetostratigraphic datasets, over key intervals of the last 100 Myr of the Earth's history.

This thesis presents the results of Task II.3 of the GTSnext project, which focused on refining the radio-isotopic age constraints of the Eocene-Oligocene transition through high-precision $^{206}Pb/^{238}U$ dating of zircons from volcanic tuffs from key sedimentary successions in Italy and North America with the aim of i) assessing the accuracy of recalculated $^{40}Ar/^{39}Ar$ dates used in the calibration of the Late Eocene –Early Oligocene time scale, ii) verifying the validity of the astronomically tuned Oligocene time scale, iii) providing highly precise radio-isotopic constraints on the age of Late Eocene magnetic polarity reversals, and iv) improving the objective comparison between marine and terrestrial records of the EOT.

1.2 Marine and terrestrial records of the EOT

The Early Oligocene greenhouse-icehouse shift represents the abrupt culmination of a long-term cooling trend that characterized much of the Eocene (Zachos et al., 2001; Cramer et al., 2009; Westerhold and Röhl, 2009), and occurred as a result of a combination

of decreasing atmospheric pCO_2 levels (Pagani et al., 2005; DeConto and Pollard, 2003), changes in ocean circulation patterns caused by the opening of Southern Ocean gateways (Katz et al., 2011, Huber and Nof, 2006, Sijp and England, 2004, Livermore et al., 2005) and favourable orbital configurations (Coxall et al., 2005) which led to the growth of a permanent, continent-scale Antarctic ice sheet for the first time in the Earth's recent history (Shackleton and Kennett, 1975; Miller et al., 2009; Sagnotti et al., 1998; Zachos et al., 2001; Ivany et al., 2006; Coxall and Pearson, 2007). Late Eocene – Early Oligocene high-resolution stable isotope and $CaCO_3$ mass accumulation records from multiple oceanic basins show a stepwise 1.2-1.5 ‰ positive shift in benthic foraminiferal $\delta^{18}O$ values, coupled with a ca. 1 km deepening of the carbonate compensation depth (CCD) (Coxall et al., 2005; Rea and Lyle, 2005; Pearson et al., 2008, Katz et al., 2008, Pälike et al., 2012). The $\delta^{18}O$ shift, commonly termed the Oi-1 event, consistently occurs near the base of magnetic polarity chron C13n in the Pacific, Atlantic, Indian, and Southern Oceans (Coxall et al., 2005; Pearson et al., 2008, Katz et al., 2008; Zachos et al., 1996), and its numerical age, and duration are constrained by astronomical tuning at ODP Site 1218 in the Equatorial Pacific (Coxall et al., 2005; Pälike et al., 2006).

By contrast paleoclimate proxies from terrestrial records of the Eocene-Oligocene transition often yield conflicting information concerning both the magnitude and the timing of changes associated with the Oi-1 event (Kohn et al., 2004; Sheldon and Retallack, 2004; Grimes et al., 2005; Retallack, 2007; Zanazzi et al., 2007, 2009; Sheldon, 2009; Costa et al., 2011; Boardman and Secord,2013; Hren et al., 2013). This disparity in global terrestrial paleoclimate records indicates that, in addition to climate change, other factors, such as the position of sampled sites relative to orographic features, and changes in drainage patterns and groundwater circulation might have played a significant role in the recording of paleoclimate signals in terrestrial proxy records (Sheldon 2009; Boardman and Secord, 2013).

The timing of environmental change recorded in land-based Late Eocene – Early Oligocene successions relative to the marine record of the Oi-1 event has implications for the interpretation of the Early Oligocene benthic foraminifera $\delta^{18}O$ shift in terms of ice volume and temperature effects. Studies reporting stable mean annual temperature (MAT) values across the EOT from Europe, North America and South America (Kohn et al., 2004; Sheldon and Retallack, 2004; Grimes et al., 2005; Retallack, 2007; Sheldon, 2009; Costa et al., 2011; Boardman and Secord,2013) support the interpretation of the Early Oligocene benthic foraminiferal $\delta^{18}O$ shift as an expression of ice growth, with only a subordinate temperature component (Retallack et al., 2004; Sheldon and Retallack, 2004). This interpretation is supported by deep-sea Mg/Ca records (Lear et al., 2000, 2004; Billups and Scharg, 2003) however it implies Early Oligocene ice volumes that are too large to be accommodated on Antarctica alone, and require coeval Northern Hemisphere glaciation (Tripati et al., 2008), however evidence for the presence of continent-scale Northern Hemisphere ice sheets in the Early Oligocene remains controversial (Eldrett et al., 2007). Mg/Ca records from shallower settings (i.e. from above the CCD), and alkenone unsaturation index data from high-latitudes are consistent with a 2.5-5 ˚C drop in sea surface temperatures (Lear et al., 2008; Liu et al., 2009). This suggests that the lack of temperature change exhibited by deep-sea records is due to the Early Oligocene deepening of the CCD which resulted in a change in the carbonate saturation state of the deep ocean, and might have affected the partitioning of Mg into benthic foraminiferal calcite (Elderfield et al., 2006).

Cooling at the Eocene – Oligocene transition is also supported by terrestrial records of clumped isotope data from aragonitic freshwater gastropod shells from the Solent Group on the Isle of Wight which show a 4-6 ˚C drop in MAT (Hren et al., 2013) and stable isotope data from fossil bone and teeth from the White River Group in western

Nebraska which revealed a 7.1 ± 3.1 ˚C drop in MAT (Zanazzi et al., 2007, 2009). Of these, only the North American record is amenable to direct radio-isotopic dating, while the numerical age calibration of the Solent Group relies upon indirect dating (e.g., bio- and magnetostratigraphy) which carries uncertainties that are often difficult to quantify. Importantly, calibration of the North American terrestrial EOT data through published $^{40}Ar/^{39}Ar$ dates (e.g. Swisher and Prothero, 1990, recalculated to currently accepted values for the ^{40}K decay constant and neutron flux monitor age), and relative to recent editions of the geomagnetic polarity time scale, yield significantly different dates for the timing of the Early Oligocene drop in MAT (Zanazzi et al., 2007, 2009) relative to the marine Oi-1 event. This opens the possibility that terrestrial archives record diachronous cooling compared to the onset of glaciation and/or temperature shift in the ocean basins.

1.3 Eocene-Oligocene time scale calibration methods and application

Accurate and precise numerical age constraints are essential for the regional and global integration of Late Eocene – Oligocene bio- and chemo-stratigraphic proxy records, the development of climate models of the greenhouse-icehouse transition, and the quantification of the duration of events and/or rates of change across the EOT. A limited number of Late Eocene – Oligocene successions are amenable to direct dating using astronomical tuning (Pälike et al., 2006; Jovane et al., 2006; Brown et al., 2009; Hyland et al., 2009; Xiao et al., 2010) or radio-isotopic dating (Montanari et al. 1985; Swisher and Prothero, 1990; Odin et al., 1991a, 1991b; Obradovich et al., 1995; Coccioni et al., 2008; Dunn et al., 2012) however the majority of the available records of the EOT lack datable material, and are instead calibrated relative to various time scales of regional or global applicability. Methods for relative dating include the geomagnetic polarity time scale (Florindo et al., 2005; Dupont-Nivet et al., 2007; Costa et al., 2011), and marine and terrestrial biozonation schemes (Alegret et al., 2008; Pearson et al., 2008;

Fenero et al., 2012, 2013). The absolute nature of each of these time scale schemes is underpinned by geochronology (i.e. radio-isotopic and/or astronomically tuned dates), the accuracy and precision of which determines the accuracy and precision of the derived time scale. However additional uncertainty often exists due to the nature of the data on which relative time scales are based (i.e. magnetic polarity records, first/last occurrence datums of biotic taxa), and such uncertainties are often difficult to quantify. The fidelity of biostratigraphic zonation schemes is determined by the degree to which locally observed first and last occurrence datums reliably represent the true global sequence of origination and extinction events (Sadler, 2004). In turn, the accuracy of magnetostragraphic dating is determined by the temporal resolution of local magnetic polarity patterns, and the accuracy of magnetic reversal ages extracted from the geomagnetic polarity time scale (GPTS) (Huestis and Acton, 1997; Agrinier, 1999)

1.3.1 Astronomical tuning of the EOT

Astronomical tuning, often termed cyclostratigraphy is a numerical dating method based on matching, or tuning, climate-controlled cyclic patterns in the sedimentary record to numerical models of the Earth's insolation quantities as a function of time. Changes in insolation are controlled by quasi-periodic oscillations in the Earth's orbital parameters, known as Milankovich cycles, caused by the interaction between the Earth's axial precession and the gravitational pull of other planets. Astronomical tuning requires the identification of sedimentary cycles resulting from changes in the eccentricity of the Earth's orbit, with periods of ca. 100 kyr, 405 kyr, and 2.26 Myr, and the tilt and precession of the Earth's rotational axis, with principal periods at 41 kyr, and ca. 21 kyr respectively (for a recent review see Hinnov and Hilgen, 2012). The applicability of astronomical tuning at the resolution of precession and obliquity cycles is limited to the last 40-50 Myr (Laskar et al., 2004, 2011), due to the chaotic behaviour of the solar system, uncertainties

related to the initial conditions of the model, and numerical integration error, however the ca. 405 kyr eccentricity signal is thought to have been stable over at least the past 250 Myr (Laskar et al., 2004, Hinnov and Hilgen, 2012).

Astronomically tuned ages are typically quoted to the nearest 1 kyr, without uncertainty estimates. The accuracy and precision of the method are controlled by the accuracy of the numerical model, and the correctness of the tuning itself (i.e. complete expression and accurate identification of cycles), and are difficult to assess. Rigorous propagation of errors through the numerical models of Laskar et al. (1993, 2004, 2011) is not feasible given the large number of parameters involved, and the complexity of the model. The main sources of uncertainty are thought to be changes in the dynamical ellipticity of the Earth, and tidal dissipation in the Earth-Moon system which affect the precession and obliquity frequencies (Laskar et al., 1993, 2004). Lourens et al (2001, 2004) estimated the uncertainty arising from changes in tidal dissipation and dynamical ellipticity to be around 68 kyr for precession, and 123 kyr for obliquity at 25 Ma, however, these effects are likely to be mitigated by taking into account amplitude modulations of precession and obliquity, and precession - obliquity interference patterns. The uncertainty in tuning to the 405 kyr cycle was estimated by Laskar et al (2004) to be about ± 0.1 % over the last 100 Myr. Additional significant sources of uncertainty for astronomical age models are in the expression, identification and quantification of orbital forcing in a given stratigraphic record, combined with the (in)completeness of the record over the stratigraphic interval of interest.

Reproducibility of astronomical tuning is difficult to determine, as few workers have attempted to reassess previously tuned sedimentary successions, either by collecting their own, independent data, or by re-evaluating pre-existing cyclostratigraphic interpretations of proxy records. Beacuse such an approach would provide a measure of

the potential errors related to the statistical treatment of proxy data and the tuning process itself, we highlight two examples from recent publications. Tuning of the Massignano section in the central Apennines to the 40 kyr and 100 kyr components of the Laskar et al. (2004) numerical solution by Jovane et al (2006) and Brown et al. (2009) resulted in durations of ca. 2.2 Myr and respectively ca. 1.7 Myr for the same stratigraphic interval. Westerhold et al. (2008) reported a duration of 24 x 405 kyr cycles for the Paleocene, however, a critical evaluation of their cyclostratigraphic interpretation by Hilgen et al. (2010) identified 25 cycles which is consistent with $^{40}Ar/^{39}Ar$, and $^{206}Pb/^{238}U$ dating of the Cretaceous – Paleogene, and respectively of the Paleocene Eocene Thermal Maximum (PETM) (Charles et al., 2011, Renne et al., 2013). These examples serve to demonstrate that in isolation, astronomical tuning of pre-Neogene sections can be problematic and uncertainties arising from subjective interpretation can be significant (> 0.4 Myr).

1.3.2 K-Ar and $^{40}Ar/^{39}Ar$ dating of the EOT

The K-Ar and $^{40}Ar/^{39}Ar$ dating methods rely on the branching decay of ^{40}K to ^{40}Ar, and ^{40}Ca, and the accumulation of radiogenic ^{40}Ar ($^{40}Ar^{*}$) over time, to measure the crystallization age of potassium-rich minerals. K-Ar dating of volcanic rocks has played an important role in the calibration of geologic time and the development of the GPTS, however, the precision and accuracy of the method are limited by the relatively large amount of sample required for each analysis (10-100 mg), and the requirement to measure K and ^{40}Ar on separate aliquots, which may yield spurious data due to the presence of impure or inhomogeneous starting material. The development of the $^{40}Ar/^{39}Ar$ method by Merrihue and Turner (1966), which relies on measurement of a single aliquot to determine a daughter-parent isotope ratio, led to greater flexibility of analysis, decreased sample size, and improved precision, resulting in the preferential use of $^{40}Ar/^{39}Ar$ data in more recent time scale compilations (Cande and Kent, 1992; 1995; Ogg and Smith,

2004; Vandenberghe et al., 2012). The $^{40}Ar/^{39}Ar$ method relies on the measurement of the ratio between $^{40}Ar^*$, the product of the electron capture decay of ^{40}K, and ^{39}Ar, produced through neutron irradiation in a nuclear reactor prior to analysis, which serves as a proxy for the amount of ^{40}K present in the sample. Because the rate at which ^{39}Ar is produced is monitored through simultaneous irradiation of a reference material of assumed age, the accuracy of the method depends on the accuracy of the ^{40}K decay constants and the accuracy of the "assumed" age of the mineral standard.

Sanidine from the Fish Canyon Tuff (FCs), is one of the most commonly used mineral standards in $^{40}Ar/^{39}Ar$ dating. The age of FCs was originally calibrated relative to primary K/Ar standards, with a commonly used value of 27.84 Ma (Renne et al., 1994), later revised to 28.02 ± 0.28* Ma (Renne et al., 1998), which was adopted for the 2004 edition of the Geological Time Scale (GTS04). Subsequent studies have attempted to calibrate the age of FCs relative to dating methods that are independent of the K/Ar system (Figure 1.1). Inter-calibration with astronomically dated tuffs from the Melilla basin in Morocco and the Faneromeni section on Crete arrived at mutually consistent dates of 28.201 ± 0.046 Ma (Kuiper et al., 2008) and 28.172 ± 0.028 Ma (Rivera et al., 2011) for FCs. An alternative 'inter-calibration' approach based on statistical optimization of $^{40}Ar/^{39}Ar$ and $^{206}Pb/^{238}U$ data pairs combined with existing constraints on the $^{40}Ar^*/^{40}K$ ratio of FCs, and the ^{40}K decay constants, yielded an age of 28.305 ± 0.072 Ma for FCs, which is consistent, at the 2σ level, with the age reported by Kuiper et al., (2008), but not that of Rivera et al. (2011). An additional constraint on the age of FCs comes from the U-Pb (zircon) geochronology study of Wotzlaw et al (2013), who reported an age of ca. 28.196 ± 0.038 Ma, the accuracy of which is underpinned by gravimetric isotopic tracer calibration (see section 1.5), the inference being that the sanidine age must be equal to or younger than the zircon eruption age. Combined, these experiments indicate an age

** unless otherwise specified, all uncertainties are quoted at the 2σ level*

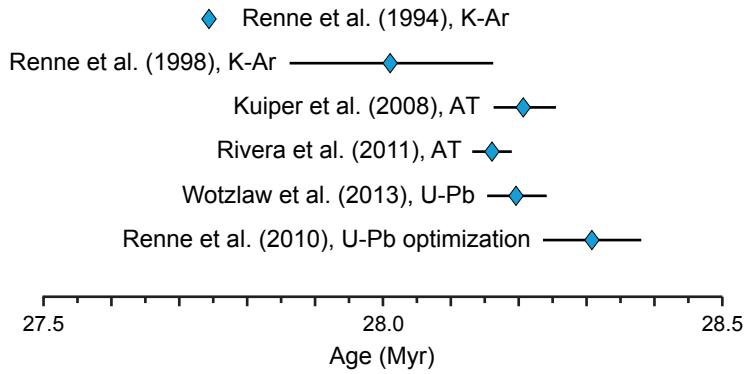

Figure 1.1 Results of FCs numerical age calibration experiments relative to primary K-Ar standards, astronomical tuning (AT), and the U-Pb system (see text for details). Recent studies converge at a value of ca. 28.2 Ma, with the slightly older estimate of Renne et al. (2010) possibly reflecting pre-eruptive magma chamber residence of zircons. All uncertainties are 2σ.

of ca. 28.20 Ma, but the variance between experiments implies an uncertainty on the order of 0.2% (2σ). Revisions of the consensus values of the ^{40}K decay constants (Steiger and Jäger, 1977) were also carried out by Min et al. (2000) and Renne et al. (2010). The FCs age of Kuiper et al. (2008), and the ^{40}K decay constants of Min et al. (2000) were adopted by consensus in the 2012 edition of the Geological Time Scale (GTS12), and emphasis was put on the propagation of systematic uncertainties associated with these values, to allow for comparisons between ^{40}Ar/^{39}Ar dates, and data obtained using other radio-isotopic systems and cyclostratigraphy. For the ^{40}Ar/^{39}Ar dates used to calibrate the Paleogene time scale, this resulted in total uncertainties of ca. ± 0.5 %, however several additional factors could be affecting the accuracy of these dates:

- Based upon the results of recent calibration experiments, estimates of the age of the FCs fluence monitor show scatter beyond the uncertainties reported by Kuiper et al. (2008; Renne et al., 2010; Rivera et al., 2011; Phillips and Matchan, 2013). This reflects differences in the calibration models (see above) and their related assumptions, likely inter-laboratory bias, and purported real age variation within FCs (Phillips and Matchan, 2013).

- Dates calibrating the EOT interval were obtained on biotite, which has been shown to be susceptible to ^{39}Ar recoil phenomena and incorporation of excess ^{40}Ar (Min et al., 2000; Kuiper et al., 2008; Hora et al., 2010).
- High-precision (± 0.2%), inverse variance weighted mean $^{40}Ar/^{39}Ar$ dates reported in the literature are based on large sets of relatively imprecise (1%) single crystal dates that are assumed to represent a single age population, normally distributed around the "true" age of the sample. Recent studies, especially those exploiting multi-collector mass spectrometry, are revealing non-normally distributed sanidine age populations interpreted as reflecting the analyses of extraneous Ar, and/or exocrystic material incorporated during eruption which may invalidate the use of high-n low precision single analyses data to derive higher-precision interpreted (weighted mean) dates (e.g. Phillips and Matchan, 2013)
- Inter-calibration experiments carried out during the past eight years, using three common sanidine standards have shown the inter-laboratory reproducibility of the $^{40}Ar/^{39}Ar$ method to be around 1% (Schmitz and Kuiper, 2013), and a greater bias may exist in older legacy data sets.

Legacy $^{40}Ar/^{39}Ar$ datasets constraining the EOT interval have been published from the continental succession of North America (Swisher and Prothero, 1990; Obradovich et al., 1995) and the pelagic marine record of the Northern Apennines in Italy (Odin et al., 1991a, 1991b; Coccioni et al., 2008). Except for Odin et al. (1991a), who used LP-6 biotite with an age of 127.7 Ma as a neutron fluence monitor, these data were originally calibrated relative to an age of 27.84 Ma for FCs. Recalibrating these dates relative to the FCs age of 28.02 (Renne et al., 1998) used in GTS04 (using the LP-6 – FCs intercalibration factor of Baksi et al. (1996) where applicable) and the FCs age of 28.201 Ma of Kuiper et al. (2008) used in GTS12 results in dates that are ca. 0.64%, and respectively ca. 1.28%

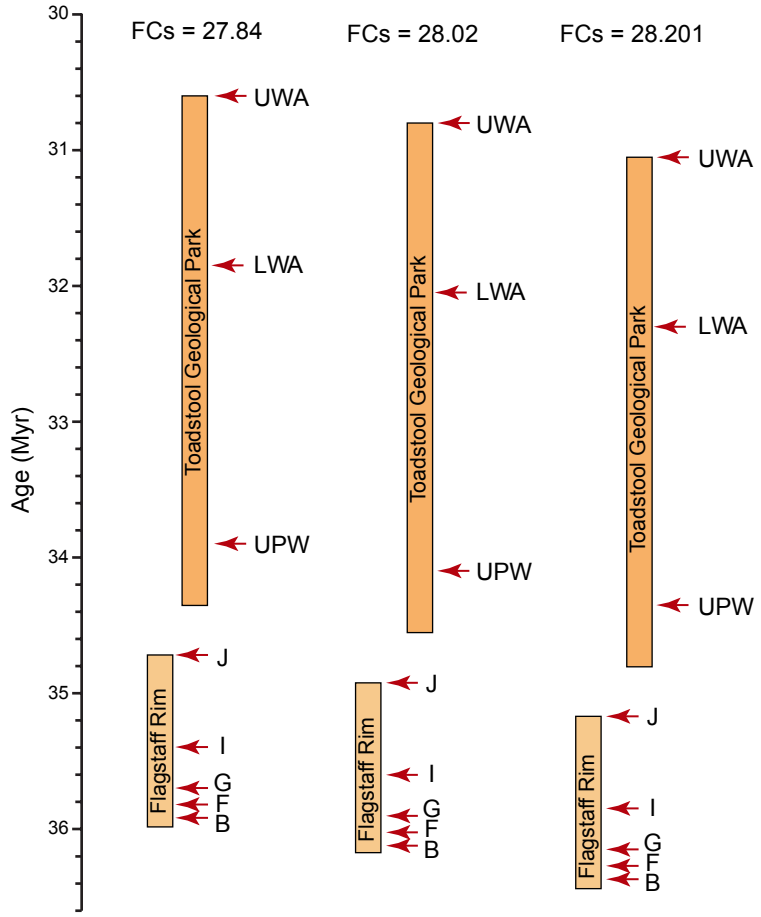

Figure 1.2 Impact of recalibration relative to progressively older values for the age of the FCs fluence monitor on data from the Flagstaff Rim and Toadstool Geological Park sections from the terrestrial record of North America, published by Swisher and Prothero (1990). Dates calculated relative to FCs=28.201 Ma are ca 1.28% (or 400 kyr) older than those originally published relative to FCs = 27.84 Ma. UWA – Upper Whitney Ash, LWA – Lower Whitney Ash, UPW – Upper Purplish White Layer.

older than the originally published ages (Figure 1.2).

1.4 The geomagnetic polarity time scale

Geomagnetic polarity time scales (GPTS) published over the last two decades relied on seafloor spreading models fitted to synthetic marine magnetic anomaly profiles (Heirtzler, 1968; Cande and Kent, 1992) using a small set of magnetostratigraphically well calibrated radio-isotopic dates from land-based sections as tie-points (Cande and

Kent, 1995; Huestis and Acton, 1997; Ogg and Smith, 2004; Vandenberghe et al, 2012). Progress in time scale calibration was focused on increasing the number and improving the quality of the tie-points through the preferential use of high-precision $^{40}Ar/^{39}Ar$ dates which have gradually replaced less precise K-Ar data, while, at the same time, incorporating the results of successive revisions of the FCs fluence monitor age and the ^{40}K decay constant.

The GPTS of Cande and Kent (1992) relied on only seven Paleogene tie-points, while the GPTS in GTS04 included 16 dates, of which six were based on combined radio-isotopic and cyclostratigraphic calibration, and the remaining 10 were a mixture of K-Ar and ^{40}Ar-^{39}Ar dates, with the latter calibrated relative to an FCs age of 28.02 Ma (Renne et al., 1998) and the decay constants of Steiger and Jäger (1977). By the time GTS12 was published, the number of radio-isotopic tie-points had almost doubled, and included both $^{40}Ar/^{39}Ar$ and $^{206}Pb/^{238}U$ dates, with updated values for the age of $^{40}Ar/^{39}Ar$ standards (28.201 Ma, Kuiper et al., 2008) and the total ^{40}K decay constant (0.5463, Min et al., 2000). GTS12 also included, for the first time, a rigorous assessment of the uncertainties associated with the age of individual magnetic reversals. In spite of this, the calibration of the EOT interval is still mostly constrained by recalculated legacy biotite $^{40}Ar/^{39}Ar$ dates from the Northern Apennines (Odin et al., 1991a, 1991b; Coccioni et al., 2008) (Figure 1.3). Alternative dates published by Swisher and Prothero (1990), from the terrestrial record of North America were rejected because they were inconsistent (i.e. 300-400 kyr older) with data published in an abstract by Obradovich et al (1995), and additionally, concerns have been raised over the magnetostratigraphic calibration of some of the tuffs analysed (Hilgen and Kuiper, 2009).

Owing to the widespread application of astronomical tuning to Paleogene and Late Cretaceous records, the GPTS is currently in a state of transition from radio-isotopic

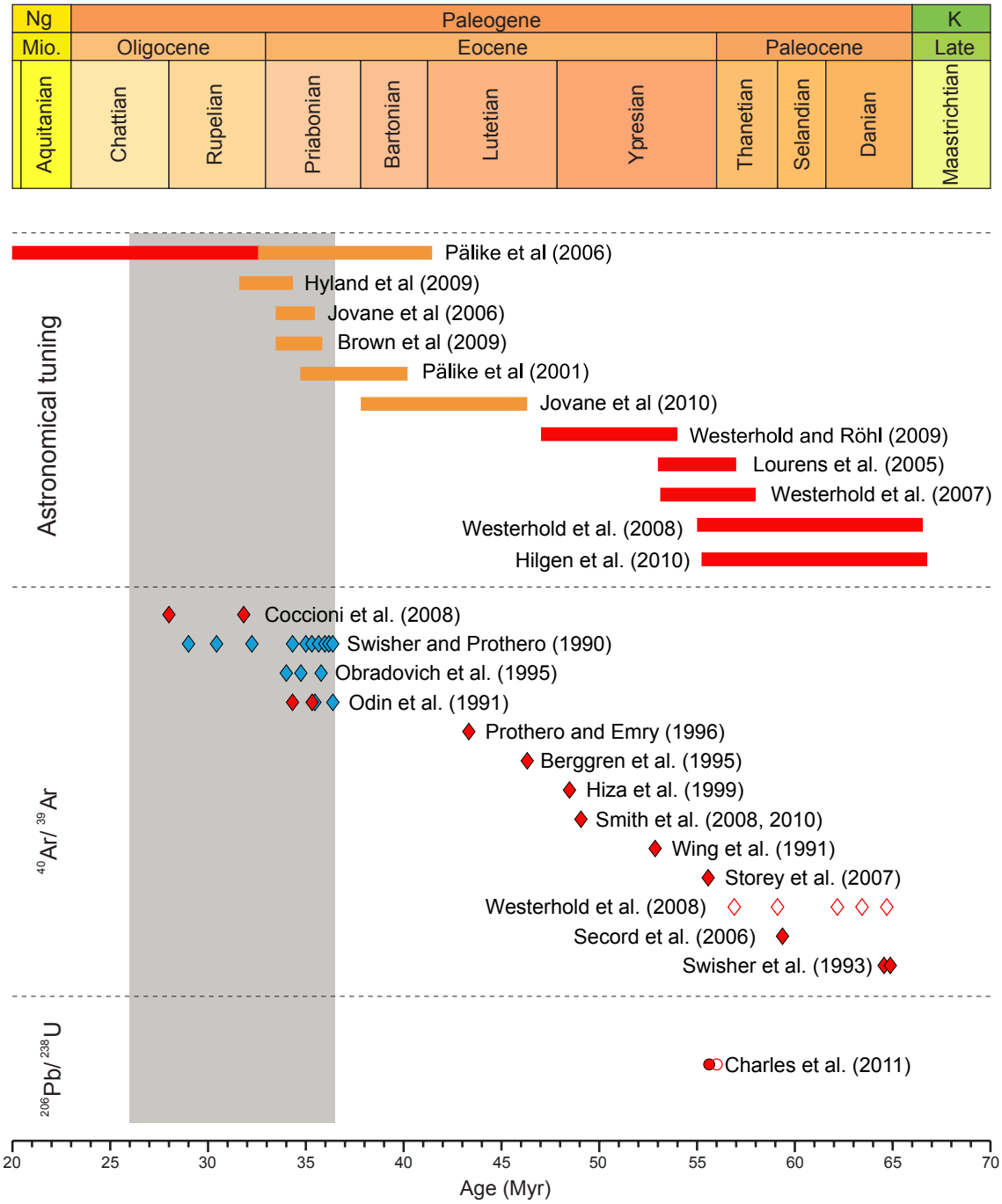

Figure 1.3 Data used to calibrate the GPTS in GTS12, plotted as red symbols, with additional astronomically tuned and $^{40}Ar/^{39}Ar$ datasets covering the Late Eocene also shown, as orange lines, and blue diamonds respectively. Closed diamonds and circles represent radio-isotopic dates, while open symbols indicate data with mixed radio-isotopic and cyclostratigraphic calibration.

to cyclostratigraphic age calibration. GTS12 includes an alternative, astronomically tuned GPTS, in which the Oligocene was calibrated based on the tuning of ODP Site 1218 by Pälike et al. (2006), and a series of interlinked orbital chronologies was presented for the Paleocene and Early Eocene (Figure 1.3). The ODP Site 1218 tuning is tied to present-day through the astronomical calibration of the Neogene time scale (Lourens et al., 2004; Hüsing et al., 2007; Hüsing et al., 2009), and provides an age model at the resolution of precession cycles. The calibration of the Paleocene is based on the tuning of Westerhold et al. (2008) with revisions by Hilgen et al. (2010) and is anchored by an age of 66.04 for the Cretaceous/Paleogene boundary. Linking these data to the tuning of ODP Site 1258 (Demerara Rise) and ODP Site 1262 (Walvis Ridge) (Westerhold et al., 2007; Westerhold and Röhl, 2009) resulted in an astronomically tuned time scale, at the resolution of the 405 kyr eccentricity cycles, for the interval between 66-47 Myr.

The tuning of the Late Eocene has not yet been accomplished, due, at least in part, to the relatively shallow position of the CCD during this period, which prevented the accumulation of long, continuous, carbonate rich pelagic successions suitable for tuning. Although several attempts have been made to tune parts of the Late Eocene (Pälike et al., 2001; Jovane et al., 2006, 2010; Brown et al., 2009; Hyland et al., 2009) discrepancies between individual tuned records have not been fully resolved and the Late Eocene "gap" in the tuned time scale was instead bridged by interpolation relative to the synthetic marine anomaly profile of Cande and Kent (1992), between the older end of the Oligocene time scale (base of C13n at 33.705 Ma), and the younger end of the Early Eocene tuned record (base of C21n at ca. 47.8 Ma) using a 6th order polynomial.

1.4.1 Discrepancies between the astronomically and radio-isotopically calibrated GPTS

The astronomically tuned and radio-isotopically calibrated GPTS of GTS12 present fully independent age estimates for Oligocene magnetic reversals. The two models are somewhat linked between 47-66 Ma, as radio-isotopic dates for the PETM (Charles et al., 2011), and the Cretaceous - Paleogene boundary (Kuiper et al., 2008; Renne et al., 2013) were used to inform the choice between the three Paleocene tuning options, each offset by one 405 kyr eccentricity cycle, provided by Westerhold et al. (2008).

Although the astronomically tuned and radio-isotopically calibrated GPTS of GTS12 are in relatively good agreement for parts of the Eocene and the Paleocene, discrepancies on the order of 0.4-0.8 Myr exist between the two in the Oligocene and the Early Eocene (Figure 1.4). In the final GPTS compilation, which combined the results of the two calibration options, the Early Eocene discrepancy was attributed to errors in the magnetic polarity pattern of ODP Site 1258 on which the tuning is based, and a radio-isotopic calibration was preferred for this interval. The Oligocene discrepancy is thought to be caused by the incorporation, in the absence of more reliable sanidine dates, of potentially inaccurate biotite $^{40}Ar/^{39}Ar$ data for the EOT interval. This interpretation is supported by a recent study by Hora et al. (2010) who demonstrated that offsets of several hundreds of kyr between dates on cogenetic biotites and sanidines may be recorded in Cenozoic samples. Nevertheless, the biotite dates, if accurate, would indicate that the tuning of the Oligocene at ODP Site 1218 by Pälike et al. (2006) is inaccurate. This hypothesis is also supported by recalculated $^{40}Ar/^{39}Ar$ dates from terrestrial sedimentary successions in Wyoming and western Nebraska, which imply that the (magnetostratigraphically calibrated) Eocene – Oligocene boundary is ca. 400 kyr older than astronomically tuned estimates (Hilgen and Kuiper, 2009), however an error in the magnetostratigraphy of the North American records cannot be ruled out.

The discrepancy between the astronomically calibrated Late Eocene – Oligocene

time scale and $^{40}Ar/^{39}Ar$ dates from western Nebraska also has implications for the correlation of marine and terrestrial records of the Oi-1 event. When benthic foraminiferal $\delta^{18}O$ data from the Atlantic, Pacific, Indian, and Southern oceans are calibrated relative to the astronomically tuned GPTS of GTS12, the Early Oligocene $\delta^{18}O$ shift appears to be globally synchronous, with peak $\delta^{18}O$ values reached around 33.6 Ma, with small

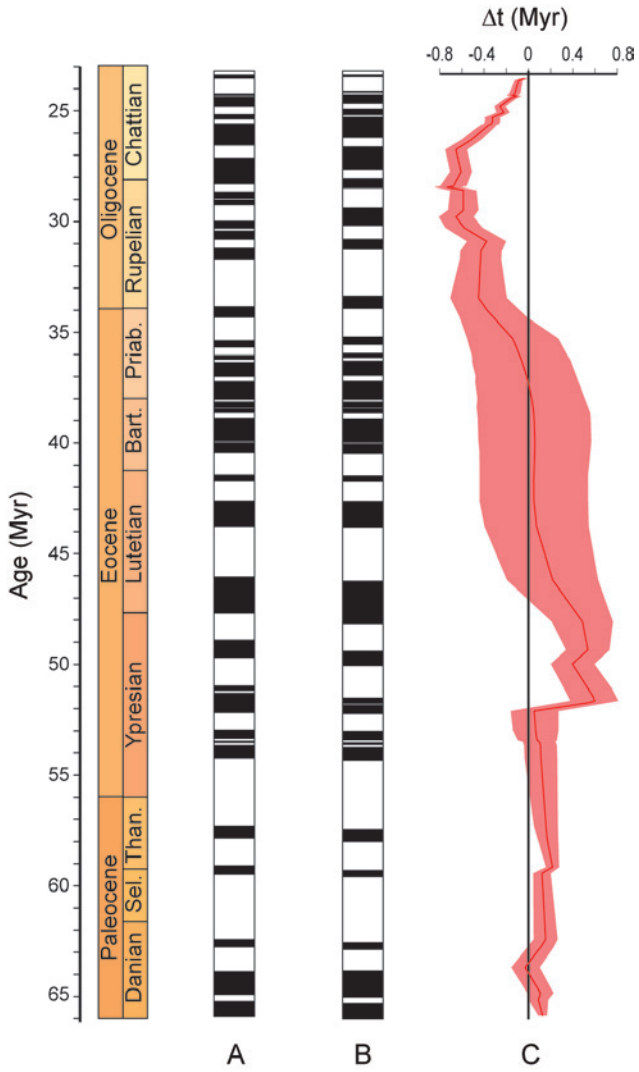

Figure 1.4 Comparison between different calibration options for the GPTS in GTS12 showing A- the radio-isotopically calibrated GPTS, with $^{40}Ar/^{39}Ar$ data calculated relative to an age of 28.201 for FCs (Kuiper et al., 2008) and the decay constants of Min et al. (2000), B – the astronomically tuned GPTS, and C – the difference between magnetic reversal dates obtained using the two calibration options, in Myr, with negative (positive) values indicating that the astronomically tuned dates are younger (older) than those based on interpolation between radio-isotopic tie-points, and an uncertainty envelope reflecting the 2σ uncertainty of radio-isotopically calibrated magnetic reversal ages.

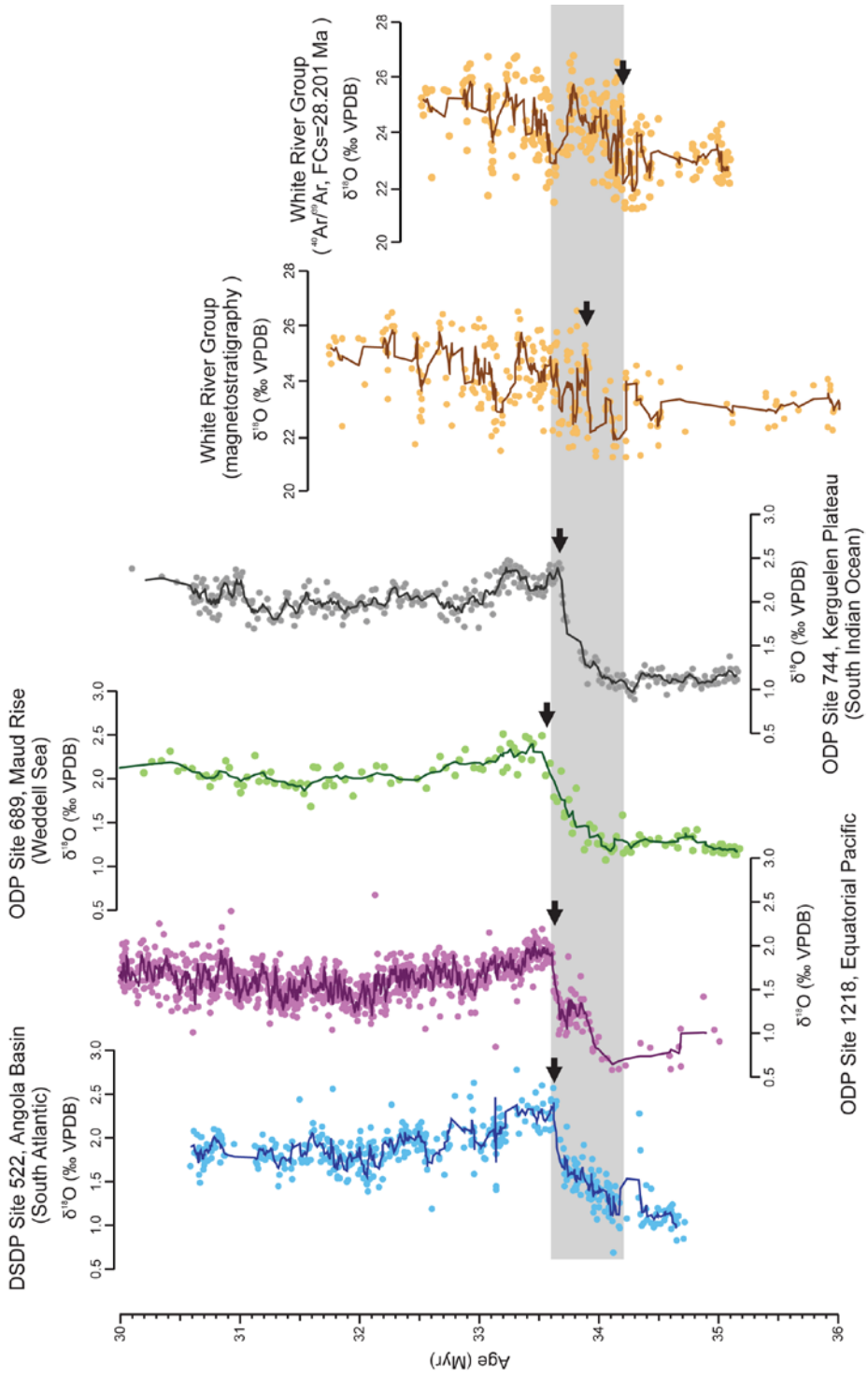

Figure 1.5 Numerical age calibration of marine and terrestrial records of the Early Oligocene $\delta^{18}O$ shift. Marine $\delta^{18}O$ data were extracted from the stable isotope compilation of Cramer et al. (2009), recalibrated to the astronomically tuned GPTS of GTS12. Two calibration options are shown for the terrestrial $\delta^{18}O$ record of the White River Group from western Nebraska (Zanazzi et al., 2007, 2009) (see text for details). Black arrow shows the position of early Oligocene $\delta^{18}O$ shift at each locality.

discrepancies potentially caused by varying sampling resolution and small errors in magnetostratigraphy (Figure 1.5). Calibration of the terrestrial $\delta^{18}O$ data of Zanazzi et al. (2007, 2009) from western Nebraska relative to GTS12, using the magnetostratigraphy of Prothero (1996), places a sharp increase in $\delta^{18}O$ values, indicative of cooling, at ca. 33.9 Ma, around 300 kyr before the marine $\delta^{18}O$ peak, while calibration of the same record relative to the $^{40}Ar/^{39}Ar$ data of Swisher and Prothero (1990), recalculated to an age of 28.201 for FCs (Kuiper et al., 2008) results in an even older date (ca. 34.2 Ma), increasing the discrepancy to ca. 600 kyr.

Combined these studies demonstrate the strength and weakness of the different methods available for the calibration of the Cenozoic timescale. Ultimately an objective integrated approach that exploits the strengths of one method to inform another will be best served to develop a robust (stable and high-accuracy/precision) timescale for the EOT.

1.5 High-precision $^{206}Pb/^{238}U$ dating and the stratigraphic record

Pre-2000, U-Pb zircon isotope dilution thermal ionization mass spectrometry (ID-TIMS) has not been applied to the calibration of the Cenozoic time scale, because high Pb analytical blanks precluded the accurate measurement of Pb ratios in young zircons. Notable exceptions relevant to this thesis include relatively low precision (± 1%) U-Pb data on zircon and monazite from the Northern Apennines published by Oberli and Meier (1991), and a small set of U-Pb zircon dates from the terrestrial record of North America (Scott et al., 1999). From the late 1990s onward, gradual improvements in laboratory procedures resulted in a reduction of analytical Pb and U blank levels to a few hundred femtograms, allowing age determination with uncertainties of less than ± 0.2% for zircons crystals, or crystal fragments, containing only a few picograms of radiogenic Pb.

In contrast to $^{40}Ar/^{39}Ar$ dating, $^{206}Pb/^{238}U$ dates are calculated relative to enriched isotope tracer solutions such that accuracy and precision of the U/Pb dates are determined by the accuracy and precision of the gravimetric calibration of the isotopic tracer (Condon et al., in-review), and that of the ^{238}U decay constant, which has been determined through counting experiments and has an uncertainty of ± 0.11 % (Jaffey et al., 1971). Two mixed U-Pb tracer solutions (ET535 - ^{205}Pb-^{233}U-^{235}U, and ET2535 - ^{202}Pb-^{205}Pb-^{233}U-^{235}U), along with three mixed U/Pb gravimetric solutions, and three synthetic mixed U/Pb "age" solutions equivalent to concordant (at ca. 10, 100, 500, and 2000 Ma) isotopic compositions were developed as part of the EARTHTIME initiative in order to improve the overall accuracy and inter-laboratory reproducibility of the U-Pb method (Condon et al., 2007), and were distributed to laboratories specializing in high-precision ID-TIMS U-Pb age determinations. The systematic uncertainty arising from the use of the EARTHTIME isotopic tracers is equivalent to less than 0.03% of the calculated ages, and the isotopic composition of the solution is traceable, through gravimetric calibration, to the definition of SI units for mass (kg) and radioactivity (Bq) (Condon et al., in review). Given these improvements, it can be confidently said that measured $^{206}Pb/^{238}U$ ratios accurately represent the isotopic composition of analysed zircon crystals, or fragments, however the degree to which these zircon dates can be interpreted as deposition/eruption ages is influenced by a series of geological factors.

Post-crystallization Pb-loss is one such factor that can perturb the U-Pb system, and results in younger apparent U-Pb dates. The strength of the U-Pb method lies in the presence of two independent, but chemically identical decay chains, ^{238}U-^{206}Pb and ^{235}U-^{207}Pb, with different parent half-lives yielding independent radio-isotopic dates. Concordance between $^{206}Pb/^{238}U$ and $^{207}Pb/^{235}U$ ages is typically used to assess closed system behaviour in Precambrian zircons, however this method becomes ineffective at identifying subtle Pb loss or inheritance for samples from the younger end of the time

scale, due to the shape of the concordia curve and the relatively large uncertainty of the $^{207}Pb/^{235}U$ dates. In order to mitigate Pb loss in zircons, Mattinson et al. (2005) developed a 'chemical abrasion' pre-treatment technique that is now commonly employed in high-accuracy U-Pb time scale studies (Mundil et al., 2004; Davydov et al., 2010; Charles et al., 2011; Dunn et al., 2012; Wotzlaw et al., 2013; Rivera et al., 2013). Although this method has been shown to be very efficient at selectively removing crystal volumes susceptible to Pb loss due to radiation damage arising from high U content (Mattinson et al., 2005, 2010) it cannot guarantee complete mitigation of Pb loss effects. However studies of older zircons where concordance can be quantified to a high-degree of resolution demonstrate the effectiveness of the method and illustrate that when Pb-loss does occur, it is not reproducible. Provided that the dataset is sufficiently large, and the individual analyses are sufficiently precise, data points affected by Pb-loss can be identified, as these processes tend to result in non-reproducible ages (i.e., lone 'young' dates).

Another factor relates to the high closure temperature of zircons, such that crystallization prior to a volcanic eruption can be recorded in the U-Pb systematics of the zircon, resulting in older apparent ages, with pre-eruptive magma chamber residence times of up to a few hundred kyr, which is significant for samples of Paleogene age. This issue has been discussed in recent literature. One group suggests, based upon a dataset of limited quality, that pre-eruptive zircon residence is prevalent and the probability of deriving an eruptive age from an interpreted zircon U-Pb data set is limited, proposing that an ad hoc additional uncertainty (+ 0/-200 kyr) be added to all U-Pb zircon dates (Simon et al., 2008). An alternative view is that although pre-eruptive residence does occur, high-precision single crystal/fragment U-Pb data can be used to mitigate the effect of protracted zircon growth, by selecting the youngest group of statistically equivalent (at the 2σ level) closed system dates for the calculation of an inverse variance weighted mean age. Increasingly this approach is resulting in U-Pb zircon dates that are in concordance

with $^{40}Ar/^{39}Ar$ data sets (Crowley et al., 2008; Rivera et al., 2013; Sageman et al., in review, Macho et al., in review). Although the interpretation of an eruption age based on a relatively small set of single zircon dates from an isolated sample can be somewhat subjective, the identification of data points affected by Pb-loss or pre-eruptive magma chamber residence becomes more straightforward in successions that host several closely spaced volcanic tuffs, because, in the absence of stratigraphic disturbances, interpreted $^{206}Pb/^{238}U$ dates must conform to the law of superposition.

Following from these caveats, $^{206}Pb/^{238}U$ dates typically rely on the interpretation of a set of single crystal analyses where the single data point uncertainty is on the order of 0.1-0.2 % (compared to ca. 1% for $^{40}Ar/^{39}Ar$). Weighted mean dates are normally based upon a relatively small number of analyses (3 to 7) such that the interpreted date uncertainty is typically close to the uncertainty of the most precise analyses.

1.6 Thesis structure

This chapter introduces and summarises the current state of knowledge on the numerical age calibration of the Late Eocene and Oligocene, and the integration of marine and terrestrial records of environmental change at the EOT, and discusses the numerical dating methods currently used in time scale calibration studies. The following four chapters deal with specific issues related to Late Eocene and Oligocene time scale calibration, by integrating high-accuracy $^{206}Pb/^{238}U$ (zircon) geochronology of volcanic tuffs from key Eocene-Oligocene sedimentary successions with new and previously published magnetostratigraphic and biostratigraphic datasets.

Chapter 2 focuses on $^{206}Pb/^{238}U$ dating of zircons from volcanic tuffs from the Umbria-Marche succession in Italy, which hosts the Global Stratotype Section and

Point (GSSP) of the Eocene-Oligocene boundary at Massignano, and a proposed site for the GSSP of the Chattian at Monte Cagnero. The aim of this chapter is to assess the accuracy of legacy/recalculated $^{40}Ar/^{39}Ar$ dates used for the radio-isotopic calibration of the GPTS in GTS12 via comparison with new U-Pb (zircon) ID-TIMS data, test the validity of the astronomically tuned age model for the Oligocene based on published magnetostratigraphy of the Monte Cagnero section, provide accurate and precise dates for the Eocene-Oligocene and Rupelian-Chattian boundaries, and evaluate the potential diachroneity of planktonic foraminifera events between the western Tethys and other oceanic basins during the Late Eocene and Oligocene.

Chapter 3 focuses on refining the geochronology of the North American terrestrial record of the EOT through $^{206}Pb/^{238}U$ (zircon) geochronology of volcanic tuffs from the White River Group at two localities, Flagstaff Rim, in Wyoming, and Toadstool Geological Park, in western Nebraska. The aim of this chapter is to improve the objective comparison between marine and terrestrial records of environmental change at the EOT, to evaluate the accuracy of previously published $^{40}Ar/^{39}Ar$ dates, and to provide an accurate and precise chronostratigraphic framework for the evolution of North American land mammals during the Late Eocene and Oligocene.

Chapter 4 presents a high-resolution magnetostratigraphic study of the Flagstaff Rim and Toadstool Park successions, the results of which are integrated with radio-isotopic data from Chapter 3 to provide high-accuracy temporal constraints for magnetic reversals between 36-30 Ma.The resulting magnetic polarity time scale is tested through comparison with the $^{206}Pb/^{238}U$ calibrated magnetic polarity record of the Umbria-Marche succession discussed in Chapter 2, and is used to evaluate the accuracy of recent editions of the radio-isotopically calibrated and astronomically tuned GPTS.

Chapter 5 brings together the key findings of the previous chapters, summarizing their implications for the numerical age calibration of the Late Eocene and Oligocene, and the integration of marine and terrestrial records of the EOT. Chapters 2, 3, and 4, were written as stand-alone manuscripts and are intended for publication.

2. A U-Pb (zircon) based age model for the marine Eocene-Oligocene transition

Abstract: The Paleogene time scale has been subject to a series of revisions over the last two decades, reflecting revisions in the assigned age of the Fish Canyon sanidine (FCs) neutron fluence monitor commonly used in $^{40}Ar/^{39}Ar$ geochronology, and a transition towards high-resolution astronomically tuned age models. In the 2012 edition of the Geological Time Scale (GTS12), legacy biotite $^{40}Ar/^{39}Ar$ dates from 'biotite-rich' beds from the pelagic Umbria – Marche sedimentary succession in Italy formed the basis for the radio-isotopic calibration of the Late Eocene and Oligocene. When calibrated relative to an FCs age of 28.201 Ma, these dates imply magnetic chron boundary ages that are up to 0.6 Myr older than those extracted from astronomically tuned age models of the interval between 26-36 Ma. In this chapter I present high-precision weighted mean $^{206}Pb/^{238}U$ (zircon) CA-ID-TIMS dates for eleven biotite-rich beds from the Umbria-Marche sedimentary succession, and evaluate the impact on these dates on the calibration of the Eocene – Oligocene time scale. Interpreted $^{206}Pb/^{238}U$ dates are 0.4-0.5 Myr younger than recalculated legacy $^{40}Ar/^{39}Ar$ biotite data. The data are used to test and quantify the potential diachroneity of planktonic foraminifer bioevents between the western Tethys and other oceanic basins. While several Oligocene taxa persists up to 0.6 kyr longer in the western Tethys than in lower latitude open ocean settings the last occurrence of hantkeninids and the last common occurrence of *Chiloguembelina cubensis,* used as indicators for the Eocene –Oligocene and Rupelian-Chattian boundaries respectively, represent robust biostratigraphic markers, and do not appear to be time-transgressive. Integrating our data with the established magnetic polarity record of the Umbria-Marche succession yields magnetic reversal ages that support the accuracy of the astronomically tuned Oligocene time scale.

2.1 Introduction

In recent editions of the Geological Time Scale radio-isotopic dating has been gradually replaced by astronomical tuning of deep marine records recovered through ODP and IODP expeditions as a preferred calibration method for the Paleogene Period (Luterbacher et al., 2004; Vandenberghe et al., 2012). The main advantage of astronomical tuning lies in the method's potential for the development of high-resolution chronologies for continuous records spanning several Myr, and its ability to directly date events of interest (e.g. magnetic reversals, and biostratigraphic markers), thereby eliminating the uncertainties inherent to time scale calibration based on interpolation between a relatively small number of published radio-isotopic dates.

At present, a series of interlinked orbital chronologies, which are anchored to present day, provide continuous coverage for the Neogene and Oligocene (Lourens et al, 2004; Pälike et al., 2006; Hüsing et al., 2009; Hilgen et al., 2012) and "floating" astronomical time scales, anchored to an age of 66.04 ± 0.05 (2σ) Ma for the Cretaceous – Paleogene boundary (Vandenberghe et al., 2012), have been developed for the Paleocene and much of the Early and Middle Eocene (Westerhold et al., 2007; Westerhold et al., 2008; Westerhold and Röhl, 2009; Hilgen et al., 2010). The astronomically calibrated Oligocene time scale (ATPS06) is based on the tuning of benthic foraminifera stable isotope data from ODP Site 1218 in the Equatorial Pacific at the resolution of precession cycles (Pälike et al., 2006), and although this record extends back to ca 41 Ma, the tuning of the Late Eocene is considered unreliable, because sedimentation at this locality took place below the carbonate compensation depth prior to the Eocene-Oligocene transition (Coxall et al., 2005; Pälike et al., 2006). Several other workers have published "floating" astronomical time scales for parts of the Late Eocene (Pälike et al., 2001; Jovane et al., 2006, 2010; Brown et al., 2009; Hyland et al., 2009), however the presence of interpretative

discrepancies and gaps between these time scales precludes the development of a complete orbital age model for the Paleogene.

The 2012 edition of the Geological Time Scale (GTS12) presented two options for bridging the Late Eocene "gap" in the tuned records, which extends between 34-47 Ma, both based on numerical age calibration of the marine magnetic anomaly profile of Cande and Kent (1992). One of these options relied on astronomically tuned magnetic reversal ages from the older end of the Oligocene time scale (33.71 Ma for the base of C13n), and the younger end of the Paleocene –Middle Eocene astrochronology (47.8 Ma for the base of C21n) for numerical age control. The other option used various biotite and sanidine $^{40}Ar/^{39}Ar$ dates, calibrated relative to an age of 28.201 ± 0.046 Ma (2σ) for the Fish Canyon sanidine (FCs) neutron fluence monitor (Kuiper et al., 2008) and, subordinately, $^{206}Pb/^{238}U$ data to develop a radio-isotopically calibrated Paleogene geomagnetic polarity time scale (Vandenberghe et al., 2012). Late Eocene – Early Oligocene magnetic reversal ages derived from the radio-isotopically calibrated age model were up to 600 kyr older than those yielded by astronomically tuning and interpolation between astronomically tuned dates (Vandenberghe et al., 2012).

This discrepancy between the radio-isotopically and astronomically calibrated age models was attributed to the use of anomalously old $^{40}Ar/^{39}Ar$ biotite dates from the Umbria Marche succession in Italy to calibrate the Late Eocene and Early Oligocene, This hypothesis is supported by recent studies indicating that biotite dates can potentially record ages that are biased towards older values due to ^{39}Ar recoil phenomena and incorporation of excess ^{40}Ar (Min et al., 2001; Kuiper et al., 2008; Hora et al., 2010; Schmitz, 2012). However, the fact that recalculated biotite $^{40}Ar/^{39}Ar$ dates from the Umbria-Marche succession indicate that Late Eocene and Oligocene magnetic reversals may be ca 600 kyr older than astronomically tuned estimates also raises the possibility

of an error in the tuning of the ODP Site 1218 record from the Equatorial Pacific (Pälike et al., 2006), which forms the backbone of the astronomically calibrated Oligocene time scale. An error in the ODP Site 1218 tuning would also be consistent with legacy $^{40}Ar/^{39}Ar$ biotite and sanidine dates from the terrestrial Eocene-Oligocene record of North America (Swisher and Prothero, 1990; Obradovich et al., 1995), which, when calibrated relative to an FCs age of 28.201 Ma, give an age of ca. 34.35 Ma for the Eocene-Oligocene boundary, 600 kyr older than the astronomically tuned age of 33.79 Ma reported from ODP Site 1218 (Pälike et al., 2006). This makes the Eocene-Oligocene transition a key interval for time scale calibration, and it is critical that uncertainties in both radio-isotopic and cyclostratigraphic datasets are examined and objectively evaluated.

The pelagic record of the Umbria-Marche basin provides continuous coverage of Late Eocene and Oligocene time, with a sedimentary succession that contains radio-isotopically datable volcanosedimentary beds, and consists of rhythmic alternations of marls and limestones, amenable to the development of floating astronomical time scales. The Umbria-Marche succession hosts the GSSP for the base of the Oligocene at metre level 19 of the Massignano section based on the last occurrence (LO) of the planktonic foraminifer genus *Hantkenina* (Premoli-Silva and Jenkins, 1993), as well as a proposed site for the GSSP of the base of the Chattian stage at metre level 189 of the Monte Cagnero section based on the last common occurrence (LCO) of *Chiloguembelina cubensis* (Coccioni et al., 2008). As a result, the Umbria-Marche record has been the focus of a series of high-resolution studies which resulted in the development of an excellent bio- and magnetostratigraphic framework (Bice and Montanari, 1988; Coccioni et al., 1988, 2008, 2013; Parisi et al., 1988; Nocchi et al., 1988; Lowrie and Lanci, 1994; Spezzaferri et al., 2002; Coccioni and Galeotti, 2003; Dal'Antonia et al., 2003; Jovane et al., 2004; Coccioni et al., 2009; Jovane et al., 2013), making it an ideal setting in which to test the accuracy of radio-isotopically calibrated and astronomically tuned time scales of the

Eocene-Oligocene transition (EOT).

Although significant effort has been directed towards the numerical age calibration of the Umbria-Marche succession, published age constraints are not in mutual agreement. In addition to the potential inaccuracy of $^{40}Ar/^{39}Ar$ biotite dates discussed above, floating astronomical time scales developed for the Massignano and Monte Cagnero sections yield a range of ages for the Eocene-Oligocene transition between 33.71-34.10 Ma (van Mourik et al., 2005; Jovane et al., 2006; Brown et al., 2009; Hyland et al., 2009). These discrepancies become significant in light of the role played by the Umbria-Marche succession in the formal subdivision of geological time through the definition of GSSPs, as concerns have been raised over the possible diachroneity of key biostratigraphic markers, in particular the LO of hantkeninids (van Mourik and Brinkhuis, 2006) and the LCO of *Chiloguembelina cubensis* (van Simaeys et al., 2004) between the western Tethys and lower latitude open ocean settings, such as the ODP Site 1218 record. Although the planktonic foraminifera biozonation of the Cenozoic has recently been revised to include up-to-date age constraints calibrated relative to ATPS06, an accurate assessment of potential diachroneity is not possible using currently available data from the Umbria-Marche succession.

Efforts to improve the consistency of radio-isotopic and astronomically tuned Paleogene time scales must include a critical assessment of the accuracy of recalculated $^{40}Ar/^{39}Ar$ dates from the Umbria-Marche succession. This may be achieved through high-precision $^{206}Pb/^{238}U$ dating of zircons from the biotite-rich volcanic layers from the Massignano and Monte Cagnero sections, the accuracy of which is controlled by gravimetric calibration of isotopic tracer solutions developed through the EARTHTIME initiative, which can be traced back to SI units (Condon et al., in review; McLean et al., in review), and the accuracy of the ^{238}U decay constant, which has been determined through

counting experiments to a precision of ± 0.11% (Jaffey et al., 1971). The U/Pb method has benefited from the development of sample pre-treatment techniques that mitigate post-depositional Pb-loss through open system behaviour (Mattinson, 2005), and crucially, although zircon populations can include older, pre-eruptive crystals, the precision of single crystal Pb/U ratio measurements is sufficiently low (0.1-0.2%, or ca 30-60 kyr) to allow the detection of geological scatter. As a result, weighted mean ages calculated based on the youngest population of reproducible single crystal dates can be assumed to accurately represent eruption, and respectively deposition ages for volcanic tuff beds, and, significantly, the total uncertainties of calculated dates, including analytical, U/Pb tracer calibration, and decay constant components, are sufficiently low (on the order of 0.12-0.2% or 40 to 60 kyr at 30 Ma) to constrain Milankovitch frequencies. These uncertainties are also significantly smaller than the discrepancies between published astronomically calibrated Late Eocene-Oligocene time scales (i.e. the tuning of ODP Site 1218, and the interpolated astronomical age model for the Late Eocene in GTS12).

In this chapter I present $^{206}Pb/^{238}U$ dates from eleven volcanosedimentary beds intercalated in the Umbria-Marche succession with the aim of: i) establishing high-precision $^{206}Pb/^{238}U$ calibrated age-depth models for the Massignano and Monte Cagnero sections ii) testing the accuracy of astronomically calibrated time scales for the late Eocene and Oligocene and recently developed floating orbital chronologies for the Umbria-Marche succession itself; iii) evaluating the numerical age of the Eocene – Oligocene and Rupelian – Chattian boundaries; and iv) testing for potential diachroneity of planktonic foraminifera bioevents between the western Tethys and other oceanic basins.

2.2 Geologic setting and previous work

The Umbria-Marche sedimentary succession was deposited on the continental

margin of the Adriatic promontory, in a basin characterized by near continuous subsidence and sediment accumulation from the Triassic until the onset of folding and thrusting in the Apennines in Miocene times during closure of the Mesozoic Tethys Ocean (Alvarez and Montanari, 1988; Marchegiani et al., 1999). The Late Eocene – Oligocene part of the succession was deposited at a palaeodepth of 1000-1500 m (Coccioni and Galeotti, 2003) and comprises the Priabonian Scaglia Variegata Formation which consists of interbedded white and pink limestones and reddish marls and overlying late Priabonian - Chattian Scaglia Cinerea Formation which consists of alternating grey marls and marly limestones. Several volcanosedimentary beds, commonly referred to as biotite-rich layers in the literature, characterized by the presence of large (mm diameter) euhedral biotite flakes have been identified in both the Scaglia Variegata and Scaglia Cinerea formations. Their occurrence is thought to be connected to explosive volcanism linked to orogenesis in the Alps, although their exact source remains unknown (Montanari et al., 1988; Odin et al., 1991). Samples for this study were collected from three sections spanning the Late Eocene – Oligocene part of the Umbria Marche succession: Massignano, Monte Cagnero, and Pieve d'Accinelli (Figure 2.1).

2.2.1 Massignano

The Massignano section (43˚32'13"N, 13˚35'36"E) is located in an abandoned quarry in the Monte Conero area, ca 10 km south-east of Ancona. The section is 23 m thick, with the contact between the Scaglia Variegata and Scaglia Cinerea formation occurring at metre level 12 (Coccioni et al., 1988). Biostratigraphically, the section spans planktonic foraminifer zones E14-O1 of Berggren and Pearson (2005) (Figure 2.2), with the GSSP for the base of the Oligocene defined at metre level 19 relative to the base of the section based on the LO of genus *Hantkenina* (Premoli-Silva and Jenkins, 1993). The discovery of two Iridium-rich layers at metre levels 5.61 and 10.25 (Montanari

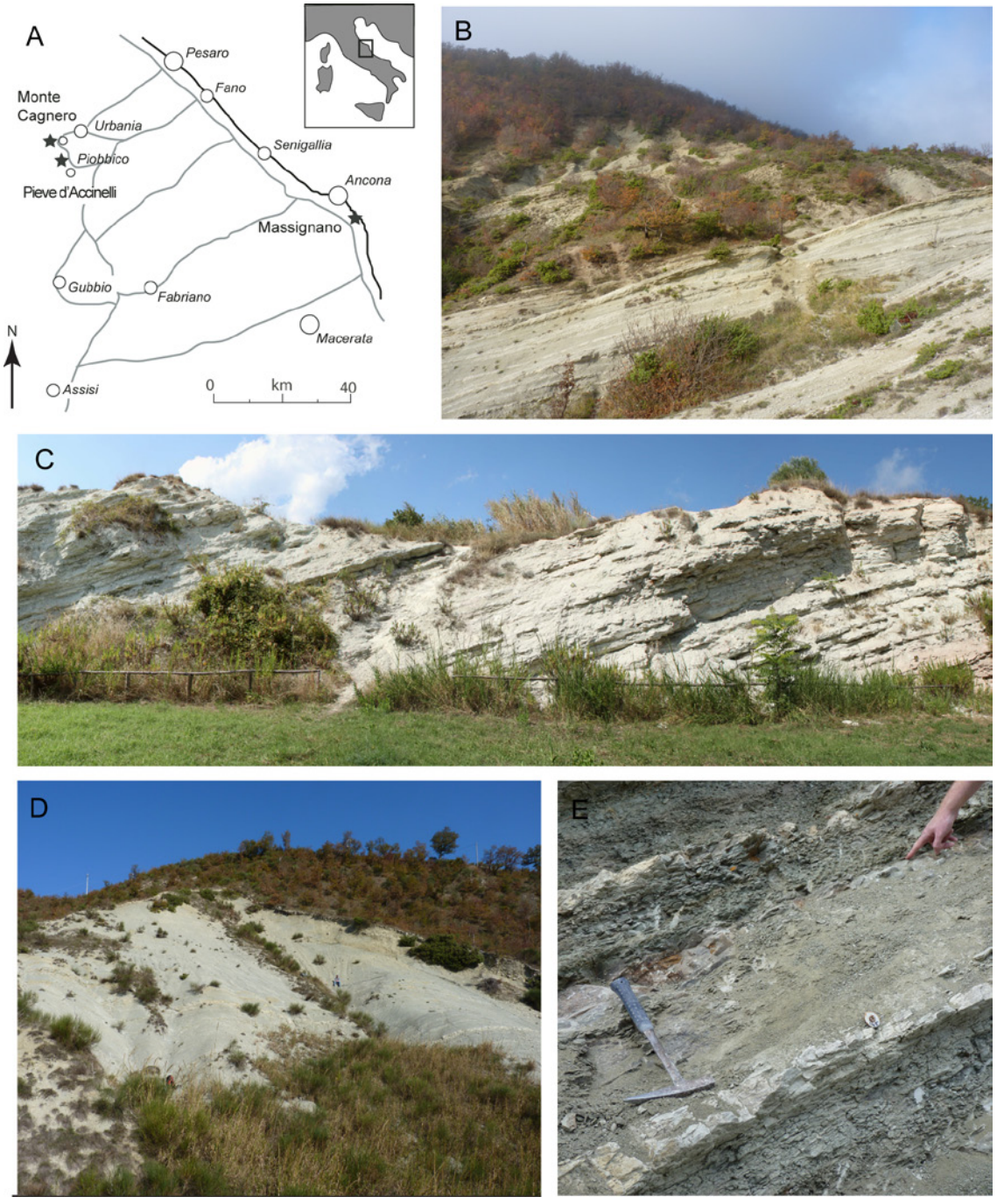

Figure 2.1 Sampled section. A – map showing the location of sampled sections from the Umbria – Marche basin, B – Monte Cagnero, C – Massignano, D – Pieve d'Accinelli, E – biotite-rich layer at metre level 145.2 of the Monte Cagnero section

et al., 1993), associated with Ni-rich spinel (Pierrard et al, 1998) and shocked quartz (Langenhorst and Clymer, 1996), as well as a broad ^{3}He anomaly between metre levels 2-15, thought to indicate a comet shower lasting ca 2.5 Myr (Farley et al., 1998) prompted a series of studies aimed at assessing the potential contribution of extra-terrestrial impacts to climatic deterioration in the Late Eocene. These studies indicated that the Late Eocene impacts had no quantitative effect on marine biotic communities where extinctions were driven by a long-term cooling trend initiated in the middle Eocene (Molina et al.,

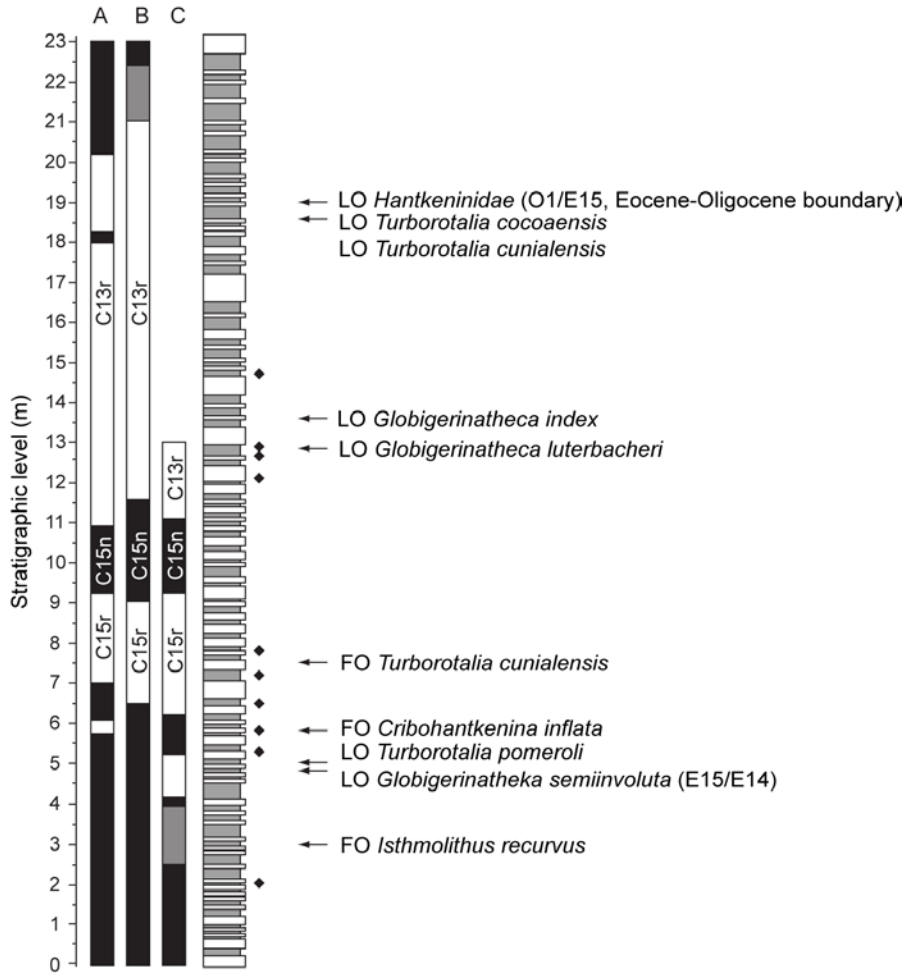

Figure 2.2 Lithostratigraphy, magnetostratigraphy and planktonic foraminifera biostratigraphy of the Massignano section. Alternating light and dark strata represent carbonate and marly beds, with black diamonds indicating biotite-rich volcanic beds. Magnetostratigraphy is based on A – Bice and Montanari (1988), B – Lowrie and Lanci (1994), and C- Jovane et al. (2004). Planktonic foraminifera biostratigraphy is based on Coccioni et al. (1988).

1993; Coccioni et al., 2000). However, quantitative analysis of planktonic and benthic foraminifera, ostracods, and dinocysts, and bulk rock $\delta^{18}O$ and $\delta^{13}C$ data indicated that significant changes in water mass structure occurred shortly after the impact at metre level 5.61, possibly related to the arrival of cold bottom waters from higher latitudes (Coccioni et al., 2000; Coccioni and Galeotti, 2003; Dal'Antonia et al., 2003). The lack of high resolution benthic foraminifera stable isotope records, and the limited extent of Oligocene deposits at Massignano, precluded the identification of the Early Oligocene 1-1.5 ‰ positive $\delta^{18}O$ shift that characterises other marine records of the EOT (Coxall et al., 2005, Katz et al., 2008; Pearson et al., 2008).

Established numerical age control for the Massignano section relies on magnetostratigraphy, K-Ar and $^{40}Ar/^{39}Ar$ dating of biotite from volcanosedimentary layers, and floating orbital age models. The first published magnetic polarity pattern for the outcrop was based on a sampling resolution of ca 0.5 m and identified five normal polarity zones which were correlated to magnetochrons C16n – C13n, and included a short normal polarity zone within chron C13r (Bice and Montanari, 1988). A second study, with an average sampling resolution of 35 cm for the 3 m interval surrounding the Eocene – Oligocene boundary and 70 cm for the rest of the section, was conducted by Lowrie and Lanci (1994) and yielded a similar magnetic polarity pattern, although it failed to identify any normal polarity samples within C13r (Figure 2.2). The discrepancy between the stratigraphic placement of magnetic reversals between the two studies is on the order of 40 cm (equivalent to ca 40 kyr assuming a sedimentation rate around 10 m/Myr, Brown et al., 2009) with the exception of the base of chron C13n which occurs ca 2 m higher up in the section in the study of Lowrie and Lanci (1994), although its precise position could not be constrained due to the poor magnetic quality of the samples. More recently Jovane et al. (2007) conducted a magnetostratigraphic study focused on the interval between metre levels 0-13 of the section, with samples collected roughly every 15 cm. This higher

resolution record allowed the identification of a previously unreported reversed polarity zone which correlates to C16n.1r, however sampling could not be extended into the upper part of the section due to the lack of suitable lithologies.

Ten biotite-rich layers have been identified in the Massignano section, and published radio-isotopic dates are summarized in Table 2.1. The first K/Ar and Rb/Sr dates were published by Montanari et al. (1985), and together with selected dates from the Contessa Quarry and Monte Cagnero sections yielded an interpolated age of 33.7 ± 0.5 Ma for the Eocene – Oligocene boundary (Montanari et al., 1988), which was ca. 2.7 Myr younger than the, at that time, widely accepted age of 36.3 Ma of Berggren et al. (1985). The first stepwise-heating $^{40}Ar/^{39}Ar$ biotite dates with reliable plateaus were reported by Odin et al., (1991a, 1991b) for biotite-rich layers at metre levels 14.7 (34.1 ± 0.2 Ma) and 12.7 (34.9 ± 0.2 Ma). These dates were obtained on multigrain fractions and were calculated relative to an age of 127.7 for the LP-6 biotite standard. Recalibration relative to the astronomically calibrated age of 28.201 ± 0.046 for the Fish Canyon sanidine (Kuiper et al., 2008) using the intercalibration factor of Baksi et al. (1996), resulted in ages of 34.4 ± 0.2 Ma and 35.2 ± 0.2 Ma respectively. Alternative dates for the biotite-rich beds at metre levels 7.2, 12.7 and 14.7 were published by Montanari et al., (1993) based on a compilation of all available K-Ar, Rb-Sr (Montanari et al., 1988; Montanari et al., 1985), $^{40}Ar/^{39}Ar$ (Odin et al., 1991), and limited U-Pb zircon and Th-Pb monazite dates (Oberli and Meier, 1991).

Jovane et al., (2006) tuned the interval between metre levels 4-20 of the section, using the magnetic reversal dates of Cande and Kent (1995) as a starting point. They performed spectral analysis of a high-resolution (5 cm) magnetic susceptibility dataset, which showed statistically significant peaks at 32, 72, and 284 cm in the depth domain, corresponding to obliquity (41 kyr) and short (110 kyr) and long eccentricity (405 kyr)

BRL	Age (± 2σ, Ma)	Mineral	System	Reference
Monte Cagnero				
208.3 m	28.0 ± 0.7	biotite	K-Ar	Montanari et al., 1988
	27.0 ± 0.2	biotite	$^{40}Ar/^{39}Ar$	Coccioni et al., 2008
145.5 m	31.7 ± 0.6	biotite	K-Ar	Montanari et al., 1998
	31.8 ± 0.2	biotite	$^{40}Ar/^{39}Ar$	Coccioni et al., 2008
Massignano				
14.7 m	34.6 ± 0.3	biotite	K-Ar	Montanari et al., 1988
	34.1 ± 0.2	zircon	U-Pb	Oberli and Meier, 1991
	34.3 ± 0.3	zircon	U-Pb	Oberli and Meier, 1991
	34.0 ± 0.4	monazite	U-Th	Oberli and Meier, 1991
	34.2 ± 0.4	monazite	U-Th	Oberli and Meier, 1991
	34.4 ± 0.2	biotite	$^{40}Ar/^{39}Ar$	Odin et al., 1991
12.9 m	33.7 ± 0.4	biotite	K-Ar	Montanari et al., 1988
	34.0 ± 0.4	biotite	K-Ar	Montanari et al., 1988
	34.4 ± 0.2	biotite	Rb-Sr	Montanari et al., 1988
12.7 m	35.2 ± 0.2	biotite	$^{40}Ar/^{39}Ar$	Odin et al., 1991
7.2 m	34.7 ± 0.9	biotite	K-Ar	Montanari et al., 1988
	35.1 ± 0.8	biotite	K-Ar	Montanari et al., 1988
	36.1 ± 1.0	biotite	K-Ar	Montanari et al., 1988
	36.0 ± 0.5	biotite	Rb-Sr	Montanari et al., 1988
	36.5 ± 0.6	biotite	Rb-Sr	Montanari et al., 1988
	34.9 ± 0.4	monazite	U-Th	Oberli and Meier, 1991
	34.9 ± 0.3	monazite	U-Th	Oberli and Meier, 1991

Table 2.1 Summary of published radio-isotopic age constraints from the Massignano and Monte Cagnero sections. All $^{40}Ar/^{39}Ar$ data recalculated relative to FCs = 28.201 Ma (BRL - biotite-rich layer)

signals. First order tuning was carried out by matching their 284 cm cycle to the 405 kyr component of the La2004 numerical solution (Laskar et al., 2004), assuming that susceptibility minima correspond to eccentricity minima. The tuning was then refined by correlating minima and maxima in the obliquity (41 kyr) filtered time series of the La2004 solution to the midpoint of consecutive marl and carbonate beds, identifying 53 obliquity cycles, resulting in a duration of ca. 2.1 Myr for the investigated interval between metre

levels 4 and 20, with an average sedimentation rate of ca. 7 m/Myr , and an age of 33.714 Ma for the Eocene – Oligocene boundary.

An alternative astronomically tuned time scale for the Massignano section was published by Brown et al. (2009) who matched band-pass-filtered $CaCO_3$ concentration and magnetic susceptibility data from the interval between metre levels 0.5 and 23 to the long and short eccentricity components of the La2004 solution (Laskar et al., 2004), using the mean radio-isotopic dates calculated by Montanari et al. (1993) for biotite-rich beds at metre level 7.2, 12.7 and 14.7 as a starting point. Using a phase relationship similar to that of Jovane et al. (2004), with susceptibility minima corresponding to eccentricity minima, Brown et al. (2009) arrived at an age of 33.91 ± 0.05 Myr for the Eocene – Oligocene boundary, and also reported astronomically tuned ages for the biotite-rich layers at metre levels 7.2 (35.13 ± 0.05 Ma), 12.7 (34.56 ± 0.05 Ma) and 14.7 (34.32 ± 0.05 Ma).

2.2.2 Monte Cagnero

The Monte Cagnero section (43˚38’50”N, 12˚28’05”E) is located ca. 6 km southwest of Urbania, and ca. 100 km north-west of the Massignano section (Figure 2.1). The section is 225 m thick and covers the Late Eocene and most of the Oligocene with metre level 100 correlated to the base of the Massignano section based on the presence of a regionally recognisable pink band in the upper part of the Scaglia Variegata Formation (Hyland et al., 2009). The Eocene – Oligocene boundary has been identified at metre level 114.1 based on the LO of hantkeninids (Hyland et al., 2009). We focused on the stratigraphic interval between metre levels 100 – 215 (Figure 2.3).

The part of the Monte Cagnero section investigated spans planktonic foraminifer zones E14-O6 of Berggren and Pearson (2005) and calcareous nannoplankton zones

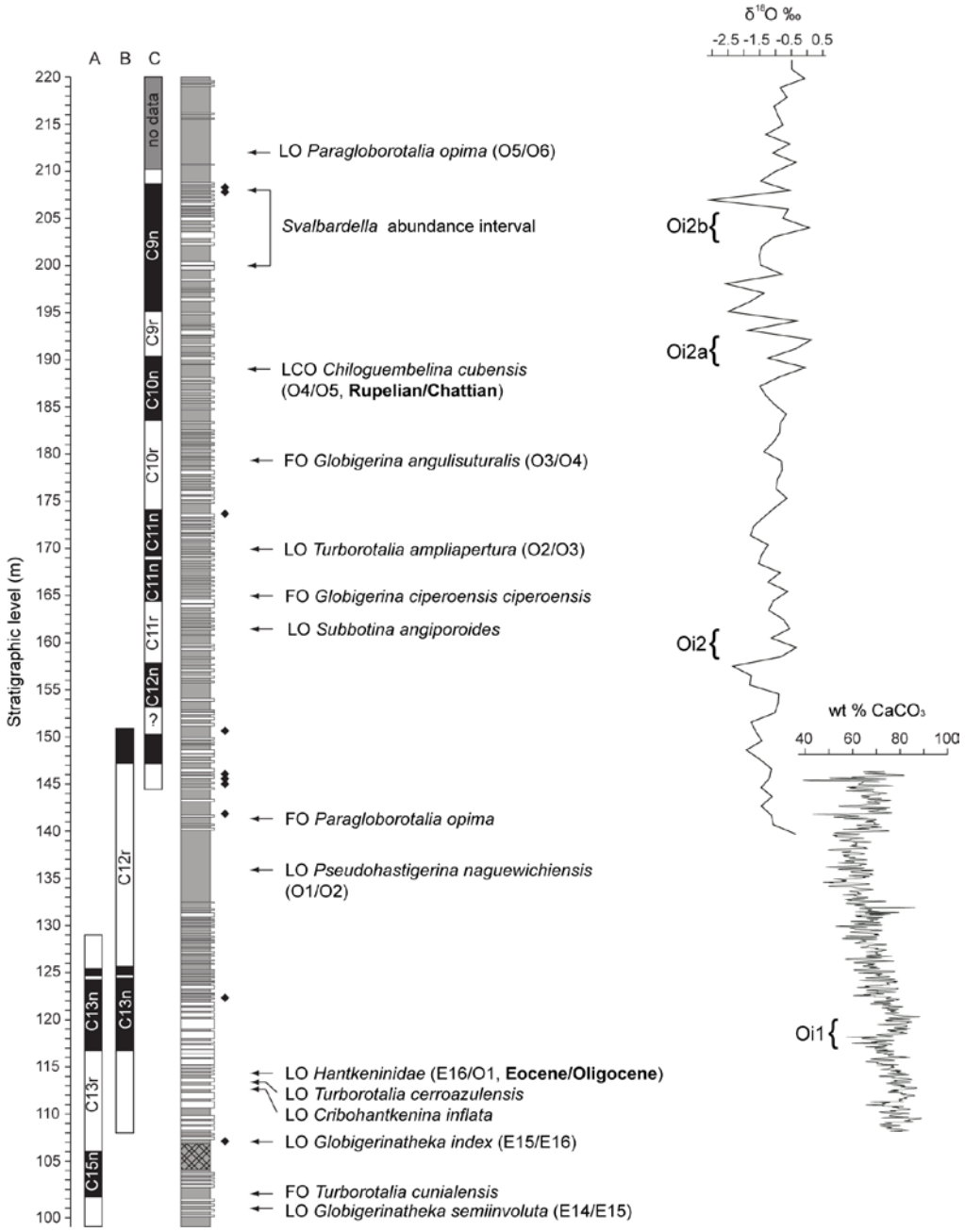

Figure 2.3 Lithostratigraphy, biostratigraphy and magnetostratigraphy of the Monte Cagnero section. Light/dark strata indicate alternating limestone/marl beds, with black diamonds marking biotite-rich volcanic beds. Cross-hatching represent a stratigraphic interval affected by low angle faulting and slumping Magnetostratigraphy is based on A – Jovane et al. (2013), B – Hyland et al. (2009), C – Coccioni et al. (2008). Planktonic foraminifera biostratigraphy is based on Jovane et al (2013) between 100-114m, Hyland et al. (2009) between 114-145m, and Coccioni et al. (2008) between 145-220 m, with zonal boundaries of Berggren and Pearson (2005) indicated in brackets. Paleoclimate proxy data (bulk rock $\delta^{18}O$ data from Coccioni et al. (2008), and weight percentage $CaCO_3$ data from Hyland et al. (2009) is shown along with the inferred stratigraphic position of major cooling events.

NP25-NP20 of Martini (1971; see also Jovane et al., 2013; Hyland et al., 2009; Coccioni et al., 2008). The LCO of the planktonic foraminifer *Chiloguembelina cubensis* at metre level 188 has been proposed as a potential site for the GSSP of the base of the Chattian (Coccioni et al., 2008). A 20% positive shift in bulk $CaCO_3$ content occurring at metre level 118 has been correlated to the deepening of the carbonate compensation depth (CCD) during the Oi-1 glaciation (Coxall et al., 2005), with the relatively small magnitude of the shift, and its condensed nature compared to the ODP Site 1218 record, being due to the fact that sedimentation in the Umbria-Marche succession took place above the CCD in the Eocene (Hyland et al., 2009). A low resolution bulk-rock $\delta^{18}O$ and $\delta^{13}C$ record from the upper part of the Monte Cagnero section revealed positive $\delta^{18}O$ shifts around metre levels 160, 190, and 203, which could potentially correlate to the Oi-2, Oi-2a, and Oi-2b glacial pulses respectively, with the latter coinciding with an interval characterized by the abundance of the dinoflagellate cyst *Svalbardella*, which is indicative of cold surface conditions (Coccioni et al., 2008).

Three magnetostratigraphic studies have been conducted at Monte Cagnero, targeting different parts of the section. Coccioni et al. (2008) sampled the interval between metre levels 145-210 at an average resolution of 0.7m, and correlated the resulting magnetic polarity pattern to magnetochrons C8r – C12r of the GPTS, although some magnetochrons (C10n.1r, C11n.1r) could not be identified, or were recognized based on a single sample. The interval between 108-150 m was sampled by Hyland et al. (2009) at a resolution of 0.5 m and was correlated to magnetochrons C13r-C12r. Jovane et al. (2013) extended the magnetic polarity record of the Monte Cagnero section further into the Eocene by analysing the interval between metre levels 58 and 128 with a sampling resolution of 0.3 m, which allowed the identification of magnetochrons C18r-C12r. The studies of Hyland et al. (2009) and Jovane et al (2013) overlap over an interval of ca 20 m and are in excellent agreement regarding the stratigraphic position of the base and top

of the normal polarity zone correlated to C13n.

Montanari et al. (1988) published K-Ar dates on biotite from volcanic layers at metre level 145.5 (31.7 ± 0.6 Ma) and 208.3 (28.0 ± 0.7 Ma) which were more recently re-dated using the $^{40}Ar/^{39}Ar$ method relative to FCs=27.84 Ma by Coccioni et al., (2008) yielding dates of 31.5 ± 0.2 Ma, and 26.7 ± 0.2 Ma respectively (Table 2.1). These two $^{40}Ar/^{39}Ar$ dates, recalculated to FCs=28.201 Ma (resulting in ages of 31.8 ± 0.2 Ma and 27.0 ± 0.2 Ma respectively) have been included as tie-points in the radio-isotopic age model of GTS12 (Vandenberghe et al., 2012).

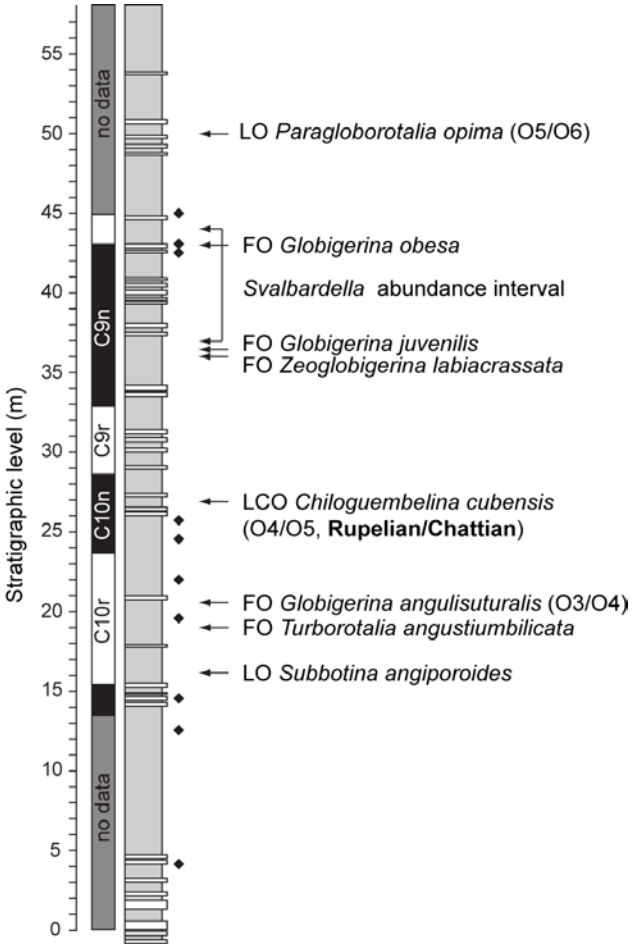

Figure 2.4 Lithostratigraphy, biostratigraphy and magnetostratigraphy of the Monte Cagnero section. Light/dark strata indicate alternating limestone/marl beds, with black diamonds marking biotite-rich volcanic beds. Magnetostratigraphy and planktonic foraminifer biostratigraphy based on Coccioni et al. (2008).

An astronomically tuned time scale is available for the interval between metre levels 108-146 of the Monte Cagnero section (Hyland et al., 2009). The tuning could not be extended back beyond the latest Eocene because the interval between 107-104 m is affected by low angle faulting and slumping. Spectral analysis of $CaCO_3$ percentage data in the depth domain showed statistically significant peaks related to one another by ratios similar to those found between Milankovitch cycles, and were assumed to represent precession, obliquity and eccentricity, however wavelengths were found to vary between the upper and lower part of the record, indicating that a change in sedimentation rates took place around metre levels 142 and 125. The record was tuned to the La2004 numerical solution (Laskar et al., 2004) using the astronomically tuned age of Brown et al. (2009) for the Eocene – Oligocene boundary at Massignano, and the age of the biotite-rich layer at metre level 145.5 of Coccioni et al., (2008) (relative to FCs=27.84) as a starting point, resulting in an age of 33.95 Ma for the Eocene – Oligocene boundary.

2.2.3 Pieve d'Accinelli

The Pieve d'Accinelli section (12˚29'40"N, 43˚35'20"E) is located ca 1 km west of Piobbico, and ca 10 km south-east of the Monte Cagnero section (Figure 2.1). Detailed biostratigraphic and magnetostratigraphic data for the upper 43 m of the 58 m thick section were published by Coccioni et al. (2008) (Figure 2.4). The section spans planktonic foraminifer zones O3-O6 of Berggren and Pearson (2005), with the LCO of *Chiloguembelina cubensis* at metre level 27, marking the base of the Chattian (Coccioni et al., 2008). Although the section overlaps with the upper part of the Monte Cagnero succession, several planktonic foraminifer bioevents (e.g the FO of *Turborotalia angustiumbilicata*, the FO of *Zeoglobigerina labiacrassata*, the FO of *Globigerina juvenilis* and *G. obesa*) reported by Coccioni et al. (2008) were not identified at Monte

Cagnero. The magnetic polarity pattern between metre levels 13 and 46 was determined based on a sampling resolution of 1.5 m and correlates to magnetochrons C11n.1n to C9n of the GPTS. There are no radio-isotopic or orbital age constraints available for the Pieve d'Accinelli section.

2.3 U/Pb dating of biotite-rich layers

Eleven samples were collected from biotite-rich volcanic beds intercalated in the Umbria-Marche succession: seven from Massignano, three from Monte Cagnero, and one from Pieve d'Accinelli. Because the Umbria –Marche sedimentary succession shows signs of bioturbation, with abundant ichnofossils of *Planolites* and *Zoophycos*, sampling was restricted to those beds for which a clear basal contact could be identified in the field, however contamination of individual beds with detrital zircons from the background sedimentation of the Umbria-Marche succession cannot be ruled out.

Samples weighing between 1-2 kg each were processed using the methodology described in Appendix A. Zircon populations dominated by faceted volcanic crystals measuring 100-200 μm in length, with aspect ratios between 3 and 6 (Figure 2.5), and a subordinate component of rounded zircon grains were recovered from all samples. Late Eocene samples from Massignano generally showed higher zircon yield, and contained larger crystals than the Oligocene samples from Monte Cagnero and Pieve d'Accinelli.

A total of 85 single zircons were dated using the CA-ID-TIMS methodologies employed at the NERC Isotope Geoscience Laboratory (NIGL), details of which are outlined Appendix A along with the tabulated results of the analytical programme (Table A.1), however the pertinent points are briefly outlined here. All zircons analysed were subjected to a modified version of the chemical abrasion procedure of Mattinson (2005)

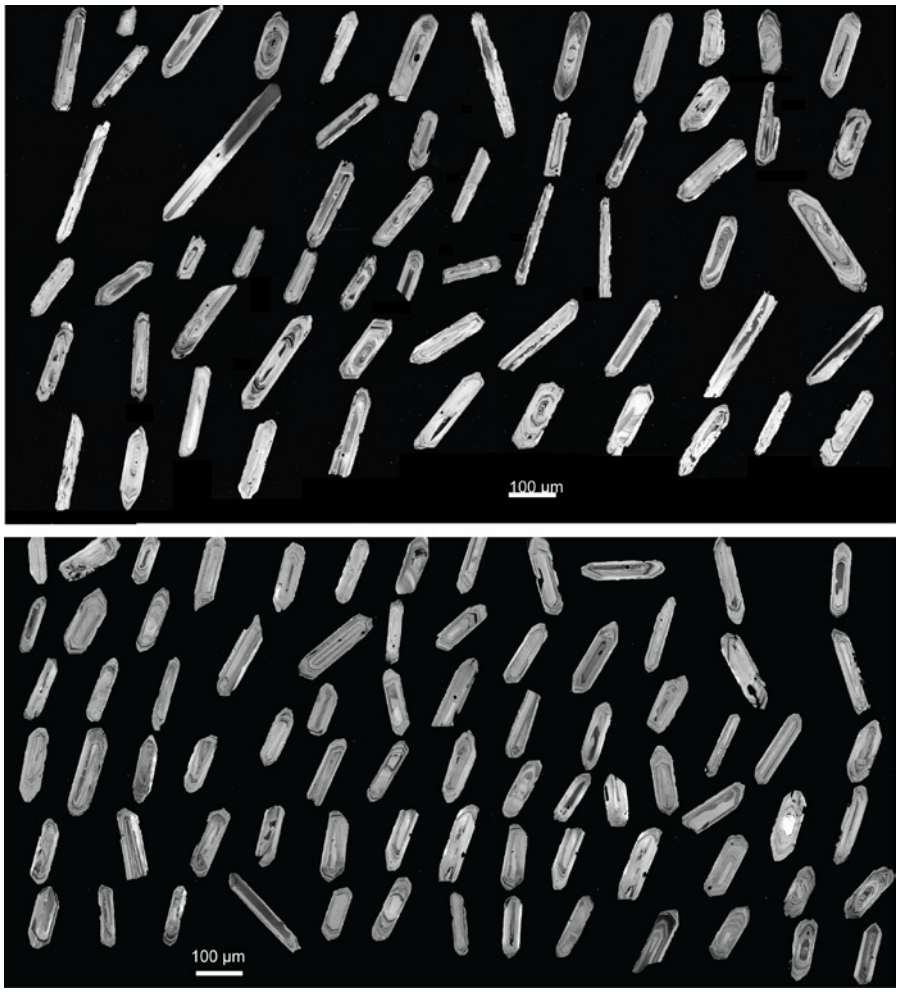

Figure 2.5 Cathodoluminescence images of zircons from biotite-rich layers from metre levels 5.8 (above) and 7.2 (below) of the Massignano section.

prior to dissolution, and were then spiked with the EARTHTIME ET535 (^{205}Pb-^{233}U-^{235}U) or ET2535 (^{202}Pb-^{205}Pb-^{233}U-^{235}U) isotopic tracer solutions. The accuracy of the reported ^{206}Pb/^{238}U dates is underpinned by the gravimetric calibration of the EARTHTIME tracers (Condon et al., in review; McLean et al., in review), and the determination of the ^{238}U decay constant through counting experiments (Jaffey et al., 1971). The analytical uncertainties of single crystal ^{206}Pb/^{238}U dates were between 0.1-0.7% (2σ) with radiogenic to common Pb ratios (Pb*/Pb$_c$) ratios between 0.14 and 51. The highest analytical uncertainties were recorded due to laboratory blank subtraction for samples with Pb*/Pb$_c$ < 1, which were excluded from further interpretation, but are included in the data table.

$^{206}Pb/^{238}U$ data from individual biotite rich beds showed a spread in dates, between 0.3-5 Myr, that exceeds the analytical precision of single data points. This is likely caused by a combination of two factors: (1) real age variation within the sample, due to the presence of zircons that formed at/close to the eruption and grains that crystallized prior to the eruption and give older apparent $^{206}Pb/^{238}U$ dates (i.e. antecrystic or xenocrystic zircons); and/or (2) post-crystallization Pb-loss resulting in younger apparent $^{206}Pb/^{238}U$ ages. All samples have undergone the chemical abrasion pre-treatment in order to minimize the occurrence of Pb-loss, and many studies have demonstrated that this method is highly effective in producing concordant data that represent analyses of closed system materials, however minor occurrences of Pb-loss cannot be ruled out. In CA-ID-TIMS data, Pb-loss typically manifests as a single data point that is younger than the main population, thought to represent zircons crystallized at eruption. Less frequently, a number of analyses, characterised by apparent $^{206}Pb/^{238}U$ ages that are younger than the main zircon population, may be interpreted as recording Pb-loss, however such analyses will show scatter, with non-overlapping U-Pb dates, reflecting the non-systematic nature of Pb-loss. The identification of single analyses affected by Pb-loss is significant because, given the possibility that zircon populations may incorporate grains that have crystallized prior to eruption, the underlying assumption of U-Pb dating of zircons from volcanic rocks applied to numerical age calibration of the stratigraphic record is that the youngest (reproducible) zircon dates from a sample will provide the most accurate estimate of the age of the eruption. However, if Pb-loss is present, the youngest measured apparent $^{206}Pb/^{238}U$ date may in fact be younger than the age of the eruption of the analysed volcanic material. Consequently, our interpretation of U-Pb data is based on the identification of a coherent population of youngest $^{206}Pb/^{238}U$ dates, which we assume to represent the age of eruption, and use to calculate the inverse variance weighted mean age of each sample, the inference being that younger non-reproducible dates represent open system behaviour,

while older dates reflect the incorporation of pre-eruptive zircon.

The selection of a youngest coherent population is necessarily subjective, however software packages designed for the interpretation of U-Pb data, such as Isoplot (Ludwig, 2003), and Redux (McLean et al., 2011) provide statistical parameters, such as the mean square of the weighted deviates (MSWD), and probability of fit, which can be used as a guide. It is important to note that these statistical parameters are dependent on the precision of single data points. The MSWD provides a measure of the "coherence" of a dataset and can be used to assess whether observed scatter is within the range of the analytical uncertainties of single data points or due to external, geological factors. MSWD values for which the scatter can be considered due to analytical factors alone vary according to the number of data points included in the calculation (Wendt and Carl, 1991) with acceptable values ranging between 0-2.61 for n=4, and 0.1-2.13 for n=7, and approaching 1 for high-n datasets. Within these ranges, if real age variation is present, it cannot be distinguished within the precision of individual analyses.

We interpret U-Pb zircon ages based on a population (4 to 7 analyses) of the youngest precise $^{206}Pb/^{238}U$ dates using the probability of fit and MSWD as a guide. Alternative interpretations, involving the incorporation of more data points, are considered to have low probability. A summary of calculated weighted mean dates, and associated statistical parameters is provided in Table 2.2. Individual analyses are plotted in Figure 2.6. and their interpretation for each sample is summarized below. Uncertainties on the weighted mean dates are reported as ± X/Y/Z, where X denotes analytical uncertainty, while Y and Z contain additional uncertainty components related to the calibration of the EARTHTIME tracer solution, and the uncertainty of the ^{238}U decay constant (Jaffey et al., 1971).

2.3.1 Massignano

Samples were collected from biotite-rich beds at metre levels 5.8, 6.5, 7.2, 8.0, 12.7, 12.9, and 14.7 of the Massignano section (Table 2.2, Figure 2.6):

- MASS-5.8 – 11 zircons were analysed, of which two were excluded based on their low Pb^*/Pb_c ratio, with the remaining fractions giving a range of $^{206}Pb/^{238}U$ dates between 35.406-36.370 Ma. A weighted mean age of 35.476 (± 0.025/0.031/0.049) Ma with an MSWD of 0.86 was calculated based on the six youngest analyses.
- MASS-6.5 – 10 zircons were analysed, yielding $^{206}Pb/^{238}U$ dates between 35.373 - 37.791 Ma. The five youngest grains gave a weighted mean age of 35.413 (± 0.017/0.023/0.045) Ma with an MSWD of 1.05.
- MASS-7.2 – 10 zircons were analysed, with three data points excluded based on their $Pb^*/Pb_c < 1$, with the remaining fractions giving $^{206}Pb/^{238}U$ dates between 35.251 – 37.655 Ma. The weighted mean $^{206}Pb/^{238}U$ age of the youngest five grains is 35.321 (± 0.034/0.036/0.052) Ma with an MSWD of 1.22.
- MASS-8.0 - 12 zircons were analysed yielding $^{206}Pb/^{238}U$ ages between 35.255 – 35.526 Ma, with a weighted mean age of 35.265 (± 0.021/0.026/0.046) Ma with an MSWD of 0.10 based on the five youngest dates.
- MASS-12.7 - 10 zircons were analysed, and yielded $^{206}Pb/^{238}U$ dates between 34.506 and 35.120. The youngest analysis could not be reproduced and was therefore assumed to represent Pb-loss. The remaining seven youngest grains yielded equivalent dates with a weighted mean $^{206}Pb/^{238}U$ date of 34.720 (± 0.017/0.024/0.044) Ma and an MSWD of 0.41.
- MASS-12.9 – four zircons were analysed, with one data point excluded based on its low Pb^*/Pb_c, and another was discordant, with a Cretaceous $^{207}Pb/^{206}Pb$

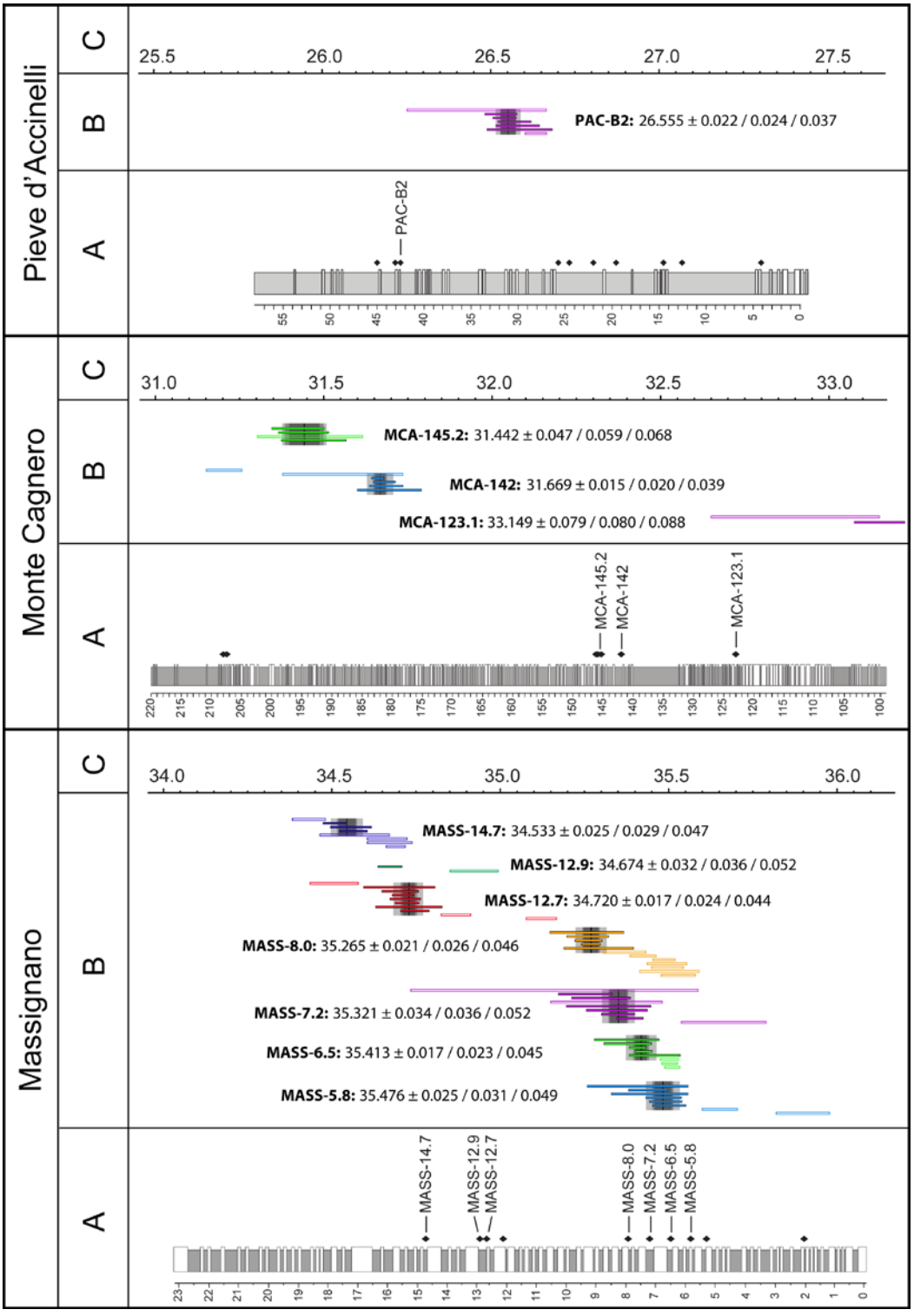

Figure 2.6 Summary plots of $^{206}Pb/^{238}U$ data and interpreted depositional ages based upon the weighted mean $^{206}Pb/^{238}U$ of the youngest coherent population. A - Lithostratigraphy and tuff ID, B - CA-ID-TIMS $^{206}Pb/^{238}U$ single zircon and interpreted weighted mean dates, C - Age in Myr. Note that section A provides reference lithostratigraphic logs scaled in metres for each locality, however the zircon U-Pb dates are plotted against time (C) and not against height of the sample.

age. The youngest of the two remaining fractions, with a $^{206}Pb/^{238}U$ age of 34.674 (± 0.032/0.036/0.052) Ma, is interpreted as a maximum age constraint for the deposition of this biotite-rich bed.

- MASS-14.7 - 11 zircons were analysed. Two discordant data points, with Cretaceous $^{207}Pb/^{206}Pb$ ages, and one analysis with $Pb^*/Pb_c < 1$ were excluded. The remaining seven analyses gave $^{206}Pb/^{238}U$ dates between 34.432 – 34.688 Ma. The youngest of these was interpreted as representing Pb-loss, and the next three youngest data-points gave a weighted mean age of 34.533 Ma (± 0.025/0.029/0.047) with an MSWD of 2.1.

2.3.2 Monte Cagnero

Three samples were collected from the Monte Cagnero section, from biotite-rich beds at metre levels 123.1, 142, and 145.2, with results of single analyses plotted in Figure 2.6:

- MCA-123.1 – three zircons were analysed. Only one analysis had $Pb^*/Pb_c > 1$, giving an age of 33.149 ± 0.079/0.80/0.88 Ma, which is interpreted as a constraint on the maximum age for this sample.
- MCA-142 – nine zircons were analysed, with one data point rejected due to having $Pb^*/Pb_c < 1$. One analysis gave a concordant, but non-reproducible date of 31.206 ± 0.053 Ma, while three grains gave discordant results with Cretaceous, Jurassic and Precambrian $^{207}Pb/^{206}Pb$ ages. The remaining four grains gave a weighted mean $^{206}Pb/^{238}U$ age of 31.669 (± 0.015/0.020/0.039) Ma, with an MSWD of 0.69.
- MCA-145.2 – four grains were analysed, with one data point excluded due to having $Pb^*/Pb_c < 1$, with the remaining three fractions giving a weighted mean

Sample	$^{206}Pb/^{238}U$ date	Uncertainty (2σ)	MSWD	Probability of fit	n
PAC-B2	26.555	± 0.022 / 0.024 / 0.037	0.76	0.55	5 of 8
MCA-145.2	31.442	± 0.047 / 0.059 / 0.068	0.28	0.75	3 of 4
MCA-142	31.669	± 0.015 / 0.020 / 0.039	0.69	0.56	4 of 9
MCA-123.1*	33.149	± 0.079 / 0.080 / 0.088			
MASS-14.7	34.533	± 0.025 / 0.029 / 0.047	2.10	0.12	4 of 8
MASS-12.9*	34.674	± 0.032 / 0.036 / 0.052			
MASS-12.7	34.720	± 0.017 / 0.024 / 0.044	0.41	0.87	7 of 10
MASS-8.0	35.265	± 0.021 / 0.026 / 0.046	0.10	0.98	5 of 12
MASS-7.2	35.321	± 0.034 / 0.036 / 0.052	1.22	0.30	5 of 7
MASS-6.5	35.413	± 0.017 / 0.023 / 0.045	1.05	0.38	5 of 10
MASS-5.8	35.476	± 0.025 / 0.031 / 0.049	0.86	0.51	6 of 11

Table 2.2 Weighted mean $^{206}Pb/^{238}U$ dates calculated for volcanosedimentary layers from the Massignano, Monte Cagnero and Pieve d'Accinelli sections. MSWD – mean square of the weighted deviates, n – number of grains included in the calculation of the weighted mean date out of the total number of grains analysed (after rejection of analyses with $Pb^*/Pb_c<1$). Weighted mean dates and uncertainties were calculated using Redux (McLean et al., 2011), and statistical parameters are outputs from Isoplot (Ludwig, 2003). * - maximum age constraint

age of 31.442 (± 0.047/0.059/0.068) Ma and an MSWD of 0.28.

2.3.3 Pieve d'Accinelli

Nine zircons were analysed from sample PAC-B2 (Figure 2.6) collected from metre level 42.5 of the Pieve d'Accinelli section (bed B2 of Coccioni et al., 2008), One grain was rejected based on its low Pb*/Pbc ratio with the remaining eight giving $^{206}Pb/^{238}U$ dates between 26.533-33.545 Ma. The five youngest analyses define a coherent population and yield a weighted mean age of 26.555 (± 0.022/0.024/0.037) Ma, with an MSWD of 0.76.

2.4 Numerical age of the Umbria-Marche succession

2.4.1 U-Pb data compared to published radio-isotopic age constraints.

Six of the 11 samples collected from the Umbra-Marche succession coincide with, or are situated stratigraphically very close to biotite rich beds that were previously dated using the K-Ar, Rb- Sr (Montanari et al., 1985, 1988), U-Pb (Oberli and Meier, 1991), and $^{40}Ar/^{39}Ar$ techniques (Odin et al., 1991; Coccioni et al., 2008, see section 2.1 and 2.2 for details). With the exception of a few data-points, our weighted mean $^{206}Pb/^{238}U$ ages tend to overlap with, but are up to an order of magnitude more precise than published K-Ar, Rb-Sr and U-Pb dates, and are usually younger than $^{40}Ar/^{39}Ar$ data calibrated relative to FCs=28.201 (Figure 2.7).

$^{40}Ar/^{39}Ar$ data from biotite rich beds at metre level 12.7 and 14.7 of the Massignano section, and 145.2, and 208.3 of the Monte Cagnero section was used for the radio-isotopic calibration of the GPTS in GTS12 (Vandenberghe et al., 2012), and a comparison between these dates and our weighted mean $^{206}Pb/^{238}U$ ages is outlined below, taking into account uncertainties related to the calibration of the ET535 tracer, the ^{238}U decay constant, and respectively, neutron fluence monitor age, and the ^{40}K decay constant, at the 2σ level. Sample MASS-12.7 gave a weighted mean $^{206}Pb/^{238}U$ age of 34.72 ± 0.05 Ma, which is ca. 0.5 Myr younger than the recalculated $^{40}Ar/^{39}Ar$ date of 35.2 ± 0.2 Ma, however, the weighted mean $^{206}Pb/^{238}U$ age of sample MASS-14.7 (34.53 ± 0.05 Ma) is indistinguishable at the 2σ level from the recalculated $^{40}Ar/^{39}Ar$ date of 34.4 ± 0.2 Ma (Odin et al., 1991; Kuiper et al., 2008). At Monte Cagnero, a sample MCA-145.2 yielded a weighted mean $^{206}Pb/^{238}U$ age of 31.442 ± 0.068 Ma. Based on a mean sedimentation rate of 10 m/Myr (Hyland et al., 2009), this sample would be expected to be ca 30 kyr older than the biotite-rich layer at metre level 145.5 (MCA-145.5 in

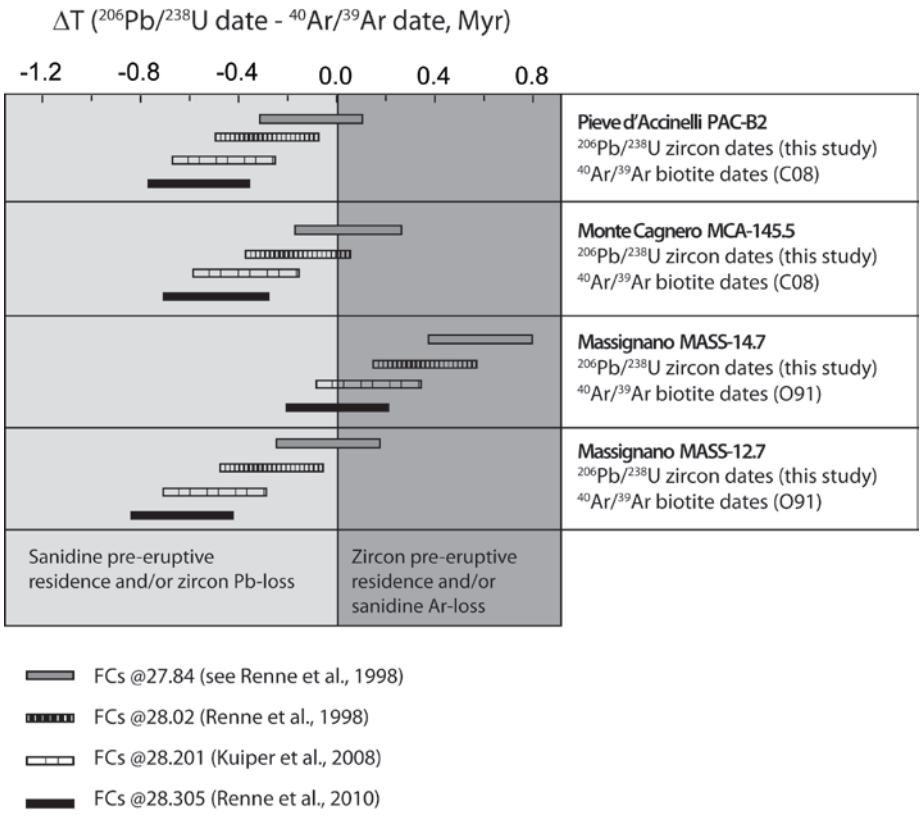

Figure 2.7 Summary of the comparison between weighted mean $^{206}Pb/^{238}U$ dates from this study, and legacy $^{40}Ar/^{39}Ar$ biotite dates of Odin et al. (1991) and Coccioni et al. (2008) calibrated relative to a selection of widely used values for the age of the FCs neutron fluence monitor. Zircon U-Pb and biotite $^{40}Ar/^{39}Ar$ dates that are equivalent at the 2σ level overlap with 0. Negative differences indicate data pairs affected by either zircon Pb-loss or contamination with pre-eruptive or detrital biotite, while positive differences imply zircon pre-eruptive magma chamber residence or open system behaviour of biotite (see text for details). Plot for sample PAC-B2 is based on the assumption of equivalence with the biotite rich layer at metre level 208.3 of the Monte Cagnero section. Plot for MCA-145.5 is based on the assumption that the difference between the depositional age age of the biotite-rich beds at metre levels 145.2 and 145.5 is 30 kyr (based on the tuning of Hyland et al. 2009).

Figure 2.12) dated by Coccioni et al. (2008), however a recalculated $^{40}Ar/^{39}Ar$ date of 31.8 ± 0.2 Ma has been reported for the latter (Coccioni et al., 2008; Vandenberghe et al., 2012). Biotite rich beds from metre level 42.8 of the Pieve d'Accinelli section (PAC-B2) and 208.3 of the Monte Cagnero section both lie very close to the top of magnetochron C9n (magnetostratigraphic calibration of both samples is ca C9n(.05) based on Coccioni et al., 2008), and given the resolution of the respective magnetic polarity records they are expected to have been deposited within about 100 kyr of each other, however our

PAC-B2 sample yielded a weighted mean $^{206}Pb/^{238}U$ date of 26.55 ± 0.04 Ma, ca. 0.45 Ma younger than the recalculated $^{40}Ar/^{39}Ar$ date of 27.0 ± 0.1 Ma reported by Coccioni et al (2008) from metre level 208.3 of the Monte Cagnero section.

Because each $^{206}Pb/^{238}U$ weighted mean age is supported by multiple, reproducible single crystal dates, and because all samples were subjected to chemical abrasion prior to dissolution, it is unlikely that the observed ca. 0.5 Myr discrepancies between $^{206}Pb/^{238}U$ weighted mean dates and recalculated $^{40}Ar/^{39}Ar$ ages are an artefact of post-crystallization Pb-loss. Recent studies on the intercalibration between $^{40}Ar/^{39}Ar$ dating and astronomical tuning, and the $^{206}Pb/^{238}U$ system respectively, consistently point towards an FCs age in the 28.2-28.3 Myr range (Kuiper et al., 2008; Renne et al., 2010; Rivera et al., 2011; Wotzlaw et al 2013), and it is therefore unlikely that anomalously old (>1%) recalculated $^{40}Ar/^{39}Ar$ dates could be the result of inaccuracy of the FCs age of Kuiper et al. (2008) adopted in GTS12. The fact that the original $^{40}Ar/^{39}Ar$ dates of Odin et al. (1991) were calibrated relative to the LP-6 biotite points towards heterogeneity of this standard (Hilgen and Kuiper, 2009), or inaccuracy of the FCs – LP-6 intercalibration factor as potential causes for the observed discrepancy, although the latter is less likely, as the good agreement between the $^{206}Pb/^{238}U$ and recalculated $^{40}Ar/^{39}Ar$ date for the biotite-rich layer at metre level 14.7 indicates a random rather than systematic effect.

The same argument cannot be made for the $^{40}Ar/^{39}Ar$ dates published by Coccioni et al. (2008) from the Monte Cagnero section, as these ages were originally calibrated relative to FCs, with an age of 27.84 Ma. In this case, assuming that the magnetic polarity records of the Monte Cagnero and Pieve d'Accinelli sections, and their correlation to the geomagnetic polarity time scale, are accurate, the older apparent $^{40}Ar/^{39}Ar$ biotite dates of Coccioni et al. (2008) from metre levels 145.5 and 208.3 (calibrated relative to FCs = 28.201, Kuiper et al., 2008) are likely to be the result of geological complexity of the

analysed biotite samples, and/or the $^{40}Ar/^{39}Ar$ dates being systematically too old due to inter-laboratory bias.

2.4.2 U-Pb data compared to floating astronomical time scales for Massignano and Monte Cagnero

The floating astronomical time scales developed for the Massignano and Monte Cagnero sections rely on matching cyclic oscillations in high-resolution magnetic susceptibility and carbonate content records to the 40 kyr obliquity (Jovane et al., 2006) and 100 kyr eccentricity components (Brown et al., 2009; Hyland et al., 2009) of the La2004 solution. Because of this, assuming that cycle expression and identification is complete and accurate, they can provide estimates for the amount of time elapsed between the deposition of individual biotite-rich beds at a precision comparable to that of $^{206}Pb/^{238}U$ dates, and integrating data from both systems can increase the robustness of numerical age models developed for the Umbria-Marche sedimentary succession.

At Massignano, the orbital chronologies developed by Jovane et al. (2006) and Brown et al (2009) yield numerical ages that differ by up to 200 kyr. The two records overlap between metre levels 4-20 of the section, with durations of ca. 2.1, and respectively 1.6 Myr reported for this interval. Weighted mean $^{206}Pb/^{238}U$ dates from the Massignano section show a clear upward-younging trend (Figure 2.8) and are older than the ages determined by Jovane et al. (2006) and Brown et al. (2009) for individual biotite-rich beds. For the orbital chronology Jovane et al. (2006) the discrepancy increases linearly from ca 100 kyr for sample MASS-5.8 to ca 300 kyr for sample MASS-14.7. Weighted mean $^{206}Pb/^{238}U$ dates from biotite-rich beds at metre levels 5.8, 6.5, 7.2, and 8.0 are consistently older than the astronomical age model of Brown et al. (2009), by ca 250 kyr, and the discrepancy is reduced to ca 150 kyr for the biotite-rich beds at metre levels 12.7

and 14.7.

The mean sedimentation rate inferred based on our $^{206}Pb/^{238}U$ data is ca 9.5 m/Myr, close to the value of 10.6 m/Myr used by Brown et al. (2009), which may explain the differences between the two astronomically tuned time scales. Jovane et al. (2006) performed spectral analysis of their magnetic susceptibility proxy data in the depth domain, and identified cycles with wavelengths of 72 and 284 cm, which they assumed to represent short (100 kyr) and long (405 kyr) eccentricity signals based on an average sedimentation rate of 6.9 m/Myr calculated using the magnetic reversal dates of Cande and Kent (1995). Using our $^{206}Pb/^{238}U$ derived mean sedimentation rate, these wavelengths would correspond to periodicities of ca 70 kyr, and respectively 300 kyr in the time domain. Brown et al. (2009) converted their proxy data from the depth to the time domain using a mean sedimentation rate of 10.6 m/Myr, calculated based on the average radio-isotopic dates of Montanari et al. (1993), and spectral analysis of their magnetic susceptibility proxy data revealed statistically significant peaks not only at orbital frequencies (100, and 405 kyr) but also at 69, 254, and 348 kyr, raising the possibility that the cycles identified by Jovane et al., (2006) do not represent long and short eccentricity signals.

At Monte Cagnero the weighted mean $^{206}Pb/^{238}U$ dates for samples MCA-142, and MCA-145.2 are ca 300 kyr younger than dates derived from the astronomical age model of Hyland et al. (2009) (Figure 2.8). This is likely a consequence of the fact that Hyland et al. (2009) used the $^{40}Ar/^{39}Ar$ date of Coccioni et al. (2008) for the biotite-rich bed at metre level 145.5, recalibrated relative to FCs = 28.201 Ma, as a tie-point, and by comparison to our data, this date appears to be anomalously old (see previous section). Our date for sample MCA-123.1 overlaps with the astronomically tuned age model at the 2σ level, however this date is based on a single zircon analysis and only represents a maximum age constraint on the deposition of this biotite-rich bed. Given

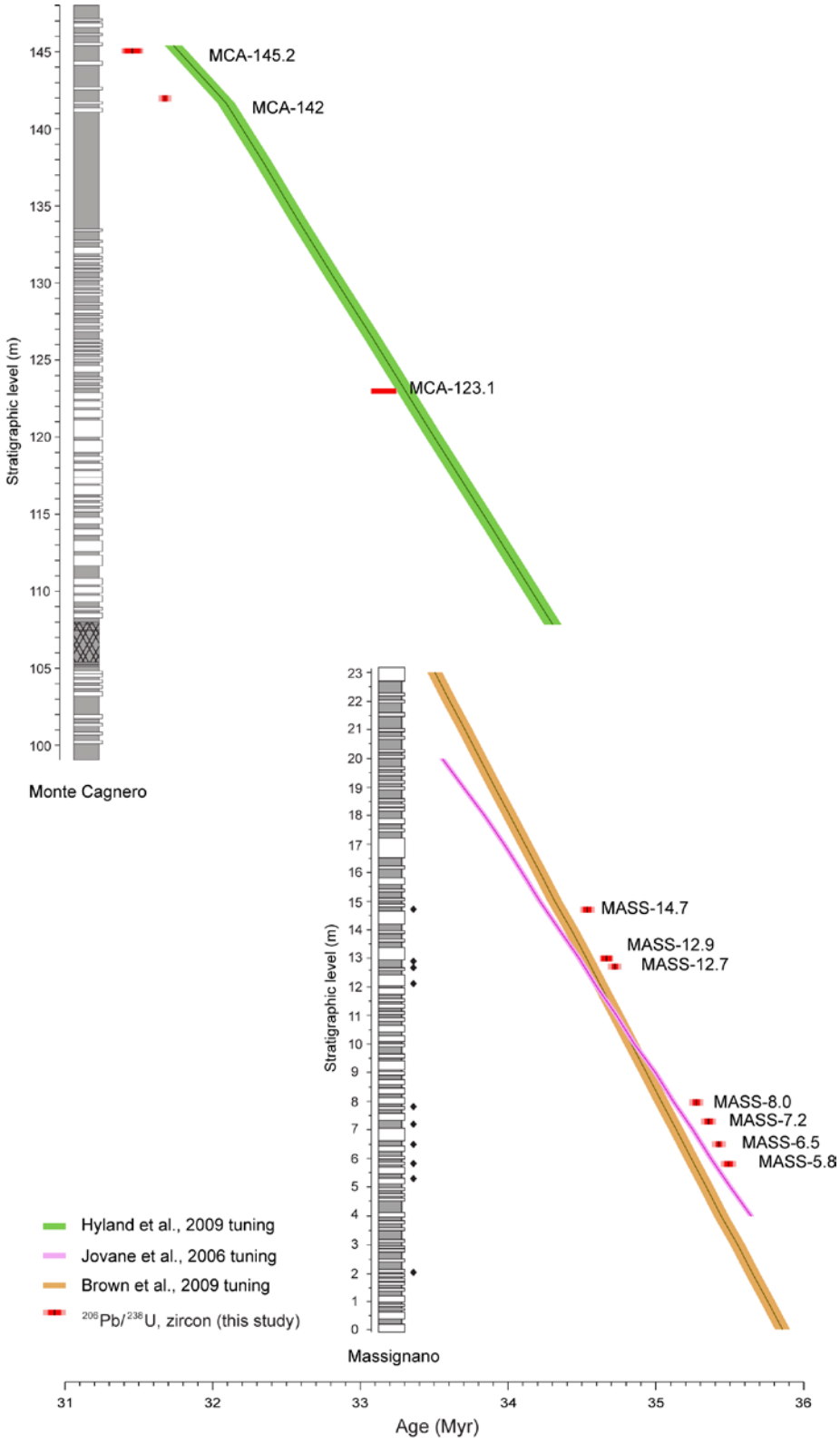

Figure 2.8 Comparison between weighted mean $^{206}Pb/^{238}U$ zircon dates and astronomically tuned age models of the Massignano and Monte Cagnero sections. Note that the thickness scales for the two stratigraphic sections are not the same.

that samples MCA-142 and MCA-145.2 gave weighted mean $^{206}Pb/^{238}U$ dates that are consistent with the relative stratigraphic positions of the two biotite-rich beds, and each mean date is based on several reproducible chemically abraded single zircon analyses, the results are unlikely to represent post-depositional Pb-loss. The good agreement between short eccentricity band-pass filtered carbonate content records for Massignano and Monte Cagnero (Hyland et al., 2009; Brown et al., 2009) indicates the tuning of at least the Late Eocene part of the Monte Cagnero record is correct, however the accuracy of the tuning of the Early Oligocene cannot be assessed using the existing data.

2.4.3 Age-depth models

We developed age-depth models for the Massignano and Monte Cagnero sections, in order to constrain the numerical age of magnetic reversals, planktonic foraminifer bioevents, and climate shifts recorded in the Umbria-Marche succession. Age-depth models for pre-Quaternary sedimentary successions typically rely on linear or polynomial regression to estimate the numerical age of events situated between stratigraphic levels of known age (Machlus et al., 2004; Mundil et al., 2004; Zanazzi et al., 2007, 2009; Smith et al. 2010; Coccioni et al. 2008, 2013) with cubic spline regression used to develop geomagnetic polarity time scales (Cande and Kent, 1992, 1995; Wei et al., 1995; Acton and Huestis, 1997; Ogg and Smith, 2004). A large number of software packages aimed at constructing depositional models have been developed by the Quaternary geochronology community, and while these are intended primarily for use with U-series (Scholtz and Hoffmann, 2011; Hercman and Pawlak, 2012) and ^{14}C data (Blaauw and Christen, 2005; Heegard et al., 2005; Bronk Ramsey, 2008; Christen and Perez, 2009) many of them are able to process radio-isotopic data obtained using other isotope systems. For this study we selected the OxCal program of Bronk Ramsey (2008), which relies on a Bayesian approach, primarily because the interface of this software is sufficiently flexible to

allow the integration of $^{206}Pb/^{238}U$ data and other stratigraphic information, such as the astronomically tuned duration of the stratigraphic intervals between individual biotite-rich beds.

We used the *P_Sequence* model implemented in OxCal 4.2, which, rather than assuming that sediment accumulation follows a predetermined functional form (e.g. linear or polynomial), treats sediment accumulation as a random Poisson process, in which sediment layers of finite thickness are deposited at discrete points in time, and are separated by gaps of variable duration. This approach results in wider uncertainty envelopes compared to linear interpolation between consecutive radio-isotopic dates, but interpolated ages are likely to be more accurate (Bronk Ramsey, 2008). The model requires an input parameter *k*, defined as the number of accumulation events per unit depth and allows the definition of a range of possible *k* values.

OxCal treats radio-isotopic date uncertainties as random, which means that when correlated systematic uncertainties are present, the resulting age model will have an unrealistically narrow uncertainty envelope for stratigraphic intervals with closely spaced $^{206}Pb/^{238}U$ dates with overlapping uncertainties. For this reason, only the analytical uncertainties of weighted mean $^{206}Pb/^{238}U$ dates were modelled in OxCal, and additional uncertainties equivalent to ± 0.03 %, and 0.11% of the interpolated ages, representing tracer calibration, and respectively ^{238}U decay constant uncertainties at the 2σ level, were added in quadrature to the 95% uncertainty envelope of the age model.

2.4.3.1 Massignano age-depth model

Input data for our Massignano age-depth model consists of weighted mean $^{206}Pb/^{238}U$ dates for biotite-rich beds at metre levels 5.8, 6.5, 7.2, 8.0, 12.7, 14.7 and

astronomically tuned estimates for the duration of the interval between consecutive biotite-rich beds and the lowest (highest) biotite-rich bed and base (top) of the succession, derived from the tuning of Brown et al. (2009). We ran six versions of the age-depth model, all with a *k* parameter set at a nominal value of 100 and allowed to vary by two orders of magnitude in either direction. W assumed an uncertainty for the astronomically tuned durations between ± 0.05 – 0.10 Myr (at the 2σ level, with 0.01 Myr increments), with the lowest value representing an uncertainty of ± one half of a short eccentricity cycle, while the highest one takes into account the possibility of a missing/spurious cycle in any interval. Increasing the uncertainty of the astronomically tuned durations was found to have no significant effect on the absolute value of interpolated ages, however it resulted

Event	Metre level	Age (± 2σ)
Base C13n	20.2	33.968 ± 0.080
LO *Hantkeninidae*	19.0	34.090 ± 0.074
LO *T. cocoanensis*	18.6	34.131 ± 0.072
LO *T. cunialensis*	18.6	34.131 ± 0.072
LO *C. inflata*	15.0	34.496 ± 0.048
LO *G. index*	13.5	34.648 ± 0.047
LO *G. luterbacheri*	12.9	34.710 ± 0.044
Base C13r	11.1	34.907 ± 0.054
Base C15n	9.3	35.108 ± 0.052
FO *T. cunialensis*	7.5	35.303 ± 0.044
Base C15r	6.2	35.439 ± 0.044
FO *C. inflata*	5.8	35.479 ± 0.045
Base C16n.1n	5.2	35.542 ± 0.050
LO *T. pomeroli*	5.0	35.562 ± 0.050
LO *G. semiinvoluta*	4.8	35.582 ± 0.054
Base C16n.2n	4.2	35.645 ± 0.057
LCO *I. recurvus*	3.0	35.768 ± 0.065

Table 2.3 Interpolated ages for magnetic reversals and planktonic foraminifer events recorded in Massignano section. Stratigraphic positions are based on Coccioni et al. (1988), Bice and Montanari (1988), and Jovane et al. (2007). Uncertainties include $^{206}Pb/^{238}U$ analytical, ET535 tracer calibration, ^{238}U decay constant, and astronomical tuning uncertainty components.

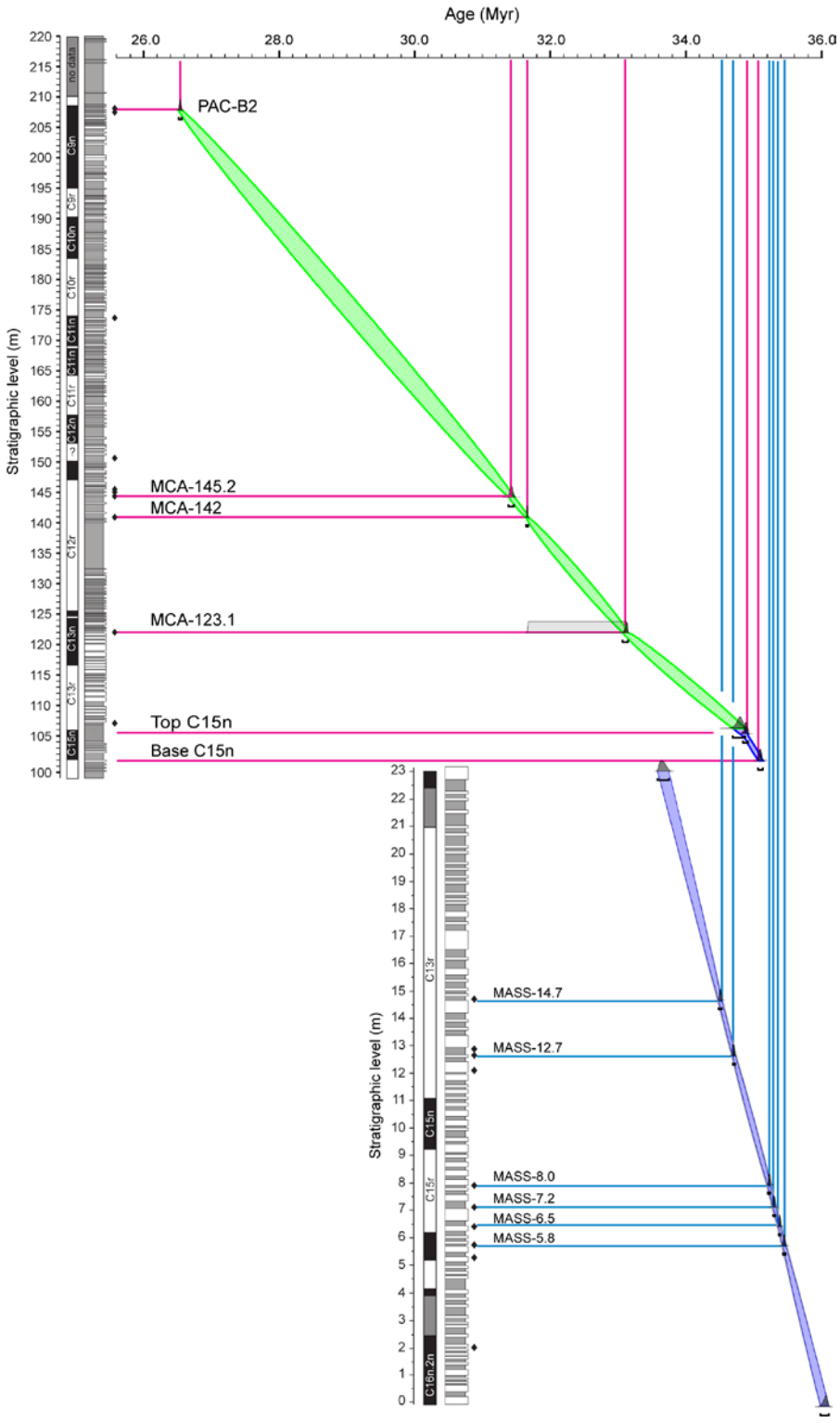

Figure 2.9 OxCal (v. 4.2.2) age-depth models for the Massignano and Monte Cagnero sections. Uncertainty envelopes represent 95% confidence intervals based on the propagated analytical uncertainty of weighted mean $^{206}Pb/^{238}U$ dates, and, for Massignano, a ± 80 kyr uncertainty on the duration of astronomically tuned intervals (see text for details), with ET535 tracer calibration (0.03%) and ^{238}U decay constant (0.11%) uncertainties addedd in quadrature.

in a proportional increase in the width of the 95% uncertainty envelope of the model. The uncertainty of the astronomically tuned durations had a strong influence on the agreement index of the model (*A model*, returned by OxCal as a measure of how well the model matches the input data), which varied between 32.4 and 82.3 (for uncertainties of ± 0.05 and 0.10 Myr respectively). Our preferred age-depth model (Figure 2.9), obtained using an uncertainty of ± 0.08 Myr for the duration of astronomically tuned intervals, was selected as the lowest uncertainty model that yielded an agreement index above the 60% threshold suggested by Bronk Ramsey (2008). Interpolated ages for magnetic reversals and planktonic foraminifer bioevents reported from the Massignano section are listed in Table 2.3.

2.4.3.2 Monte Cagnero age-depth model

At Monte Cagnero, Hyland et al. (2009) estimated the duration of the interval between the Eocene-Oligocene boundary (114.1 m), and the biotite-rich bed at metre level 145.5 at ca. 2.24 Myr. Based on their tuning, the biotite-rich layers at metre levels 145.2 and 142 would have ages of ca 31.74, and 32.03 Myr, which are 300, and respectively 360 kyr older than our weighted mean $^{206}Pb/^{238}U$ dates for samples MCA-145.2, and MCA-142. Anchoring the tuning to our $^{206}Pb/^{238}U$ dates would give an age of 33.68 Ma for the Eocene-Oligocene boundary, close to the astronomically tuned estimate of 33.79 Ma of Pälike et al (2006) from ODP Site 1218, however it also implies an age of ca 33.46 Ma for the base of magnetochron C13n. The base of C13n has been identified close to the top of the Massignano section by both Bice and Montanari (1988) and Lowrie and Lanci (1994), and while some uncertainties persist regarding the exact placement of this chron boundary, its age is expected to be older than the top of the Massignano record, estimated at 33.68 ± 0.10 based on the age-depth model discussed in the previous section. Additionally, the lower end of the tuned time scale of Hyland et al. (2009), at metre level 108 of the Monte

Event	Metre level	Age (± 2σ)
Base C9n.1n	203.9	26.881 ± 0.099
Base C9n.1r	203.4	26.920 ± 0.103
Base C9n.2n	196.0	27.494 ± 0.149
Base C9r	191.3	27.855 ± 0.166
LCO *C. cubensis*	188.0	28.126 ± 0.175
Base C10n	184.4	28.387 ± 0.184
FO *G. angulisuturalis*	179.0	28.804 ± 0.191
Base C10r	175.0	29.119 ± 0.187
Base C11n.1n	170.2	29.488 ± 0.183
LO *T. ampliapertura*	170.0	29.494 ± 0.184
Base C11n.1r	169.8	29.826 ± 0.178
Base C11n.2n	165.4	29.856 ± 0.178
FO *G. ciperoensis ciperoensis*	165.0	29.888 ± 0.174
LO *S. angiporoides*	161.5	30.236 ± 0.165
Base C11r	158.9	30.359 ± 0.160
Base C12n	147.6	31.234 ± 0.089
LO *I. recurvus*	139.0	31.881 ± 0.081
LO *P. naguewichiensis*	137.0	32.035 ± 0.096
Base C12r	124.1	33.030 ± 0.073
Oi-1	118.0	33.653 ± 0.134
Base C13n	117.3	33.728 ± 0.137
LO *Hantkeninidae*	114.1	34.070 ± 0.149
LO *T. cerroazulensis*	113.6	34.122 ± 0.149
LO *C. inflata*	112.9	34.197 ± 0.149
LO *G. index*	107.5	34.780 ± 0.106
FO *T. cunialensis*	102.5	35.098 ± 0.055

Table 2.4 Interpolated ages for magnetic reversals and planktonic foraminifer events recorded in events recorded in Monte Cagnero section. Stratigraphic positions are based on Coccioni et al. (2008), Hyland et al (2009), and Jovane et al (2013). Uncertainties include ET535 tracer calibration, and ^{238}U decay constant components.

Cagnero section would have an age of 34.13 Ma when anchored to our $^{206}Pb/^{238}U$ dates, and at Massignano, we have interpolated an age of 34.91 Ma for the top of C15n, which lies at metre level 106.1 of the Monte Cagnero section. This would imply the presence of a ca 600 kyr hiatus between metre levels 106-108 of the Monte Cagnero section, however,

a recent high-resolution biostratigraphic and magnetostratigraphic study of this interval found no evidence of a prolonged gap in sedimentation (Jovane et al., 2013). For this reason, we did not attempt to construct an integrated radio-isotopic /astronomically tuned age-depth model for the Monte Cagnero section, and relied instead only on weighted mean $^{206}Pb/^{238}U$ dates from samples MCA-142, MCA-145.2, and PAC-B2 (assuming that the latter is equivalent to the biotite-rich bed at metre level 208.3), the maximum age constraint from sample MCA-123.1, and the ages interpolated for the top and base of C15n from the Massignano section as input data, allowing for a change in sedimentation rate at the lithological boundary between the Scaglia Variegata and Scaglia Cinerea formations at metre level 107.5 of the section (Jovane et al., 2013). The age-depth model (Figure 2.9) was run with a *k* parameter set at a nominal value of 100, and allowed to vary by two orders of magnitude in either direction, and returned an agreement index of 93.3 %. Interpolated ages for the magnetic reversals and planktonic foraminifer bioevents recorded in the Monte Cagnero section are listed in Table 2.4.

2.5 Discussion

2.5.1 Radio-isotopic calibration of the GPTS

K/Ar and $^{40}Ar/^{39}Ar$ dates from the Umbria-Marche succession have been used as tie-points for the numerical age calibration of the marine magnetic anomaly profile of Cande and Kent (1992) in most recent editions of the radio-isotopically calibrated GPTS (Cande and Kent, 1995; Wei et al., 1995; Ogg and Smith, 2004; Vandenberghe et al., 2012). Because the majority of the dates used in these time scales were obtained using the $^{40}Ar/^{39}Ar$ method, their accuracy is controlled by the accuracy of the age of neutron fluence standards, notably the age of the Fish Canyon sanidine, which has been repeatedly revised from 27.84 Ma, at the time of the publication of the Cande and Kent (1995) time

scale to 28.02 Ma (Renne et al., 1998) used in GTS04 (Ogg and Smith, 2004), and 28.201 Ma (Kuiper et al., 2008) in GTS12 (Vandenberghe et al. 2012).

The astronomical tuning of the Late Eocene – Oligocene record of ODP Site 1218 (Pälike et al., 2006), provides an alternative to traditional radio-isotopically calibrated GPTSs, and presents the advantage of directly dating individual magnetic reversals, thus eliminating the uncertainties associated with the magnetostratigraphic calibration and numerical age of widely spaced radio-isotopically dated tie-points.

In GTS12, in addition to a radio-isotopic age model for the Paleogene, Vandenberghe et al (2012) also presented a composite astronomically tuned GPTS, which relies on the tuning of ODP Site 1218 to calibrate the Oligocene, and numerical age calibration of the marine magnetic anomaly profile of Cande and Kent (1992) for the Late Eocene, using age data from the older end of the Oligocene tuning and the younger end of their Paleocene – Middle Eocene astrochronology (Westerhold et al., 2008; Westerhold and Röhl, 2009; Hilgen et al., 2010).

Discrepancies between these time scales are on the order of 100-500 kyr in the Late Eocene and Oligocene, with radio-isotopically calibrated estimates generally older than those derived from astronomical tuning. Our $^{206}Pb/^{238}U$ dates from the Umbria-Marche succession provide a means to directly calibrate the magnetic polarity record of the interval between 36-26 Myr, and can be used to determine whether observed discrepancies between astronomically tuned and radio-isotopically calibrated GPTSs of the Late Eocene and Early Oligocene are due to an error in the tuning of the ODP 1218 record, or inaccuracy of the radio-isotopic dates used as tie-points. Interpolated ages for the magnetic reversals recorded in the Umbria-Marche succession, along with age estimates from the time scales of Cande and Kent (1995), GTS04 (Ogg and Smith, 2004),

Monte Cagnero	This study	CK95	GTS04	ATPS06	GTS12
Base C8r*	26.505 ± 0.150	27.03	26.71	26.51	26.42
Base C9n	27.494 ± 0.149	27.97	27.83	27.41	27.44
Base C9r	27.855 ± 0.166	28.28	28.19	27.87	27.86
Base C10n	28.387 ± 0.184	28.75	28.72	28.32	28.28
Base C10r	29.119 ± 0.187	29.40	29.45	29.17	29.18
Base C11n.2n	29.856 ± 0.178	30.10	30.22	29.96	29.97
Base C11r	30.359 ± 0.160	30.48	30.63	30.62	30.59
Base C12n	31.234 ± 0.089	30.94	31.12	31.02	31.03
Base C12r	33.030 ± 0.073	33.06	33.27	33.23	33.16
Base C13n	33.728 ± 0.137	33.55	33.74	33.71	33.71
Massignano					
Base C13r	34.907 ± 0.054	34.66	34.78	35.13	35.00
Base C15n	35.108 ± 0.052	34.94	35.04	35.25	35.29
Base C15r	35.439 ± 0.044	35.34	35.40	35.33	35.71
Base C16n.1n	35.542 ± 0.050	35.53	35.57	35.55	35.89
Base C16n.1r	35.645 ± 0.057	35.69	35.71	35.64	36.05

Table 2.5 Comparison between interpolated magnetic reversal ages and published geomagnetic polarity time scales. CK95 = Cande and Kent (1995), GTS04 = Ogg and Smith (2004), ATPS06 = Pälike et al. (2006), GTS12 = Vandenberghe et al. (2012). * - age calculated based on the interpolated age for the base of C9n, assuming that the biotite-rich layer at metre level 208.3 is situated at C9n(.05).

the tuning of ODP Site 1218 (Pälike et al., 2006), and the astronomically tuned age model of GTS12 (Vandenberghe et al., 2012) are summarized in Table 2.5, with discrepancies between these time scales and our data plotted in Figure 2.10. The radio-isotopic age model of GTS12 (Vandenberghe et al., 2012) is based, among others, on $^{40}Ar/^{39}Ar$ dates from biotite-rich beds at metre levels 12.7 and 14.7 at Massignano and 145.5 and 208.3 at Monte Cagnero. The accuracy of these dates is discussed in section 2.4.1, and will not be considered further here.

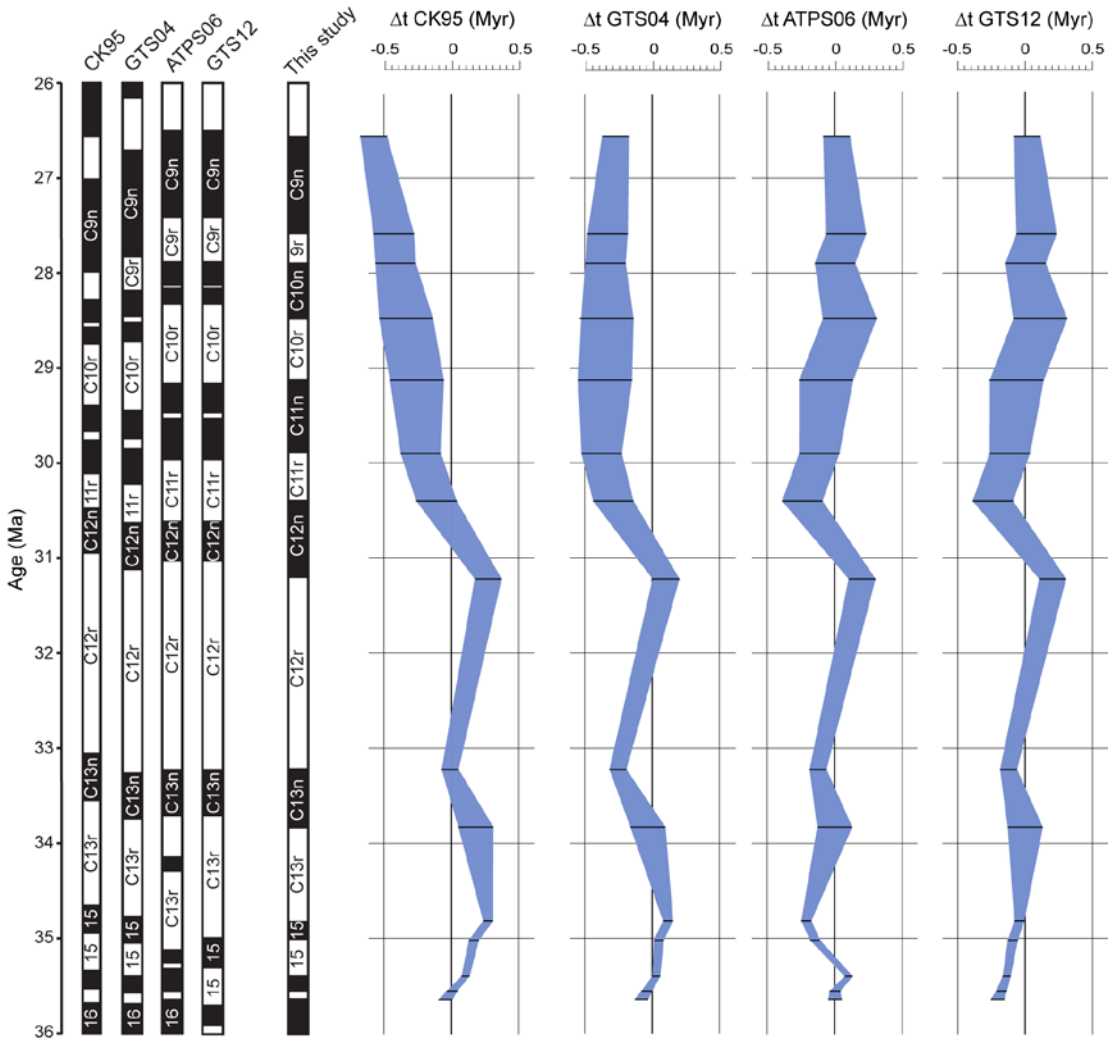

Figure 2.10 Comparison between interpolated magnetic reversal dates from the Massignano and Monte Cagnero sections and recent editions of the geomagnetic polarity time scale. CK95 – Cande and Kent (1995). ATPS06 – astronomically tuned time scale from ODP Site 1218 (Pälike et al., 2006). Positive (negative) values indicate that $^{206}Pb/^{238}U$ calibrated reversal ages are older (younger) than the respective GPTS.

Interpolated ages from magnetic reversals between the base of C11r and the base of C8r are 100-500 kyr younger than reported in the time scale of Cande and Kent (1995) and GTS04 (Ogg and Smith, 2004). This is due to the use of an age of 23.8 Ma for the Oligocene – Miocene boundary in the time scale of Cande and Kent (1995), which has since been revised to 23.03 through astronomical tuning of the Carrosio-Lemme section in northern Italy (Shackleton et al., 2000; Lourens et al., 2004), and the use of a tie-point

with an age of 28.1 ± 0.3 Ma (2σ), calibrated at the base of C9n in GTS04. The age of 28.1 Ma is based on $^{40}Ar/^{39}Ar$ dating of biotite-rich beds at metre level 274 of the Contessa Highway section and metre level 190 of the Monte Cagnero section. Attempts to re-date the Contessa Highway biotite-rich bed by Coccioni et al. (2008) were unsuccessful due to interlayer alteration of biotite flakes, while the magnetostratigraphic calibration of the Monte Cagnero biotite rich layer to the base of C9n is not consistent with the magnetic polarity pattern of Coccioni et al. (2008), in which the base of C9n occurs ca. 6 m higher (equivalent to ca 500 kyr, based on our age-depth model).

Interpolated late Eocene and Oligocene magnetic reversal ages are in good overall agreement with the astronomically tuned time scale of Pälike et al. (2006) from ODP Site 1218, and while small discrepancies (up to 200 kyr) do exist at the level of individual chron boundaries, these are not systematic, which suggests that the tuning of the ODP 1218 record to the 405 kyr eccentricity signal is correct at least back to 35.6 Ma. The observed discrepancies may be due to inconsistencies in the tuning of shorter cycles, or the identification of chron boundaries in the Umbria-Marche and/or ODP 1218 successions.

The interpolated ages of Late Eocene magnetic reversals from the Massignano section are up to 350 kyr younger than those from the astronomically tuned age model of GTS12 (Vandenberghe et al., 2012). Between 34-37 Ma, the GTS12 age model relies on sixth order polynomial interpolation between the astronomically tuned age of the base of C13n at ODP Site 1218 (which, at 33.71 Ma is in agreement with our interpolated age of 33.728 ± 0.137 Ma), and an astronomically tuned age of 47.8 Ma for the base of C21n, based on the tuning of ODP Site 1258 (Westerhold and Röhl, 2009), which marks the younger end of the floating Paleocene – Middle Eocene astronomical time scale (Westerhold et al., 2007, 2008; Westerhold and Röhl, 2009; Hilgen et al., 2010). However, the relative duration of magnetochrons C23n.2n and C23n (1:1) at ODP Site

1258 is not consistent with that reported in the magnetic anomaly profile of Cande and Kent (1992) (1:2), which implies the possibility of a 400-500 kyr hiatus, or an error in the tuning of the ODP Site 1258 record to the 405 kyr cycle (Vandenberghe et al., 2012), which could potentially be the source of the discrepancy between our $^{206}Pb/^{238}U$ calibrated magnetic reversal ages and the GTS12 age model.

2.5.2 Diachroneity of Late Eocene – Oligocene planktonic foraminifer bioevents between the western Tethys and low latitude settings

The Umbria-Marche succession hosts the GSSP of the base of the Oligocene, defined at metre level 19 of the Massignano section, based on the LO of planktonic foraminifera genus *Hantkenina* (Premoli Silva and Jenkins, 1993), and a proposed site for the definition of the GSSP of the Chattian based on the LCO of *Chiloguembelina cubensis* at metre level 188 of the Monte Cagnero section (Coccioni et al., 2008), however, concerns have been raised over the diachroneity of these biostratigraphic markers between the western Tethys and lower latitude settings (van Mourik and Brinkhuis, 2005; van Simaeys, et al., 2004).

A comprehensive review of the magnetostratigraphic and numerical age calibration of planktonic foraminifer zones relative to the astronomical tuning of ODP Site 1218 has been recently published by Wade et al. (2011). A comparison between interpolated ages for planktonic foraminifer bioevents reported from the Massignano and Monte Cagnero section based on our $^{206}Pb/^{238}U$ calibrated age-depth models, and the dates of Wade et al. (2011) (Figure 2.11) shows that events marking the base of planktonic foraminifer zones E16 and O2 of Berggren and Pearson (2005), namely the LO of *Globigerinatheca index*, and the LO of *Pseudohastigerina naguewichiensis* are in good agreement with the dates of Wade et al. (2011), while the LO of hantkeninids which marks the base of zone O1

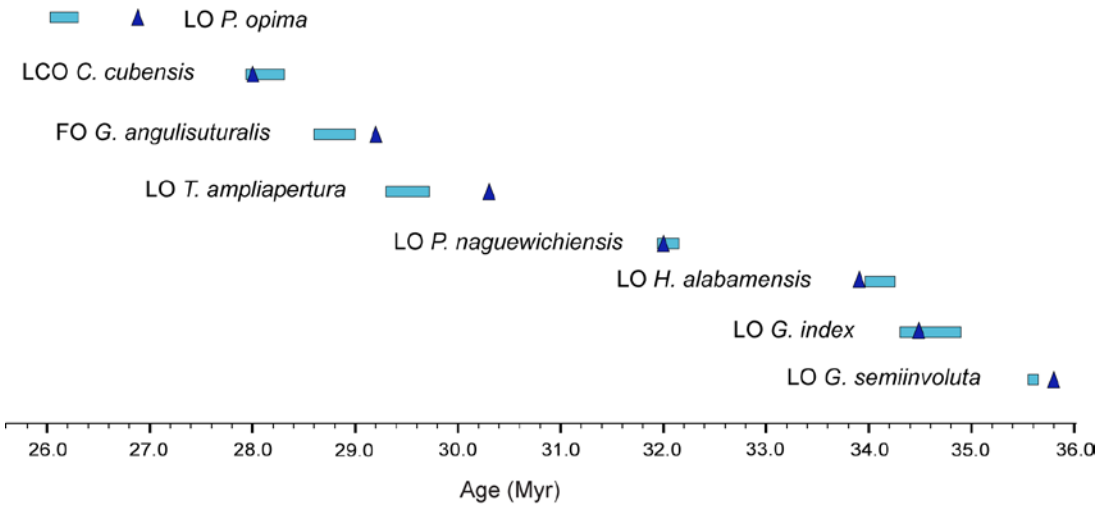

Figure 2.11 Diachroneity between planktonic foraminifer bioevents reported from the Umbria-Marche succession (blue bars) and the revised planktonic foraminifer biozonation scheme of Wade et al. 2011 (blue triangles) calibrated relative to the tuning of ODP Site 1218 (Palike et al., 2006), which is aplicable to tropical and subtropical settings.

appears to be slightly older in the Umbria-Marche basin, however this is likely to be an artefact of magnetostratigraphic calibration as discussed in section 2.5.4.

In the Oligocene part of the record, the LO of *Turborotalia ampliapertura* (base of O3), the FO of *Globigerina angulisuturalis* (base of O4) and the LO of *Paragloborotalia opima* (base of O6) all appear to be between 0.4 and 0.8 Myr younger than their calibration in open ocean environments. It is difficult to determine whether these age discrepancies are the result of poor preservation or inadequate sampling resolution in the Umbria-Marche succession. Because bioevents can reasonably be expected to be synchronous within the Umbria-Marche basin, the magnitude of preservation and sampling related effects can be assessed by looking at the distribution of bioevents relative to magnetostratigraphy in several coeval sections. Table 2.6 shows a compilation of the Late Eocene – Oligocene bio-magnetostratigraphy of the Massignano, Contessa Highway, Monte Cagnero, Contessa Barbetti and Pieve d'Accinelli sections. These data quantify the robustness of the bio-magnetostratigraphic calibration of the Umbria-Marche succession, as with the exception

of isolated events such as the LO of *Subbotina angiporoides*, and the FO of *Turborotalia cunialensis*, discrepancies between individual sections are on the order of 0.2 Myr, significantly smaller than those between Oligocene planktonic foraminifera events at Monte Cagnero and in the open ocean compilation of Wade et al. (2011). Our interpolated planktonic foraminifer ages, in combination with the good agreement between our magnetic reversal dates and the orbital tuning of ODP Site 1218, could be interpreted as representing genuine diachroneity of foraminiferal bioevents between the western Tethys and other oceanic basins. However, based on the available data, it is not possible to assess whether the diachroneity of planktonic foraminiferal bioevents is a characteristic feature of just the Umbria-Marche basin, or if it affects the western Tethys in general, because although high resolution biostratigraphic studies have been conducted elsewhere in the

Oligocene	Monte Cagnero		Contessa Barbetti		Pieve d'Accinelli	
LCO *C. cubensis*	C10n(.26)	28.12	C10n(.46)	28.08	C10n(.32)	28.02
FO *G. angulisuturalis*	C10r(.52)	28.76	C10r(.54)	28.78	C10r(.44)	28.69
LO *S. angiporoides*	C11r(.53)	30.15	-	-	C10r(.88)	29.05
FO *G. ciperoensis*	T_C11n.2n	29.54	C11n.2n(.37)	29.67	-	-
LO *T. ampliapertura*	T_C11n.2n	29.54	C11n.2n(.37)	29.67	-	-
Eocene	**Monte Cagnero**		**Massignano**		**Contessa Highway**	
LO *H. alabamensis*	C13r(.28)	34.04	C13r(.27?)	34.03	-	-
LO *T. cunialensis*	C13r(.37)	34.14	C13r(.31)	34.07	C13r(.32)	34.08
LO *C. inflata*	C13r(.58)	34.37	C13r(.67)	34.43	-	-
LO *G. index*	C13r(.67)	34.47	C13r(.78)	34.59	C13r(.55)	34.33
FO *T. cunialensis*	C13r(.91)	34.73	C15r(.58)	35.23	C15r(.13)	35.06

Table 2.6 Magnetostratigraphic calibration of planktonic foraminifera and dinocyst event from the Late Eocene and Oligocene of the Umbria-Marche succession. All data for the Oligocene are from Coccioni et al., (2009). Calibration of the Massignano section is based on the biostratigraphy of Coccioni et al., (1988) combined with the magnetostratigraphy of Jovane et al. (2007) and Lowrie and Lanci (1994). Calibration of the Monte Cagnero section is based on the biostratigraphy of Parisi et al. (1988) and magnetostratigraphy of Jovane et al. (2013). The calibration of the Contessa Highway section is based on Premoli Silva et al. (1988).

Mediterranean region (e.g. Fuente Caldera, Alegre et al., 2007, Zarabanda, Fenero et al., 2013) no magnetostratigraphy or radio-isotopic dates have been reported from these localities.

A notable exception to the above is the LCO of *Chiloguembelina cubensis*, which marks the base of zone O5 of Berggren and Pearson (2005), and has been proposed by Coccioni et al. (2008) as a potential GSSP for the base of the Chattian. Van Simaeys et al (2004) argued against the use of the *Chiloguembelina* criterion for the definition of the base of the Chattian based on the supposed diachroneity of this event, however consistent calibration of this bioevent to chron C10n has been reported from the Umbria Marche basin (Coccioni et al., 2008), ODP Site 1218 (Wade et al., 2007), and DSDP Sites 516, 558 and 529 (Pujol, 1983; Miller et al., 1985; Hess et al., 1989) while sporadic Chattian occurrences of chiloguembelinids at DSDP Site 522 and ODP Sites 628 and 803 have been attributed to reworking (Poore et al., 1982; Leckie et al., 1993). Our interpolated age for the LCO of *C. cubensis* at metre level 188 of the Monte Cagnero section is 28.126 ± 0.175 Ma, in agreement with the astronomically tuned estimate of 28.0 Ma of Wade et al (2011) based on the ODP Site 1218 tuning.

2.5.3 The ages of climatic events recorded in the Umbria-Marche succession

In terms of palaeoclimate, the Oligocene is characterized by a series of cooling events of global extent interspaced with warmer intervals. The timing of cooling events is linked to fluctuations of Antarctic ice volume, which are in turn controlled by orbital forcing of the Earth's climate (Wade and Pälike, 2004). The benthic foraminifer $\delta^{18}O$ record of ODP Site 1218 shows intervals characterised by heavier oxygen isotopic compositions broadly coinciding with minima in the 1.2 Myr amplitude modulation of the

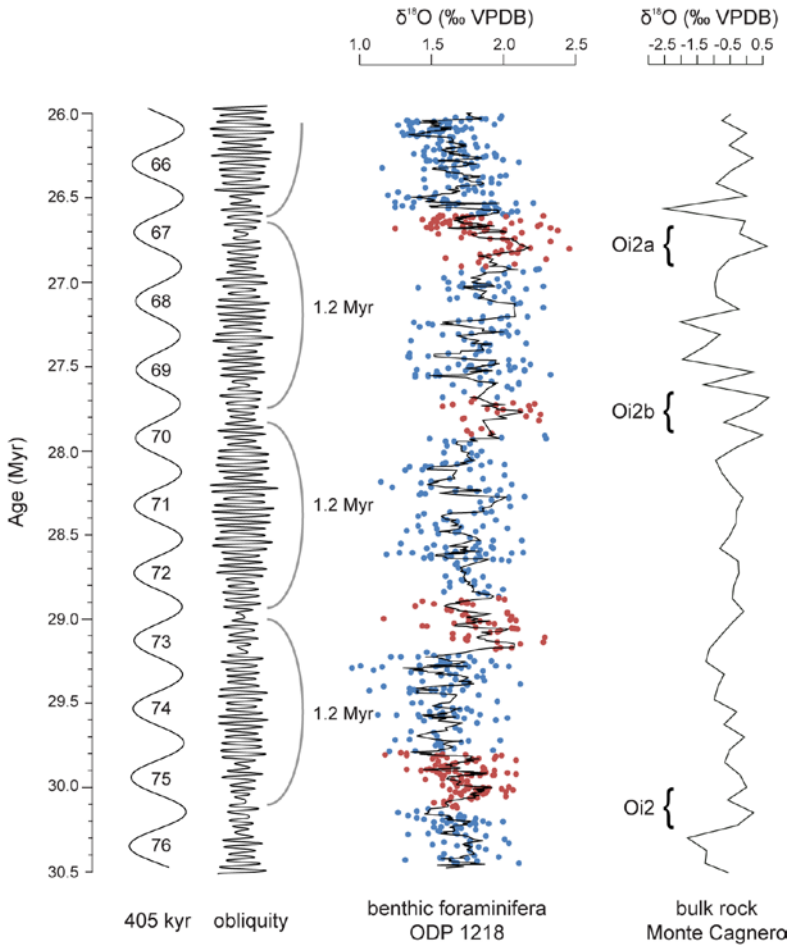

Figure 2.12 Comparison between oxygen isotope events reported from the Monte Cagnero section (Coccioni et al., 2008) and the benthic foraminifera $\delta^{18}O$ record of ODP Site 1218 (Wade and Pälike, 2004; Pälike et al., 2006) with data corresponding to positive oxygen isotope excursions plotted as red symbols. Also shown are the 405 kyr cycle naming scheme of Wade (2011), and the amplitude modulation of obliquity through the 1.2 Myr cycle (see text for details).

40 kyr obliquity cycles (Wade and Pälike, 2004; Pälike et al., 2006), the inference being that the low amplitude of obliquity cycles favours low seasonality with cooler summers which inhibit summer ice melt and promote ice sheet growth (Wade et al., 2004; Zachos et al., 2001). Although no high-resolution benthic foraminifer $\delta^{18}O$ records have been published from the Massignano and Monte Cagnero sections, several cooling events have been identified in the Monte Cagnero section based on $CaCO_3$ concentration, and low-resolution bulk rock $\delta^{18}O$ data. The oldest and most dramatic of these cooling events is

the Early Oligocene Oi-1 event which marks the development of the first continent scale permanent ice-sheet on Antarctica (Miller et al., 1991 Zachos et al., 1996, 2001; Coxall et al., 2005). In deep-sea records the Oi-1 event is expressed as an abrupt (ca 300 kyr) 1-1.5 ‰ positive shift in benthic foraminifera $\delta^{18}O$, and an increase in carbonate content signifying a ca 1 km deepening of the carbonate compensation depth occurring close to the base of magnetochron C13n (Coxall et al., 2005). At Monte Cagnero, Hyland et al. (2009) identified a ca 20% positive shift in $CaCO_3$ weight percentage data, which occurs at metre level 118, also in close proximity to the base of C13n. Because deposition of the Umbria-Marche succession occurred above the CCD in the Eocene, the small magnitude and limited temporal extent of the $CaCO_3$ shift precludes an assessment of the duration of the Oi-1 event, however our interpolated age of 33.65 ± 0.134 is consistent with the data of Coxall et al. (2005) who estimated that the Oi-1 event took place between ca 33.6-33.4 Ma based on astronomical tuning at ODP Site 1218. Coccioni et al. (2008) identified a series of cooling events based on bulk rock $\delta^{18}O$ data from the upper part of the Monte Cagnero section, which they tentatively correlated to oxygen isotope events Oi2, Oi2a and Oi2b of Wade and Pälike (2004), and these correlations are confirmed by our age-depth model (Figure 2.12), however, given the limited stratigraphic resolution of the data it is not possible to determine the precise timing and duration of these events.

2.5.4 The age of the Eocene - Oligocene boundary

Recent estimates of the age of the Eocene – Oligocene boundary range between 33.71 and 34.1 Ma (Figure 2.18). A number of these estimates are based on the magnetostratigraphic calibration of the boundary at C13r(.14) (Premoli Silva and Jenkins, 1993), such as the age of 33.79 Ma reported by Pälike et al. (2006) based on the tuning of the ODP Site 1218 record, and dates of 33.9 ± 0.1 Ma reported in GTS04 and GTS12. Other workers have dated the boundary based on the LO of the planktonic foraminifer

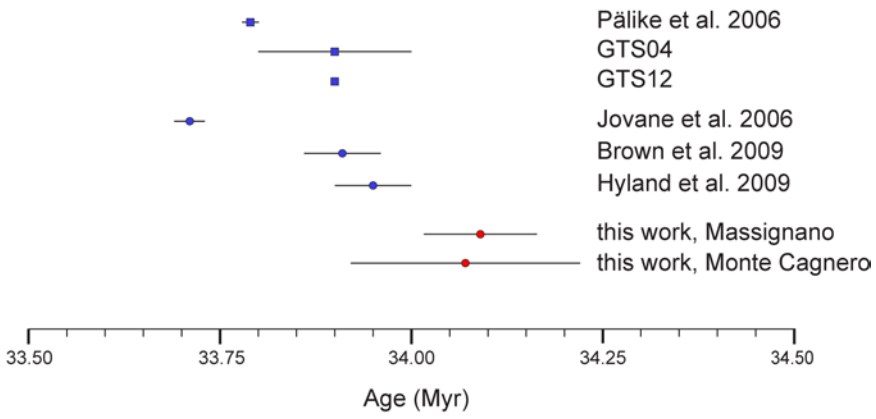

Figure 2.13 Comparison between recent estimates of the age of the Eocene – Oligocene boundary and interpolated dates for the LO of hantkeninids from the Massignano and Monte Cagnero sections.

genus *Hantkenina*, through the development of floating astronomical time scales for the Massignano and Monte Cagnero section and arrived at dates of 33.71 ± 0.02 Ma (Jovane et al., 2007), 33.90 ± 0.05 Ma (Brown et al., 2009) and 33.95 ± 0.05 Ma (Hyland et al., 2009).

Our age-depth models yielded statistically indistinguishable (at the 2σ level) $^{206}Pb/^{238}U$ calibrated age estimates for the LO of hantkeninids at Massignano and Monte Cagnero, at 34.090 ± 0.074 Ma, and respectively, 34.070 ±0.149 Ma. These dates are slightly older than previous estimates, although statistical equivalence is difficult to assess because the uncertainties of the astronomically tuned dates, and respectively the $^{40}Ar/^{39}Ar$ and K/Ar calibrated date from GTS04, do not include systematic components. The 33.79 Ma estimate for the age of the Eocene – Oligocene boundary defined at C13r(.14) reported by Pälike et al. (2006) from ODP Site 1218 is ca. 300 kyr younger than our interpolated dates for the LO of hantkeninids in the Umbria – Marche succession, and given the overall agreement between our magnetic reversal dates and the ODP Site 1218 geomagnetic polarity time scale (see section 2.5.1) , this might indicate an inconsistency

between the biostratigraphic and magnetostratigraphic definitions of the boundary. The magnetostratigraphic calibration of the LO of hantkeninids is somewhat uncertain in the Massignano section, because the base of magnetochron C13n has been placed at metre level 20.2 in the magnetic polarity record of Bice and Montanari (1988) and between 21-22.5 in the record of Lowrie and Lanci (1994). At Monte Cagnero, the LO of hantkeninids falls at C13r(.28) based on the magnetic polarity record of Jovane et al. (2013), while a point situated at C13r(.14) would fall at metre level 115.7, and based on our age-depth model, would have an age of 33.92 ± 0.14 Ma, within uncertainty of the date reported by Pälike et al. (2006).

2.6 Conclusions and summary

Analysis of zircons from the biotite-rich beds of the Umbria-Marche succession yielded weighted mean $^{206}Pb/^{238}U$ ages that are ca. 0.5 Myr younger than legacy $^{40}Ar/^{39}Ar$ data recalculated to an age of 28.201 Myr for the Fish Canyon sanidine. This indicates that the 0.4-0.6 Myr discrepancy reported between radio-isotopically and orbitally calibrated age models in the 2012 edition of the Geological Time Scale is due to the use of anomalously old recalculated $^{40}Ar/^{39}Ar$ data and brings the chronostratigraphic framework of the Umbria Marche succession in line with the astronomically tuned age model developed for the Oligocene at ODP Site 1218.

Interpolated ages for the LO of hantkeninids and the LCO of *Chiloguembelina cubensis* indicate that, when uncertainties in both magnetostratigraphic calibration and numerical age dating are taken into account, these events represent robust biostratigraphic markers for the identification of the base of the Rupelian and respectively the Chattian as they do not appear to be time-transgressive between the Umbria-Marche and oceanic basins.

Interpolated ages for the LO of *Turborotalia ampliapertura*, the FO of Globigerina angulisuturalis, and the LO of *Paragloborotalia opima*, indicate that these events occurred 0.4-0.8 Myr later in the Umbria-Marche basin than in open ocean settings. Further investigations are needed to determine whether this is a common feature in the Mediterranean, and potential diachroneity should be taken into account in studies that rely on planktonic foraminifera zonation for numerical age control.

3. Dating terrestrial environmental change and North American Land Mammal Ages across the Eocene – Oligocene transition

Abstract: Records of terrestrial environmental change during the Eocene – Oligocene greenhouse to icehouse transition (EOT) have been used to infer diachroneity compared to marine $\delta^{18}O$ records for the same interval. In North American terrestrial successions, such diachroneity is based on published $^{40}Ar/^{39}Ar$ data, which is directly compared to astronomically tuned age models developed for marine records of the EOT. This chapter presents the results of $^{206}Pb/^{238}U$ dating of zircons from 15 volcanic tuffs intercalated in two key sedimentary successions at Toadstool Park (Nebraska) and Flagstaff Rim (Wyoming) that contain proxy records of environmental change, and are type sections for the Chadronian, Orellan, and Whitneyan North American Land Mammal Ages (NALMAs). Interpreted weighted mean $^{206}Pb/^{238}U$ dates are 0.4-1.0 Myr younger than published $^{40}Ar/^{39}Ar$ dates calibrated relative to an age of 28.201 Ma for the Fish Canyon sanidine, indicating that reported discrepancies between marine and terrestrial records of the EOT were caused by anomalously old $^{40}Ar/^{39}Ar$ data. $^{206}Pb/^{238}U$ calibrated age-depth models developed for the Flagstaff Rim and Toadstool Park successions facilitate a robust intercomparison between marine and terrestrial archives of environmental change, and indicate that: (i) cooling recorded in the Toadstool Park succession in the Early Orellan is synchronous with the early Oligocene Antarctic glaciation, and (ii) the last appearance datums of key Chadronian mammal taxa are diachronous by ca. 1 Myr between the two localities.

3.1 Introduction

The Eocene – Oligocene transition (EOT) was characterised by a shift in the Earth's climate from greenhouse to icehouse mode, leading to the development of a permanent, continent-scale Antarctic ice sheet (Shackleton and Kennett, 1975; Sagnotti et al., 1998; Zachos et al, 2001; Ivany et al., 2006; Coxall and Pearson, 2007; Miller et al., 2009). It is postulated that this transition was the result of a combination of declining atmospheric pCO_2 levels, changes in ocean circulation, and/or orbital configurations favouring cool summers and low seasonality (DeConto and Pollard, 2003; Sijp and England, 2004; Coxall et al., 2005; Livermore et al., 2005; Pagani et al., 2005; Huber and Nof, 2006; DeConto et al., 2008; Katz et al., 2011). High-resolution marine records of the EOT, recovered via DSDP and ODP expeditions from the Atlantic, Pacific, Indian and Southern oceans, are characterised by an abrupt, stepwise, 1.2-1.5 ‰ positive shift in benthic foraminiferal $\delta^{18}O$ values (Oi-1 event), interpreted as the combined expression of deep-sea cooling and Antarctic ice growth (Zachos et al., 1996; Coxall et al., 2005; Pearson et al, 2008; Katz et al., 2008), although the relative contribution of these two effects remains a matter of debate (Lear et al., 2000; 2004; 2008; Billups and Schrag, 2003; Coxall and Pearson, 2007; Liu et al., 2009). The $\delta^{18}O$ shift, which lasted about 300 kyr based on a cyclostratigraphic age model developed at ODP site 1218 in the Equatorial Pacific (Coxall et al., 2005; Palike et al., 2006), appears to by synchronous across ocean basins, with peak $\delta^{18}O$ values reached around 33.6 Ma, close to the base of magnetochron C13n (Zachos et al., 1996, 2001; Coxall et al., 2005; Katz et al., 2008; Cramer et al., 2009, see Chapter 2).

In contrast to the marine record of the EOT, coeval terrestrial successions from North and South America, Europe, and Asia show substantial apparent differences in the extent and timing of changes associated with the EOT in terms of cooling, aridification,

and seasonality (Evanoff et al., 1992; Retallack, 1992; Hutchinson, 1992; Wolfe, 1994; Prothero and Heaton, 1996; Meng and McKenna, 1998; Terry et al., 2001; Kohn et al., 2004; Grimes et al., 2005; Zanazzi et al., 2007; Hooker et al., 2009; Xiao et al., 2010; Costa et al., 2011; Hren et al., 2013). Assessing the extent to which these terrestrial successions record environmental and faunal change that is either offset from, or coincident with, and therefore possibly related to changes in the marine realm requires a robust and highly-resolved temporal framework. This chapter focuses on the numerical age and nature of the terrestrial White River Group (WRG) sedimtentary succession that outcrops in Nebraska and Wyoming, and has been the basis for earlier bio-, magneto- and chrono-stratigraphic studies of the terrestrial EOT in North America (Prothero 1985; Prothero et al., 1983; Swisher and Prothero, 1990; Prothero and Swisher, 1992; Obradovich et al., 1995; Prothero and Whitlesey, 1998; Terry 2001; Zanazzi et al., 2007,2009; Boardman and Secord, 2013).

3.1.1 Palaeoclimate proxy record of the WRG

The WRG of North America is a predominantly fluvial-eolian sedimentary succession which hosts vertebrate fossil assemblages that form the basis for the definition of the Chadronian, Orellan, and Whitneyan North American Land Mammal Ages (NALMAs) (Wood et al., 1941; Prothero and Emry, 1996; Prothero and Whittlesey, 1998). The transition between the Chadronian and Orellan NALMAs is thought to be roughly equivalent to the EOT, based on $^{40}Ar/^{39}Ar$ dating of biotite and sanidine from primary air-fall tuffs intercalated in the WRG sedimentary succession (Swisher and Prothero, 1990; Obradovich et al., 1995). Lithostratigraphic, palaeopedologic, and palaeobotantic studies, along with changes in aquatic reptile and amphibian assemblages indicate cooling and progressive aridification in the Late Chadronian and Early Orellan (Retallack, 1992; Evanoff et al., 1992; Hutchinson, 1992; Terry, 2001), however the magnitude and timing

of environmental change is a matter of debate.

Zanazzi et al. (2007, 2009) used $\delta^{18}O$ data from fossil bone and teeth collected from WRG outcrops at Toadstool Geologic Park in western Nebraska to infer cooling on the order of 7.1 ± 3.1˚C across the Chadronian – Orellan transition. A similar study by Boardman and Secord (2013) found no evidence of a significant drop in mean annual temperature (MAT), however this may be the result of sampling bias caused by the presence of a hiatus at the level of the Chadronian – Orellan boundary in part of the Toadstool Park outcrop. Zanazzi et al. (2007) reported that cooling recorded in the Toadstool Geologic Park succession lags behind the marine Oi-1 event by ca. 400 kyr, based on an age-depth model calibrated using one $^{40}Ar/^{39}Ar$ date from the Toadstool Park record (pers. com. by A. Deino in LaGarry, 1998), tephrostratigraphic correlation to other WRG successions containing dated tuffs (Swisher and Prothero, 1990; Larson and Evanoff, 1998), and magnetic reversal ages from the geomagnetic polarity time scale (GPTS) of Cande and Kent (1995). However, calibration of the $\delta^{18}O$ curve of Zanazzi et al. (2007, 2009) relative to magnetic reversal ages extracted from the astronomically tuned Oligocene time scale of Palike et al. (2006) places the Chadronian – Orellan cooling step ca. 300 kyr before the Oi-1 event, while calibration relative to $^{40}Ar/^{39}Ar$ biotite and sanidine data of Swisher and Prothero (1990) from Toadstool Park (recalculated relative to an age of 28.201 Myr for the Fish Canyon sanidine, FCs) implies an even greater age gap of ca. 600 kyr (Figure 3.1). This raises the possibility that the North American terrestrial succession records diachronous cooling compared to the onset of glaciation and/or temperature shift in ocean basins.

An absence of terrestrial cooling coeval with the Oi-1 event would favour the interpretation of the Early Oligocene benthic foraminiferal $\delta^{18}O$ shift as an expression of Antarctic ice growth, with only a subordinate temperature component (Retallack et

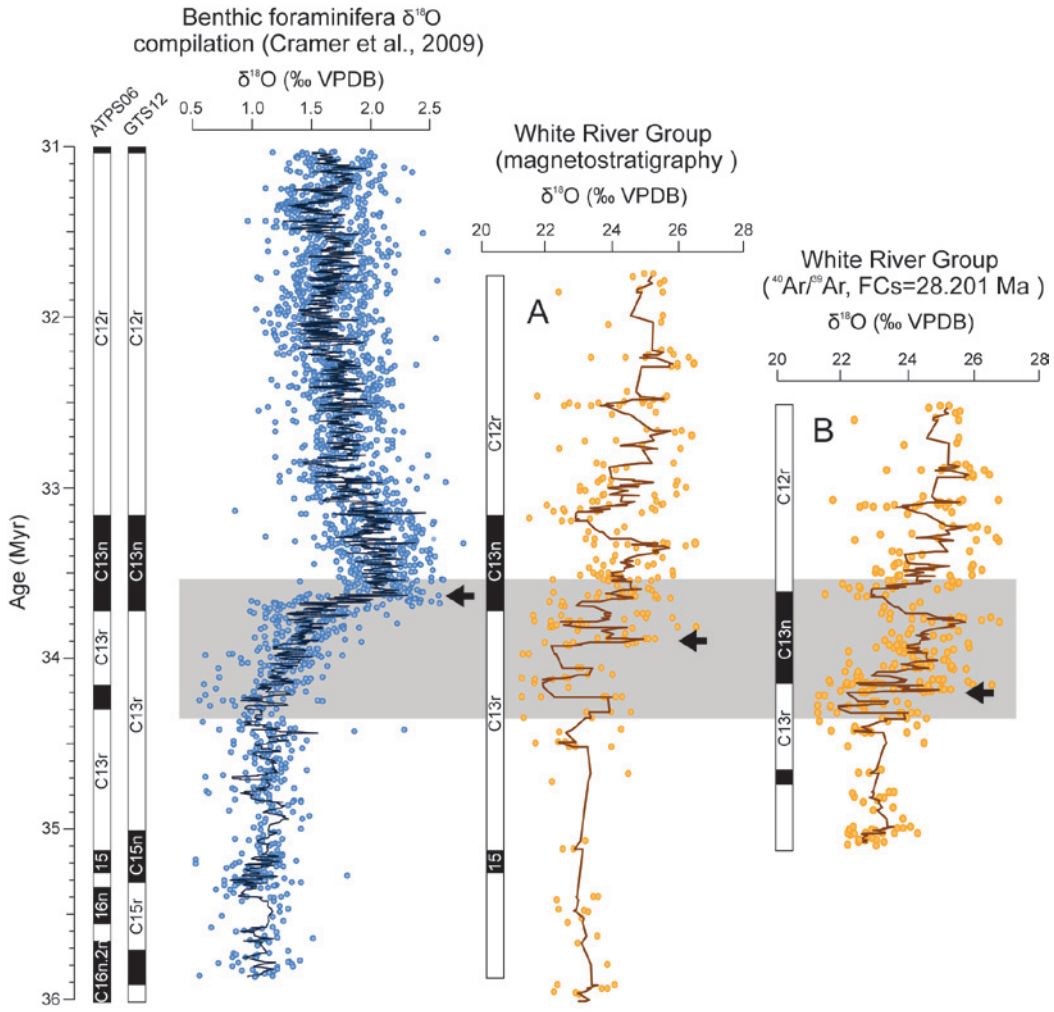

Figure 3.1 Numerical age calibration of the magnetostratigraphy of the Toadstool Park record, and the $\delta^{18}O$ data of Zanazzi et al. (2007, 2009) based on A - the magnetic polarity pattern of Prothero (1983) relative to ATPS06 – the astronomically tuned GPTS of Palike et al. (2006), and B - the $^{40}Ar/^{39}Ar$ dates of Swisher and Prothero (1990) relative to an age of 28.201 Ma for the Fish Canyon sanidine. Benthic foraminifer $\delta^{18}O$ compilation of Cramer et al. (2009) calibrated relative to ATPS06 is shown for comparison. GTS12 – astronomically calibrated GPTS of Vandenberghe et al. (2012). Black arrow marks the position of the Oi-1 event in the marine record, and the Chadronian – Orellan cooling step in the WRG

al., 2004; Sheldon and Retallack, 2004), as indicated by deep-sea Mg/Ca records (Lear et al., 2000, 2004; Billups and Schrag, 2003), although this conflicts with Mg/Ca data from shallower marine settings, and alkenone unsaturation index data from high-latitudes which are consistent with a 2.5-5˚C drop in sea surface temperatures across the EOT

(Lear et al., 2008; Liu et al., 2009).

3.1.2 Existing White River Group geochronology

Published chronologies for the WRG rely on legacy radio-isotopic (predominantly $^{40}Ar/^{39}Ar$ sanidine and biotite) dating of volcanic tuffs and correlation to the geomagnetic polarity time scale. Most of the radio-isotopic dates available from the WRG are $^{40}Ar/^{39}Ar$ biotite and sanidine dates published in the 1990's (Swisher and Prothero, 1990; Obradovich et al., 1995), the accuracy of which is controlled by the accuracy of the ^{40}K decay constant, the assigned age of the neutron fluence monitors used in $^{40}Ar/^{39}Ar$ dating (usually FCs), laboratory protocols employed, and the nature of the material being analysed (i.e., age distributions, pre- and post-eruptive histories). Since the publication of the $^{40}Ar/^{39}Ar$ dates of Swisher and Prothero (1990), who reported their results relative to an FCs age of 27.84 Ma, numerous studies have focused on improving the accuracy of the age of the FCs standard through calibration relative to primary K-Ar standards (Renne et al., 1994, 1998), astronomically dated tuffs (Kuiper et al., 2008; Rivera et al., 2011) and the U-Pb system (Renne et al., 2010), with recent results converging towards a value of ca. 28.20 Ma (Kuiper et al., 2008; Rivera et al., 2011; Wotzlaw et al., 2013, Renne et al., 2010).

Recalibration of the published $^{40}Ar/^{39}Ar$ dates from the White River succession (Swisher and Prothero, 1990; Obradovich et al., 1995) to the astronomically calibrated FCs age of Kuiper et al. (2008) results in an increase of ca. 1.28%, or ca. 0.45 Myr in numerical age (Hilgen and Kuiper, 2009). This has a significant impact on the age of events recorded in the WRG when considered relative to the chronology of events during the EOT from marine archives, and significantly impacts the correlation of the magnetic polarity pattern of the White River succession to the geomagnetic polarity time scale. Magnetic reversal ages interpolated based on the recalculated $^{40}Ar/^{39}Ar$ dates are several

hundred kyr older than those reported from astronomical tuning of the Late Eocene – Oligocene at ODP Site 1218 (Palike et al., 2006), as well as the astronomical age model for the Paleogene developed in GTS12 (Vandenberghe et al., 2012) (Figure 3.1). These discrepancies can potentially arise from inaccuracy of the $^{40}Ar/^{39}Ar$ dataset, errors in the magnetic polarity pattern of the White River succession, and/or inaccuracy of the astronomical tuning of the Oligocene and Late Eocene based upon ODP Site 1218 (Palike et al., 2006). The latter option is unlikely as new $^{206}Pb/^{238}U$ (zircon) CA-ID-TIMS ages from the Umbria-Marche succession in Italy (Chapter 2) indicate that the tuning of ODP Site 1218 is accurate at least at the level of the 405 kyr eccentricity cycle in the latest Eocene. The veracity of the palaeomagnetic record of the WRG is the topic of Chapter 4.

3.1.3 Potential applicability of U/Pb geochronology to refine the chronology of the WRG

The potential applicability of U/Pb geochronology to the WRG record is supported by the presence of euhedral zircon crystals in heavy mineral assemblages recovered from volcanic tuffs intercalated in the succession (Larson and Evanoff, 1998), and U-Pb zircon data reported by Scott et al. (1999) from a pilot study of WRG tuffs in eastern Wyoming. Unlike the $^{40}Ar/^{39}Ar$ system, the accuracy of which is determined by the accuracy of the age of the mineral standard used as a neutron flux monitor and that of the ^{40}K decay constant, the accuracy of U/Pb zircon data is controlled by the gravimetric calibration of isotopic tracer solutions which can be traced back to SI units (Condon et al., in-review; McLean et al., in-review), and the ^{238}U decay constant which has been determined through counting experiments (Jaffey et al., 1971) (see appendix A). As such there is a potential to produce radio-isotopic ages with total uncertainties of less than 0.12% (2σ) and the resolving power of the method (i.e., precision which does not include systematic sources of uncertainty) on the order of 0.05% (2σ).

As the accuracy and precision of radio-isotopic dating methods increases, so does the degree to which the assigned ages for a given sample are dependent upon the subjective/objective nature of the assumptions involved in the interpretation of single analyses data sets. For both U-Pb (zircon) and $^{40}Ar/^{39}Ar$ (sanidine), the assignment of depositional ages on the basis of the geochronology of eruptive volcanics requires the identification of potential pre-eruptive bias (e.g., pre-eruptive zircon, extraneous Ar) and post-depositional modification of the isotope systematics (e.g., Pb and/or Ar loss). High-precision U-Pb zircon data sets typically have skewed date distributions that are considered to reflect a mixture of eruptive and pre-eruptive dates, with the youngest population of overlapping dates assumed to best approximate the time of eruption and deposition. Similar issues are now becoming apparent in some high-precision $^{40}Ar/^{39}Ar$ datasets where non-normally distributed data are interpreted as reflecting inclusion of extraneous Ar, and/or incorporation of inherited crystals. This interpretative approach is corroborated by several recently generated dual high-accuracy U-Pb (zircon) and $^{40}Ar/^{39}Ar$ data sets (Rivera et al., 2013; Wotzlaw et al., 2013; Macho et al., in review) which yielded statistically equivalent (at the 2σ level) U-Pb and $^{40}Ar/^{39}Ar$ data pairs. In the few data sets where the U-Pb and $^{40}Ar/^{39}Ar$ data are discordant it is typical that the data are not internally consistent when samples are considered in their stratigraphic context (i.e., dates do not conform to constraints imposed by superposition) (Meyers et al., 2012). Thus the stratigraphic coherence of a single system data set with multiple ash beds sampled/dated at high stratigraphic resolution serves as a test for the veracity of the ages assigned to the stratigraphic section.

This chapter focuses on $^{206}Pb/^{238}U$ ID-TIMS dating zircons from volcanic tuffs intercalated in the White River succession with the aim of constraining the timing of environmental change associated with the Chadronian – Orellan transition, and improving the correlation of the Chadronian, Orellan and Whitneyan NALMAs to the marine time

scale.

3.2. Geological setting of the WRG

The WRG succession comprises fluvial and eolian deposits that accummulated in the North American midcontinent and adjacent Rocky Mountain basins during the Late Eocene and Early Oligocene (ca. 37-29 Ma). These deposits can be traced laterally from SW South Dakota, and NW Nebraska, into E Wyoming (Figure 3.2.A) and consist of fine grained volcanic and sedimentary deposits, present as reworked material and primary air fall tuffs, and, to a lesser extent, siliciclastic material derived from the Hartville, Laramie and Black Hills uplifts (Clark, 1975; Stanley and Benson, 1979). The volcanic material was sourced from explosive volcanism in Nevada and Utah (Larson and Evanoff, 1998), ca. 500-800 km south-west of the main White River outcrops, and as a result, stratigraphic units in the White River Group appear more condensed from west to east, as distance from the source area increases (Emry et al., 1987). The lithostratigraphic nomenclature varies across different localities, with White River deposits ranked as a group in Nebraska and South Dakota and as a formation in Wyoming. A revised lithostratigraphic classification and correlation scheme was proposed by LaGarry (1998), Terry (1998), and Terry and LaGarry (1998). This chapter focuses on two White River localities: Flagstaff Rim in Wyoming, and Toadstool Park in Nebraska.

3.2.1 Flagstaff Rim

The Flagstaff Rim section is situated in central Wyoming, ca. 20 km south-west of Casper (Figure 3.2.A). The White River Formation, exposed in a 200 m high cliff and smaller surrounding outcrops overlies the Cretaceous Cody shale, and is in turn unconformably overlain by the Miocene Split Rock Formation.

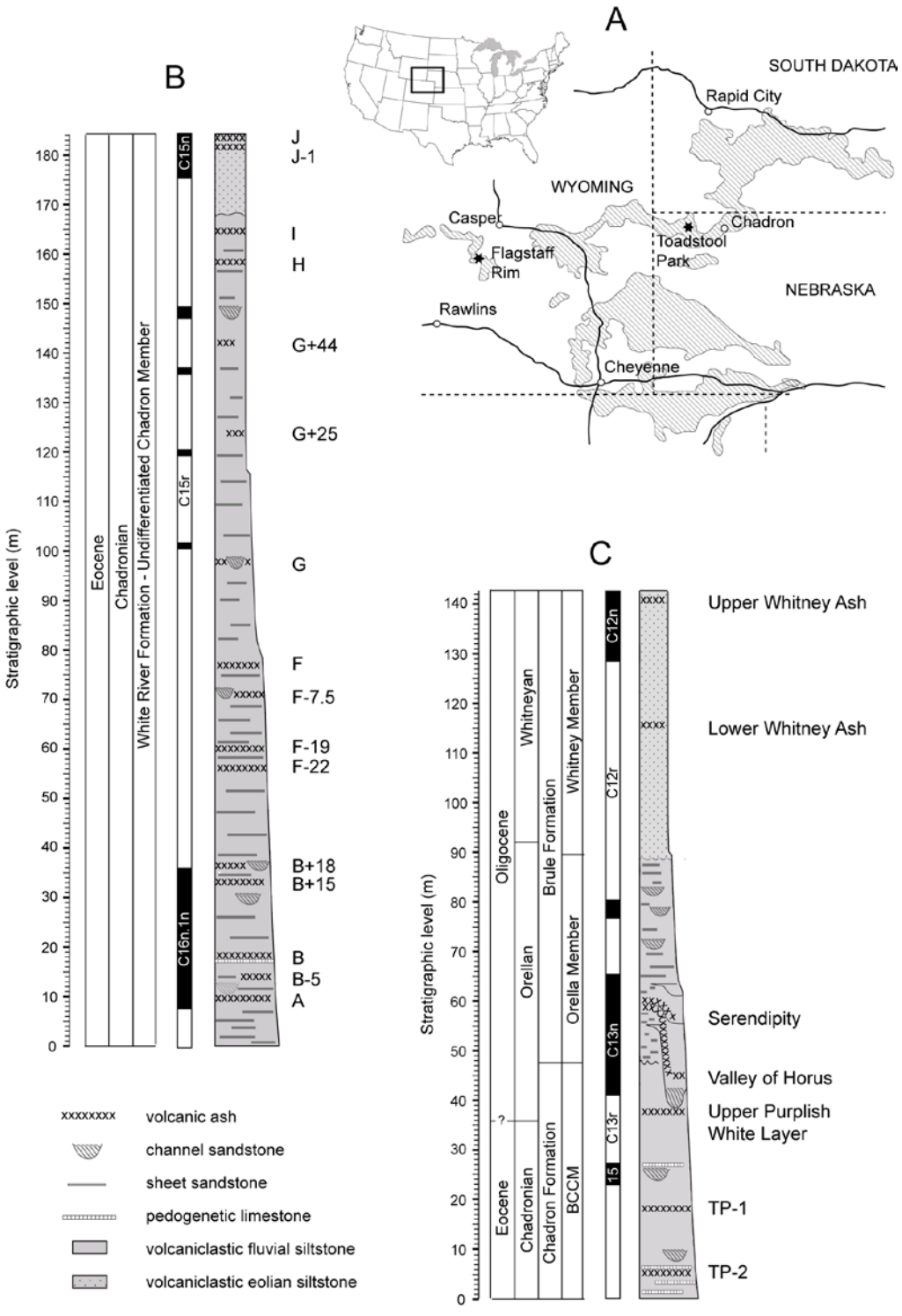

Figure 3.2 A – distribution of the White River Group succession in central North America and location of the Flagstaff Rim and Toadstool Park sections, B – lithostratigraphy of the Flagstaff Rim section, showing the stratigraphic position of volcanic tuff beds, and the magnetostratigraphy of Prothero and Swisher (1992), C – lithostratigraphy of the Toadstool Park section, showing the Early Orellan Toadstool Park channel complex (see text for details), the stratigraphic position of volcanic tuff beds, and the magnetostratigraphy of Prothero et al. (1983)

Emry (1973) was the first to provide a detailed acount of the stratigraphy of the Flagstaff Rim section, identifying more than 15 volcanic tuffs, the most prominent ones of which he labelled A to J (Figure 3.2.B). Biotite and sandinine $^{40}Ar/^{39}Ar$ dates from the B, F, G, I, and J tuffs (Swisher and Prothero, 1990), calibrated relative to a FCs age of 28.201 Ma (Kuiper et al., 2008) indicate that the Flagstaff Rim record spans an interval of ca. 1.5 Myr, between 34.9-36.4 Ma. However, this conflicts with the magnetostratigraphic calibration of the succession (Prothero and Swisher, 1992), which indicates that the record is significantly shorter than suggested by the radio-isotopic data, spanning the interval between the top of chron C16n.2n and the top of chron C15n, equivalent to ca. 0.5 Myr based on ATPS06, and the $^{206}Pb/^{238}U$ calibrated chronostratigraphic framework of the Umbria-Marche basin in Italy (Chapter 2).

The lower part of the Flagstaff Rim succession, below tuff B contains vertebrate fossil assemblages typical of the Late Early Chadronian, while the interval between tuffs B-G has been designated as the type section for the Middle Chadronian (Prothero and Whittlesey, 1998). Although vertebrate fossils are scarce above tuff G, the presence of brontotheres up to the level of the J tuff indicates that the top of the Flagstaff Rim succession is of Late Chadronian age (Emry, 1992). The succession records progressive aridification during the Late Chadronian, with a change from fluvial to eolian deposition occurring around the level of tuff I (Evanoff et al., 1992).

3.2.2 Toadstool Park

The Toadstool Geologic Park is situated in nortwestern Nebraska, ca. 20 km west of Chadron (Figure 3.2.A). and consists of a series of laterally continous outcrops spread over ca. 6 km^2 along the Big Cottonwood Creek. Lithostratigraphically the

Toadstool Park succession comprises the Big Cottonwood Creek Member of the Chadron Formation (Terry and LaGarry, 1998), and the Orella and Whitney Members of the Brule Formation (LaGarry, 1998). The Toadstool Park sedimentary succession spans the late Chadronian, Orellan and Whitneyan NALMAs (Late Eocene-Early Oligocene, Prothero and Whittlesey, 1998, Figure 3.2.C). The central part of the park is dominated by the deposits of the Toadstool Park channel complex, which developed in the Early Orellan and incised ca. 20 m into Late Chadronian deposits, however outcrops in the south-eastern part of the park contain a continuous record of the Chadronian – Orellan transition.

The magnetic polarity pattern of the section correlates to chrons C15n – C12n of the GPTS (Prothero et al., 1983; Prothero, 1996). Seven volcanic tuffs have been identified at Toadstool Park. Of these, the Upper and Lower Whiteny Ahes (UWA, LWA) have been dated using the $^{40}Ar/^{39}Ar$ technique (Swisher and Prothero, 1990). The Upper Purplish White Layer (UPW), which is situated in the uppermost part of chron C13r, and should therefore closely approximate the age of the Eocene – Oligocene transition, has not been dated at Toadstool Park, however tephrostratigraphic correlation to WRG localities in Wyoming indicates that the UPW is equivalent to the Persistent White Layer (PWL) of (Schultz and Stout, 1955) in the Douglas composite section in eastern Wyoming, and the J tuff at Flagstaff Rim (Larson and Evanoff, 1998). The PWL has been dated by means of $^{40}Ar/^{39}Ar$ dating at 34.03 Ma (Obradovich et al., 1995) and 34.43 Ma (Swisher and Prothero, 1990), with the same authors reporting dates of 34.81 Ma and 35.17 Ma respectively for the J tuff in the Flagstaff Rim section (all dates recalculated relative to FCs = 28.201 Ma). These data are not consistent with a correlation between the J tuff at Flagstaff Rim and the PWL in eastern Wyoming, but leave open the possibility that either one of the two tuffs may be an equivalent of the UPW. The Toadstool Park succession records cooling and aridification, with $\delta^{18}O$ data from fossil bone and teeth suggesting a $7.1 \pm 3.1^{\circ}C$ drop in MAT around the Chadronian – Orellan transition (Zanazzi et al., 2007,

2009), while the lithostratigraphic boundary between the Orella and Whitney Member of the Brule Formation is marked by a shift from fluvial to eolian sedimentation.

3.3 U/Pb dating of volcanic tuffs from the WRG

Twenty-three volcanic tuff samples, weighing between 4-5 kg each, were collected from measured sections at Flagstaff Rim and Toadstool Geologic Park. Volcanic tuffs were identified in the field based on their light colour and sharp basal contact. Most tuffs could be traced laterally over several hundreds of metres (Figure 3.3), while others were more localised in extent. At Flagstaff Rim, the nomenclature of the tuffs follows that of Emry (1973) with additional samples labelled based on their stratigraphic position relative to the nearest 'named' tuff. At Toadstool Geologic Park the nomenclature of the sampled tuffs follows that of LaGarry (1998), with two additional tuffs reported from the Orella Member of the Brule Formation (Valley of Horus, and Serendipity) and two from the Big Cottonwood Creek Member of the Chadron Formation (TP-1 and TP-2). The location and stratigraphic position of each sample, along with a brief description of the sampled tuffs are listed in Appendix A, Table A.2. The stratigraphic positions of individual tuffs are assumed to be accurate to within ±0.5 m. Zircons were separated from each sample based on the procedure outlined in Appendix A.

Of the 23 samples collected from the WRG, 15 yielded abundant zircon populations, dominated by euhedral zircons, with frequent melt inclusions, and aspect ratios between 5-7, while the remaining eight (the Serendipity tuff from Toadstool Geologic Park, and the A, B-5, F-22, F-18, G+24, G+44 and I tuffs from Flagstaff Rim) contained zircon populations dominated by rounded grains with only a few euhedral crystals. Overall, zircons recovered from the Toadstool Park samples were slightly smaller (100-200 μm) than those from the Flagstaff Rim samples which measured 100-400 μm in length, which

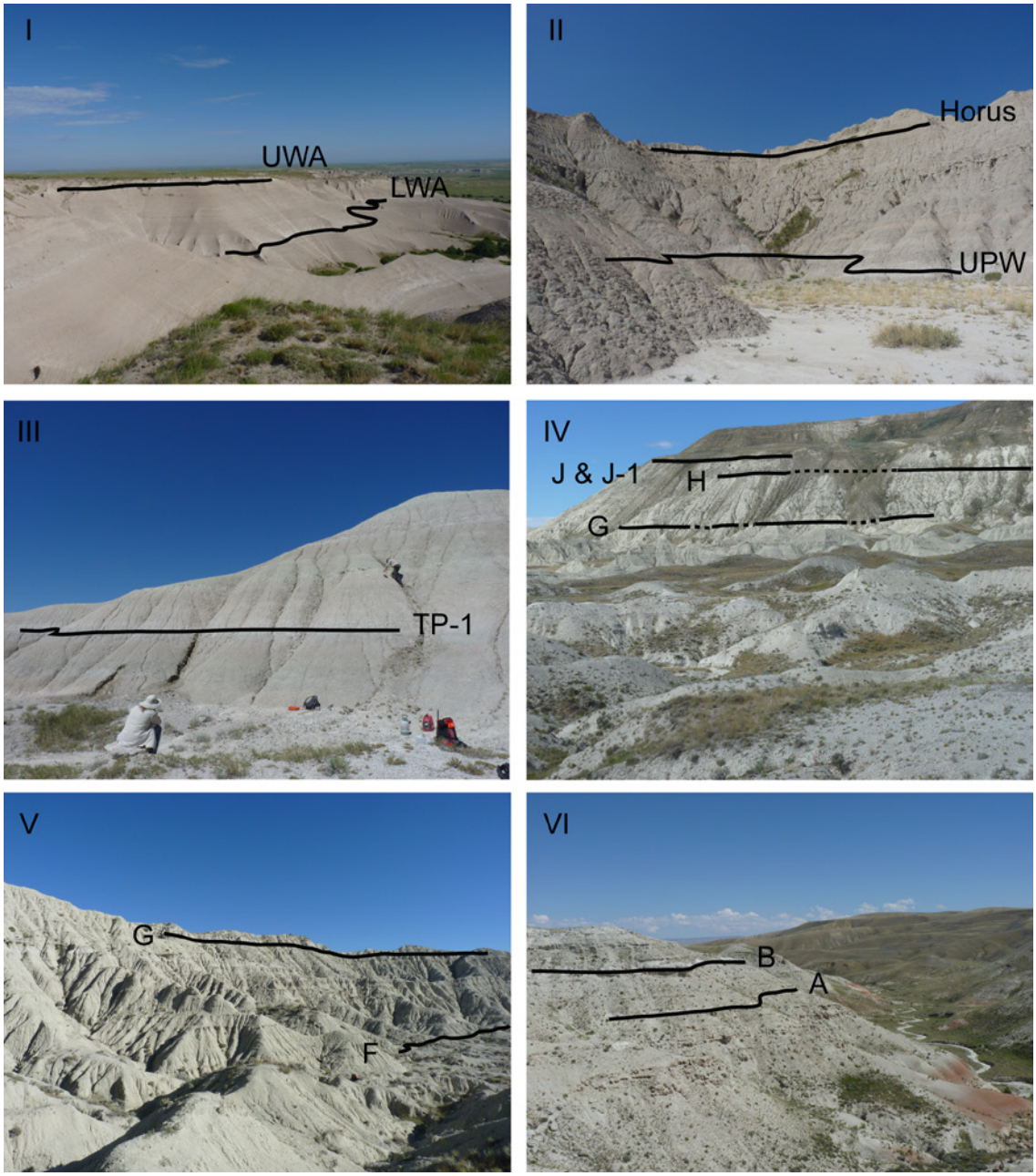

Figure 3.3 Volcanic tuffs intercalated in the WRG sedimentary succession at Toadstool Park and Flagstaff Rim. I – upper part of the Toadstool Park succession, showing the relative position of the Upper (UWA) and Lower (LWA) Whitney Ashes (the UWA is situated ca. 25 m, above the LWA), II – relative stratigraphic position of the UPW (Upper Purplish White Layer) and the Horus tuff, in the middle part of the Toadstool Park succession (the Horus tuff is situated 20 m above the UPW), III – location of the previously unreported TP-1 tuff at Toadstool Park, IV – main Flagstaff Rim outcrop, showing the relative position of the G, H, J, and J-1 tuffs V – the F and G tuffs in the middle part of the Flagstaff Rim succession (the J tuff is situated 86 m above the G tuff), VI – base of the Flagstaff Rim succession, showing relative position of the A and B tuffs (interval between the A and B tuffs is ca. 9 m thick).

is consistent with the Toadstool Park section being situated further from the source of the eruptions.

Hand-picked zircons from 15 samples were analysed using CA-ID-TIMS methodologies employed at the NERC Isotope Geoscience Laboratory (NIGL), details of which are outlined in Appendix A, along with the tabulated results of the analytical programme (Table A.3). However, two important points are briefly outlined here: (1) prior to dissolution zircons were subjected to a modified chemical abrasion pre-treatment for the effective elimination of Pb-loss (Mattinson, 2005); and (2) the accuracy of the $^{238}U/^{206}Pb$ dates presented herein are controlled by the gravimetric calibration of the EARTHTIME U-Pb tracer (ET535) employed in this study and the determination of the ^{238}U decay constant (Condon et al. 2007; Jaffey et al. 1971). Between 6 - 19 grains from each sample were dated, resulting in a total of 175 single grain analyses. The analytical uncertainties of $^{206}Pb/^{238}U$ dates were between 0.07 – 1%, with radiogenic to common Pb (Pb^*/Pb_c) ratios between 0.5 and 45. As in Chapter 2, the highest uncertainties correspond to the lowest Pb^*/Pb_c ratios, and 15 analyses with $Pb^*/Pb_c<1$ were rejected, along with five analyses that gave Cretaceous to Precambrian $^{206}Pb/^{207}Pb$ ages indicating the presence of inherited cores. The remaining zircon populations from each sample show significant scatter, on the order of 0.4-1.5 Myr. Potential causes for this scatter include magma chamber processes either through the recycling of older xenocrysts or prolonged magma chamber residence prior to eruption, and incomplete removal through chemical abrasion of crystal volumes affected by post-depositional open system behaviour. An additional complication is presented by the fact that background sedimentation in the White River group consists mainly of reworked volcaniclastic material, and most tuff samples showed signs of bioturbation.

The selection of zircon populations assumed to represent the deposition/eruption

age of each sample was guided by two criteria: reproducibility of single zircon $^{206}Pb/^{238}U$ dates (at the 2σ level), and overall stratigraphic consistency of the dataset. The latter criterion applies in particular to the Flagstaff Rim succession where ten tuff samples were collected from an interval that covers about 1.8 Myr, and thus the difference between the age of consecutive tuffs, particularly in the lower part of the succession, is comparable in magnitude to the uncertainty of single analyses. Statistical parameters such as the mean square of the weighted deviates (MSDW), and probability of fit, were used as an additional guide in the selection of a youngest coherent zircon population of each sample. Interpreted weighted mean dates had MSWD values between 0.6-1.8, within acceptable limits for populations consisting of 3-8 analyses (for a discussion on the significance and evaluation of the MSWD see Chapter 2, Section 2.3). The selection of analyses for the calculation of weighted mean $^{206}Pb/^{238}U$ dates for each sample is discussed below. Weighted mean dates and their statistical parameters are listed in Table 3.1. The uncertainties of the weighted mean ages are reported in the form of ± X/Y/Z where X signifies analytical uncertainty, while Y and Z incorporate additional uncertainty components related to the calibration of the ET535 isotopic tracer, and the ^{238}U decay constant respectively.

3.3.1 The Flagstaff Rim succession

In this section I summarise the results of the U-Pb ID-TIMS analyses and the interpreted dates that are assigned to each of the ten samples collected from the Flagstaff Rim sedimentary succession. The U-Pb data for the Flagstaff Rim section are plotted along with a summary stratigraphic section in Figure 3.4.

- Twelve zircons from the B tuff were analysed, and four data points were excluded due to having $Pb^*/Pb_c < 1$. The remaining analyses gave $^{206}Pb/^{238}U$ dates ranging between 35.286 and 36.314 Ma. Most of these dates are younger than reproducible data obtained from tuffs situated higher in the section (see

below) and could potentially be the result of incomplete removal of weathered material prior to sampling. Excluding these, three of the remaining grains gave a weighted mean age of 35.816 ± 0.081/0.085/0.093 Ma.

- Eleven zircons analysed from the B+15 tuff gave $^{206}Pb/^{238}U$ ages between 35.507 and 35.953 Ma. The two youngest grains were considered to represent either post-crystallization Pb loss, or contamination with younger material, as they are younger than the weighted mean age of the next youngest B+18 tuff (see below), while the seven youngest of the remaining analyses gave a weighed mean age of 35.754 ± 0.013/0.021/0.044 Ma.
- Of nine zircons analysed from the B+18 tuff, the youngest six gave a weighted mean age of 35.692 ± 0.017/0.023/0.044Ma while the remaining three gave $^{206}Pb/^{238}U$ ages between 35.75 and 37.33 Ma.
- Six grains were analysed from a tuff situated 18 metres below the F tuff (F-18 tuff) and gave $^{206}Pb/^{238}U$ dates between 35.500 and 45.303 Ma. The youngest of these dates is younger than the weighted mean age of the B+18 tuff, and older than reproducible dates from the next tuff situated higher up in the section, and can therefore be used as maximum age constraint for the deposition of the F-18 tuff.
- Seven grains were analysed from a tuff situated 7.5 m below the F tuff, and gave $^{206}Pb/^{238}U$ dates between 35.379 and 34.745 Ma. The weighted mean age of the youngest five grains is 35.416 ± 0.019/0.025/0.045 Ma.
- Fourteen zircons from the F tuff gave $^{206}Pb/^{238}U$ dates ranging between 35.301 and 36.500 Ma, with the youngest six grains yielding a weighted mean age of 35.336 ± 0.019/0.024/0.045 Ma.
- Fourteen grains were analysed from the G tuff, and gave $^{206}Pb/^{238}U$ dates between 34.970 and 36.28 Ma. The two youngest dates were attributed to post-crystallization Pb loss while the six youngest remaining grains gave a weighted

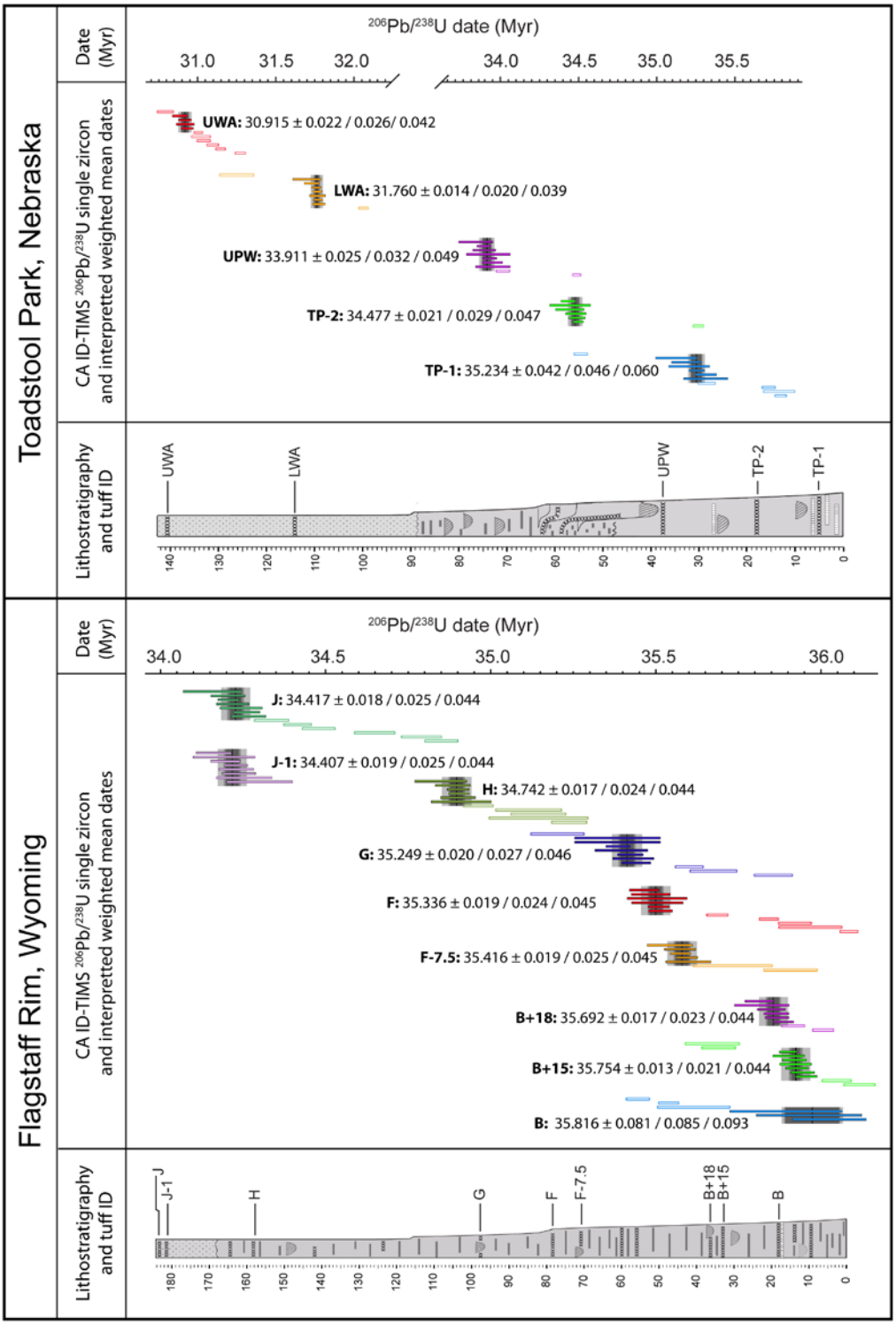

Figure 3.4 Summary plots of $^{206}Pb/^{238}U$ data and interpreted depositional ages based upon the weighted mean $^{206}Pb/^{238}U$ of the youngest coherent population. Stratigraphic logs of the Flagstaff Rim and Toadstool Park sections, showing the position of each tuff are provided for reference, with the vertical scale in metres. Note that the zircon U-Pb dates are plotted against time and not against height of the sample

mean age of 35.249 ± 0.020/0.027/0.046 Ma.

- Thirteen grains were analysed from the H tuff. Two of these gave Oligocene ages of 33.37 and 33.68 Ma respectively, which were attributed to post-crystallization Pb loss, while the remaining dates were between 34.684 and 35.073 Ma. The weighted mean age of the remaining youngest seven zircons was 34.742 ± 0.017/0.024/0.044 Myr.
- Nine zircons were analysed from a tuff located 1 m below the J tuff. The youngest eight analyses gave a weighted mean age of 34.407 ± 0.019/0.025/0.044 Ma.
- The 13 zircons analysed from the J tuff gave $^{206}Pb/^{238}U$ dates between 34.347 and 35.041 Ma. The weighted mean of the youngest seven dates is 34.417 ± 0.018/0.025/0.044 Ma. The 2σ analytical uncertainty of this date overlaps with that of the weighed mean age of the J-1 tuff, which is consistent with the relative stratigraphic positions of the two samples.

3.3.2 The Toadstool Park succession

This section summarises the results of U-Pb ID-TIMS analyses, and interpreted age of the seven tuff samples collected from the Toadstool Park locality. Three of these samples were collected from the Big Cottonwood Creek Member of the Chadron Formation (the Upper Purplish White Layer, and two previously unreported tuffs labelled TP-1 and TP-2), two from the Orella Member of the Brule Formation (Valley of Horus, Serendipity) and two from the Whitney Member of the Brule Formation (the Lower and Upper Whitney Ash). The U-Pb data for the Toadstool Park section are plotted along with a summary stratigraphic section in Figure 3.4:

- Ten grains were analysed from the TP-1 tuff and gave $^{206}Pb/^{238}U$ dates ranging between 34.532 ± 0.040 and 35.786 ± 0.036 Ma. The youngest analysis was attributed to post-crystallization Pb loss, while the youngest three of the

remaining grains yielded a weighted mean age of 35.234 ± 0.042/0.046/0.060 Ma.

- Of the nine zircons analysed from the TP-2 tuff, the youngest six gave a weighted mean age of 34.477 ± 0.021/0.029/0.047 Ma, while the remaining three analyses gave older ages between 35.150 ± 0.069 and 35.98 ± 0.15 Ma.
- Eleven zircons were analysed from the Upper Purplish White Layer, and two analyses were excluded based on low Pb^*/Pb_c (<1), with the remaining seven youngest analyses giving a weighted mean age of 33.911 ± 0.025/0.032/0.049 Ma.
- Seven zircons from the Serendipity tuff gave non-reproducible ages ranging between 34.372 ± 0.156 and 38.087± 0.133 Ma. No weighted mean age was calculated for this sample, and additionally the youngest date is older than the weighted mean age calculated for the Upper Purplish White Layer situated 20 m lower in the section and therefore cannot be used as a maximum age constraint for the deposition of this tuff.
- The Valley of Horus tuff situated ca. 1 m below the Serendipity ash, yielded eight dates ranging between 31.850 ± 0.058 Ma and 38.130 ± 0.144 Ma. The youngest date would imply a significantly higher sedimentation rate than that calculated based on the weighted mean age of the Upper Purplish White Layer and the dated tuffs from the Whitney Member (see below) and therefore cannot be used as maximum age constraint for the deposition of the Valley of Horus tuff, while all the remaining analysis are older than the weighted mean age of the Upper Purplish White Layer situated lower in the section.
- Nine grains were analysed from the Lower Whitney Ash, of which seven gave a weighted mean age of 31.760 ± 0.014/0.020/0.039 Ma. One analysis yielded a younger, non-reproducible, age of 31.25 ± 0.11 Ma, which was attributed to post-crystallization Pb-loss, and an additional analysis gave a slightly older

age of 32.057 ± 0.31 Ma.

- The Upper Whiteny Ash is the youngest sample analysed at Toadstool Park. Eleven analysed grains yielded $^{206}Pb/^{238}U$ dates between 30.792-31.247 Ma. Of these, the youngest data-point was non-reproducible, while the remaining four youngest analyses gave a weighted mean age of 30.915 ± 0.022/0.026/0.042 Ma.

Combined, these data result in interpreted U-Pb zircon dates that have an age order that is consistent with their stratigraphic context for both areas studied. The derived age model for the Flagstaff Rim and Toadstool Park sections is discussed in section 3.4.

Sample	Weighted mean $^{206}Pb/^{238}U$ date	Uncertainty (2σ)	MSWD	Probability of fit	n
UWA	30.915	± 0.022 / 0.026 / 0.042	0.78	0.51	4 of 11
LWA	31.760	± 0.014 / 0.020 / 0.039	0.79	0.58	7 of 9
UPW	33.911	± 0.025 / 0.032 / 0.049	0.77	0.59	7 of 11
TP-2	34.477	± 0.021 / 0.029 / 0.047	1.3	0.25	6 of 9
TP-1	35.234	± 0.042 / 0.046 / 0.060	0.90	0.40	3 of 11
J	34.417	± 0.018 / 0.025 / 0.044	1.8	0.10	7 of 13
J-1	34.407	± 0.019 / 0.025 / 0.044	1.4	0.19	8 of 9
H	34.742	± 0.017 / 0.024 / 0.044	1.5	0.17	7 of 13
G	35.249	± 0.020 / 0.027 / 0.046	0.97	0.43	6 of 14
F	35.336	± 0.019 / 0.024 / 0.045	0.76	0.58	6 of 14
F-7.5	35.416	± 0.019 / 0.025 / 0.045	0.60	0.66	5 of 7
F-18*	35.500	± 0.130 / 0.130 / 0.140	-	-	-
B+18	35.692	± 0.017 / 0.023 / 0.044	1.4	0.22	6 of 9
B+15	35.754	± 0.013 / 0.021 / 0.044	1.6	0.13	7 of 11
B	35.816	± 0.081 / 0.085 / 0.093	0.91	0.40	3 of 12

Table 3.1 Weighted mean ages of dated tuffs from the WRG (* maximum age constraint based on youngest date). MSWD – mean square of the weighted deviates, n – number of grains included in the calculation of the weighted mean date out of total number of grains analysed (after rejection of analyses with $Pb^*/Pb_c<1$). Weighted mean dates and uncertainties were calculated using Redux (McLean et al., 2011), and statistical parameters are outputs from Isoplot (Ludwig, 2003).

3.4 Age models for the WRG

Age-depth models for the Flagstaff Rim and Toadstool Park sedimentary successions (Figure 3.5) were developed using the Bayesian approach implemented in the OxCal software package of Bronk Ramsey (2008). We used the *P_Sequence* routine implemented in OxCal 4.2, which presents two advantages over conventional linear or polynomial regression between stratigraphic levels of known age: (i) it allows for the integration of radio-isotopic data and other constraints, such as the stratigraphic position of lithological boundaries, which are likely to correspond to changes in sedimentation rate, and (ii) rather than assuming that sedimentation rates follow a predetermined functional form, it treats sediment accumulation as a random Poisson process, in which sediment layers of finite thickness are deposited at discrete points in time, and are separated by gaps of variable duration.

The stratigraphic resolution of the model is determined by an input parameter *k*, defined as the number of accumulation events per unit depth. The selection of an appropriate value for *k* is based on grain size, with higher values (>100 per metre) recommended for fine grained material, resulting in a model that approximates uniform deposition (Bronk Ramsey, 2008). For the Flagstaff Rim and Toadstool Park successions, the best agreement between input and modelled $^{206}Pb/^{238}U$ dates was obtained using *k* values between 5-10. This implies an average thickness of individual accumulation events between 10-20 cm, and likely reflects the episodic nature of sediment accumulation on a fluvial floodplain. This approach results in wider uncertainty envelopes than linear regression between consecutive dated tuffs, but results are likely to be more accurate (Bronk Ramsey, 2008).

OxCal treats radio-isotopic date uncertainties as random, which means that when correlated systematic uncertainties are present, the resulting age model will have

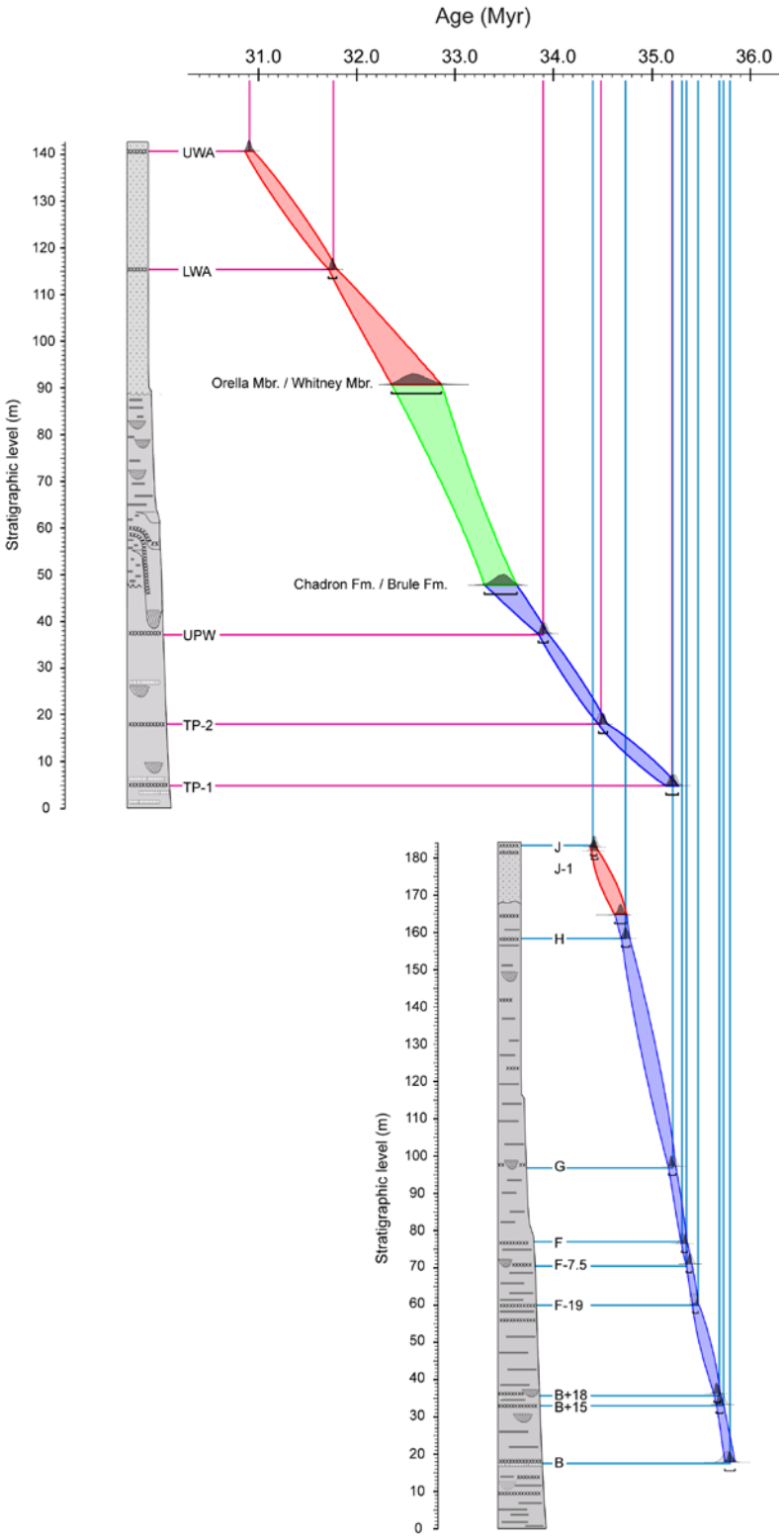

Figure 3.5 Plot of (U-Pb zircon calibrated) time against stratigraphic position/thickness showing the dated tuff and the age model developed from these data. Note that the thickness scales for the two stratigraphic sections are not the same.

an unrealistically narrow uncertainty envelope for stratigraphic intervals with closely spaced $^{206}Pb/^{238}U$ dates with overlapping uncertainties. For this reason, only the analytical uncertainties of weighted mean $^{206}Pb/^{238}U$ dates were modelled in OxCal, and additional uncertainties equivalent to ± 0.03 %, and 0.11% of the interpolated ages, representing tracer calibration, and respectively ^{238}U decay constant uncertainties at the 2σ level, were added in quadrature to the 95% uncertainty envelope of the age model.

At Flagstaff Rim, weighted mean $^{206}Pb/^{238}U$ dates indicate that mean sedimentation rates decrease from ca. 150 m/Myr to ca. 60 m/Myr between tuffs H and J, and in our model, this change was constrained to the level of the I tuff, where Evanoff et al. (1992) reported a shift from fluvial to eolian sedimentation.

At Toadstool Park, mean sedimentation rates are on the order of 25 m/Myr in the Big Cottonwood Creek Member of the Chadron Formation, based on the age and stratigraphic position of the TP-1 and UPW tuffs, and ca. 30 m/Myr in the Whitney Member of the Brule Formation, based on data from the Upper and Lower Whitney Ashes. The analysis of zircons from tuffs intercalated in the Orella Member of the Brule Formation did not yield meaningful eruption ages, therefore we assume that if changes in sedimentation rate did occur in the middle part of the Toadstool Park succession, they are likely to correspond to lithological changes at the boundaries between the Orella Member and the underlying Chadron Formation, and respectively the overlying Whitney Member.

Because most of the WRG consists of overbank deposits accumulated on a fluvial floodplain, both the Flagstaff Rim and Toadstool Park records are likely to contain hiatuses of unknown duration. Although the continuity and completeness of these successions is difficult to assess, three lines of evidence seem to indicate that gaps in the record are of sufficiently short duration so as not to have a significant impact on the development of

age depth models:

- The $^{206}Pb/^{238}U$ dates of the ten tuffs sampled at Flagstaff Rim indicate relatively constant mean sedimentation rates on the order of 150 m/Myr, except for the uppermost part of the succession, between tuffs H and J, which is consistent with sedimentological evidence indicating a shift from fluvial to eolian deposition in this interval (Evanoff et al., 1992), and the high stratigraphic resolution of the dated tuffs makes the presence of hiatuses exceeding a few tens of kyr unlikely.
- Palaeo-channel structures are present at both Flagstaff Rim and Toadstool Park, however owing to the good quality of the outcrops which allows for the verification of lateral continuity of individual strata, and the presence of coarse sand and gravel deposits at the base of individual channels, these are easily identified in the field. Tuff samples for this study were collected in tandem with the palaeomagnetic samples discussed in Chapter 4, and as such, their stratigraphic positions are tied into composite measured sections the trajectory of which was chosen so as to avoid palaeo-channel structures in order to ensure, as far as possible, the completeness of the palaeomagnetic record at both Flagstaff Rim and Toadstool Park.
- Intervals of non-deposition in terrestrial records are likely to be marked by pedogentic modifications. Paleosols have been identified at both Flagstaff Rim, at the level of the A, B, F, and J tuffs, and in the lower part of the Toadstool Park succession, and although their temporal significance is difficult to determine, comparison with modern equivalents indicates that they are unlikely to represent hiatuses lasting longer than a few tens of kyr (Terry, 2001; Griffis, 2011)

3.5 Discussion

3.5.1 Comparison with legacy $^{40}Ar/^{39}Ar$ data

The assigned weighted mean $^{206}Pb/^{238}U$ ages from this study are younger than $^{40}Ar/^{39}Ar$ biotite and anorthoclase dates reported by Swhisher and Prothero (1990) for the B, F, G, and J tuffs from Flagstaff Rim and the Lower Whitney Ash from Toadstool Park. Because $^{40}Ar/^{39}Ar$ dates are reported relative to FCs neutron fluence monitor, the magnitude of the discrepancy between the $^{206}Pb/^{238}U$ and $^{40}Ar/^{39}Ar$ datasets is determined by the age assigned to the FCs (Figure 3.6). Published estimates of the age of the FCs range between 27.84 and 28.305 Ma, with the results of recent inter-calibration experiments with astronomically dated tuffs and the $^{206}Pb/^{238}U$ system converging towards a value of 28.20 Ma, with an uncertainty of less than 0.1 Myr (Renne et al., 1998, 2010; Kuiper et al., 2008; Rivera et al., 2011; Wotzlaw et al., 2013). Calibration of the $^{40}Ar/^{39}Ar$ data of Swisher and Prothero (1990) relative to the FCs age of 28.201 Ma (Kuiper et al., 2008) adopted in the 2012 edition of the Geological Time Scale results in dates that are 0.4-1.0 Myr older than our weighted mean $^{206}Pb/^{238}U$ ages. While the discrepancy is reduced to ca 0.1-0.5 Myr when using younger values for the age of FCs (i.e. 28.02 or 27.84 Ma, Renne et al., 1994, 1998), none of the available calibration options result in equivalent $^{206}Pb/^{238}U$ and $^{40}Ar/^{39}Ar$ data pairs.

Because U-Pb and $^{40}Ar/^{39}Ar$ dates are obtained on different minerals, with different characteristics (e.g. closure temperature for the retention of parent/daughter isotopes), and individual analyses can be affected by the nature of the material being analysed and the employed analytical protocols (see discussion in section 3.1.3, and Chapter 1, section 1.2.2) the equivalence of U-Pb and $^{40}Ar/^{39}Ar$ dates cannot always be assumed. In their discussion on radio-isotopic age constraints on the age of the Eocene – Oligocene

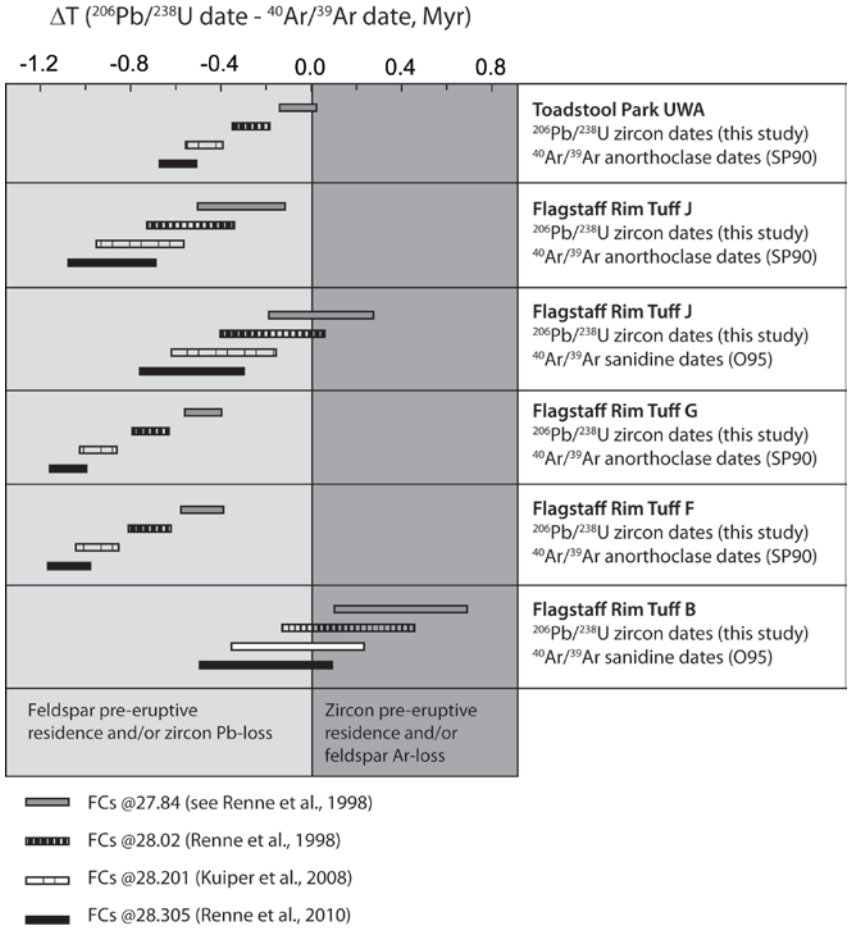

Figure 3.6 Summary of the comparison between weighted mean $^{206}Pb/^{238}U$ dates from this study, and legacy $^{40}Ar/^{39}Ar$ anorthoclase dates of Swisher and Prothero (1990) and sanidine dates of Obradovich et al. (1995) calibrated relative to a selection of widely used values for the age of the FCs neutron fluence monitor. Data of Obradovich et al. (1995) is assumed to have been initally published relative to an FCs age of 27.84 Ma (see text for details). Zircon U-Pb and feldspar $^{40}Ar/^{39}Ar$ dates that are equivalent at the 2σ level overlap with 0. Negative differences indicate data pairs affected by either zircon Pb-loss and/or contamination with pre-eruptive/xenocrystic or detrital anorthoclase or sanidine, while positive differences imply zircon pre-eruptive magma chamber residence or open system behaviour of feldspars.

boundary Hilgen and Kuiper (2008) noted that the $^{40}Ar/^{39}Ar$ dates published by Swisher and Prothero (1990) from the WRG are likely to be anomalously old, based on comparison with astronomically tuned marine records, and suggested that this may be the result of chemical preparation techniques applied to the ash samples prior to dating. However, this seems unlikely given that for most of their samples Swisher and Prothero (1990) reported data obtained on both biotite and anorthoclase separates, which overlapped within their

respective uncertainties. Another possibility is that the statistics underpinning the mean ages of Swisher and Prothero (1990) are causing a bias towards older ages. The 2σ analytical uncertainties of single zircon analyses discussed in this chapter are on the order of 30-50 kyr, which allowed us to distinguish between a "youngest" population of grains, assumed here to represent the age of the volcanic eruption that led to the emplacement of the dated tuff, and older grains. Assuming that the 0.4-0.8 Myr scatter seen in individual tuff samples is at least in part caused by detrital contamination related to the volcaniclastic background sedimentation of the WRG, rather than magma chamber processes alone, a similar degree of scatter could reasonably be expected to be present in feldspar and biotite populations as well. The single grain biotite and feldspar analyses from most of the samples of Swisher and Prothero (1990) show a scatter of 0.5-1 Myr, however their 2σ uncertainties are on the order of 0.2-0.9 Myr which would make it difficult to isolate primary biotite and feldspar grains from potential detrital contamination.

Additional $^{40}Ar/^{39}Ar$ dates were published by Obradovich et al. (1995) for the B and J tuffs from Flagstaff Rim, however it is unclear whether these dates were obtained relative to FCs=27.84 Ma as suggested by Hilgen and Kuiper (2009) or using the Taylor Creek Rhyolite as a neutron fluence monitor with and age of 28.32 Ma, as was done in other papers published by the same author around that time (e.g. Obradovich et al., 1993). Assuming that the original data were calculated relative to FCs, the recalculated age for the J tuff (relative to FCs = 28.201 Ma, Kuiper et al., 2008) is ca. 0.4 Myr older than our weighted mean $^{206}Pb/^{238}U$ age, while the recalculated age for the B tuff, overlaps within uncertainty with our date. Alternatively, if the data of Obradovich et al (1995) were originally determined relative to Taylor Creek Rhyolite, recalibration to the astronomically tuned FCs age of 28.201 of Kuiper et al (2008) using the intercalibration coefficient of Renne et al. (1998) implies a smaller adjustment of ca. 0.67% in numerical age, resulting in an age of 34.58 ± 0.11 Ma for the J tuff, and 35.64 ± 0.14 Ma for the B

tuff, both of which are statistically equivalent to the $^{206}Pb/^{238}U$ dates obtained in this study, when uncertainties are considered at the 2σ level.

An alternative interpretation of the data, in which the discrepancy between our weighted mean $^{206}Pb/^{238}U$ dates and the recalculated $^{40}Ar/^{39}Ar$ dates of Swisher and Prothero (1990) is attributed to pervasive post-crystallization Pb-loss is considered highly unlikely, given that each weighted mean $^{206}Pb/^{238}U$ date is supported by multiple (n = 3 - 8) reproducible, high-precision single crystal analyses, and all samples were subjected to a chemical abrasion pre-treatment in order to remove crystal volumes affected by open system behaviour. This, in combination with the high stratigraphic resolution of our study, and the fact that individual weighted mean ages are consistent with the relative stratigraphic context of each sample at both localities implies that the $^{206}Pb/^{238}U$ data set presented here provides a robust calibration of the WRG and its record of environmental change across the EOT.

3.5.2 Integration of the Flagstaff Rim and Toadstool Park data sets

One objective of this study was to quantify the temporal association of the Flagstaff Rim and Toadstool Park WRG successions. Tephrostratigraphic studies of the WRG have indicated that the J tuff from Flagstaff Rim is potentially equivalent to the Upper Purplish White Layer from the Toadstool Park section, and the Persistent White Layer identified in composite sections in eastern Wyoming (Larson and Evanoff, 1998). Based on our dates, the J tuff is ca. 0.5 Myr older than the Upper Purplish White Layer, which is consistent with the magnetic polarity pattern of the two sections, as the two tuffs are situated close to the base and top, respectively, of a reversed polarity zone correlated to C13r (Prothero et al., 1983; Prothero and Swisher, 1992; see also Chapter 4), which has a duration of ca. 1 Myr. A correlation between the Upper Purplish White Layer from Toadstool Park

and the Persistent White Layer from eastern Wyoming seems more likely, given that both tuffs are thought to located in the upper part of C13r (Prothero 1996). The weighted mean $^{206}Pb/^{238}U$ age of the G tuff from Flagstaff Rim, and the TP-1 tuff from Toadstool Park are equivalent at the level of their 2σ analytical uncertainties, while the $^{206}Pb/^{238}U$ age of the TP-2 tuff is close, but not statistically equivalent to the age of the J and J-1 tuffs. This implies that the interval between metre levels 5 and 18 of the Toadstool Park section corresponds to the upper 90 m of the Flagstaff Rim record.

3.5.3 Dating the WRG biostratigraphy and the age of the Chadronian, Orellan and Whitneyan NALMAs

Together, the stratigraphic record of the Flagstaff Rim and Toadstool Park WRG sections span most of the Chadronian, Orellan and Whitneyan NALMAs (Figure 3.2). Figure 3.7 shows the temporal range of key mammalian taxa from Flagstaff Rim and Toadstool Park, based upon their stratigraphic occurrence (Emry, 1992; Prothero and Whittlesey, 1998; Zanazzi et al., 2009), combined with the age models developed for both successions, and the position of the dated volcanic tuffs.

The lowest part of the Flagstaff Rim section, from the base of the measured section of Emry (1973) to ca. 15 m below the B tuff has been assigned to the Late Early Chadronian, also referred to as the *Leptomeryx yoderi* interval zone (Prothero and Emry, 1996). Based on its stratigraphic position, the top of the Early Chadronian must be older than the weighted mean $^{206}Pb/^{238}U$ age of the B tuff (35.81 ± 0.09 Ma) however a more precise age constraint cannot be derived because increased weathering and oxidation of sediments in the lowest part of the Flagstaff Rim section indicates that a change in sedimentation rates took place below the B ash (Emry, 1973, 1992) and therefore extrapolating our age model below the stratigraphic position of the oldest dated tuff is not feasible. At Toadstool

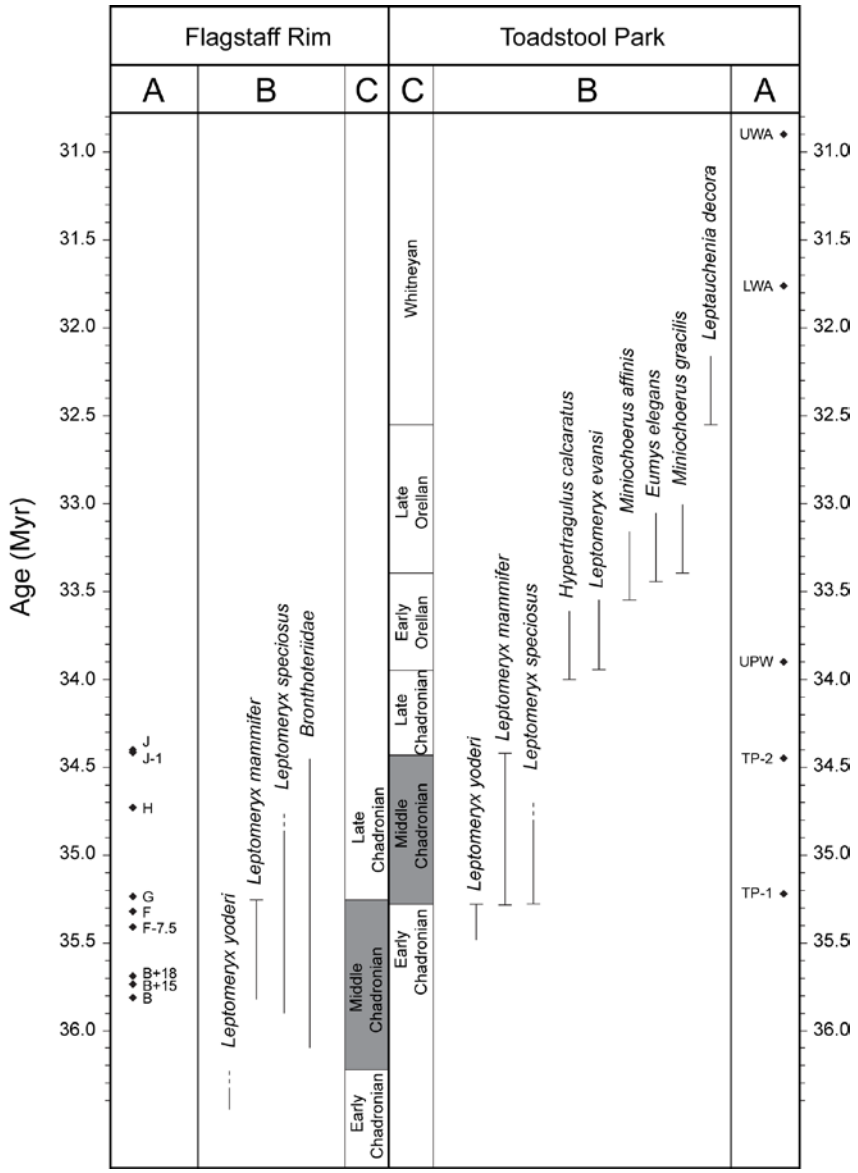

Figure 3.7 Plot showing the A. Dated ash beds plotted against time; B. Temporal range of key NALMA index taxa that occur in the Flagstaff Rim and Toadstool Park stratigraphic sections. Temporal ranges are determined based upon the stratigraphic distribution of the fossil assemblages combined with the ages of dated tuff and the stratigraphic age models based upon those dates; C. NALMA

Park, Zanazzi et al. (2009) placed the top of the Early Chadronian 34 m below the Upper Purplish White Layer, at around metre level 4 of our measured section, ca. 1m below the TP-1 tuff, based on the co-occurrence of the artiodactyls *Leptomeryx speciosus*, *L.*

mammifer, and *L. yoderi*. This implies that the top of the Early Chadronian is older than the weighted mean $^{206}Pb/^{238}U$ age of the TP-1 tuff (35.23 ± 0.06 Ma) and is potentially younger than in the Flagstaff Rim type section (Figure 3.7).

The type section of the Middle Chadronian also referred to as the *Leptomeryx mammifer* Interval Zone extends from ca. 15m below the B tuff to 15 m above the G tuff in the Flagstaff Rim section (Prothero and Emry, 2004). The last occurrence of L. mammifer has been reported from approximately 3 m below the G tuff (Emry, 1992), implying an age of ~ 35.25 ± 0.05 Ma (Emry, 1992) for the Middle/Late Chadronian boundary in the Flagstaff Rim section. In the Toadstool Park section, Zanazzi et al. (2009) reported the highest occurrence of *L. mammifer* from 18 ± 2 m below the UPW, around metre level 20 of our measured section, close to the position of the TP-2 tuff. This implies a $^{206}Pb/^{238}U$ calibrated age of 34.44 ± 0.06 Ma, significantly younger than in the Flagstaff Rim type section. It is unclear if these dates represent true faunal diachroneity or if they are a reflection of the temporal resolution of Chadronian vertebrate palaeontology in the WRG. Although the Flagstaff Rim section has been designated as a type section for part of the Early Chadronian and the Middle Chadronian, Emry (1992) cautioned that the reported pattern of mammalian range zones may be an artefact of fossil preservation rather than a representation of true first and last occurrences, as fossils were usually found in large quarry samples, rather than randomly dispersed through the stratigraphic record.

The presence of brontotheres up to a few metres below the J tuff indicates that the Flagstaff Rim record does not extend beyond the top of the Chadronian (Emry, 1992). The first definition of the Chadronian – Orellan transition was based on the last occurrence of brontotheres (Wood et al., 1941), however Prothero and Whittlesey (1998) argued that the scarcity of brontothere fossils makes their use as a biostratigraphic marker impractical, and proposed instead the use of the first occurrence of the artiodactyls *Leptomeryx evansi*

and *Hypertragulus calcaratus* to mark the base of the Orellan. In the Toadstool Park section, these two species first appear around the level of the Upper Purplish White Layer (Zanazzi et al., 2009) giving an age of ca. 34.00 ± 0.07 Ma for the Chadronian – Orellan transition, however in eastern Wyoming their first occurrence has been reported from 5-7 m above the Persistent White Layer (Prothero and Whittlesey, 1998), a potential equivalent of the UPW, implying a slightly younger age.

Other notable first occurrences from the early Orellan at Toadstool Park include the oreodonts *Miniochoerus affinis* (33.58 ± 0.14 Ma) and the rodent *Eumys elegans* (33.46 ±0.15 Myr), while the first occurrence of *Miniochoerus gracilis* (33.42 ± 0.15 Ma) marks the base of the Late Orellan. The earliest Whitneyan fossil assemblages, characterized by the first appearance of the oreodont *Leptauchenia decora* have been reported from 54 m above the UPW at Toadstool Park, with an approximate $^{206}Pb/^{238}U$ calibrated age of 32.56 ± 0.23 Ma. It should be noted that although the Brule Formation at Toadstool Park has been subdivided into two members labelled Orella and Whitney, the lithostratigraphic boundaries of these units do not coincide with biostratigraphic boundaries.

The integration of the radio-isotopically calibrated age models for the WRG and the existing biostratigraphy for the Flagstaff Rim and Toadstool Park sections allows the assessment and comparison of regional biochrons/NALMAs. Diachroneity of mammalian appearance and last occurrence events, on the order of a few Myr across a single continent, has been demonstrated through multivariate analysis of the North American mammal fossil record by Alroy (1998), who concluded that most of the observed diachroneity appears to be the result of under sampling. The results of our calibration of the NALMA index taxa from the WRG demonstrate apparent diachroneity on the order of 1 Myr (over a distance of 400 km) in the Chadronian, which may represent either real age variation or an artefact of fossil preservation and sampling.

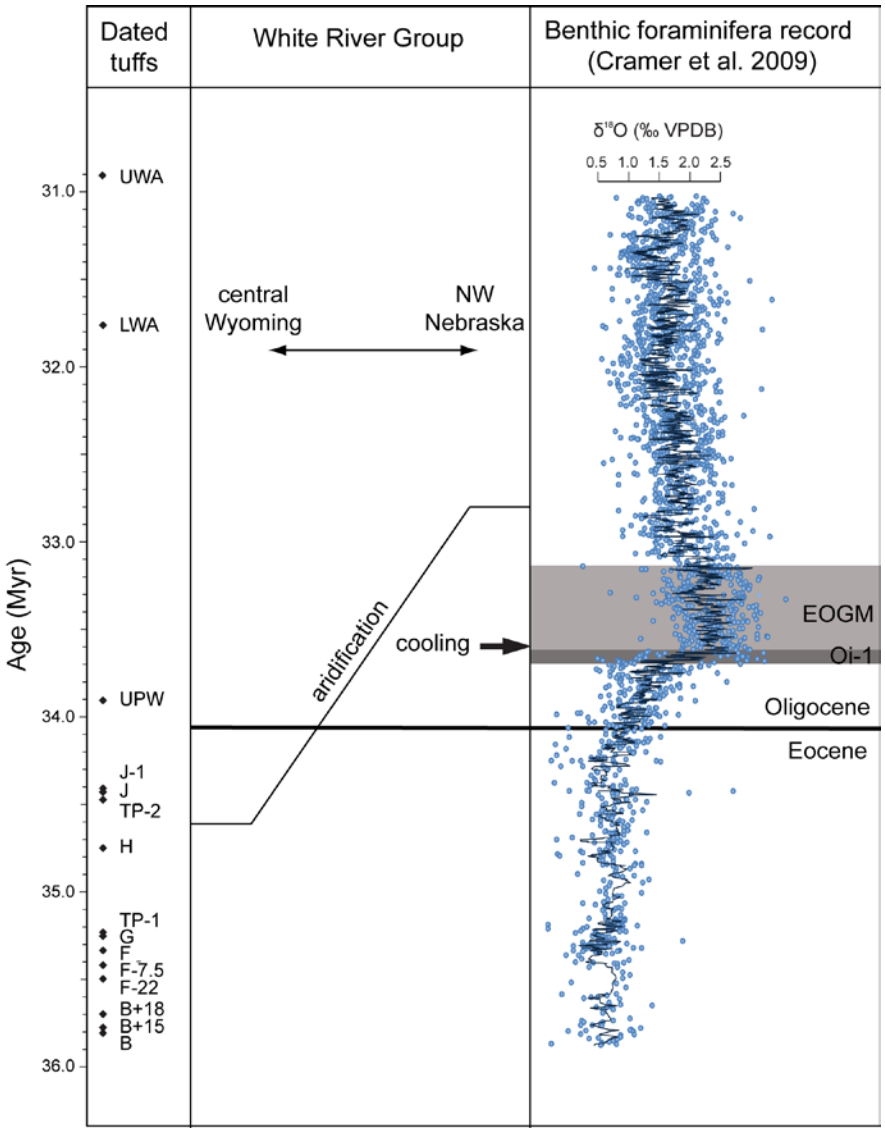

Figure 3.8 Environmental proxy record of the White River Group compared to the marine benthic foraminifera $\delta^{18}O$ record of the EOT. EOGM – Early Oligocene Glacial Maximum.

3.5.4 Timing of environmental change in the WRG

Environmental change in central North America at around 34 Ma is supported by both lithostratigraphic evidence and palaeoclimatic records, however, its relationship to the Early Oligocene glaciation recognized in marine records is somewhat unclear because magnetostratigraphic and $^{40}Ar/^{39}Ar$ dating have so far yielded conflicting results.

Increasing aridification is indicated by the change from fluvial to eolian deposition, which occurs around the level of the I tuff at Flagstaff Rim, and around the Orella-Whitney lithostratigraphic boundary in the Toadstool Park section. Our $^{206}Pb/^{238}U$ data indicate that this change was time-transgressive, and occurred at around 32.8 Myr in western Nebraska, and ca. 1.8 Myr earlier in central Wyoming (Figure 3.8). The marine $\delta^{18}O$ shift, which records the glaciation of Antarctica in the Early Oligocene, takes place over a significantly shorter time interval of about 400 kyr (Coxall et al., 2005) therefore it seems plausible that additional processes, acting on longer time scales, were also active at the time of the deposition of the WRG.

A high resolution stable isotope record derived from fossil bones and tooth enamel from the Toadstool Park section indicates a drop of ca. 7.1 ± 3.1˚C in mean annual temperatures in the early Orellan (Zanazzi et al., 2007; 2009). At the time of their publication these data were inconsistent with paleosol studies from North America (Sheldon and Retallack, 2004; Retallack, 2007) and fossil tooth enamel studies from Argentina (Kohn et al., 2004) which indicate smaller or no change in mean annual temperatures around the time of the Eocene-Oligocene transition, and it has been suggested that the large shift towards more positive $\delta^{18}O$ values reported by Zanazzi et al. (2007) reflects aridification and diagenetic changes rather than cooling (Sheldon et al., 2009). Although a subsequent study of vertebrate fossils from the Toadstool Park record failed to reproduce the results of Zanazzi et al. (2007) (Boardman and Secord, 2013) terrestrial cooling of similar magnitude has since been reported from Northern Europe based on clumped isotope analysis of freshwater gastropod shells (Hren et al., 2013).

Our $^{206}Pb/^{238}U$ calibrated age model for the Toadstool Park section places the maximum $\delta^{18}O$ values from the record of Zanazzi et al. (2007) at around 33.60 ± 0.15 Myr, within the uncertainty of the astronomically calibrated age of ca. 33.4-33.6 Ma

reported for the benthic foraminifera $\delta^{18}O$ maximum from ODP Site 1218 by Coxall et al. (2005) (see Chapter 2), and synchronous with the maximum extent of Early Oligocene glaciation of Antarctica. To a certain extent this agreement may be an artefact of the interpolation technique used for the Toadstool Park section, however effects related to the choice of age-depth model are not likely to have a significant impact on our conclusion, as simple linear regression between the age of the Upper Purplish White Layer, and the Lower Whitney Ash would yield an only slightly younger age of 33.33 ± 0.07 Myr, which is ca. 0.1 Myr younger than the benthic foraminifera $\delta^{18}O$ maximum from ODP Site 1218 (Coxall et al., 2005).

3.6 Conclusions

The application of high-accuracy U-Pb (zircon) ID-TIMS geochronology to fourteen volcanic tuffs from the WRG has permitted the construction of a robust age model for the terrestrial EOT (36-31 Ma) in North America. This age model provides quantitative information on the sediment accumulation rates and absolute age of two key WRG successions, Flagstaff Rim in Wyoming, and Toadstool Park in Nebraska. The U-Pb (zircon) ID-TIMS based constraints developed in this study are significantly younger than previously published $^{40}Ar/^{39}Ar$ dates (Swisher and Prothero, 1990), which given consideration of the issues surrounding the different datasets suggests significant inaccuracy in the legacy $^{40}Ar/^{39}Ar$ data. The integration of U-Pb (zircon) calibrated age models with existing mammalian biostratigraphic records of the Flagstaff Rim and Toadstool Park successions indicates that key taxa, used to define the subdivisions of the Chadronian NALMA may be diachronous by as much as 1 Myr over a relatively short distance of ca. 400 km, however further investigation of other Chadronian sedimentary successions is necessary in order to determine whether this represents real age variation or an artefact of fossil preservation. Based on our data, environmental change recorded by

the WRG across the EOT is the combined result of both global and regional effects, with early Orellan cooling synchronous with the marine record of Antarctic glaciation, while aridification progressed gradually from west to east and was diachronous by ca. 1.5 Myr between the Flagstaff Rim and Toadstool Park records.

4. Radio-isotopic calibration of the late Eocene - early Oligocene geomagnetic polarity timescale

Abstract: This chapter revisits the magnetic polarity pattern of the White River Group (WRG) of North America, and its implications for the numerical age calibration of the Late Eocene – Early Oligocene geomagnetic polarity time scale (GPTS). A revised, high-resolution magnetostratigraphic data set is presented for the two WRG localities discussed in Chapter 3: Flagstaff Rim (central Wyoming) and Toadstool Park (NW Nebraska). Combined with $^{206}Pb/^{238}U$ (zircon) CA-ID-TIMS dating of volcanic tuffs from the two localities, and the associated age-depth models developed in Chapter 3, this data set is used to assign high-precision ages to magnetic reversals between the top of chron C16n.2n and the base of chron C12n (36-31 Ma). A comparison between these ages and recent time scale calibration studies supports the accuracy of the 405 kyr tuning of the ODP Site 1218 record at least as far back as 36 Ma. Our data are compatible with relatively constant seafloor spreading rates during the Late Eocene and Early Oligocene, and mutual consistency with magnetic reversal ages extracted from the $^{206}Pb/^{238}U$ calibrated age model of the Umbria-Marche sedimentary succession (Chapter 2) indicates that they represent a robust calibration of the Late Eocene – Early Oligocene GPTS.

4.1 Introduction

Magnetostratigraphic dating is a widely used technique for the development of first order correlations between disparate sedimentary successions, and relies on matching local magnetic polarity patterns to a geomagnetic polarity time scale (GPTS) in order to extract numerical age estimates for observed magnetic polarity reversals. The GPTS itself requires calibration by numerical dating methods, typically achieved through cubic spline interpolation between radio-isotopically or astronomically dated tie-points relative to a synthetic marine magnetic anomaly profile (Cande and Kent, 1992, 1995), astronomical tuning of deep marine records recovered through ODP and IODP expeditions (Pälike et al., 2006; Westerhold et al., 2007,2008; Westerhold and Röhl, 2009), or a combination of the above (Ogg and Smith, 2004; Vandenberghe et al., 2004). As such, progress in the numerical age calibration of the GPTS has been linked to the development of astronomical solutions that are stable beyond 30 Myr (Laskar et al., 2004, 2011). In parallel, community-based initiatives in the field of radio-isotopic geochronology (i.e. EARTHTIME) led to improvements in the accuracy and precision of the $^{40}Ar/^{39}Ar$ and $^{206}Pb/^{238}U$ techniques, which are commonly used to date K-rich (e.g., feldspar) and U-rich (e.g., zircon) minerals from volcanic material intercalated in the stratigraphic record (see Chapters 2 and 3).

The Eocene – Oligocene transition (EOT) represents a prime interval for the application of magnetostratigraphic dating, owing to the scarcity of sedimentary successions containing intercalated marine and terrestrial deposits, and the presence of endemic faunas on continental land masses. However, numerical age calibration of the Late Eocene – Early Oligocene GPTS has proven to be somewhat problematic, with discrepancies of up to 600 kyr reported between radio-isotopically calibrated and astronomically tuned time scales (Cande and Kent, 1992,1995; Ogg and Smith, 2004; Pälike et al., 2006; Vandenberghe et al., 2012).

4.1.1 The radio-isotopically calibrated GPTS

The radio-isotopically calibrated GPTS relies on the numerical age calibration of the synthetic marine magnetic anomaly profile developed by Cande and Kent (1992) for the South Atlantic, using radio-isotopically dated, and magnetostratigraphically calibrated tie-points, with the underlying assumption that sea-floor spreading rates varied smoothly over the calibrated time interval. The GPTS of Cande and Kent (1992, 1995) used nine tie-points to calibrate the magnetic polarity history of the Cenozoic and Late Cretaceous. Subsequent editions of the GPTS (Ogg and Smith, 2004; Vandenberghe et al., 2012) continued to rely on the Cande and Kent (1992) anomaly profile, and have focused on increasing the number of radio-isotopic tie-points and improving the consistency of the time-scale by calibrating the age of all $^{40}Ar/^{39}Ar$ dated tie-points relative to the assigned age of the Fish Canyon sanidine (FCs) standard. The age of the FCs has itself been revised from 27.84 Ma at the time of the publication of the Cande and Kent (1992) time scale to 28.02 ± 0.28 Ma (Renne et al., 1998), used in the GPTS of Ogg and Smith (2004), and, more recently to an astronomically calibrated value of 28.201 ± 0.046 Ma (Kuiper et al., 2008) adopted in the 2012 edition of the Geological Time Scale (GTS12) and the GPTS of Vandenberghe et al. (2012). Because an FCs age of around 28.20 Ma is supported by additional "inter-calibration" with astronomically tuned records (Rivera et al., 2011) and comparison with the $^{206}Pb/^{238}U$ system (Renne et al., 2010; Rivera et al., 2013; Wotzlaw et al., 2013), the GPTS of Vandenberghe et al. (2012) is, in principle, more accurate, and supersedes previous editions, however recent publications dealing with magnetostratigraphic dating of the sedimentary record (Wade et al., 2011; Coccioni et al., 2012; Jovane et al., 2013) typically also include numerical age calibration relative to a selection of older GPTSs (e.g. Cande and Kent, 1995; Ogg and Smith, 2004; Pälike et al., 2006).

Magnetic reversal dates extracted from the GPTS are typically quoted to the nearest 1 kyr however, their accuracy and precision are difficult to quantify, and are determined by a combination of four factors (1) the accuracy of the synthetic marine magnetic anomaly profile of Cande and Kent (1992); (2) the validity of the assumption of smoothly varying sea-floor spreading rates; (3) the magnetostratigraphic calibration of individual tie-points; and (4) the accuracy of the radio-isotopic dates used for numerical age calibration.

The synthetic marine magnetic anomaly profile developed by Cande and Kent (1992) along a transect of the South Atlantic at ca. 30˚ S latitude is a reference sequence of the relative spacing of normally and reversely magnetized bands of oceanic crust formed over the last 118 Myr. For the Late Eocene – Early Oligocene, the profile is based on data from the South Atlantic, supplemented by additional information from the averaging of five separate profiles crossing anomalies 12-15 from the NE Pacific, with uncertainties of ± 1-6 % (2σ) on the width of each anomaly.

The assumption of smoothly varying seafloor spreading rates along the South Atlantic reference profile is difficult to verify experimentally, and while long term (>1 Myr) averaging of spreading rates may yield a smooth curve, short term fluctuations cannot be ruled out, and may distort the relative spacing of magnetic polarity zones (Agrinier et al., 1999). Huestis and Acton (1997) noted that the assumption of a smooth spreading-rate function for the South Atlantic results in more erratic rate functions at other mid-ocean ridges, and proposed a statistical approach that minimizes non-smooth spreading behaviour at all ridges, resulting in adjustments of up to 5% in the age of individual Neogene and Oligocene magnetic reversals.

The majority of tie-points used for numerical age calibration of the Cande and Kent

(1992) reference profile in recent editions of the GPTS were either $^{40}Ar/^{39}Ar$ dates obtained on volcanic tuffs, or dates extracted from astronomically tuned ODP and IODP records, anchored relative to a $^{40}Ar/^{39}Ar$ age (i.e. 12 out of 12 in Ogg and Smith, 2004, and 25 out of 26 in Vandenberghe et al., 2012). The accuracy of the $^{40}Ar/^{39}Ar$ method, particularly as it relates to the accuracy of the assigned age of the Fish Canyon sanidine (FCs) neutron fluence monitor standard is discussed in detail elsewhere (Chapters 1, 2, and 3). In summary, following a series of 'inter-calibration' experiments with astronomically tuned records and the $^{206}Pb/^{238}U$ system, which support an FCs age of ca. 28.20 Ma (Kuiper et al., 2008; Rivera et al., 2011; Wotzlaw et al., 2013), and revision of the ^{40}K decay constants (Min et al., 2000) the accuracy of the $^{40}Ar/^{39}Ar$ method theoretically approaches 0.25% (Kuiper et al., 2008). However, a comparison between published $^{40}Ar/^{39}Ar$ dates from key Late Eocene – Oligocene sedimentary successions (Swisher and Prothero, 1990; Odin et al., 1991a, 1991b), recalculated relative to an FCs age of 28.201 Ma (Kuiper et al., 2008), and new high-precision $^{206}Pb/^{238}U$ dates from the same tuffs indicates that the accuracy of legacy $^{40}Ar/^{39}Ar$ data from this interval is, in practice, limited to ca. 1-3% (Chapters 2 and 3). The relatively low accuracy of the legacy $^{40}Ar/^{39}Ar$ dates is due to the nature of the analysed material (i.e. biotite dates recording anomalously old ages), potential inter-laboratory bias, and statistical treatment of the data (i.e. weighted mean dates calculated from low-precision, potentially non-normally distributed age populations).

Vandenberghe et al. (2012) estimated the precision of their radio-isotopically calibrated Late Eocene – Oligocene magnetic reversals dates at ± 200-500 kyr (0.6-1.4 %), based on propagated uncertainties related to the geometry of the Cande and Kent (1992) reference profile, and the radio-isotopic age (including systematic uncertainty), and magnetostratigraphic calibration of their tie-points. However, taking into account the above considerations, the accuracy of the GPTS is likely to be somewhat lower than their estimate.

4.1.2 The astronomically tuned GPTS

Astronomical tuning of deep marine records recovered through ODP and IODP expeditions may provide a means to circumvent the uncertainties associated with radio-isotopic calibration of the GPTS, as the method can be used to directly date individual magnetic reversals, and, assuming that cycle expression and identification are complete and accurately known, uncertainties are estimated to be on the order of ± 0.1 % of the tuned ages (Laskar et al., 2004). In addition to their radio-isotopically calibrated GPTS, Vandenberghe et al. (2012) also presented an astronomically tuned age model for the Paleogene, which relied on the tuning of ODP Site 1218 in the Equatorial Pacific (ATPS06, Pälike et al., 2006), at the level of precession cycles (21 kyr), to calibrate the Oligocene, and a compilation of floating astrochronologies anchored to the radio-isotopic age of the Cretaceous – Paleogene boundary to calibrate the Paleocene and Early and Middle Eocene (Westerhold et al., 2007, 2008; Westerhold and Rohl, 2009; Hilgen et al., 2010). Although the ODP Site 1218 tuning extends back to 41 Ma, and several workers have developed floating time scales for parts of the Late Eocene (Pälike et al., 2001; Jovane et al., 2006, 2010; Brown et al., 2009; Hyland et al., 2009), the presence of gaps and discrepancies between these age models precludes the development of a complete astronomically tuned Paleogene time scale. Vandenberghe et al. (2012) relied on calibration of the magnetic anomaly profile of Cande and Kent (1992) using astronomically tuned ages for the base of magnetochron C13n (33.705 Ma) and the base of C21n (47.8 Ma) to bridge the Late Eocene 'gap' between tuned records.

4.1.3 The Late Eocene – Oligocene discrepancy

The final Paleogene GPTS of GTS12 incorporates elements of both the

astronomically tuned, and radio-isotopically calibrated age model of Vandenberghe et al. (2012), and, for intervals where the two age model diverge, the choice between radio-isotopically calibrated and, respectively, astronomically tuned ages was based on an objective evaluation of the underlying data. The two age models are in close agreement for the Late Eocene (C13r-C20n), however, in the Oligocene part of the time scale, radio-isotopically calibrated magnetic reversal dates were up to 700 kyr older than indicated by the astronomically tuned age model. This discrepancy was attributed to the incorporation of anomalously old $^{40}Ar/^{39}Ar$ biotite dates from the Umbria-Marche basin in Italy (Odin et al., 1991; Coccioni et al., 2008), as biotite is susceptible to ^{39}Ar recoil phenomena and incorporation of excess ^{40}Ar (Min et al., 2001; Hora et al., 2010), and the astronomically tuned age model was chosen as the preferred option for the calibration of the Oligocene and Late Eocene.

The high-precision $^{206}Pb/^{238}U$ zircon CA-ID-TIMS dataset presented in Chapter 2 of this thesis reveals that the $^{40}Ar/^{39}Ar$ biotite dates of Odin et al. (1991) and Coccioni et al. (2008) from the Massignano, and Monte Cagnero section, recalculated to a FCs age of 28.201 Ma (Kuiper et al., 2008), are too old, by 400-500 kyr. Interpolated dates for the age of magnetic reversals between the top of C9n and the base of C11n, extracted from the $^{206}Pb/^{238}U$ calibrated age-depth model of the Monte Cagnero section, were in agreement (at the 2σ level) with the astronomically tuned age model of GTS12, and implicitly the tuning of ODP Site 1218. This effectively eliminates the 600-700 kyr discrepancy between radio-isotopically calibrated and astronomically tuned time-scales of the Oligocene. However, $^{206}Pb/^{238}U$ calibrated magnetic reversal dates from the Late Eocene Massigano section (Chapter 2) were 100-300 kyr younger than the astronomically tuned / interpolated GTS12 age model (see Chapter 2, Figure 2.10), and appear to be in better agreement with the Late Eocene part of the ODP Site 1218 tuning, which was not included in the calibration of GTS12, as the tuning is considered unreliable due to the lack

of carbonate based proxy data (Pälike et al., 2006, Vandenberghe et al., 2012).

The high-accuracy $^{206}Pb/^{238}U$ zircon CA-ID-TIMS data set from the White River

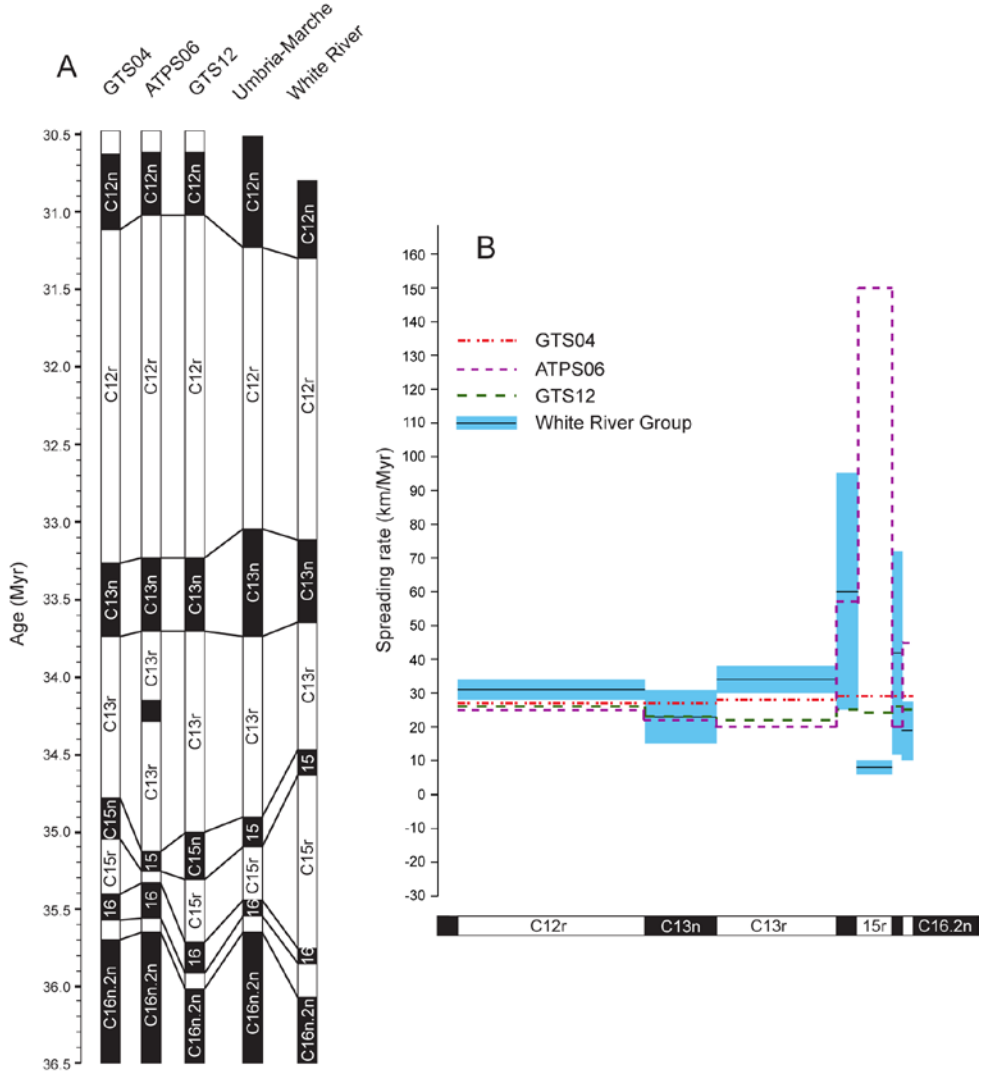

Figure 4.1 Comparison between the published magnetic polarity record of the Flagstaff Rim and Toadstool Park sections (Prothero et al., 1983, 1985; Prothero and Swisher 1992), calibrated using the age-depth models developed in Chapter 3, and other recent time scale calibration studies. Inset shows seafloor spreading rates calculated using the reference profile of Cande and Kent (1992), with uncertainty envelope based on age-depth model uncertainty, and the uncertainties quoted by Cande and Kent (1992) for the width of individual magnetic polarity zones from the S Atlantic anomaly profile, added in quadrature. GTS04 – Ogg and Smith (2004); ATPS06 - PalikePälike et al. (2006); GTS12 – astronomically calibrated age model of Vandenberghe et al. (2012); Umbria – Marche – $^{206}Pb/^{238}U$ calibrated age model of the Massignano and Monte Cagnero sections (Chapter 2) with magnetic polarity data from Jovane et al. (2007), and Hyland et al. (2009)

Group (WRG) of North America and derived age models, discussed in Chapter 3 of this thesis, could provide a means to more accurately constrain the timing of Late Eocene-Early Oligocene magnetic reversals, however, when combined with the published magnetic polarity pattern of the Flagstaff Rim and Toadstool Park sections (Prothero, 1985; Prothero and Swisher, 1992), this approach yields reversal ages that are not compatible with any of the calibration options discussed above (Figure 4.1). The data imply a significantly shorter duration for chron C13r (on the order of 0.8 Myr, compared to 1.2 – 1.3 Myr in Chapter 2 and GTS12), and a significantly longer duration for C15r (1.14 Myr compared to 0.10 Myr in Chapter 2 and 0.18 Myr in GTS12). When plotted against the magnetic anomaly profile of Cande and Kent (1992), $^{206}Pb/^{238}U$ calibrated magnetic reversal ages from the WRG result in abrupt changes in sea-floor spreading rates during the latest Eocene, indicating a possible error in the magnetic polarity pattern of the North American terrestrial record.

In this chapter I present a revised magnetic polarity record for White River Group sedimentary deposits from Flagstaff Rim (central Wyoming), and Toadstool Geologic Park (NW Nebraska), which, when integrated with the high-accuracy $^{206}Pb/^{238}U$ zircon CA-ID-TIMS dataset discussed in Chapter 3 of this thesis, provides a highly resolved chronostratigraphic framework for the Eocene-Oligocene transition.

4.2 Geological setting and published magnetostratigraphy of the White River Group

The White River Group comprises Late Eocene – Oligocene (ca. 37-29 Ma) mainly fluvial and eolian sedimentary deposits that can be traced laterally from South Dakota to NW Nebraska, and E Wyoming (Figure 4.2). The deposits consist of fine-grained reworked volcanic material and primary air-fall tuffs sourced from explosive

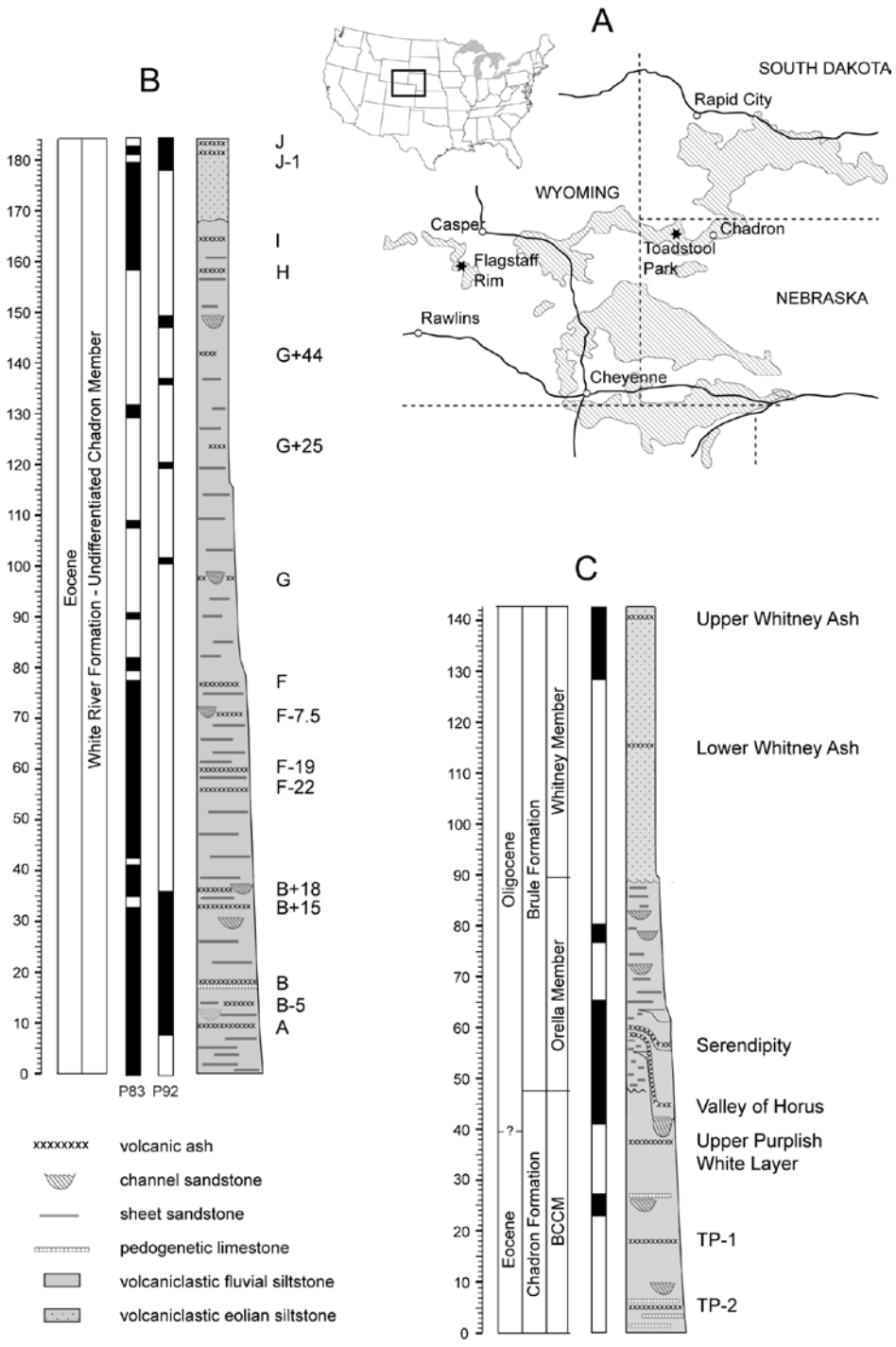

Figure 4.2 A – distribution of the White River Group succession in central North America and location of the Flagstaff Rim and Toadstool Park sections, B – lithostratigraphy of the Flagstaff Rim section, showing the stratigraphic position of volcanic tuff beds, along with the conflicting magnetostratigraphic interpretations of P83- Prothero et al. (1983) and P92 - Prothero and Swisher (1992) see text for details, C – lithostratigraphy of the Toadstool Park section, showing the stratigraphic position of volcanic tuff beds and the magnetostratigraphy of Prothero et al. (1983)

volcanism in Nevada and Utah (Larson and Evanoff, 1998), with additional siliciclastic input derived from the Hartville, Laramie and Black Hills uplifts (Clark, 1975; Stanley and Benson, 1979).The White River group contains rich vertebrate fossil assemblages, which form the basis for the definition of the Chadronian, Orellan and Whitneyan North American Land Mammal Ages (NALMA), and has therefore been the subject of numerous magnetostratigraphic (Prothero et al., 1982; Prothero 1985, 1996; Prothero and Swisher 1992), and geochronologic investigations (Evernden, 1964; Swisher and Prothero, 1992; Obradovich et al., 1995, Chapter 3), attempting to refine the correlation between the North American terrestrial record and marine records of the EOT. Samples for this study were collected from the same localities as the volcanic tuff samples discussed in Chapter 3: Flagstaff Rim, in central Wyoming, and Toadstool Park, in NW Nebraska, which provide continuous coverage of the interval between 35.8-30.9 Ma (Chapter 3). A detailed description of the two localities is provided in Chapter 3, Section 3.2.

The magnetostratigraphy of the Flagstaff Rim section has been subject to a series of revisions, both in terms of the identification of individual magnetic polarity zones, and their correlation to the GPTS (Figure 4.2). Prothero et al. (1982, 1983) identified two normal polarity zones, one spanning the lower half of the section, and one between tuffs I and J of Emry (1973), based on a record consisting of samples collected at a stratigraphic resolution of 0.8 m, and analysed using alternating field (AF) demagnetization techniques. Because K-Ar dates obtained by Evernden et al. (1964) on biotites from tuffs F, G and J indicated an early Oligocene age, the two normal polarity zones were correllated to magnetochrons C13n, and respectively C12n of the GPTS. Prothero (1985), and Prothero and Swisher (1992) presented a revised magnetic polarity pattern for Flagstaff Rim, based on thermal demagnetization of sets of three replicate samples collected at a stratigraphic resolution of 1.7 m. In this revised record the lower half of the Flagstaff Rim section is dominated by reversed polarity samples, with only a ca. 30 m thick normal polarity

zone identified around the level of tuff B. This was attributed to the use of thermal demagnetization, which, unlike the AF techniques used by Prohero et al. (1983) is able to remove present-day normal polarity overprints carried by low blocking temperature, but high-coercivity minerals, such as goethite (Prothero, 1985; Prothero and Swisher, 1992). Following the publication of the biotite and anorthoclase $^{40}Ar/^{39}Ar$ dates of Swisher and Prothero (1990), which showed that the Flagstaff Rim section spanned the Late Eocene, and not the Early Oligocene as previously thought (Evernden et al., 1964), the correlation of the magnetic polarity pattern to the GPTS was revised, from C11r-C13n, to C13r-C16n.

The magnetic polarity pattern of the Toadstool Park section is based on samples collected at a stratigraphic resolution of 1.7 m, with three samples from each site analysed using AF, and subordinately thermal demagnetization techniques (Prothero et al., 1983). The interval between the base of the Toadstool Park section and the Upper Whitney ash was originally correlated to C13r-C10n of the GPTS (Pothero et al., 1983), later revised to C15r-C12n (Prothero and Swisher, 1992), based on the biotite and anorthoclase $^{40}Ar/^{39}Ar$ dates of Swisher and Prothero (1990) for the Lower and Upper Whiteny ashes.

4.3.Materials and methods

We collected 717 oriented samples at Flagstaff Rim and Toadstool Park, at an average stratigraphic resolution of 0.5 m, using a hand-held, generator-powered drill with a diamond-coated, water-cooled drill bit. Weathered material was removed from outcrops prior to sampling which was conducted along sections spanning 5-50 m in stratigraphic thickness (Figure 4.3, 4.4), with individual sections correlated using laterally continuous volcanic tuffs. At Flagstaff Rim, our composite section spans 183 m, from 18.3 m below the level of the B tuff, to the J tuff of Emry (1973). The Toadstool Park composite section

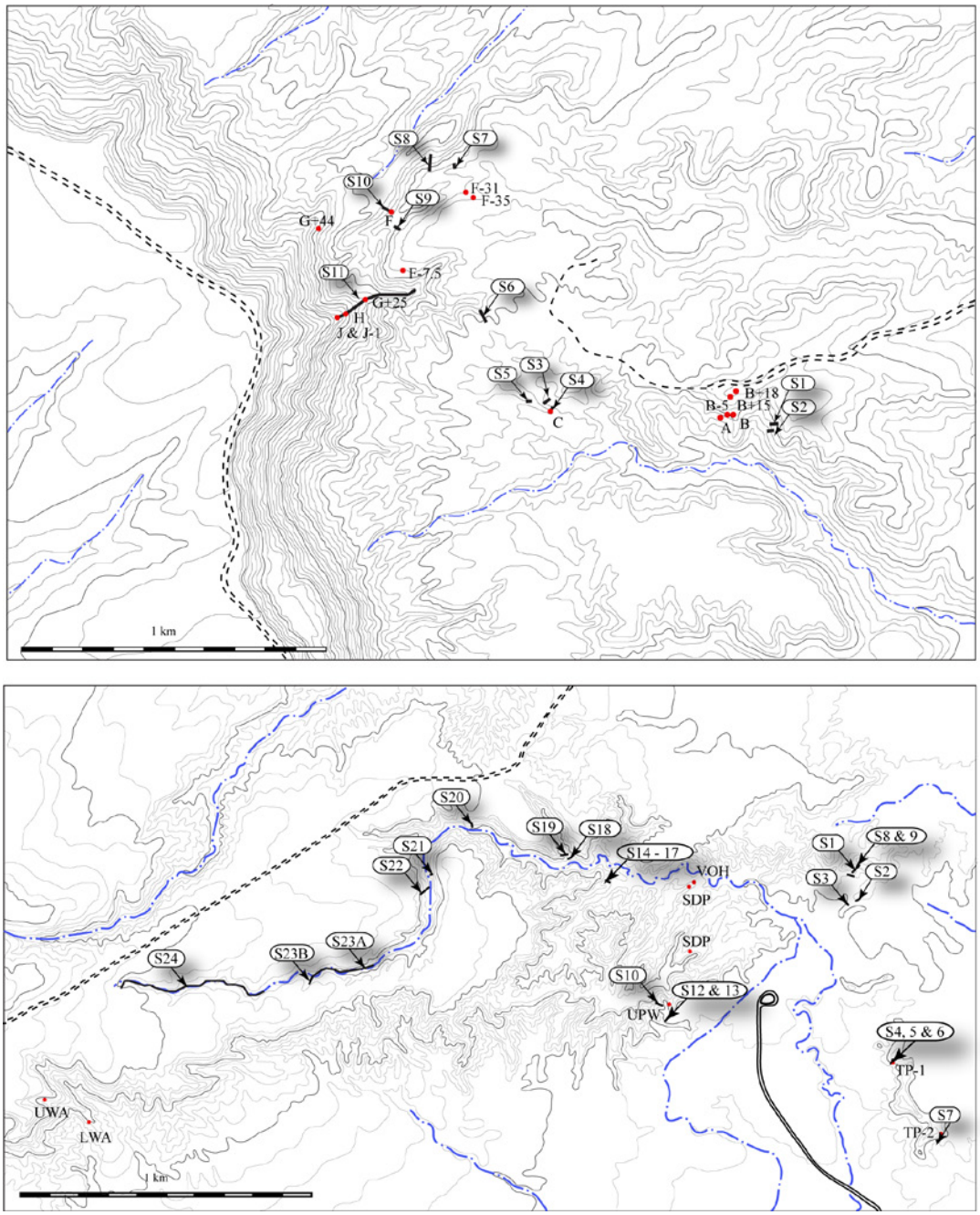

Figure 4.3 Topographic maps of Flagstaff Rim (above) and Toadstool Park (below), showing the spatial distribution of the measured sections that make up the composite records developed at the two localities. Section numbers correspond to those listed in Appendix B, Tables B.1 and B.2. Red dots indicate the location of volcanic tuff samples discussed in Chapter 3

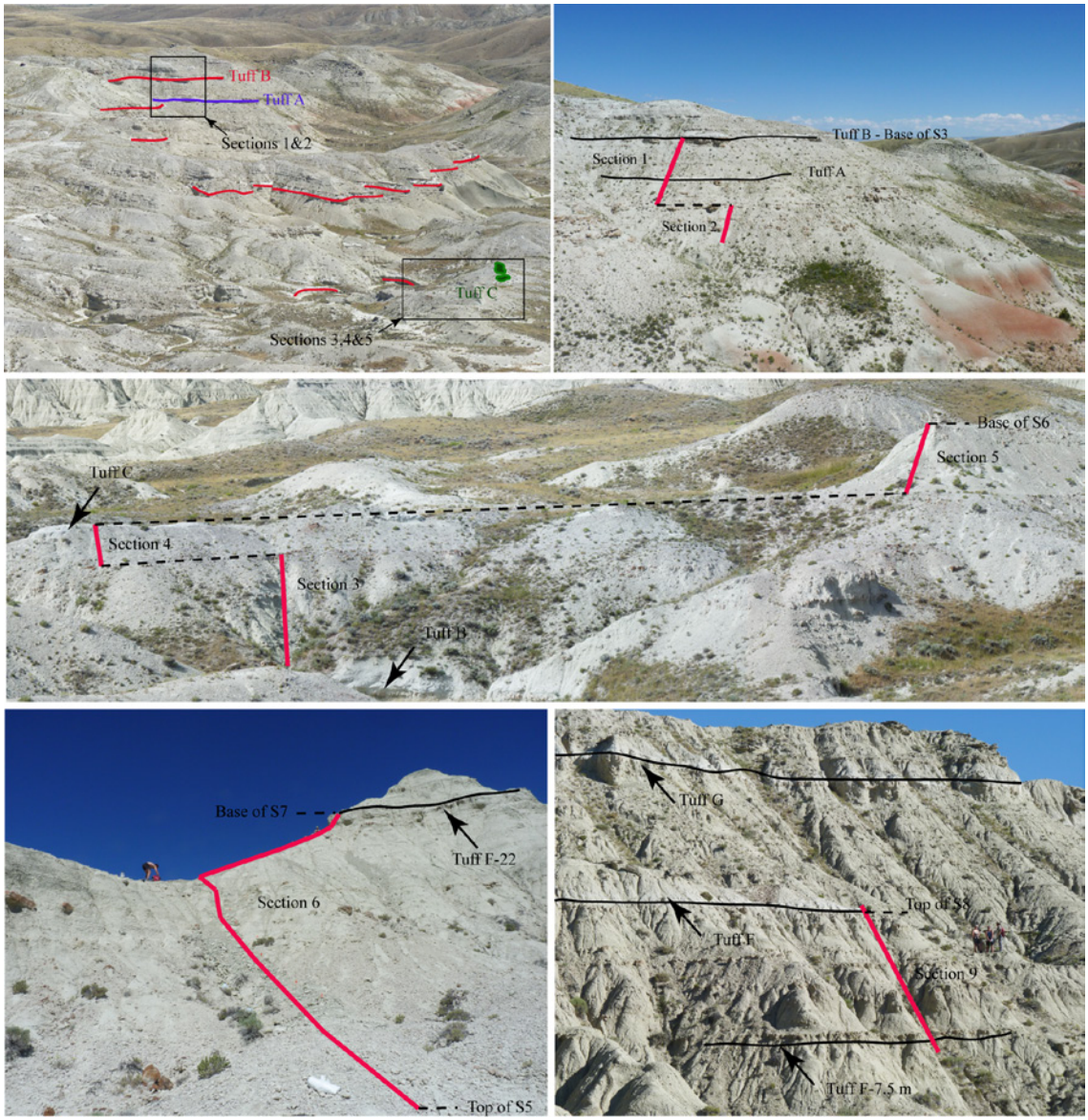

Figure 4.4 Correlation of measured sections from the lower 96 m of the Flagstaff Rim sedimentary succession. The thicknesses of stratigraphic intervals covered by each section are: Section 1 - 13.7 m (18 samples), Section 2 - 4.8 m (7 samples), Section 3 - 9.2 m (16 samples), Section 4 - 2.5 m (8 samples), Section 5 - 4.6 m (11 samples), Section 6 - 21 m (22 samples, low resolution due to upper half of the section not being suitable for drilling), Section 7 - 4.2 m (6 samples)

spans 142 m, with its base situated 38.2 m below the Upper Purplish White Layer, and its top at the level of the Upper Whitney Ash. Sample positions were measured with a Jacob staff and Abney level, and are directly tied into the measured sections used for the development of $^{206}Pb/^{238}U$ calibrated age-depth models for the Toadstool Park and Flagstaff Rim section in Chapter 3. Sample orientations were recorded using an orientation stage

consisting of a clinometer, and a magnetic compass, and were corrected for present-day declination (-10˚ at Flagstaff Rim, and -8˚ at Toadstool Park).

4.3.1 Laboratory methods

Magnetic analysis was carried out at the Fort Hoofddijk Paleomagnetic Laboratory, Utrecht University. In order to identify magnetization carrying mineral assemblages, selected samples were subjected to high-field thermo-magnetic runs in air using a modified horizontal translation type Curie balance (Mullender et al., 1993) with a sensitivity of ~ 5 x 10^{-9} Am^2. 50-80 mg of powdered sample held in a quartz sample holder was placed inside a cycling magnetic field that varied between 100-300 mT. Analysis over different heating and cooling cycles performed at a rate of 10°C/min to a maximum temperature of 700°C showed the destruction of a mineral phase up to 560-600°C indicating the presence of iron oxides, such as magnetite, as the main carrier of remanent magnetisation (Figure 4.5).

An initial set of 100 samples with a stratigraphic resolution of ~ 2 m was subjected to stepwise thermal demagnetisation up to a temperature of 660°C, in a magnetically shielded oven, using 30-40°C increments. Natural remanent magnetisation (NRM) was measured following each demagnetisation step using a horizontal 2G Enterprise DC SQUID cryogenic magnetometer (noise level 3 x 10^{-12} Am^2). These data were used to determine the characteristic demagnetization behaviour of the samples, and to provide initial constraints on the stratigraphic position of magnetic reversals. Subsequent batches of samples were demagnetised using either thermal demagnetisation up to 660°C (~ 60% of the samples) or a combined approach using both thermal and AF techniques. In the latter case samples were thermally demagnetised up to 270°C in order to remove potential overprint carried by low blocking temperature high-coercivity minerals, followed by AF

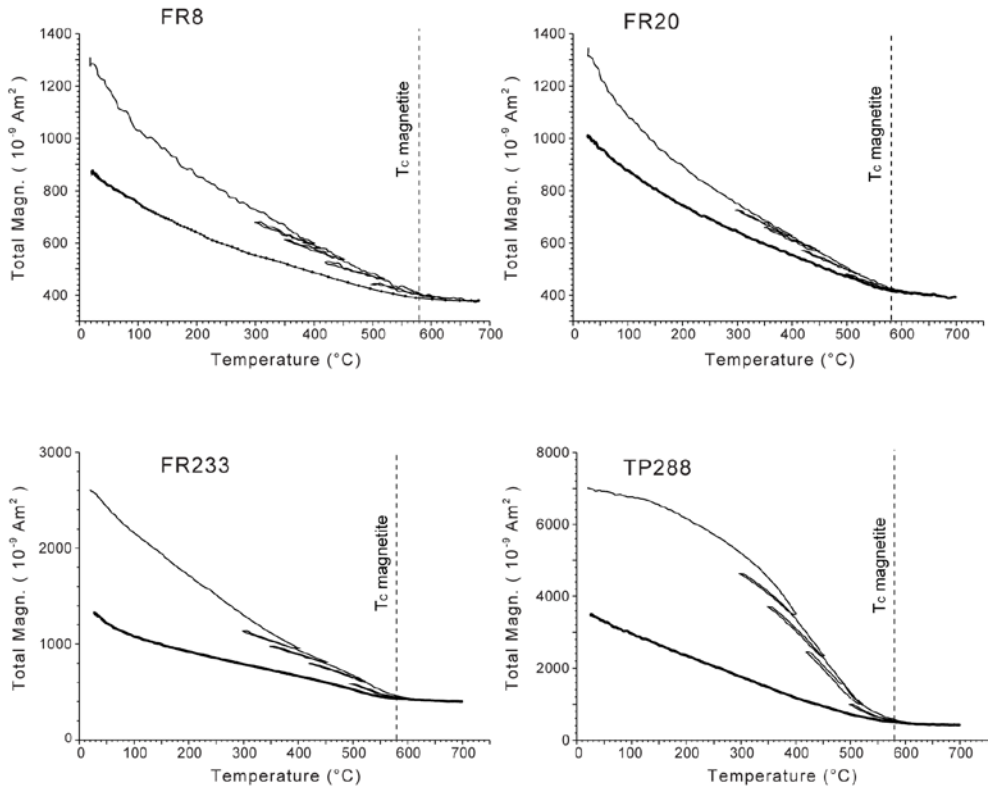

Figure 4.5 Curie balance plots of four representative samples from the Toadstool Park (TP) and Flagstaff Rim (FR) records. The change in slope at ca. 580˚C points towards magnetite as the main magnetic signal carrier. Tc – Curie temperature.

demagnetization in a 2G degausser, using 5 mT increments up to 40 mT, and then 10 mT increments up to a maximum intensity of 100 mT. AF demagnetization was mainly used for stratigraphic intervals where thermal demagnetization above 270°C resulted in unstable magnetic directions.

4.4 Results

A total of 185 samples from Flagstaff Rim and 186 from Toadstool Park were analysed (Appendix B, Tables B.1 and B.2). Demagnetisation data were plotted on Zijderveld diagrams (Kirschvink, 1980; Zijderveld, 1967). At least three successive demagnetization steps were used to define different magnetic components, and their directions were determined using best fit lines with principal component analysis

(Kirschvink, 1980). Mean normal and reverse polarity directions were calculated using Fischer statistics (Fischer, 1953). As the White River sedimentary deposits consist of horizontal strata, no tectonic correction was applied.

4.4.1 Demagnetization behaviour

Initial NRM intensities were between 0.02-4 mA/m and were found to increase up-section at both localities, possibly due to the increasing volcanic ash content of the sedimentary deposits, particularly following the change from fluvial to eolian deposition which occurs around the level of the I tuff at Flagstaff Rim (Evanoff et al., 1992), and ca. 50 m above the Upper Purplish White Layer at Toadstool Park. Gradual decrease of NRM intensities below a threshold of 0.02-0.05 mA/m usually resulted in unstable behaviour characterized by oscillating NRM intensities and directions. Ca. 30% of the samples reached this stage during thermal demagnetization at temperatures below 240°C and were excluded from further interpretation (23% of analysed samples, category D in tables B.1 and B.2), while the remaining 70% remained stable, and retained ca. 20-30% of their original NRM at 240°C. Samples that were subjected to further thermal demagnetization above 240°C generally yielded data that could be interpreted up to temperatures of 400-520°C. Data from AF demagnetized samples could be interpreted up to field intensities of 70-90 mT. Samples that remained stable throughout the demagnetization process typically retained less than 10% of their original NRM signal when demagnetized at 660°C or 100 mT respectively.

A low temperature, normal polarity component (LTC) is distinguishable in 96% of the samples, between 100 and 240°C (Figure 4.6) . Mean declination (D) and inclination (I) of this component cluster close to the parameters of the present day magnetic field (Figure 4.7). Samples that remained stable above 240°C exhibit a high-temperature

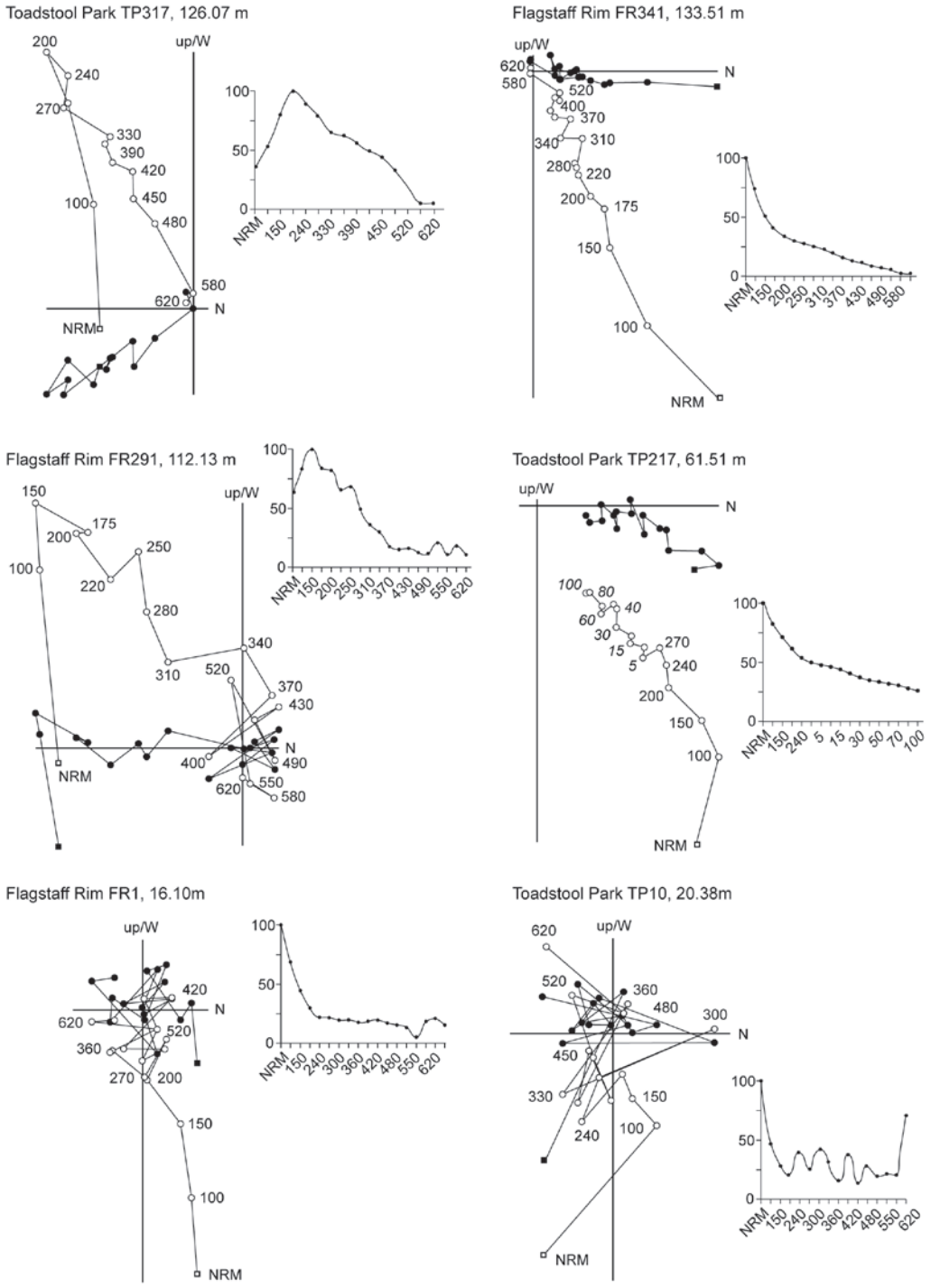

Figure 4.6. Representative Zijderveld diagrams for samples demagnetised using thermal (TP317, TP334, FR291 and FR 341) and combined thermal and alternating field demagnetisation techniques (TP217 and FR183). Stratigraphic position is indicated next to the diagrams. Closed (open) symbols denote the horizontal (vertical) components of the magnetic field, and rectangles indicate the natural remanent magnetisation (NRM) Plain numbers next to the graphs indicate demagnetisation temperature steps in ˚C, numbers in italics indicate alternating field intensities in mT. A diagram indicating the relative decrease in magnetic moment with each demagnetisation step is show for each sample.

component (HTC) which steadily decays towards, but does not reach zero, and shows dual polarity. Isolating the low and high-temperature components in samples for which the latter shows normal polarity is difficult because the directions of the two components

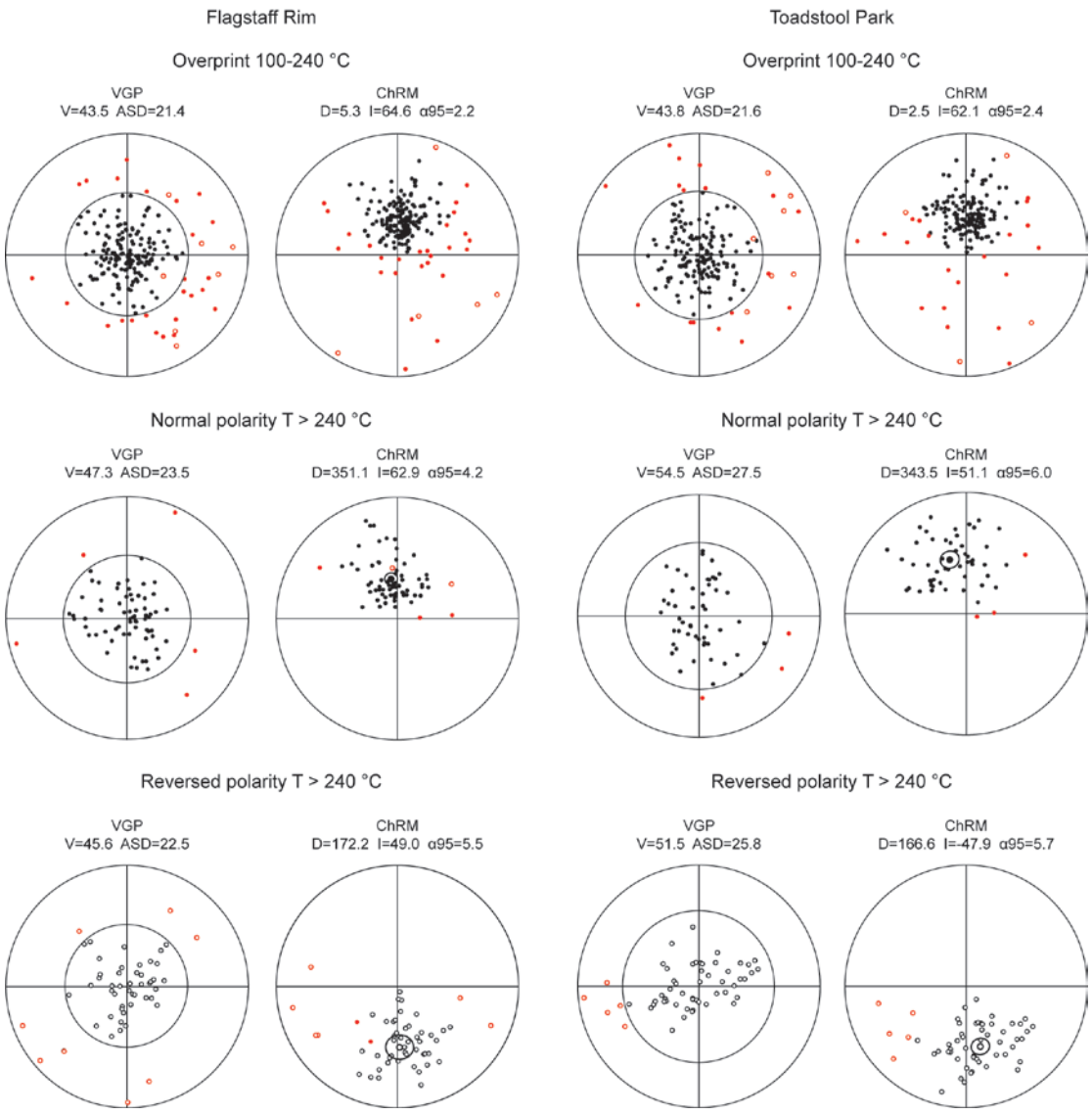

Figure 4.7 Equal area plots showing low temperature normal polarity overprint, and high temperature normal and reversed polarity directions for the Flagstaff Rim and Toadstool Park records. Both the ChRM (characteristic remanent magnetization) and the calculated VGP positions are shown. D – mean declination, I – mean inclination, α95 – 95% confidence interval of the mean, V – cut-off distance from the mean VGP determined using the variable cut-off algorithm of Vandamme (1994), ASD – angular standard deviation of the mean VGP. Red (black) symbols represent data excluded from (included in) the calculation of mean directions / VGP positions based on the respective cut-off angles.

are nearly parallel. In samples for which the HTC shows reversed polarity, the LTC is completely removed through thermal demagnetization at 150 – 240°C. For this reason, all data obtained from thermal demagnetization steps below 240°C in samples that showed a normal polarity HTC were attributed to present day overprint, while the HTC was defined based on data obtained above 240°C. As the HTC shows dual, normal and reversed polarity, it was interpreted as a primary characteristic remnant magnetization (ChRM) signal. Samples for which the mean angular deviation (MAD) of the HTC exceeded 20°C (9 % of analysed samples, category C in tables B.1 and B.2) were excluded from further interpretation.

The polarity record of the Flagstaff Rim and Toadstool Park sections was interpreted in terms of virtual geomagnetic pole (VGP) latitude calculated based on HTC data. VGP data showed high scatter, and were filtered using the variable cut-off algorithm of Vandamme (1994), which excluded outliers, interpreted as representing transitional VGP positions (Figure 4.7, category B in tables B.1 and B.2, accounting for 5% of analysed samples), based on angular distance from the mean VGP. The remaining samples (63% of analysed samples, category A in tables B.1 and B.2) were used to interpret the magnetic polarity pattern of the Flagstaff Rim and Toadstool Park sections. At Toadstool Park normal and reversed polarity directions passed the reversal test of Tauxe (2010), however mean inclinations are ca. 10° lower than expected from plate tectonic models (Torsvik et al., 2008) indicating some degree of post-depositional compaction. The Flagstaff Rim samples failed the reversal test of Tauxe (2010) due to a difference of 11° between mean normal and reversed polarity inclinations. Although this indicates incomplete removal of the present day overprint, we interpret the ChRM as a primary signal, because of its dual polarity and because the mean directions of the high and low temperature components are distinct at the 95% confidence level.

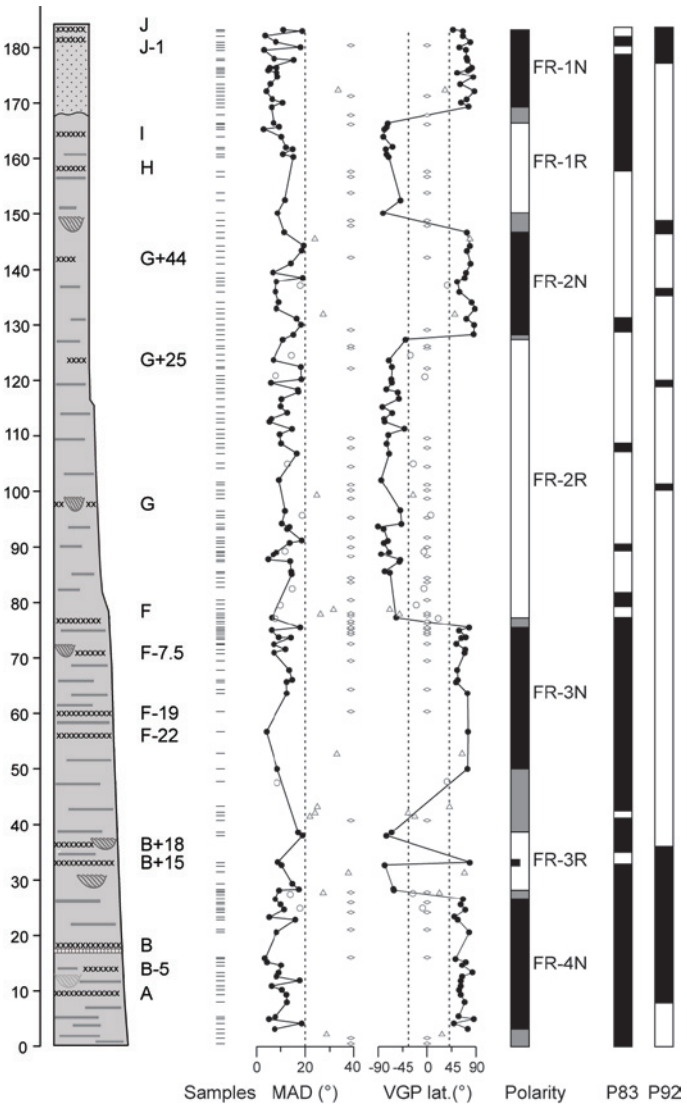

Figure 4.8 Magnetostratigraphy of the Flagstaff Rim section. Mean angular deviation, and VGP latitude is plotted for each analysed sample. Normal and reverse polarity is derived from virtual geomagnetic pole (VGP) latitude data. Diamonds – category D samples showing unstable magnetic directions above 240 ˚C, triangles – category C samples, with MAD > 20˚, open circles – category B points excluded through filtering of VGP latitude data using the variable cut-off algorithm of Vandame (1994), closed circles – category A data used for interpretation of magnetic polarity pattern. In the polarity columns black, white and gray indicate normal, reversed, and respectively uncertain polarity. Magnetostratigraphic records of (P83) Prothero et al., (1983) and (P92) Prothero and Swisher (1992) are shown for comparison.

4.4.2 Magnetic polarity record of the Flagstaff Rim and Toadstool Park sections

VGP latitudes of category A samples were plotted in stratigraphic order at both localities in order to determine the magnetic polarity pattern of the Flagstaff Rim and Toadstool Park sections. Polarity zones were defined based on at least two consecutive samples with identical polarity, and magnetic reversals were inferred to lie halfway between consecutive samples showing opposite polarities.

4.4.2.1 Flagstaff Rim

At Flagstaff Rim we identified four normal and three reversed polarity zones (Figure 4.8, Table 4.1):

- Normal polarity zone FR-N4 extends from the base of our measured section to metre level 27.0 (8.7 m above the B tuff), with the position of its top constrained to within ± 0.45 m. This zone roughly corresponds to normal polarity zones identified in the records of both Prothero et al. (1983) and Prothero and Swisher (1992).
- Reversed polarity zone FR-R3 extends from metre level 27.0 up to a 9 m thick zone of uncertain polarity between metre levels 38.51-47.51, caused by the exclusion of three samples with MAD values above 20˚. The top of zone FR-R3 is tentatively placed halfway through this interval, at metre level 43.01. This zone is characterized by mostly opposite, normal polarity samples in the record of Prothero et al. (1983) and corresponds to a transition from normal to reversed polarity in the revised record of Prothero and Swisher (1992).
- Normal polarity zone FR-N3 extends between metre levels 43.01 – 76.13 with the position of its top constrained to within ± 0.91 m. This zone corresponds

to a normal polarity zone in the record of Prothero et al. (1983), and is characterized by opposite, reversed polarity in the revised record of Prothero and Swisher (1992).

- Reversed polarity zone FR-R2 lies between 76.1 – 127.4 m above the base of our measure section, with the stratigraphic position of its top constrained to within ± 0.42 m. This interval was reported as having identical, reversed polarity in both the records of Prothero et al. (1983) and Prothero and Swisher (1992).
- Normal polarity zone FR-N2 lies between metre levels 127.4 – 147.9 with the stratigraphic position of its top constrained to within ± 1.7 m. This normal polarity zone has not been previously identified, and both Prothero et al. (1983) and Prothero and Swisher (1992) report this interval as showing opposite, reversed polarity.
- Reversed polarity zone FR-R1 lies between metre levels 147.9 – 167.2, with the stratigraphic position of its top constrained to within ± 1.44 m. This interval is partially characterized by normal polarity in the record of Prothero et al. (1983), and reversed polarity in the revised record of Prothero and Swisher (1992).
- Normal polarity zone FR-N1 extends from metre level 167.2 to the top of our measured section, at the level of the J tuff (183.2 m), and occupies a stratigraphic interval reported as having normal polarity by both Prothero et al. (1985) and Prothero and Swisher (1992).

The two previously published magnetic polarity records of the Flagstaff Rim section show discrepancies in terms of the number of identified magnetic polarity zones, and their relative thicknesses (Prothero et al., 1985; Prothero and Swisher, 1992), and our interpretation differs significantly from both of them. Prothero and Swisher (1992)

attributed the discrepancies between their thermal demagnetization based data and earlier interpretation of Prothero et al (1982, 1983), who used AF demagnetization, to incomplete removal of present day field overprints carried by low blocking temperature, high-coercivity minerals, such as goethite, which can result in the presence of spurious normal polarity samples. Because all our samples were thermally demagnetized up to a temperature of at least 240˚C, such overprints are unlikely to have a significant impact on our record. Because most of our Flagstaff Rim record consists of interspaced samples for which the HTC was analysed using thermal, and respectively alternating field demagnetization techniques, with no systematic differences detected between results obtained using the two methods, and mean directions calculated for each normal polarity interval overlap at the 95% confidence level, the presence of spurious normal polarity zones in our interpreted magnetic polarity pattern is considered unlikely.

Zone	Minimum	Maximum	Average
TP-N1	130.09	130.99	130.54
TP-R1	64.62	66.63	65.62
TP-N2	43.24	48.51	45.88
TP-R2	13.10	16.36	14.73
FR-N1	165.80	168.67	167.24
FR-R1	146.17	149.65	147.91
FR-N2	126.96	127.80	128.38
FR-R2	75.22	77.04	76.13
FR-N3	38.51	47.51	43.01
FR-R3	26.52	27.42	26.97

Table 4.1 Stratigraphic position of magnetic reversals recorded in the Flagstaff Rim and Toadstool Park sections. Stratigrapic levels are reported relative to the base of the Flagstaff Rim (18.35 m below the B tuff) and respectively Toadstool Park (38.25 m below the Upper Purplish White Layer) composite sections. Minimum and maximum values relate to the stratigraphic position of consecutive samples showing opposite polarity, with the position of the magnetic reversal, assumed by convention to lie halfway between the two, listed in the last column.

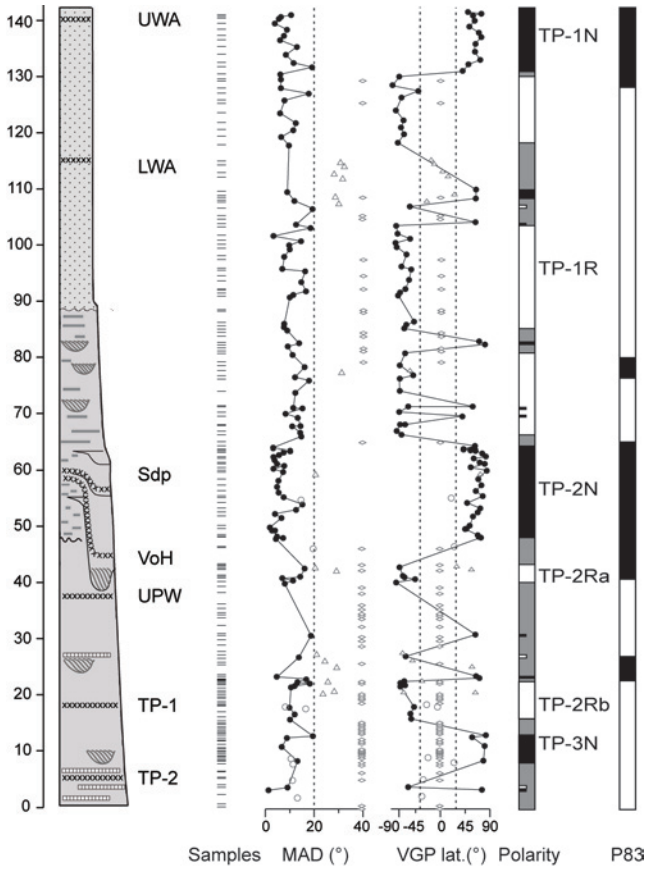

Figure 4.9 Magnetostratigraphy of the Toadstool Park section. Mean angular deviation, and VGP latitude is plotted for each analysed sample. Normal and reverse polarity is derived from virtual geomagnetic pole (VGP) latitude data. Symbols are the same as in Figure 4.8. Magnetostratigraphic record of (P83) Prothero et al., (1983) shown for comparison.

4.4.2.2 Toadstool Park

Of the 71 samples analysed from the lower 40 m of the Toadstool Park section (from the base of the section to just above the Upper Purplish White Layer), 42 exhibited unstable magnetic signals when demagnetized above 240˚C, and six of the remaining samples were excluded based on high MAD values. Samples yielding good quality data appear to be clustered in distinct bands around metre levels 3, 8, 12, 18, and 21-28, however above metre level 45 the magnetic quality of the samples improves significantly. In total, we identified three normal and two reversed polarity zones:

- Normal polarity zone TP-N3 is represented by four normal polarity samples,

between metre levels 8.4 and 13.1 above the base of our measured section. Due to the poor magnetic quality of the samples, no polarity information is available for the interval between 0-8.4 m.

- TP-R2a and TP-R2b are two short reversed polarity zones identified between 16.3-23.0 m, and 40.53 – 43.24 m respectively, separated by an interval of uncertain polarity. The transition between TP-R2a and the underlying normal polarity zone TP-N3 was constrained to within ± 1.63 m, while the stratigraphic position of the top of zone TP-R2b, at 45.88 m, has an uncertainty of ± 2.63 m.
- Normal polarity zone TP-N2 lies between 45.88-65.62 m, with the stratigraphic position of its top constrained to within ± 1 m.
- Reversed polarity zone TP-R1 lies between 65.62 – 130.54 m, and includes a ca. 15 m interval of uncertain polarity below the Lower Whitney Ash. The stratigraphic position of the top of this polarity zone has an uncertainty of ± 0.45 m.
- Normal polarity zone TP-N1 extends from metre level 130.54 to the top of our measured section, at the level of the Upper Whitnew Ash.

Our interpretation of the magnetic polarity record of the Toadstool Park section is in overall agreement with that of Prothero et al. (1983) with the exception of polarity zone TP-N3 which corresponds to an interval of reversed polarity in the previously published record. Details of the stratigraphic positions of the identified magnetic reversals are listed in Table 4.1.

4.5 Dating the magnetic polarity record of the WRG

The high-resolution palaeomagnetic data from the Flagstaff Rim and Toadstool Park sections, combined with the age-depth models developed in Chapter 3 on the basis

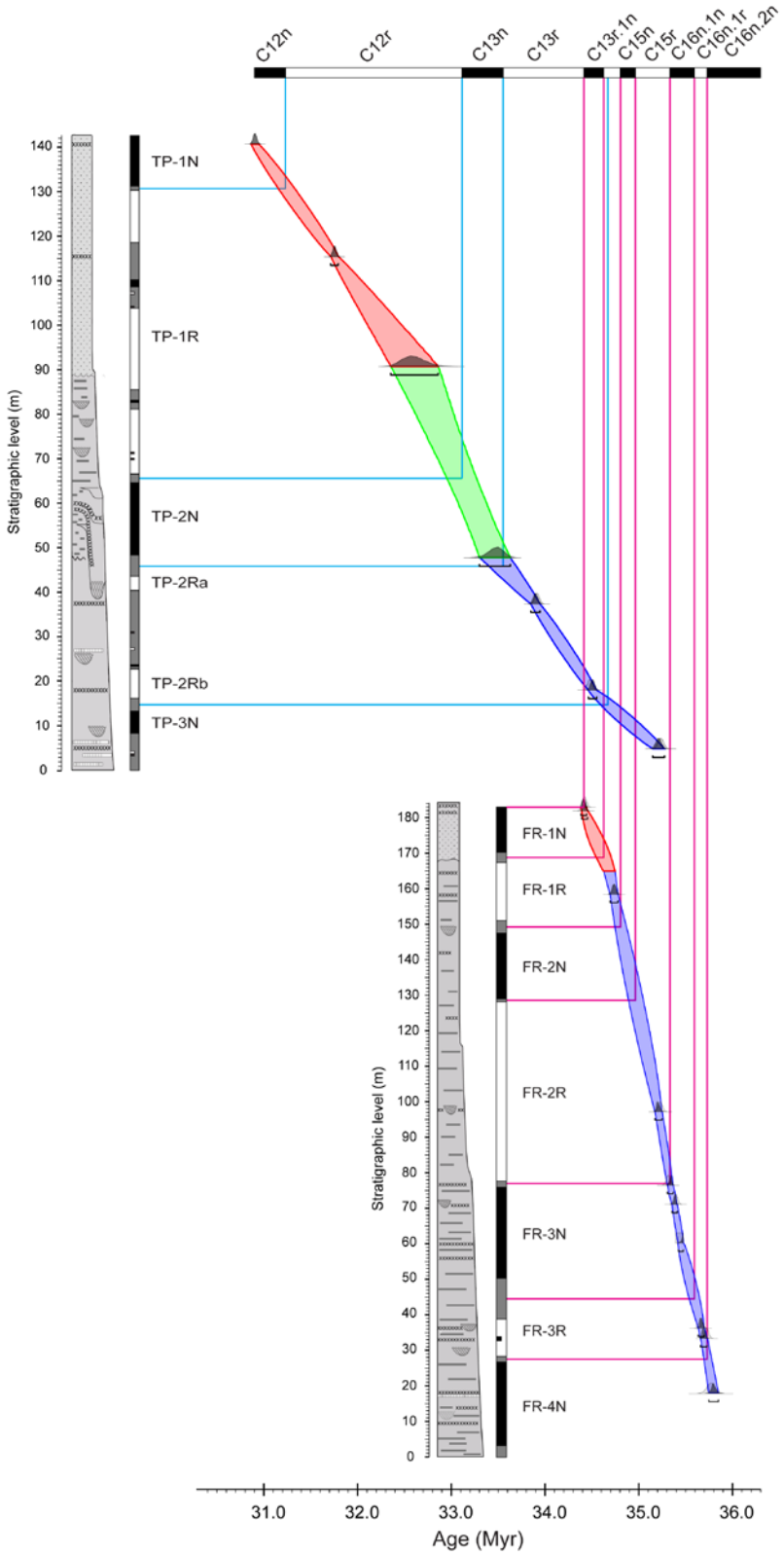

Figure 4.10 Magnetic polarity pattern of the Flagstaff Rim and Toadstool Park sections, correlated to the GPTS using the age-depth models developed in Chapter 3 of this thesis, based on the weighted mean $^{206}Pb/^{238}U$ zircon dates obtained for tuffs intercalated in the WRG sedimentary succession.

of high-accuracy $^{206}Pb/^{238}U$ zircon CA-ID-TIMS dating of volcanic tuffs from the same sections, provide a fully integrated record of the magnetic polarity history of the WRG. Owing to the relatively high sediment accumulation rates that characterize the WRG, the temporal resolution of this record is ca. 6 kyr at Flagstaff Rim, and 20 kyr at Toadstool Park. In this section, the established age model of the WRG (Chapter 3) is used to develop a first order correlation between the WRG magnetic record, and the GPTS, such that each normal and reversed polarity interval can be assigned to numbered chrons. I then use the WRG data to explore issues related to the accuracy of the GPTS of Vandenberghe et al. (2012), the astronomically tuned GPTS of Pälike et al. (2006), and the $^{206}Pb/^{238}U$ calibrated age model of the Umbria-Marche succession (Chapter 2).

The fourteen high-precision $^{206}Pb/^{238}U$ zircon dates presented in Chapter 3 make the correlation of the magnetic polarity pattern of the Flagstaff Rim and Toadstool Park sections to the GPTS relatively straightforward (Figure 4.10):

- A weighted mean $^{206}Pb/^{238}U$ age of 30.915 ± 0.022/0.026/0.042 (with uncertainty values signifying analytical, and added tracer calibration, and respectively ^{238}U decay constant uncertainty) was obtained for the Upper Whitney Ash (Chapter 3), indicating that normal polarity zone TP-N1, situated at the top of the Toadstool Park section, corresponds to magnetochron C12n.
- The correlation of magnetic polarity zone TP-R1 to C12r is supported by the weighted mean $^{206}Pb/^{238}U$ age of the Lower Whitney Ash, at 31.760 ± 0.014/0.020/0.039 Ma. The five isolated normal polarity samples identified in zone TP-R1 (Figure 4.9) may correspond to some of the eight 'tiny wiggles' identified by Cande and Kent (1992) within C12r, which have been interpreted as representing either very short (<30 kyr) normal polarity intervals, or periods of low magnetic field intensity (Tauxe, 2010).
- The weighted mean $^{206}Pb/^{238}U$ age of 33.911 ± 0.025/0.032/0.049 Ma determined

for the Upper Purplish White Layer is consistent with the correlation of magnetic polarity zone TP-N2 to chron C13n.

- The weighted mean $^{206}Pb/^{238}U$ age of the TP-2 tuff (34.477 ± 0.021/0.029/0.047 Ma) supports the correlation of the TP-R2a, and TP-R2b polarity zones to magnetochron C13r.
- Magnetic polarity zone TP-N3 is bracketed by the TP-2 and TP-1 tuffs, and the weighted mean $^{206}Pb/^{238}U$ ages of the two tuffs (34.477 ± 0.021/0.029/0.047 Ma, and respectively 35.234 ± 0.042/0.046/0.060 Ma) support a correlation to magnetochron C15n.

The age of the TP1-tuff overlaps within analytical uncertainty, at the 2σ level, with that of the G tuff at Flagstaff Rim (35.249 ± 0.020/0.027/0.046 Ma), while that of the TP-2 tuff is close, although not statistically equivalent to that of the J (34.417 ± 0.018/0.025/0.046 Ma), and respectively J-1 tuffs (34.407 ± 0.19/0.025/0.044 Ma). Because sedimentation rates recorded in the Flagstaff Rim section (60-150 m/Myr), are significantly higher than in the lower 20 m of the Toadstool Park section (ca. 20 m/Myr), the magnetic polarity record of the former locality provides a much better temporal resolution for the interval between 34.4-35.2 Ma.

Normal polarity zone FR-N1, situated at the top of the Flagstaff Rim section has been previously correlated to magnetochron C15n (Prothero and Swisher, 1992), however, the overlapping $^{206}Pb/^{238}U$ weighted mean ages of the closely spaced J and J1 tuffs provide a robust age constraint around 34.40 Ma, which indicates that polarity zone FR-N1 is younger than the top of C15n, which occurs between 34.8-35.1 Ma in GTS04, ATPS06, and is also too old to be assigned to the lower part of magnetochron C13n, the base of which would be expected to occur at around 33.7 Ma (Ogg and Smith, 2004; Pälike et al., 2006; Vandenberghe et al., 2012, Chapter 2). The presence of normal polarity subchrons

within chron C13r is a matter of some debate. Four short normal polarity zones, lasting on average 20 kyr, were identified in the marine magnetic anomaly profile of Cande and Kent (1992), however given that zone FR-N1 covers the uppermost 16 m, of the Flagstaff Rim section, its minimum duration is estimated to be about one order of magnitude greater based on the age-depth model discussed in Chapter 3. A normal polarity zone designated as C13r.1n, with a duration estimated at ca. 140 kyr has been reported from the magnetic polarity record of ODP Site 1218 (Pälike et al., 2006), and is potentially also present in the magnetic polarity record of ODP Site 1090 (Channell et al., 2003), although precise correlation to the GPTS at the latter locality was hampered by the presence of a hiatus of unknown duration in chron C11r. Here we tentatively correlate the base of polarity zone FR-N1 to the base of subchron C13r.1n of Pälike et al. (2006). The top of the Flagstaff Rim measured section, and the age of the J and J-1 tuffs, provide a maximum constraint on the top of C13r.1n. However it is important to note, that at Toadstool Park, the TP-2 tuff, which is ca. 60 kyr older than the J tuff, appears to be located in a stratigraphic interval characterized by reversed polarity, which may be due to the lower stratigraphic resolution, and poorer magnetic quality of the lower part of the Toadstool Park record.

The previously undetected polarity zone FR-N2 is bracketed by the H and G tuffs, and the weighted mean $^{206}Pb/^{238}U$ ages of these tuffs (34.742 ± 0.017/0.024/0.044 Ma, and respectively 35. 249 ± 0.020/0.027/0.047 Ma) support a correlation to C15n of the GPTS. Based on the their relative position in the WRG magnetic polarity record, polarity zones FR-N3 and FR-N4 are correlated to chrons C16n.1n, and C16n.2n.

The age of observed magnetic reversals was calculated by integrating this revised magnetic polarity pattern with the radio-isotopic age of the volcanic tuffs intercalated in the Flagstaff Rim and Toadstool Park sections, via the $^{206}Pb/^{238}U$ calibrated age-depth models presented in Chapter 3. The results are summarized in Table 4.2, which includes

Chron (base)	Minimum	Maximum	Average
C12n	31.282 ± 0.092	31.249 ± 0.092	31.266 ± 0.092
C12r	33.151 ± 0.155	33.109 ± 0.153	33.130 ± 0.158
C13n	33.698 ± 0.109	33.482 ± 0.157	33.590 ± 0.134
C13r.1n	33.674 ± 0.066	34.627 ± 0.066	34.647 ± 0.066
C13r	34.845 ± 0.066	34.818 ± 0.062	34.834 ± 0.066
C15n	35.001 ± 0.076	34.994 ± 0.076	34.998 ± 0.076
C15r	35.366 ± 0.048	35.345 ± 0.045	35.355 ± 0.046
C16n.1n	35.678 ± 0.049	35.597 ± 0.06	35.636 ± 0.058
C16n.1r	35.802 ± 0.053	35.797 ± 0.052	35.799 ± 0.052

Table 4.2 Age of magnetic reversals recorded in the Flagstaff Rim and Toadstool Park sections. Maximum – the age of the highest sample situated below the reversal, Minimum – the age of the lowest sample situated above the reversal, Average – the age of the reversal assumed, defined as a point situated halfway between consecutive samples showing opposite polarity

calculated ages for the upper and lower limit of the uncertain polarity intervals separating normally and reversely magnetized zones, with the fourth column of the table giving the age of the magnetic reversal assumed to be located halfway between consecutive samples showing opposite polarity. Although the stratigraphic position of most reversals could not be constrained to better than ± 1 m, this does not appear to have a significant impact on calculated reversal ages, because due to the high sedimentation rate of the White River Group, ages derived for consecutive samples of opposite polarity are statistically indistinguishable at the 95% confidence level.

4.6 Discussion

The revised magnetic polarity pattern of the Flagstaff Rim and Toadstool Park sections, combined with the high-precision $^{206}Pb/^{238}U$ geochronology and associated age-depth models developed at these two localities (Chapter 3) yields a fully integrated and highly-resolved chronostratigraphic framework for the Late Eocene and Early Oligocene

(36-31 Ma). The implications of this data-set for the numerical age calibration of the GPTS are discussed below, through comparison with other recent time scale calibration efforts (Figure 4.11, Table 4.3).

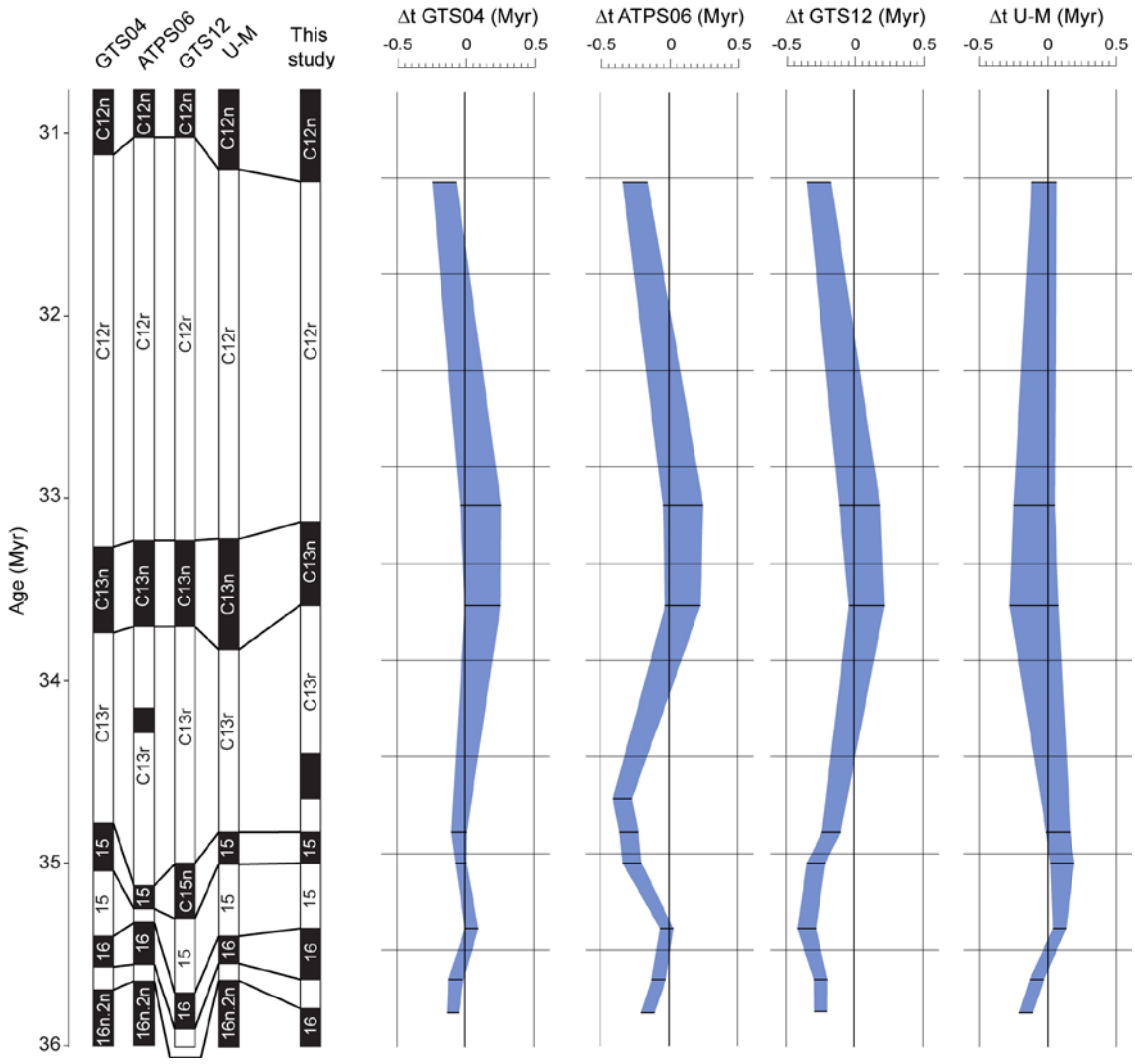

Figure 4.11 Comparison between interpolated magnetic reversal dates from the Flagstaff Rim and Toadstool Park sections and recent editions of the geomagnetic polarity time scale. GTS04 – Ogg and Smith (2004), ATPS06 – astronomically tuned time scale from ODP Site 1218 (Pälike et al., 2006), GTS12 – Vandenberghe et al. (2012), U-M – $^{206}Pb/^{238}U$ calibrated chronostratigraphic framework of the Umbria – Marche succession (Chapter 2). Positive (negative) values indicate that reversal ages from the WRG sedimentary succession are older (younger) than the respective time scales.

4.6.1 The 2004 Geological Time Scale

With the exception of the base of chron C12n, and the top of chron C16n.2n, magnetic reversal dates extracted from the GPTS of Ogg and Smith (2004) fall within the 2σ uncertainties of chron boundary ages calculated in this study. This is somewhat surprising, given that the numerical age calibration of the GPTS of Ogg and Smith (2004) is based on $^{40}Ar/^{39}Ar$ dates calculated relative to a FCs age of 28.02 Ma (Renne et al., 1998). Recent experiments seeking to improve the accuracy of the $^{40}Ar/^{39}Ar$ system do not support an FCs age that is significantly younger than 28.20 Ma (Kuiper et al., 2008; Renne et al., 2010; Rivera et al., 2011), and these revised values have been shown to generate $^{40}Ar/^{39}Ar$ dates that are statistically equivalent to $^{206}Pb/^{238}U$ dates of co-genetic zircons (Smith et al., 2010; Renne et al., 2013; Sageman et al., in press; Macho et al., in-review). As a result, we would expect chron boundary ages from the GPTS of Ogg and Smith to be ca. 250 kyr younger than those from our study. The observed agreement between the two data sets is likely the result of a fortuitous coincidence, in that Ogg and Smith (2004) used a tie-point calibrated to the base of magnetochron C15n, with an age

Chron (base)	This study	GTS04	ATPS06	GTS12	Umbria-Marche
C12n	31.266 ± 0.092	31.12	31.02	31.03	31.234 ± 0.089
C12r	33.130 ± 0.158	33.27	33.23	33.16	33.030 ± 0.073
C13n	33.590 ± 0.134	33.74	33.71	33.71	33.728 ± 0.137
C13r.1n	34.647 ± 0.066	-	34.29	-	-
C13r	34.834 ± 0.066	34.78	35.13	35.00	34.907 ± 0.054
C15n	34.998 ± 0.076	35.04	35.25	35.29	35.108 ± 0.052
C15r	35.355 ± 0.046	35.40	35.33	35.71	35.439 ± 0.044
C16n.1n	35.636 ± 0.058	34.57	35.55	35.89	35.542 ± 0.050
C16n.1r	35.799 ± 0.052	35.71	35.64	36.05	35.645 ± 0.057

Table 4.3 Comparison between interpolated magnetic reversal ages and published geomagnetic polarity time scales. GTS04 = Ogg and Smith et al. (2004), ATPS06 = Pälike et al. (2006), GTS12 = Vandenberghe et al. (2012), Umbria - Marche - Chapter 2

of 35.20 ± 0.27 Ma, which is statistically equivalent to the age calculated in this study (35.001 ± 0.076). However, the numerical age of this tie-point is based on a compilation of legacy $^{40}Ar/^{39}Ar$ dates from the Umbria-Marche basin and the WRG, which have been shown to be inaccurate (Chapters 2 and 3).

4.6.2 ATPS06

Interpolated ages for the upper and lower boundaries of C13n, and C16n.1n at Flagstaff Rim are in agreement with the astronomically tuned time scale of Pälike et al. (2006), while the base and top of C15n are ca 250 kyr younger than reported from ODP Site 1218. These findings indicate that although the tuning of the Late Eocene part of the ODP Site 1218 record was hampered by low $CaCO_3$ content, correlation to the 405 kyr eccentricity cycle is correct at least as far back as 36 Ma, a conclusion that is also supported by the $^{206}Pb/^{238}U$ calibrated marine record of the Umbria-Marche succession (Chapter 2). The observed discrepancy may be due to inconsistencies in the tuning of higher frequency cycles (e.g. 100 kyr eccentricity, obliquity, precession) or errors in the magnetic polarity record or composite depth scale of the ODP 1218 succession.

4.6.3 The 2012 Geological Time Scale

The radio-isotopically calibrated Paleogene age model of Vandenberghe et al. (2012) relies on legacy $^{40}Ar/^{39}Ar$ dates from the Italian Umbria-Marche succession, which have been shown to be anomalously old by 0.4-0.5 Myr (Chapter 2), and therefore is not considered further here. Magnetic reversal ages from this study are up to 350 kyr younger than those from the astronomically tuned age model of GTS12. Because a complete tuning of the Late Eocene is yet to be achieved, Vandenberghe et al. (2012) relied on interpolation relative to the reference profile of Cande and Kent (1992) using a 6th order

polynomial, and two astronomically tuned tie-points: an age of 33.71 Ma for the base of chron C13n, based on the ODP Site 1218 tuning of Pälike et al. (2006), and an age of 47.8 Ma for the base of C21n based on the ODP Site 1258 tuning of Westerhold and Rohl (2009). The accuracy of the younger tie-point is verified by this study, and the $^{206}Pb/^{238}U$ calibrated magnetic polarity record of the Umbria-Marche succession (Chapter 2), which implies that the discrepancy between the two age models is the result of inaccuracy of the age used for the base of C21n. This may result from an error in either the tuning or the magnetic polarity pattern of the ODP Site 1258 record, with the latter option supported by the fact that the relative durations of magnetochrons C23n.2n and C23n (1:1) at this locality are not consistent with that reported in the magnetic anomaly profile of Cande and Kent (1992) (1:2), which implies the possibility of a 400-500 kyr hiatus (Vandenberghe et al., 2012).

4.6.4 The $^{206}Pb/^{238}U$ calibrated magnetic polarity record of the Umbria-Marche basin

Based on the data presented in Table 4.3, $^{206}Pb/^{238}U$ calibrated magnetic reversal ages from the Umbria-Marche sedimentary succession (Chapter 2) and the WRG are statistically equivalent at the 2σ level. However, uncertainties quoted in Table 4.3 include systematic components related to the $^{206}Pb/^{238}U$ zircon CA-ID-TIMS weighted mean ages that underpin the respective age-depth models developed in Chapters 2 and 3 (i.e. the calibration of the ET535 isotopic tracer, and the ^{238}U decay constant). When the two data sets are considered at the level of the analytical uncertainty of the $^{206}Pb/^{238}U$ dates alone, as is done in Figure 4.11, small discrepancies on the order of 20-70 kyr become apparent for magnetic reversals between the top of chron C16n.2n and the base of C15n. Such inconsistencies may arise from uncertainties related to the stratigraphic position of individual magnetic reversals, or short term fluctuations in sedimentation rate that

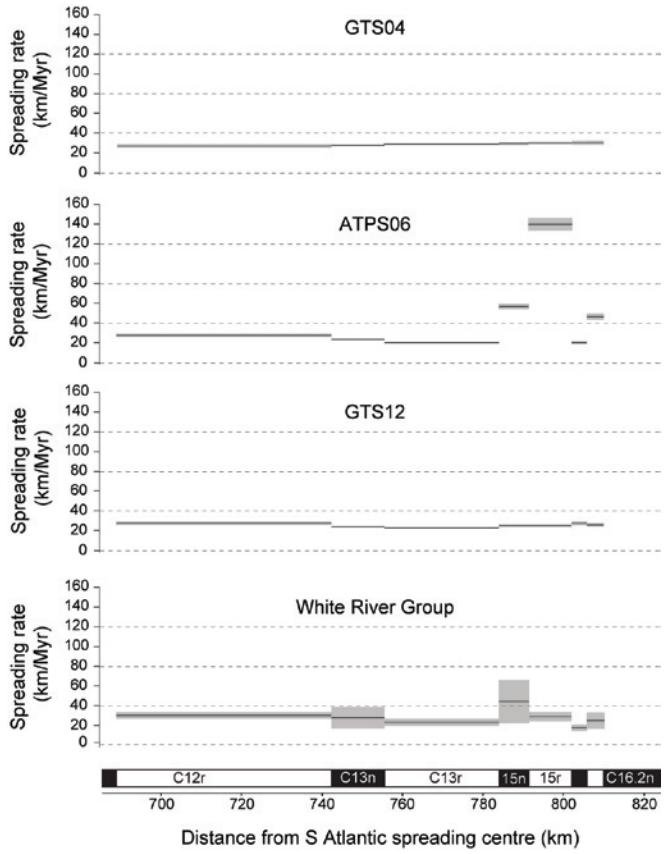

Figure 4.12 Sea floor spreading rates between 31-36 Ma. Uncertainty envelopes represent the uncertainty on the width of individual polarity zones as determined by Cande and Kent (1992) except for the White River Group, where they include age uncertainties added in quadrature. GTS04 – Ogg and Smith (2004), ATPS06 – Pälike et al. (2006), GTS12 – astronomically calibrated Paleogene age model of Vandenberghe et al. (2012)

were not accurately captured by the age-depth models developed in Chapters 2 and 3. Our data indicate that, given the high sedimentation rate that characterizes the lower part of the Flagstaff Rim section (ca. 150 m/Myr), uncertainties related to the stratigraphic position of these reversals (Table 4.2) amount to ca. 10-40 kyr, and may, at least in part, explain the observed discrepancies. The calibration of the C16n.2n – C15n interval in the Umbria-Marche basin (Chapter 2) relies on the magnetic polarity pattern published by Jovane et al. (2007) for the Massignano section. Although the authors did not explicitly discuss uncertainties related to the stratigraphic position of identified magnetic reversals, the resolution and quality of their data (Figure 1 in Jovane et al., 2007) indicate that such

uncertainties are likely to be slightly higher than in the WRG record, on the order of 20-100 kyr.

No normal polarity subchron, with duration comparable to that of the C13n.1n interval reported from Flagstaff Rim has been identified in the magnetic polarity pattern of the Massignano and Monte Cagnero sections. At Massigano, based on the age-depth models developed in Chapters 2, and 3, such a subchron would be expected to occur ca. 13.5-15.5 m above the base of the section. In the relatively low resolution (50-70 kyr) datasets of Bice and Montanari (1988) and Lowrie and Lanci (1994) this interval is represented by five, and respectively two reversed polarity samples, while the higher-resolution (15 kyr) record of Jovane et al. (2007) only covers the lowermost 13 m of the section. At Monte Cagnero, Jovane et al. (2013) identified a normal polarity zone between metre levels 102.25-106.10 of their measured section, which they assigned to magnetochron C15n, and this correlation underpins the age depth model developed for the Monte Cagnero record in Chapter 2. An assessment of whether this correlation of the Monte Cagnero magnetic polarity pattern to the GPTS is accurate would require a clear identification of normal and reversed magnetic polarity subchrons corresponding to C16n, particularly the long (>1 Myr) C16n.2n subchron in the Monte Cagnero record, however this was precluded by the poor magnetic quality of the samples collected by Jovane et al. (2013) from this interval. Correlating the 102.25-106.10 m normal polarity zone from Monte Cagnero to C13n.1n instead of C15n would eliminate the discrepancy between the radio-isotopically calibrated age-depth model developed for this section in Chapter 2, and the astronomical tuning of Hyland et al. (2009), however it would also imply an age of 33.684 ± 0.128 Ma for the Eocene – Oligocene boundary defined as the last occurrence of hantkeninids at Monte Cagnero, 400 kyr younger than suggested by the age-depth model developed for the Massignano section (Chapter 2). In summary, further studies may be necessary to provide a conclusive answer regarding the presence/absence

of a normal polarity subchron within C13r in the Umbria-marche record, by extending the high resolution mangetic polarity record of the Massignano section, and/or radio-isotopic dating of biotite-rich layers from the Late Eocene part of the Monte Cagnero section.

Aside from the presence/absence of the C13n.1n subchron, the overall consistency of the WRG and Umbria-Marche age models indicates that these studies provide a robust calibration of the Late Eocene – Early Oligocene GPTS. Because the temporal resolution of the WRG magnetic polarity pattern (10-20 kyr) is overall higher than that of published polarity records from the Umbria – Marche basin considered in Chapter 2 (20-70 kyr, Jovane et al., 2007; Hyland et al., 2009), we infer that magnetic reversal ages from this study are likely to be more accurate than those derived from the $^{206}Pb/^{238}U$ calibrated age-depth models of the Massignano and Monte Cagnero sections (Chapter 2).

4.5.2 Implications for Late Eocene – Oligocene seafloor spreading rates

The synthetic marine magnetic anomaly profile of Cande and Kent (1992) represents the standard for the magnetic polarity history of the Cenozoic and Late Cretaceous, and the assumption of smoothly varying seafloor spreading rates along this profile is one of the fundamental elements of GPTS calibration through the use of radio-isotopically dated tie-points. Although small deviations from this smooth spreading rate model cannot be ruled out (Huestis and Acton, 1997; Agrinier et al., 1999), large jumps of over 50% in spreading rate are unlikely (Ogg, 2012). Figure 4.12 shows spreading rates derived from the radio-isotopically calibrated GPTS of GTS04 (Ogg and Smith 2004), ATPS06 (Pälike et al., 2006), the astronomically calibrated age model of GTS12 (Vandenberghe et al., 2012), and interpolated magnetic reversal ages from the Flagstaff Rim and Toadstool Park sections. The GTS04 and GTS12 age models, which rely fully and respectively partially on calibration of the Cande and Kent (1992) anomaly profile using radio-isotopic dates

and respectively astronomically tuned ages show relatively constant spreading rates between 31-36 Ma. In contrast, the astronomically tuned time scale of Pälike et al. (2006) shows significant changes in spreading rates at the level of chrons 15 and 16. A similar behaviour has been reported for astronomically tuned time scales of the Neogene, and was attributed to the fact that astronomical tuning provides independent age estimates for each chron boundary, and for short magnetochrons, even small errors in tuning (on the order of 10 kyr) can result in large shifts in apparent spreading rates (Ogg, 2012) when plotted against the Cande and Kent (1992) anomaly profile. Interpolated magnetic reversal dates from Flagstaff Rim and Toadstool Park appear to be consistent with relatively constant sea-floor spreading rate models but small variations do occur between 35-36 Myr. It is unclear whether these variations represent actual changes in spreading rates, or if they are an indication that the uncertainties of either our interpolated magnetic reversal ages, or the widths of individual polarity zones in the profile of Cande and Kent (1992) have been underestimated.

4.7 Conclusions

The revised magnetic polarity and $^{206}Pb/^{238}U$ geochronology of the White River Group provides a fully integrated and highly resolved chronostratigraphic framework for the Eocene – Oligocene transition. The robustness of this time scale is supported by the mutual consistency of interpolated magnetic reversal dates from the Flagstaff Rim and Toadstool Park sections and the marine record of the Umbria-Marche basin, and its compatibility with smoothly varying sea-floor spreading rate models. The data indicate that the tuning of ODP Site 1218 to the 405 kyr eccentricity signal is correct, at least as far back as 36 Ma, however discrepancies of up to 300 kyr relative to the astronomically tuned age model in GTS12 may indicate an inconsistency in the floating astronchronology of the Early-Mid Eocene.

5. Geochronology and chronostratigraphy of the Eocene-Oligocene transition

5.1 Introduction

A deep understanding of the Eocene-Oligocene greenhouse-icehouse transition and associated biotic response is based on the regional and global integration and correlations of disparate sedimentary successions. As environmental change across the Eocene – Oligocene transition (EOT) was relatively fast, with the development of a continent scale Antarctic ice sheet estimated to have taken place over less than 300 kyr (Coxall et al., 2005), accurate and highly-resolved time scales are essential to such correlation efforts. However, the accuracy and precision of established Eocene – Oligocene time scales is called into question by the mutual inconsistency of radio-isotopically calibrated and astronomically tuned age models for this interval. This is exemplified by the 2012 edition of the Geological Time Scale (GTS12) where a dual approach was outlined, with both radio-isotopically calibrated (mostly $^{40}Ar/^{39}Ar$ relative to an age of 28.201 Ma for the Fish Canyon sanidine) and astronomically tuned age models presented for the Paleogene. Discrepancies of up to 600 kyr were reported between the two calibration options between 26-36 Ma (Vandenberghe et al., 2012).

The accuracy and precision of the Paleogene time scale is determined by the accuracy and precision of the underlying numerical dating methods. Following recent revisions of the age of the Fish Canyon sanidine (Kuiper et al., 2008; Renne et al., 2010; Rivera et al., 2011) and the ^{40}K decay constant (Min et al., 2010; Renne et al., 2010) the potential accuracy of the $^{40}Ar/^{39}Ar$ technique approaches ± 0.25%, however legacy biotite $^{40}Ar/^{39}Ar$ data on which the calibration of the EOT was based in GTS12 are of

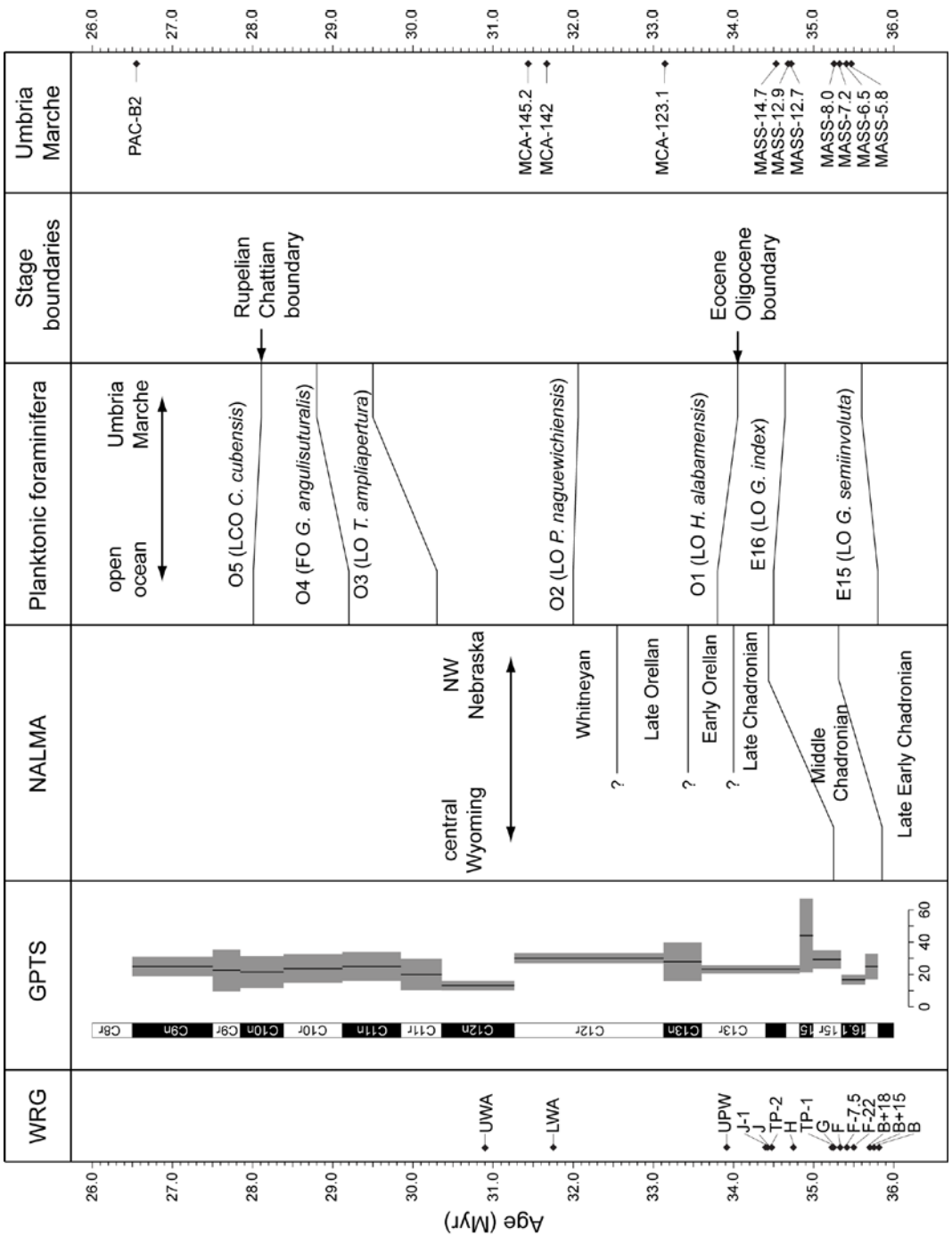

Figure 5.1 Chronostratigraphic framework developed for the Late Eocene and Oligocene on the basis of $^{206}Pb/^{238}U$ dating of volcanic tuffs from the Umbria-Marche basin and the White River Group, and integration with new and established magnetostratigraphic and biostratigraphic records (mammals, planktonic foraminifera).

lower precision (ca. ± 0.6%, Odin et al., 1991a, 1991b), with the resulting time-scale having a precision on the order of ± 1.4 % (Vandenberghe et al., 2012). Astronomical tuning of marine records recovered through ODP and IODP expeditions generates time scales that are in principle more precise than those calibrated using radio-isotopic dating methods, with Laskar et al. (2004) estimating the precision of their numerical solution at ca. 0.1% over the last 40 Myr. However, given the method's reliance on the assumption of complete and accurate cycle expression and identification, the accuracy of astronomically tuned time scales is difficult to verify without independent corroboration through radio-isotopic dating.

Twenty three high-precision/accuracy (< 0.2% total uncertainty) weighted mean $^{206}Pb/^{238}U$ (zircon) CA-ID-TIMS dates were obtained on volcanic tuff samples from key Late Eocene – Oligocene marine successions in Italy (Massignano and Monte Cagnero, Umbria-Marche basin, Chapter 2), and coeval terrestrial strata in North America (Flagstaff Rim, and Toadstool Park, White River Group, Chapter 3). The accuracy of these dates is supported by the gravimetric calibration of the ET535 isotopic tracer solution (Condon et al., in review; McLean et al., in review), and the determination of the ^{238}U decay constant through counting experiments (Jaffey et al., 1971). When integrated with existing and revised biostratigraphic (Coccioni et al., 1988, 2008; Emry, 1992; Prothero and Emry, 1996; Prothero and Whittlesey, 1998; Hyland et al., 2009; Jovane et al., 2013), and magnetostratigraphic data sets (Jovane et al., 2007, 2013; Coccioni et al., 2008; Hyland et al., 2009; Chapter 4) from the respective localities, these data form the basis of a fully integrated and highly-resolved chronostratigraphic framework for the Eocene – Oligocene transition (Figure 5.1).

5.2 Integrated radio-isotopic, astronomical and magnetic reversal time scales for the EOT

High-precision $^{206}Pb/^{238}U$ data generated in this study were used to test the accuracy of legacy $^{40}Ar/^{39}Ar$ data from volcanic tuffs intercalated in the Umbria-Marche and White River Group sedimentary successions (Swisher and Prothero, 1990; Odin et al., 1991a, 1991b; Obradovich et al., 1995), and floating astronomically tuned age models of the Massignano (Jovane et al., 2007; Brown et al., 2009) and Monte Cagnero sections (Hyland et al., 2009). Age-depth models developed on the basis of $^{206}Pb/^{238}U$ weighted mean ages, and where appropriate, integration with floating astronomically tuned time scales, at each of the four investigated localities were used to constrain the age of the respective biostratigraphic and magnetic polarity records (Chapters 2 and 3). In order to improve the accuracy and precision of the numerical age calibration of the Late Eocene – Early Oligocene (31-36 Ma) geomagnetic polarity time scale a revised high-resolution magnetostratigraphic record was generated for the Flagstaff Rim and Toadstool Park sections (Chapter 4).

Interpreted $^{206}Pb/^{238}U$ dates from this study are 0.4-1.0 Myr younger than legacy $^{40}Ar/^{39}Ar$ biotite and sanidine data from the same tuffs (Swisher and Prothero, 1990; Odin et al., 1991a, 1991b, Coccioni et al., 2008), recalculated relative to an age of 28.201 Ma (Kuiper et al., 2008) for the Fish Canyon sanidine neutron fluence monitor. Given the internal consistency of the U-Pb dataset, this discrepancy is attributed to the inaccuracy of legacy $^{40}Ar/^{39}Ar$ ages resulting from the nature of the analysed material (i.e. susceptibility of biotite to record anomalously old ages due to ^{39}Ar recoil phenomena and/or the incorporation of extraneous ^{40}Ar) and statistical treatment of the data (i.e. weighted mean dates based on low precision datasets biased towards older ages through the incorporation of detrital/pre-eruptive material).

The $^{206}Pb/^{238}U$ based age-depth models were used to constrain the age of magnetic polarity reversals recorded by the Umbria – Marche and White River Group sedimentary successions between 26.5-36 Ma (C8r-C16n.2n), with the aim of refining the numerical age calibration of the Late Eocene – Oligocene geomagnetic polarity time scale. Between 26.5-31 Ma (C8r-C11r interpolated magnetic reversal ages fall within uncertainty (at the 2σ level) of the astronomically tuned polarity time scale of Palike et al. (2006, ATPS06). Between 31-36 Ma, interpolated magnetic reversal ages from the overlapping Umbria-Marche and White River Group records are statistically equivalent (at the 2σ level) when uncertainties in the stratigraphic placement of individual magnetic reversals, and numerical dating are taken into consideration, and are up to 200 kyr younger than data extracted from ATPS06, and up to 350 kyr younger than the astronomically calibrated Paleogene age model of Vandenberghe et al. (2012). When plotted against the synthetic marine magnetic anomaly profile of Cande and Kent (1992), $^{206}Pb/^{238}U$ calibrated magnetic reversal dates are consistent with relatively constant Late Eocene – Oligocene seafloor spreading rates. Overall, our data verify the accuracy of the ATPS06 for the Oligocene, and indicate that although the tuning of ODP Site 1218 was hampered by a lack of carbonate proxy data below the Eocene – Oligocene boundary, correlation to the 405 kyr eccentricity cycle is correct, at least as far back as 36 Ma.

5.3 Quantifying the fidelity of bioevent-based chronostratigraphy across the EOT

Age-depth models developed for the Massignano and Monte Cagnero sections, on the basis of the $^{206}Pb/^{238}U$ ages assigned to individual volcanic 'biotite-rich' beds were used test and quantify the potential diachroneity of planktonic foraminifer bioevents, which mark zonal boundaries in the biozonation scheme of Berggren and Pearson (2005,

with revisions by Wade et al., 2011), between tropical and subtropical open ocean settings and the western Tethys. Our data indicate that some Oligocene planktonic foraminifer bioevents, namely the last occurrence (LO) of *Turborotalia ampliapertura* (base of zone O3 of Berggren and Pearson 2005), the first occurrence (FO) of *Globigerina angulisuturalis* (base of O4) and the LO of *Paragloborotalia opima* (base of O6) occur 0.4-0.8 Myr later in the western Tethys than in open ocean settings (Wade et al., 2011). Analysis of published bio-magnetostratigraphy of other Oligocene outcrops from the Umbria – Marche basin (i.e. Contessa Barbetti Road, Pieve D'Accinelli, Coccioni et al., 2008) indicates that these discrepancies represent real diachroneity, and do not arise from poor fossil preservation, reworking, or inadequate sampling resolution of deposits from the Umbria-Marche sedimentary succession.

The LO of hantkeninids, which marks the GSSP of the base of the Oligocene, and the last common occurrence of *Chiloguembelina cubensis*, frequently used as a marker for the base of the Chattian, do not appear to be time-transgressive between the western Tethys and other oceanic basins, when uncertainties in magnetostratigraphic calibration, and numerical dating are taken into account. Based on the stratigraphic position of these events at Massignano and Monte Cagnero, we calculated $^{206}Pb/^{238}U$ calibrated ages of 34.090 ± 0.074 Ma, and 28.126 ± 0.175 Ma for the Eocene-Oligocene boundary and the Rupelian-Chattian boundary respectively.

$^{206}Pb/^{238}U$ dating and age-depth modelling of the North American terrestrial record of the Eocene – Oligocene transition at Flagstaff Rim and Toadstool Park indicates that key mammal taxa used to define the subdivisions of the Chadronian North American Land Mammal Age show diachroneity on the order of 1 Myr over a distance of ca. 400 km.

These results highlight the potential pitfalls of biostratigraphic correlations that rely on only a small number of species, and which, while giving an appearance of high-precision may in fact be significantly inaccurate as a result of diachroneity, poor preservation, or inadequate sampling resolution. Recently developed quantitative biostratigraphic techniques (e.g. constrained optimization, Sadler, 2004), which are based on the integration of large amounts of biostratigraphic information are likely to yield more robust and accurate results, while sacrificing some degree of precision and stratigraphic resolution in order to accommodate the complexities of individual sedimentary successions.

5.4 Integrating marine and terrestrial records of environmental change across the EOT

While the timing and duration of the benthic foraminifer $\delta^{18}O$ shift (Oi-1event) that characterizes the marine record of the EOT is well constrained through astronomical tuning of ODP Site 1218 (Coxall et al., 2005; Palike et al., 2006), its interpretation in terms of ice-volume and temperature effects is less clear. The timing and magnitude of environmental change recorded by terrestrial records of the EOT may be used to inform the relative contribution of temperature vs. ice-growth during the Oi-1 event. While cooling on the order of 4-8˚C has been reported from both North America (Zanazzi et al., 2007, 2009) and Europe (Hren et al., 2013) in the Late Eocene – Early Oligocene, the resolution of established numerical age models for these records is not sufficient to allow an assessment of whether terrestrial cooling was synchronous to the Oi-1 event. An absence of terrestrial cooling coeval to the Oi-1 event favours the interpretation of the benthic foraminifer $\delta^{18}O$ shift as an expression of mainly ice growth, with only a subordinate temperature component (Retallack et al., 2004; Sheldon and Retallack, 2004), however this would require ice volumes that are too great to be accommodated on the Antactic

continent alone, raising the possibility of bipolar glaciation in the Early Oligocene. On the other hand, evidence of large ice sheets in the northern hemisphere prior to the Miocene remains circumstantial (Eldrett et al., 2007), while relatively shallow marine Mg/Ca data (above CCD), and alkenone unsaturation index data from high-latitudes are consistent with a 2.5-5˚C drop in sea surface temperatures across the EOT (Lear et al., 2008; Liu et al., 2009).

The high-precision $^{206}Pb/^{238}U$ zircon weighted mean age data set and associated age depth models presented in Chapter 3, allow us to temporally constrain the palaeoclimatic record of the White River Group. Long-term environmental change recorded by the White River Group appears to be time transgressive, as aridification, expressed by a shift from fluvial to eolian sedimentation, progressed gradually from west to east occurring ca. 1.8 Myr later at Toadstool Park than at Flagstaff Rim (distance between the two localities is ca. 400 km). Based on our data, abrupt cooling, on the order of 7.1 ± 3.1˚C, inferred by Zanazzi et al. (2007, 2009) to take place in the Early Orellan based on fossil bone and tooth $\delta^{18}O$ data from Toadstool Park is synchronous to the marine Oi-1 event which records Early Oligocene glaciation of Antarctica. Progress in the numerical age calibration of the N American terrestrial record implies that the discussion on the interpretation of the Oi-1 event in terms of ice-growth vs. cooling, on the basis of comparison between coeval marine and terrestrial records, is now limited by the uncertainty of the terrestrial proxy record, rather than time scale inaccuracy.

Appendix A. Radio-isotopic (U-Pb, zircon) dating methods and results

Outlined in this appendix are the protocols and methods used for $^{206}Pb/^{238}U$ dating of zircons at the NERC Isotope Geosciences Laboratory (NIGL), British Geological Survey, UK. Single crystal zircon data from the Umbria-Marche (Chapter 2) and the White River Group (WRG, Chapter 3) sedimentary successions are listed in Table A.1, and A.3 respectively. Table A.2 lists all volcanic tuff samples from the WRG, along with coordinates of sampled localities, and a brief description of each tuff.

A.1 Heavy mineral separation.

Zircons were separated from samples weighing 1-2 kg using conventional mineral separation techniques either at NIGL or in the mineral separation laboratory of the Department of Earth and Life Sciences at the Free University of Amsterdam (VUA). Samples processed at NIGL (those discussed in Chapter 2) were soaked in water for several days and then rinsed under running water for a period of several hours to remove the clay fraction. Rinsed samples were passed over a Rogers table for an initial coarse density separation and dried overnight. Dry samples were passed across a Franz magnetic separator several times at gradually increasing current intensities of up to 1.7 A, in order to separate diamagnetic minerals. The least magnetic fraction was placed inside a separation funnel in methylene iodide at a density of ~ 3.27 g/cm^3.Sample processed at VUA (those discussed in Chapter 3) were soaked in water for several days and then passed through an automated system which allows the separation of the clay-sized fraction through repeated agitation in water followed by a period of settling. Dried samples were further separated using a centrifuge system designed for the density separation of large sample volumes (several hundreds of grams) in methylene iodide, at densities of 2.7 and 3.27 g/cm^3. The heaviest fraction was passed across a Franz magnetic separator several times at gradually

increasing current intensities of up to 3.0 A. Both separation procedures resulted in final heavy, diamagnetic fractions consisting almost exclusively of zircon.

A.2 U-Pb radio-isotopic dating methods.

A.2.1 Sample (zircon) characterisation and selection.

Euhedral, high aspect ratio zircons were hand-picked from each sample, taking care to avoid crystals containing mineral inclusions, although most of the zircons selected from the North American tuffs (Chapter 3) contained melt inclusions.

A.2.2 Chemistry and mass spectrometry.

All selected zircons were subjected to a modified version of the chemical abrasion procedure of Mattinson et al., (2005) in order to eliminate radiation damaged crystal volumes which are susceptible to open system behaviour. Zircons from each sample were placed inside a muffle furnace in a quartz dish and annealed at a temperature of 900˚C over a period of 60 h. Selected zircons were loaded into individual FEP Teflon beakers and refluxed in 4 M HNO_3 on a hotplate at 120˚C over several hours or overnight and then ultrasonically cleaned for 20 minutes. Single zircon crystals were rinsed in acetone and 4 M HNO_3, loaded into 300 µl FEP Teflon microcapsules, and leached in 29 M HF, inside a self-sealing stainless steel jacket (Parr vessel) for 10-12 hours at 180˚C. Microcapsules containing leached zircons were rinsed with 6 M HCl, refluxed on a hotplate at 120˚C for 2-5 hours, and rinsed with 4 M HNO_3.

All leached zircons and accompanying total procedural blanks were spiked with the mixed ^{205}Pb-^{233}U-^{235}U (ET535) or ^{202}Pb-^{205}Pb-^{233}U-^{235}U (ET2535) EARTHTIME tracer solution and dissolved in ca. 150 µl 29 M HF and trace HNO_3 in a Parr vessel at 220˚C

over 60 hours. Complete dissolution of samples was assumed on the basis of previous experience with larger low-U zircon grains were the efficacy of these dissolution protocols (temperature and duration) could be verified by visual inspection. Dissolved samples were dried down as fluorides and re-dissolved in 3M HCl, in Parr vessels, overnight, at 180˚C. U and Pb were isolated using a HCl based anion exchange procedure using Teflon columns and Bio-Rad AG-1 resin. The recombined U and Pb fractions were dried down along with 10 µl of H_3PO_4. Dried samples were loaded on a Re filament in a silica gel matrix in order to enhance ionization (Gerstenberger and Haase, 1997)

Isotope ratio measurements were made using a Thermo-Electron Triton thermal ionization mass-spectrometer. Pb was measured in dynamic mode on a MassCom SEM detector and was corrected using a fractionation factor of 0.14 ± 0.02 %/amu (1σ) for samples prepared using the ET535 spike, and was corrected in real-time based on the measured $^{202}Pb/^{205}Pb$ ratio for samples spiked with the ET2535 tracer. Linearity and dead time corrections on the SEM were monitored using repeated analysis of the NBS 982, NBS 981 and U 500 standards. U was run as an oxide (UO_2), and corrected for isobaric interferences using a $^{18}O/^{16}O$ value of 0.00205 (IUPAC value, also determined through direct measurement at NIGL). U beams were measured either in static mode, on Faraday detectors equipped with 10^{12} Ω resistors for intensities greater than 4 mV, or in dynamic mode for lower intensities. U mass fractionation was calculated in real-time based on the isotopic composition of the ET535 and ET2535 tracers.

A.2.3 Data Reduction and Archiving.

Data reduction was carried out using the Tripoli program (Bowring et al., 2011) to filter raw U and Pb data. U-Pb_Redux was used to calculate dates and propagate random and systematic uncertainties based on the algorithms of McLean et al., (2011) using the U decay constants of Jaffey et al., (1971) and the $^{238}U/^{235}U$ ratio of Hiess et al. (2012).

Individual analyses contained between 0.3-2.5 pg common lead, all of which was attributed to laboratory blank and subtracted based on a common Pb isotopic composition of $^{206}Pb/^{204}Pb=18.20 \pm 0.50\%$, $^{207}Pb/^{204}Pb = 15.65 \pm 0.40\%$ and $^{208}Pb/^{204}Pb = 38.02 \pm 0.75\%$ (1σ uncertainties) . $^{206}Pb/^{238}U$ dates were corrected for initial ^{230}Th disequilibrium using a value of Th/U[magma]=2.8 ± 0.5 resulting in a increase of ca. 100 kyr for individual dates. U blanks were assumed to be 0.1 ± 0.01 pg (1σ).

All U-Pb radio-isotopic data that are presented in this thesis have been archived using the EARTHCHEM/EARTHTIME Geochron data base (Bowring et al., 2011).

A.3 Note on Tables A.1 and A.3

This section details the annotations used in tables A.1 and A.3:

- (a) isotopic date orrected for initial Th/U disequilibrium using radiogenic ^{208}Pb and Th/U[magma] = 2.80000.
- (b) Isotopic dates calculated using the decay constants $\lambda^{238} = 1.55125^{-10}$ and $\lambda^{235} = 9.8485^{-10}$ (Jaffey et al. 1971).
- (c) % discordance = 100 - (100 * ($^{206}Pb/^{238}U$ date) / ($^{207}Pb/^{206}Pb$ date))
- (d) Th contents calculated from radiogenic ^{208}Pb and the $^{207}Pb/^{206}Pb$ date of the sample, assuming concordance between U-Th and Pb systems.
- (e) Total mass of radiogenic Pb.
- (f) Total mass of common Pb.
- (g) Ratio of radiogenic Pb (including ^{208}Pb) to common Pb.
- (h) Measured ratio corrected for fractionation and spike contribution only.
- (i) Measured ratios corrected for fractionation, tracer and blank.

Fraction	Dates (Ma) $^{206}Pb/^{238}U$ (a)	±2σ abs	$^{207}Pb/^{235}U$ (b)	±2σ abs	$^{207}Pb/^{206}Pb$ (b)	±2σ abs	Pb* (pg) (e)	Pbc (pg) (f)	Pb*/Pbc (g)	Isotopic Ratios $^{206}Pb/^{204}Pb$ (h)	$^{206}Pb/^{238}U$ (i)	±2σ %	$^{207}Pb/^{235}U$ (i)	±2σ %	$^{207}Pb/^{206}Pb$ (i)	±2σ %	Corr. coef.	% disc (c)	Th/U (d)
PAC-B2																			
z1	26.458	0.206	25.438	1.898	-62.5	172.0	2.15	2.51	0.9	67	0.004100	0.79	0.025369	0.04	7.05143	7.55	0.670	142	0.73
z6	**26.533**	**0.049**	26.202	0.386	3.4	31.8	1.25	0.24	5.2	319	0.004112	0.18	0.026141	0.05	1.32036	1.49	0.954	-683	0.69
z7	**26.544**	**0.035**	26.395	0.352	20.3	31.0	1.59	0.28	5.7	350	0.004113	0.13	0.026336	0.05	1.28932	1.35	0.534	-30	0.68
z9	**26.574**	**0.050**	26.188	0.374	-1.8	30.8	1.43	0.26	5.4	328	0.004118	0.19	0.026127	0.05	1.27584	1.45	0.934	1594	0.74
z4	**26.584**	**0.065**	26.994	0.811	71.2	67.5	0.90	0.44	2.1	137	0.004119	0.25	0.026942	0.05	2.83829	3.05	0.853	63	0.66
z8	**26.589**	**0.098**	25.533	1.299	-65.4	118.7	1.67	1.39	1.2	87	0.004121	0.37	0.025465	0.04	4.86444	5.15	0.789	141	0.73
z2	26.640	0.032	26.934	0.387	60.6	32.7	2.27	0.47	4.8	296	0.004128	0.12	0.026881	0.05	1.37215	1.46	0.738	56	0.68
z5	27.927	0.689	29.919	10.424	199.3	769.5	0.87	6.39	0.1	26	0.004330	2.51	0.029904	0.05	33.13118	35.36	0.896	86	0.84
z3	33.545	0.105	34.111	1.448	79.8	96.6	1.13	0.77	1.5	101	0.005205	0.31	0.034165	0.05	4.06707	4.32	0.804	58	0.73
MCA-145.2																			
z2	**31.425**	**0.078**	32.373	1.109	108.8	77.4	0.84	0.40	2.1	132	0.004875	0.25	0.032397	0.05	3.27663	3.48	0.833	71	0.92
z5	**31.440**	**0.075**	30.900	0.927	-3.8	68.8	1.69	0.89	1.9	135	0.004875	0.24	0.030899	0.05	2.85027	3.05	0.830	920	0.44
z4	31.461	0.156	31.116	2.329	10.3	172.2	1.26	1.76	0.7	57	0.004881	0.50	0.031119	0.05	7.15673	7.60	0.891	-206	0.90
z3	**31.472**	**0.096**	31.261	1.383	20.9	101.6	0.94	0.71	1.3	91	0.004882	0.31	0.031266	0.05	4.23303	4.49	0.854	-50	0.84
MCA-142																			
z3	31.206	0.053	31.168	0.344	35.7	25.7	28.97	3.26	8.9	586	0.004838	0.17	0.031172	0.05	1.07249	1.12	0.359	13	0.32
z8	31.566	0.170	32.472	2.782	107.4	194.8	2.21	2.33	1.0	80	0.004893	0.55	0.032496	0.05	8.24550	8.70	0.849	71	0.26
z1a	**31.662**	**0.018**	31.744	0.129	45.1	9.1	6.31	0.51	12.4	798	0.004909	0.05	0.031757	0.05	0.38085	0.41	0.649	30	0.38
z2a	**31.681**	**0.033**	31.621	0.260	34.4	18.5	2.51	0.33	7.6	504	0.004912	0.10	0.031632	0.05	0.77208	0.83	0.631	8	0.32
z5a	**31.687**	**0.051**	30.769	0.453	-32.6	33.6	1.59	0.39	4.0	285	0.004912	0.16	0.030766	0.05	1.38560	1.50	0.710	197	0.20
z10	**31.697**	**0.095**	31.433	1.170	18.6	84.8	5.46	2.59	2.1	152	0.004914	0.30	0.031441	0.05	3.52984	3.78	0.839	-70	0.34
z1	35.364	0.052	36.702	0.495	131.8	30.6	11.41	2.62	4.4	304	0.005485	0.15	0.036807	0.05	1.29970	1.37	0.540	73	0.20
z6	44.593	0.042	47.005	0.316	177.1	14.7	8.69	0.92	9.4	641	0.006926	0.09	0.047381	0.05	0.63017	0.69	0.648	75	0.19
z9	132.826	0.130	338.315	0.460	2200.5	2.3	38.91	0.76	51.4	3172	0.020802	0.10	0.395412	0.14	0.13259	0.16	0.556	94	0.17
MASS-14.7																			
z2	34.432	0.049	34.263	0.561	29.3	37.2	4.46	1.43	3.1	212	0.005340	0.14	0.034320	0.05	1.55063	1.66	0.809	-17	0.40
z11	**34.511**	**0.035**	34.665	0.188	52.4	11.9	7.84	0.64	12.3	816	0.005352	0.10	0.034730	0.05	0.49885	0.55	0.580	34	0.26
z3	**34.557**	**0.061**	35.490	0.975	106.1	62.9	10.80	4.42	2.4	176	0.005359	0.18	0.035570	0.05	2.66339	2.80	0.763	68	0.26
z8	**34.564**	**0.042**	33.963	0.487	-1.2	32.8	3.15	0.56	5.6	382	0.005360	0.12	0.034014	0.05	1.35916	1.46	0.836	2874	0.26
z10	34.662	0.059	34.088	0.342	1.1	23.1	4.49	0.68	6.6	456	0.005375	0.17	0.034142	0.05	0.95747	1.02	0.443	-3152	0.20
z15	34.670	0.066	34.616	0.720	37.9	47.6	2.54	1.14	2.2	162	0.005377	0.19	0.034679	0.05	1.98847	2.11	0.680	9	0.29
z13	34.688	0.029	34.648	0.119	38.5	7.4	10.31	0.38	26.9	1670	0.005381	0.08	0.034712	0.05	0.30748	0.35	0.603	10	0.46
z12	36.889	0.032	37.119	0.258	58.8	16.0	5.33	0.58	9.2	630	0.005723	0.09	0.037233	0.05	0.66908	0.71	0.484	37	0.16
z14	37.737	0.050	38.628	0.248	100.8	14.1	8.07	1.09	7.4	508	0.005855	0.13	0.038775	0.05	0.59595	0.65	0.517	63	0.18
z4	39.408	0.035	40.947	0.185	138.2	9.6	26.52	1.73	15.3	1000	0.006116	0.09	0.041151	0.05	0.40674	0.46	0.674	72	0.29
MASS-12.7																			
z10	34.506	0.071	34.601	0.662	47.8	44.1	2.19	0.50	4.3	294	0.005352	0.21	0.034664	0.05	1.84712	1.95	0.520	28	0.33
z9	**34.702**	**0.106**	34.797	0.392	47.5	24.2	3.15	0.41	7.7	488	0.005384	0.31	0.034864	0.05	1.01173	1.15	0.547	27	0.50

Table A.1 Results of single crystal U/Pb analyses from volcanic tuffs intercalated in the Umbria - Marche sedimentary succession

	Dates (Ma)									Isotopic Ratios									
	$^{206}Pb/^{238}U$	±2σ	$^{207}Pb/^{235}U$	±2σ	$^{207}Pb/^{206}Pb$	±2σ	Pb* (pg)	Pbc (pg)	Pb*/Pbc	$^{206}Pb/^{204}Pb$	$^{206}Pb/^{238}U$		$^{207}Pb/^{235}U$		$^{207}Pb/^{206}Pb$		Corr.	% disc	Th/U
Fraction	(a)	abs	(b)	abs	(b)	abs	(e)	(f)	(g)	(h)	(i)	±2σ %	(i)	±2σ %	(i)	±2σ %	coef.	(c)	(d)
MASS-12.7 (continued)																			
z5	**34.702**	**0.055**	34.875	0.685	53.1	44.8	3.33	1.30	2.6	176	0.005383	0.16	0.034943	0.05	1.87833	2.00	0.774	35	0.44
z3	**34.711**	**0.033**	34.799	0.322	47.0	20.9	12.28	2.29	5.4	342	0.005385	0.09	0.034866	0.05	0.87574	0.94	0.737	26	0.53
z2	**34.718**	**0.045**	34.784	0.528	46.1	34.5	10.51	3.59	2.9	206	0.005385	0.13	0.034850	0.05	1.44290	1.54	0.781	25	0.29
z1	**34.723**	**0.036**	34.656	0.258	36.6	16.7	16.92	2.27	7.5	491	0.005386	0.10	0.034720	0.05	0.69692	0.76	0.623	5	0.34
z11	**34.729**	**0.099**	34.663	0.594	36.5	39.2	6.48	1.04	6.2	404	0.005387	0.29	0.034727	0.05	1.63688	1.74	0.442	5	0.41
z7	**34.747**	**0.042**	34.985	0.430	58.1	27.9	2.91	0.50	5.9	394	0.005389	0.12	0.035055	0.05	1.17046	1.25	0.676	40	0.30
z4	34.868	0.044	34.707	0.532	30.3	35.0	12.72	4.50	2.8	200	0.005408	0.13	0.034772	0.05	1.45973	1.56	0.803	-15	0.29
z6	35.120	0.045	34.807	0.613	20.0	40.5	1.01	0.33	3.0	214	0.005448	0.13	0.034874	0.05	1.68541	1.79	0.826	-75	0.26
MASS-8.0																			
z7	**35.255**	**0.110**	34.737	1.275	4.9	84.4	8.62	4.85	1.8	123	0.005471	0.31	0.034802	0.05	3.50461	3.73	0.746	-625	0.61
z8a	**35.258**	**0.062**	35.667	0.309	69.4	18.4	8.08	0.75	10.8	677	0.005470	0.18	0.035751	0.05	0.77241	0.88	0.680	49	0.47
z2	**35.260**	**0.040**	35.497	0.215	56.7	12.5	27.73	0.86	32.4	1818	0.005473	0.11	0.035578	0.05	0.52520	0.62	0.859	38	0.84
z3	**35.267**	**0.028**	35.370	0.136	48.1	8.3	15.00	0.81	18.6	1115	0.005473	0.08	0.035448	0.05	0.34826	0.39	0.630	27	0.61
z10a	**35.288**	**0.103**	34.897	1.306	14.3	86.2	7.54	3.50	2.2	150	0.005475	0.30	0.034966	0.05	3.58763	3.81	0.765	-146	0.46
z11a	35.366	0.064	34.902	0.571	9.2	37.4	10.12	2.85	3.6	234	0.005487	0.18	0.034971	0.05	1.55587	1.66	0.635	-284	0.51
z10	35.422	0.039	35.310	0.231	34.0	14.1	7.45	0.62	12.1	765	0.005496	0.11	0.035387	0.05	0.58838	0.67	0.749	-4	0.43
z1	35.483	0.033	35.621	0.141	51.0	8.7	10.85	0.35	31.3	1935	0.005505	0.09	0.035704	0.05	0.36549	0.40	0.507	31	0.47
z4	35.492	0.058	35.008	0.316	8.2	20.0	10.02	1.46	6.9	445	0.005506	0.16	0.035079	0.05	0.83242	0.92	0.580	-332	0.41
z9	35.494	0.047	35.441	0.313	37.7	20.0	11.72	1.82	6.4	399	0.005508	0.13	0.035520	0.05	0.83421	0.90	0.540	6	0.59
z7a	35.501	0.088	34.963	1.079	4.4	71.9	4.81	2.46	2.0	138	0.005508	0.25	0.035033	0.05	2.98628	3.14	0.637	-712	0.45
z11	35.526	0.051	35.525	0.289	39.7	17.6	10.82	1.03	10.5	558	0.005516	0.14	0.035606	0.05	0.73490	0.83	0.717	11	1.16
MASS-7.2																			
z4	35.171	0.433	37.777	6.786	212.6	401.3	4.53	17.40	0.3	34	0.005457	1.25	0.037905	0.05	17.32092	18.30	0.798	83	0.49
z8a	**35.251**	**0.080**	35.690	1.036	71.3	65.9	4.24	1.42	3.0	197	0.005470	0.23	0.035774	0.05	2.77201	2.95	0.815	51	0.54
z6a	**35.297**	**0.088**	34.861	0.561	9.4	36.3	5.56	1.33	4.2	236	0.005480	0.25	0.034929	0.05	1.50733	1.64	0.581	-275	1.11
z7a	35.314	0.165	33.625	2.370	-79.5	165.4	2.13	2.97	0.7	61	0.005480	0.47	0.033670	0.04	6.75972	7.17	0.866	144	0.61
z5a	**35.320**	**0.126**	32.958	1.848	-129.7	134.1	2.55	2.29	1.1	86	0.005480	0.36	0.032991	0.04	5.42567	5.70	0.774	127	0.48
z9a	**35.346**	**0.091**	34.407	1.007	-24.0	67.8	3.29	1.75	1.9	139	0.005483	0.26	0.034466	0.05	2.79803	2.98	0.711	247	0.30
z7	**35.348**	**0.049**	35.222	0.255	33.3	15.9	6.45	0.91	7.1	476	0.005483	0.14	0.035297	0.05	0.66272	0.74	0.589	-6	0.27
z6	**35.382**	**0.039**	35.467	0.314	47.4	19.9	4.14	0.78	5.3	345	0.005490	0.11	0.035547	0.05	0.83372	0.90	0.653	26	0.45
z9	35.653	0.126	36.291	1.780	85.1	112.5	0.45	0.30	1.5	115	0.005531	0.36	0.036387	0.05	4.74365	4.99	0.716	58	0.33
z27	37.655	0.301	38.062	4.579	69.3	275.8	0.38	0.60	0.6	57	0.005845	0.81	0.038196	0.05	11.59214	12.26	0.834	46	0.55
MASS-6.5																			
z14	**35.373**	**0.096**	35.182	1.395	28.5	91.2	3.44	2.64	1.3	99	0.005488	0.27	0.035256	0.05	3.80433	4.04	0.851	-24	0.41
z11	**35.376**	**0.071**	34.888	0.958	7.5	63.1	3.65	1.95	1.9	131	0.005489	0.20	0.034957	0.05	2.62217	2.79	0.858	-369	0.51
z6	**35.406**	**0.025**	35.374	0.142	39.7	9.5	11.69	0.50	23.4	1504	0.005492	0.07	0.035452	0.05	0.39637	0.41	0.235	11	0.34
z9	**35.424**	**0.026**	35.242	0.164	28.7	10.4	8.98	0.48	18.8	1133	0.005497	0.07	0.035317	0.05	0.43346	0.47	0.615	-23	0.59
z10b	**35.456**	**0.076**	35.366	0.703	35.8	45.7	5.56	2.05	2.7	191	0.005500	0.21	0.035444	0.05	1.90788	2.02	0.566	1	0.32
z7	35.500	0.027	35.464	0.155	40.7	9.7	9.80	0.73	13.4	997	0.005505	0.08	0.035544	0.05	0.40381	0.44	0.584	13	-0.12

Table A.1 Results of single crystal U/Pb analyses from volcanic tuffs intercalated in the Umbria - Marche sedimentary succession (continued)

	Dates (Ma)						Isotopic Ratios												
Fraction	$^{206}Pb/^{238}U$ (a)	±2σ abs	$^{207}Pb/^{235}U$ (b)	±2σ abs	$^{207}Pb/^{206}Pb$ (b)	±2σ abs	Pb* (pg) (e)	Pbc (pg) (f)	Pb*/Pbc (g)	$^{206}Pb/^{204}Pb$ (h)	$^{206}Pb/^{238}U$ (i)	±2σ %	$^{207}Pb/^{235}U$ (i)	±2σ %	$^{207}Pb/^{206}Pb$ (i)	±2σ %	Corr. coef.	% disc (c)	Th/U (d)
MASS-6.5 (continued)																			
z8	35.501	0.024	35.321	0.155	29.5	10.2	12.10	0.74	16.4	1044	0.005508	0.07	0.035398	0.05	0.42650	0.45	0.378	-20	0.39
z10a	35.508	0.023	35.484	0.106	40.4	6.6	13.82	0.55	25.0	1604	0.005508	0.06	0.035565	0.05	0.27515	0.30	0.534	12	0.33
z13	36.208	0.038	36.316	0.344	49.1	21.6	6.69	1.01	6.6	405	0.005619	0.10	0.036414	0.05	0.90369	0.97	0.637	26	0.64
z1	37.791	0.049	38.161	0.281	67.1	16.4	11.35	1.42	8.0	499	0.005866	0.13	0.038298	0.05	0.69087	0.75	0.524	44	0.53
MASS-5.8																			
z10	**35.406**	**0.149**	36.083	1.630	87.0	101.6	1.82	1.10	1.7	114	0.005494	0.43	0.036175	0.05	4.28557	4.60	0.758	59	0.67
z9	**35.436**	**0.058**	35.563	0.762	50.3	48.9	2.51	0.99	2.5	174	0.005498	0.17	0.035645	0.05	2.04774	2.18	0.813	30	0.44
z3	**35.441**	**0.114**	34.925	1.326	6.2	87.4	2.42	1.86	1.3	102	0.005498	0.32	0.034994	0.05	3.63109	3.86	0.732	-472	0.30
z1	**35.483**	**0.053**	35.420	0.790	37.3	51.9	5.88	2.16	2.7	184	0.005505	0.15	0.035499	0.05	2.16673	2.27	0.711	5	0.48
z6	**35.488**	**0.049**	35.191	0.637	21.3	41.9	1.97	0.54	3.7	248	0.005506	0.14	0.035266	0.05	1.74521	1.84	0.723	-66	0.40
z4a	**35.499**	**0.049**	35.694	0.431	54.0	27.2	4.23	0.63	6.7	392	0.005510	0.14	0.035778	0.05	1.13792	1.23	0.702	34	0.80
z2	35.649	0.052	35.154	0.648	8.2	42.2	4.95	1.86	2.7	192	0.005530	0.15	0.035227	0.05	1.75316	1.87	0.836	-335	0.23
z7	35.895	0.079	35.577	1.142	19.6	73.9	1.08	0.59	1.8	122	0.005571	0.22	0.035659	0.05	3.07928	3.27	0.851	-83	0.74
z17	35.949	0.281	35.361	4.501	1.9	296.2	0.41	0.77	0.5	52	0.005578	0.79	0.035438	0.05	12.29161	12.95	0.844	-1823	0.39
z4b	36.370	0.159	34.787	1.959	-67.6	131.9	0.69	0.59	1.2	86	0.005645	0.44	0.034854	0.04	5.40336	5.73	0.754	154	0.68
z8	47.760	0.236	58.638	3.403	532.9	121.8	0.97	1.30	0.7	61	0.007423	0.50	0.059450	0.06	5.56430	5.97	0.831	91	0.67

Table A.1 Results of single crystal U/Pb analyses from volcanic tuffs intercalated in the Umbria - Marche sedimentary succession (continued)

Table A.2 Summary and of tuff samples from the White River Group sedimentary succession. Stratigraphic positions are given in metres above the base of the respective composite sections, which are situated at 18.35 m below the B tuff at Flagstaff Rim, and 38.25 m below the Upper Purplish White Layer at Toadstool Park

Tuff	Location	m. level	Description
Upper Whitney Ash (UWA)	42˚49.929N 103˚34.781W	141.25	~50 cm thick intensely weathered light gray zone, overlying reddish brown siltstone. Sugary/granular texture with 1-2mm euhedral biotite crystals. Laterally continuous over several hundreds of metres. Sample collected from lowermost ~15 cm. Equivalent to the Upper Ash of Prothero et al., (1983) and Prothero and Swisher (1992)
Lower Whitney Ash (LWA)	42˚50.019N 103˚34.720W	115.90	~50 cm thick light gray zone. Greenish gray in fresh exposures, becomes light-gray or white upon drying. Difficult to distinguish from surrounding rock in outcrops but easily identifiable when viewed from a distance. Laterally continuous over several hundreds of metres. Sample collected from lowermost 10 cm. Equivalent to the Lower Ash in Prothero et al., (1983) and Prothero and Swisher (1992)
Serendipity (SDP)	42˚51.297N 103˚35.363W	59.72	5-15 cm thick white tuff with sharp bottom and top contacts. One sample was collected from a freshly exposed outcrop along the Big Cottonwood Creek and another from within the Toadstool Park Channel Complex where the tuff is slightly thicker and is preserved in a paleovalley back-fill within the Orella Member of the Brule Formation.
Valley of Horus (VoH)	42˚51.310N 103˚35.377W	58.57	~15 cm thick dark gray tuff with sharp top and bottom contacts. Situated within an ~ 70 cm thick interval of reddish-brown siltstone. Laterally traceable over several hundreds of metres.
Upper Purplish White Layer (UPW)	42˚51.252N 103˚35.014W	38.25	~60 cm thick white tuff, laterally traceable over long distances, possible equivalent to the Persistent White Layer in Wyoming (Larsen and Evanoff, 1998). Easily identifiable in outcrops, with sharp bottom and diffuse top contacts. In some outcrops it appears to be composed of 2 separate, but very closely spaced tuffs. Lowermost 15 cm sampled.

Table A.2 Summary and of tuff samples from the White River Group sedimentary succession. (continued)

Tuff	Location	m. level	Description
Toadstool Park 2 (TP-2)	42˚51.820N 103˚34.639W	18.45	~25 cm thick light gray tuff with diffuse bottom and top contacts. Contains root traces, burrows and 1-2 mm euhedral biotite crystals. Difficult to trace laterally. Possible equivalent to the 3rd or 4th Purplish White Layer of Schultz and Stout (1955)
Toadstool Park 1 (TP-1)	42˚51.728N 103˚34.854W	5.25	~20 cm thick light gray tuff with diffuse bottom and top contacts. Contains root traces, burrows and 1-2 mm euhedral biotite crystals. Difficult to trace laterally or identify in outcrop due to weathering. Possible equivalent to the 3rd or 4th Purplish White Layer of Schultz and Stout (1955)
J and J-1	42˚38.513N 106˚45.789W	183.32	~2 m thick interval containing two distinct white tuffs. The lower tuff (J-1) is ~ 20 cm thick and is separated from the upper tuff (J) by ~ 1 m of gray siltstone and sandstone. Separate samples collected from J-1 and the lowermost 20 cm of the upper tuff. Equivalent to ash J of Emry (1973).
I	42˚38.506N 106˚45.793W	164.72	~ 1 m thick white zone with diffuse top and bottom contacts. Contains abundant root traces and burrows. Middle 20 cm sampled. Equivalent to ash I of Emry (1973)
H	42˚38.511N 106˚45.777W	158.76	60 cm thick white tuff with diffuse top and bottom contacts. Contains burrows and root trace. Sample collected from middle 20 cm of bed. Equivalent to Ash H of Emry (1973)
G+44	42˚38.646N 106˚45.835W	141.82	35 cm thick white tuff. Contains burrows and root traces. Difficult to trace laterally due to topography. Possibly equivalent to Ash H of Prothero (1983) and Prothero and Swisher (1992)
G+25	42˚38.539N 106˚45.735W	123.19	25 cm thick white tuff. Contains burrows and root traces. Difficult to trace laterally due to topography.

Table A.2 Summary and of tuff samples from the White River Group sedimentary succession. (continued)

Tuff	Location	m. level	Description
G	42˚38.946N 106˚45.312W	97.52	80 cm thick white tuff. Contains abundant burrows and root traces. Laterally traceable over several hundreds of metres. Sample collected from lowermost 20 cm. Equivalent to Ash G of Emry (1973).
F	42˚38.671N 106˚45.687W	78.68	80 cm thick white tuff with sharp bottom and diffuse top contact. Contains abundant burrows and root traces. Laterally traceable over several hundreds of metres. Sample collected from lowermost 20 cm. Equivalent to Ash F of Emry (1973).
F-7.5	42˚38.585N 106˚45.650W	71.41	20 cm thick white tuff with diffuse top and bottom contacts. Contains burrows and root traces. Cannot be traced laterally.
F-18	42˚38.710N 106˚45.526W	60.53	~40 cm thick dark gray tuff with sharp top and basal contacts. Laterally traceable over several hundreds of metres. Possibly equivalent to Ash D or Ash E of Emry (1973). Sample collected from lowermost 20 cm.
F-22	42˚38.417N 106˚45.332W	56.19	15 cm thick dark gray tuff with sharp top and basal contacts. Laterally traceable over several hundreds of metres. Possibly equivalent to Ash D or Ash E of Emry (1973)
B+18	42˚38.404N 106˚44.942W	36.55	~20 cm thick white interval with diffuse top and basal contacts. Difficult to trace laterally due to topography.
B+15	42˚38.392N 106˚44.955W	33.55	~20 cm thick white interval with diffuse top and basal contacts. Difficult to trace laterally due to topography.
B	42˚38.360N 106˚44.951W	18.35	80 cm thick, white to light gray tuff containing euhedral biotite crystals. Laterally traceable over several hundreds of metres. Sharp basal contact with underlying sandstone bed, and diffuse transition to the overlying siltstone. Equivalent to Ash B of Emry (1973). Sample collected from the lowermost 20 cm of the tuff.

Table A.2 Summary and of tuff samples from the White River Group sedimentary succession. (continued)

Tuff	Location	m. level	Description
B-5	42˚38.367N 106˚44.961W	13.30	20 cm thick dark brown tuff containing clear biotite crystals. Previously unrecognized, difficult to trace laterally
A	42˚38.367N 106˚44.980W	9.27	20 cm thick white bed, distinguished from the surrounding rock by its lighter colour. Top and bottom contacts are not sharp with gradual transitions to the underlying and overlying siltstones. Contains root traces indicating pedogenetic modifications. Possibly equivalent to Ash A of Emry (1973)

Fraction	Dates (Ma) $^{206}Pb/^{238}U$ (a)	±2σ abs	$^{207}Pb/^{235}U$ (b)	±2σ abs	$^{207}Pb/^{206}Pb$ (b)	±2σ abs	Pb* (pg) (e)	Pbc (pg) (f)	Pb*/Pbc (g)	Isotopic Ratios $^{206}Pb/^{204}Pb$ (h)	$^{206}Pb/^{238}U$ (i)	±2σ %	$^{207}Pb/^{235}U$ (i)	±2σ %	$^{207}Pb/^{206}Pb$ (i)	±2σ %	Corr. coef.	% disc c	Th/ U d
Upper Whitney Ash																			
z8a	**30.832**	**0.061**	31.270	0.779	71.1	56.4	3.55	1.68	2.1	137	0.004782	0.20	0.03128	2.53	0.04746	2.37	0.823	57	0.79
z7a	**30.884**	**0.048**	30.827	0.243	32.4	17.2	10.87	0.91	11.9	687	0.004790	0.15	0.03083	0.80	0.04669	0.72	0.602	5	0.80
z8b	**30.917**	**0.040**	30.991	0.180	42.7	12.8	9.59	0.74	12.9	735	0.004796	0.12	0.03099	0.59	0.04689	0.53	0.536	28	0.84
z9	**30.919**	**0.057**	30.945	0.112	39.4	6.8	21.22	0.71	29.9	1752	0.004795	0.18	0.03095	0.37	0.04683	0.29	0.648	22	0.67
z4	**30.931**	**0.039**	30.813	0.281	28.2	20.6	7.96	1.26	6.3	386	0.004797	0.12	0.03081	0.93	0.04661	0.86	0.611	-9	0.65
z7b	31.002	0.027	31.054	0.083	40.9	6.4	8.48	0.46	18.6	1046	0.004809	0.08	0.03106	0.27	0.04686	0.27	0.206	24	0.86
z10	31.018	0.060	31.065	0.164	41.1	11.1	17.02	0.66	25.7	1503	0.004810	0.19	0.03107	0.54	0.04686	0.46	0.537	25	0.68
z2	31.028	0.042	31.011	0.390	35.6	28.5	8.48	1.87	4.5	269	0.004813	0.13	0.03101	1.28	0.04675	1.19	0.684	13	0.85
z3	31.093	0.037	30.920	0.281	23.5	20.2	6.49	0.87	7.4	434	0.004823	0.11	0.03092	0.92	0.04652	0.84	0.715	-32	0.82
z5	31.144	0.031	31.322	0.226	51.4	16.1	12.58	0.55	22.9	1345	0.004830	0.10	0.03133	0.73	0.04706	0.68	0.624	40	0.68
z6b	31.274	0.033	31.345	0.184	42.8	12.9	13.62	1.30	10.5	605	0.004851	0.10	0.03135	0.60	0.04689	0.54	0.624	27	0.80
z6a	33.198	0.085	33.154	1.091	34.9	75.5	3.43	1.57	2.2	134	0.005153	0.26	0.03319	3.34	0.04674	3.15	0.762	5	1.06
Lower Whitney Ash																			
z5	31.249	0.113	31.687	1.179	71.7	85.2	5.21	3.20	1.6	116	0.004846	0.36	0.03170	3.78	0.04747	3.58	0.571	57	0.55
z6	**31.663**	**0.076**	31.426	0.762	20.1	55.5	9.56	4.17	2.3	157	0.004910	0.24	0.03143	2.46	0.04645	2.31	0.661	-57	0.52
z2	**31.727**	**0.047**	31.998	0.505	59.2	35.3	13.37	3.36	4.0	262	0.004920	0.15	0.03202	1.60	0.04722	1.48	0.841	47	0.47
z3	**31.757**	**0.031**	31.913	0.270	50.2	19.1	15.05	2.25	6.7	416	0.004925	0.10	0.03193	0.86	0.04704	0.80	0.658	37	0.57
z7	**31.764**	**0.029**	31.749	0.087	37.5	5.6	19.99	0.75	26.6	1656	0.004925	0.09	0.03176	0.28	0.04679	0.23	0.619	16	0.44
z4	**31.767**	**0.051**	31.662	0.540	30.5	39.8	7.46	2.24	3.3	219	0.004926	0.16	0.03167	1.73	0.04665	1.66	0.477	-4	0.51
z8	**31.768**	**0.030**	31.701	0.223	33.3	15.9	7.62	0.98	7.8	490	0.004926	0.09	0.03171	0.72	0.04671	0.66	0.611	5	0.51
z10	**31.773**	**0.040**	31.843	0.336	44.0	23.0	4.79	0.75	6.4	409	0.004927	0.12	0.03186	1.07	0.04692	0.96	0.900	28	0.45
z9	32.057	0.031	31.894	0.175	26.7	13.1	8.30	0.57	14.6	929	0.004971	0.09	0.03191	0.56	0.04658	0.54	0.215	-20	0.40
Serenditipy																			
z1	33.712	0.156	34.762	2.437	113.7	159.3	15.72	20.59	0.8	62	0.005230	0.47	0.03483	7.13	0.04832	6.75	0.817	70	0.68
zC3	34.372	0.132	32.942	1.548	-64.9	108.7	35.41	21.63	1.6	107	0.005335	0.38	0.03298	4.78	0.04485	4.45	0.851	153	0.93
z5	34.540	0.048	34.183	0.424	14.8	28.0	40.10	7.98	5.0	306	0.005360	0.14	0.03424	1.26	0.04635	1.17	0.737	-133	0.73
z4	34.784	0.111	34.398	1.625	12.2	108.9	10.63	7.40	1.4	94	0.005400	0.32	0.03446	4.81	0.04630	4.53	0.875	-185	1.07
z3	35.940	0.000	35.971	2.677	42.9	172.9	6.63	8.60	0.8	60	0.005579	0.00	0.03606	7.58	0.04690	7.23	0.000	16	0.92
zC2	37.419	0.088	36.863	1.166	6.3	72.9	95.30	59.78	1.6	112	0.005808	0.24	0.03697	3.22	0.04619	3.03	0.829	-491	0.60
z2	38.087	0.113	37.838	1.480	27.6	89.7	21.03	11.61	1.8	127	0.005912	0.30	0.03797	3.98	0.04660	3.74	0.827	-38	0.54
zC5	94.131	1.883	92.636	2.261	56.6	33.3	159.67	10.06	15.9	983	0.014695	2.02	0.09552	2.55	0.04717	1.40	0.839	-66	0.49
Valley of Horus																			
z8	31.850	0.058	31.817	0.793	35.6	56.9	4.34	2.01	2.2	143	0.004940	0.18	0.03183	2.53	0.04675	2.38	0.863	11	0.69
z2	34.316	0.077	34.706	0.949	66.3	62.4	2.79	0.89	3.1	181	0.005327	0.22	0.03477	2.78	0.04736	2.62	0.732	48	1.11
z9	35.910	0.129	37.124	2.021	119.8	123.9	2.61	1.41	1.9	108	0.005578	0.36	0.03724	5.54	0.04844	5.26	0.812	70	1.44
z6	37.614	0.036	37.547	0.278	39.2	16.7	17.68	2.39	7.4	475	0.005838	0.10	0.03767	0.75	0.04682	0.70	0.623	4	0.43
z3	37.661	0.058	37.390	0.775	25.8	47.6	6.76	2.50	2.7	183	0.005845	0.16	0.03751	2.11	0.04656	1.99	0.824	-46	0.48
z1	37.664	0.099	37.238	1.388	15.6	85.9	6.36	4.93	1.3	97	0.005846	0.27	0.03735	3.80	0.04637	3.57	0.855	-141	0.48
z10	38.130	0.144	38.704	1.631	79.9	95.8	3.95	2.89	1.4	100	0.005919	0.38	0.03885	4.30	0.04763	4.04	0.705	52	0.54

Table A.3 Results of single crystal U/Pb analyses from volcanic tuffs intercalated in the White River Group sedimentary succession

Fraction	Dates (Ma) $^{206}Pb/^{238}U$ (a)	±2σ abs	$^{207}Pb/^{235}U$ (b)	±2σ abs	$^{207}Pb/^{206}Pb$ (b)	±2σ abs	Pb* (pg) (e)	Pbc (pg) (f)	Pb*/Pbc (g)	Isotopic Ratios $^{206}Pb/^{204}Pb$ (h)	$^{206}Pb/^{238}U$ (i)	±2σ %	$^{207}Pb/^{235}U$ (i)	±2σ %	$^{207}Pb/^{206}Pb$ (i)	±2σ %	Corr. coef.	% disc c	Th/ U d
Valley of Horus (continued)																			
z7	40.438	0.214	56.354	3.155	801.7	110.7	2.22	2.48	0.9	60	0.006285	0.53	0.05707	5.76	0.06588	5.28	0.898	95	1.56
Upper Purplish White Layer																			
z3	**33.863**	**0.059**	33.893	0.444	42.0	29.4	3.70	0.57	6.5	420	0.005267	0.18	0.03394	1.33	0.04688	1.23	0.639	20	0.46
z18M	**33.886**	**0.076**	33.255	1.074	-7.1	75.4	2.33	1.06	2.2	144	0.005270	0.22	0.03329	3.28	0.04593	3.12	0.746	575	0.72
z21M	**33.916**	**0.145**	35.506	2.015	149.0	127.5	2.87	2.86	1.0	75	0.005275	0.43	0.03559	5.77	0.04905	5.44	0.796	77	0.77
z1	**33.928**	**0.047**	33.764	0.336	27.1	22.1	2.94	0.29	10.3	611	0.005277	0.14	0.03381	1.01	0.04659	0.92	0.748	-25	0.71
z4	**33.947**	**0.115**	33.947	1.636	38.9	110.5	1.39	1.10	1.3	91	0.005280	0.34	0.03400	4.90	0.04682	4.62	0.843	13	0.71
z19M	33.984	0.061	34.449	0.616	72.6	40.0	2.28	0.53	4.3	279	0.005286	0.18	0.03451	1.82	0.04748	1.68	0.789	53	0.54
z42M	34.014	0.042	34.408	0.484	67.7	32.0	2.75	0.76	3.6	237	0.005290	0.12	0.03447	1.43	0.04739	1.34	0.758	50	0.50
z5	34.483	0.026	34.407	0.205	34.3	13.9	39.69	0.88	45.3	2678	0.005363	0.08	0.03447	0.61	0.04673	0.58	0.444	0	0.63
z38M	34.588	0.317	33.806	4.751	-22.6	326.5	1.54	3.01	0.5	39	0.005380	0.92	0.03385	14.29	0.04564	13.49	0.890	253	2.32
TP_2																			
z2	**34.432**	**0.046**	34.434	0.334	40.2	21.5	7.44	0.79	9.4	555	0.005343	0.13	0.03449	0.99	0.04684	0.90	0.700	15	0.72
z3	**34.443**	**0.091**	34.612	0.282	51.8	17.0	8.45	0.71	11.8	687	0.005345	0.26	0.03467	0.83	0.04707	0.71	0.570	34	0.77
z1	**34.444**	**0.130**	34.464	1.435	39.5	96.6	5.66	2.23	2.5	141	0.005349	0.38	0.03452	4.23	0.04683	4.04	0.557	13	1.44
z6	**34.482**	**0.065**	34.449	0.242	38.1	15.0	6.45	0.50	12.9	782	0.005350	0.19	0.03451	0.71	0.04680	0.63	0.563	10	0.59
z5	**34.488**	**0.052**	34.159	0.484	17.2	32.3	8.38	2.46	3.4	221	0.005351	0.15	0.03421	1.44	0.04640	1.35	0.666	-100	0.56
z8a	**34.498**	**0.032**	34.572	0.166	45.6	10.7	10.66	0.54	19.7	1175	0.005353	0.09	0.03463	0.49	0.04695	0.45	0.510	25	0.62
z4	35.150	0.069	36.989	0.517	163.6	30.3	6.83	1.47	4.6	289	0.005455	0.20	0.03710	1.42	0.04935	1.30	0.683	79	0.65
z9	35.262	0.034	35.328	0.158	44.3	9.8	13.36	0.54	24.5	1302	0.005475	0.09	0.03541	0.46	0.04692	0.41	0.595	21	1.09
z8	35.979	0.151	36.796	2.281	96.1	142.1	1.80	1.47	1.2	91	0.005583	0.40	0.03690	6.31	0.04796	6.00	0.783	63	0.58
TP_1																			
z7	34.532	0.040	34.722	0.361	53.9	23.4	6.08	0.64	9.5	587	0.005358	0.12	0.03479	1.06	0.047	0.98	0.704	36	0.56
z4	**35.143**	**0.096**	35.154	0.743	40.2	48.5	3.06	1.01	3.0	172	0.005457	0.27	0.03523	2.15	0.047	2.03	0.505	13	1.19
z3	**35.201**	**0.132**	35.856	2.362	83.6	152.0	1.32	1.04	1.3	80	0.005467	0.38	0.03594	6.71	0.048	6.41	0.801	58	1.38
z2	**35.253**	**0.050**	35.204	0.469	36.9	30.2	5.06	0.99	5.1	299	0.005472	0.14	0.03528	1.36	0.047	1.26	0.714	5	0.89
z6	**35.258**	**0.134**	33.951	1.295	-52.7	88.5	1.72	0.56	3.1	185	0.005473	0.38	0.03400	3.88	0.045	3.64	0.666	167	0.98
z11	35.348	0.047	35.383	0.449	42.3	29.1	5.07	0.79	6.4	354	0.005488	0.13	0.03546	1.29	0.047	1.22	0.622	17	1.10
z7a	35.375	0.048	35.200	0.327	27.9	20.5	4.85	0.44	11.0	602	0.005492	0.13	0.03527	0.95	0.047	0.86	0.725	-26	1.04
z13	35.711	0.042	35.530	0.318	28.7	20.4	4.26	0.57	7.4	443	0.005543	0.12	0.03561	0.91	0.047	0.85	0.551	-24	0.73
z5	35.768	0.101	35.740	1.185	39.0	75.7	3.11	1.41	2.2	141	0.005552	0.28	0.03583	3.37	0.047	3.16	0.765	8	0.84
z1	35.786	0.036	35.757	0.165	39.0	10.0	5.18	0.33	15.7	894	0.005555	0.10	0.03584	0.47	0.047	0.42	0.621	9	0.82
J																			
z11	32.393	0.254	32.603	4.153	52.3	291.6	0.55	0.79	0.7	53	0.005029	0.79	0.03263	12.94	0.047	12.22	0.921	38	1.32
z31M	33.725	0.237	33.835	3.454	42.3	233.3	1.55	2.25	0.7	45	0.005244	0.70	0.03388	10.38	0.047	9.76	0.896	20	2.54
z4	**34.347**	**0.089**	35.104	0.870	89.5	55.8	2.62	0.69	3.8	185	0.005337	0.25	0.03518	2.52	0.048	2.35	0.700	62	1.94
z10	34.380	0.192	34.355	2.815	37.1	187.6	0.79	0.97	0.8	60	0.005337	0.56	0.03441	8.33	0.047	7.84	0.885	7	1.14
z10M	**34.394**	**0.052**	34.644	0.276	53.1	17.5	6.11	0.47	12.9	538	0.005347	0.12	0.03471	0.81	0.047	0.73	0.705	35	2.38

Table A.3 Results of single crystal U/Pb analyses from volcanic tuffs intercalated in the White River Group sedimentary succession (continued)

	Dates (Ma)						Isotopic Ratios												
Fraction	$^{206}Pb/^{238}U$ (a)	±2σ abs	$^{207}Pb/^{235}U$ (b)	±2σ abs	$^{207}Pb/^{206}Pb$ (b)	±2σ abs	Pb* (pg) (e)	Pbc (pg) (f)	Pb*/Pbc (g)	$^{206}Pb/^{204}Pb$ (h)	$^{206}Pb/^{238}U$ (i)	±2σ %	$^{207}Pb/^{235}U$ (i)	±2σ %	$^{207}Pb/^{206}Pb$ (i)	±2σ %	Corr. coef.	% disc c	Th/ U d
J (continued)																			
z11	32.393	0.254	32.603	4.153	52.3	291.6	0.55	0.79	0.7	53	0.005029	0.79	0.03263	12.94	0.047	12.22	0.921	38	1.32
z31M	33.725	0.237	33.835	3.454	42.3	233.3	1.55	2.25	0.7	45	0.005244	0.70	0.03388	10.38	0.047	9.76	0.896	20	2.54
z4	**34.347**	**0.089**	35.104	0.870	89.5	55.8	2.62	0.69	3.8	185	0.005337	0.25	0.03518	2.52	0.048	2.35	0.700	62	1.94
z10	34.380	0.192	34.355	2.815	37.1	187.6	0.79	0.97	0.8	60	0.005337	0.56	0.03441	8.33	0.047	7.84	0.885	7	1.14
z10M	**34.394**	**0.052**	34.644	0.276	53.1	17.5	6.11	0.47	12.9	538	0.005347	0.12	0.03471	0.81	0.047	0.73	0.705	35	2.38
J-1																			
z6	**34.351**	**0.054**	34.402	0.625	43.9	42.5	13.91	2.67	5.2	320	0.005330	0.16	0.03446	1.85	0.047	1.78	0.467	22	0.61
z1	**34.383**	**0.094**	34.489	0.825	47.9	54.2	5.48	1.64	3.3	215	0.005334	0.27	0.03455	2.43	0.047	2.27	0.641	28	0.57
z8	**34.386**	**0.045**	34.413	0.293	42.3	18.9	8.28	1.10	7.6	466	0.005335	0.13	0.03447	0.87	0.047	0.79	0.641	19	0.57
z10	**34.418**	**0.036**	34.328	0.166	33.6	10.4	15.78	1.20	13.2	764	0.005341	0.10	0.03439	0.49	0.047	0.44	0.629	-2	0.75
z3	**34.419**	**0.053**	34.631	0.339	55.7	21.4	10.36	1.21	8.6	540	0.005339	0.15	0.03469	1.00	0.047	0.90	0.681	38	0.47
z7	**34.427**	**0.051**	34.302	0.468	31.4	30.9	12.90	1.81	7.1	432	0.005342	0.15	0.03436	1.39	0.047	1.29	0.679	-9	0.63
z2	**34.443**	**0.084**	34.026	1.193	10.4	82.2	5.91	2.02	2.9	185	0.005345	0.24	0.03408	3.57	0.046	3.42	0.631	-231	0.69
z9	**34.492**	**0.103**	34.229	0.432	22.1	27.4	17.44	1.48	11.8	728	0.005351	0.30	0.03429	1.28	0.046	1.14	0.554	-55	0.48
z4	35.955	0.030	36.007	0.279	44.9	18.0	12.88	1.59	8.1	481	0.005580	0.08	0.03610	0.79	0.047	0.75	0.501	20	0.69
H																			
z12	33.367	0.128	33.372	1.810	37.8	125.0	2.27	1.06	2.1	125	0.005181	0.38	0.03341	5.51	0.04680	5.22	0.769	12	1.31
z13	33.684	0.186	34.988	3.201	129.8	209.2	1.09	1.01	1.1	74	0.005229	0.56	0.03506	9.31	0.04865	8.89	0.763	74	1.20
z5	**34.684**	**0.079**	34.603	0.882	34.7	58.3	11.74	5.62	2.1	139	0.005382	0.23	0.03467	2.59	0.04674	2.44	0.711	0	0.70
z9	**34.720**	**0.053**	34.609	0.659	33.3	43.5	2.50	0.74	3.4	225	0.005386	0.15	0.03467	1.94	0.04671	1.81	0.818	-4	0.45
z8	**34.736**	**0.033**	34.799	0.272	44.2	17.6	7.51	0.98	7.6	438	0.005391	0.09	0.03487	0.80	0.04692	0.74	0.693	22	0.89
z4	**34.739**	**0.053**	34.632	0.654	32.7	43.5	7.62	2.45	3.1	195	0.005391	0.15	0.03470	1.92	0.04670	1.81	0.716	-6	0.75
z1	**34.739**	**0.031**	34.832	0.289	47.1	18.6	6.66	0.79	8.4	514	0.005390	0.09	0.03490	0.84	0.04698	0.78	0.773	26	0.62
z10	**34.746**	**0.091**	34.626	0.963	32.2	63.4	1.86	0.85	2.2	148	0.005391	0.26	0.03469	2.83	0.04669	2.64	0.726	-8	0.58
z11	**34.798**	**0.045**	34.978	0.441	53.7	28.8	3.58	0.67	5.3	348	0.005398	0.13	0.03505	1.28	0.04711	1.20	0.625	35	0.43
z15	34.949	0.101	33.552	0.625	-59.5	42.5	2.35	0.41	5.8	357	0.005423	0.29	0.03360	1.89	0.04495	1.74	0.572	159	0.63
z6	34.976	0.146	34.735	1.048	24.3	68.7	3.38	1.73	2.0	139	0.005426	0.42	0.03480	3.07	0.04653	2.86	0.537	-43	0.45
z14	34.979	0.083	35.254	1.095	59.6	70.7	3.04	1.66	1.8	123	0.005428	0.24	0.03533	3.16	0.04723	2.97	0.814	41	0.72
z7	35.073	0.053	34.929	0.533	29.9	34.2	2.40	0.60	4.0	235	0.005444	0.15	0.03500	1.55	0.04664	1.43	0.868	-17	0.98
G																			
z15	35.045	0.096	34.703	0.394	15.7	24.9	3.66	0.58	6.4	353	0.005441	0.27	0.03477	1.15	0.04637	1.04	0.53	-122.30	1.07
z10	**35.216**	**0.135**	34.468	1.332	-11.9	87.6	2.95	1.25	2.4	152	0.005466	0.38	0.03453	3.93	0.04584	3.63	0.81	395.62	0.77
z1	**35.222**	**0.037**	35.235	0.198	41.5	12.5	8.95	0.53	16.8	965	0.005466	0.10	0.03531	0.57	0.04687	0.52	0.57	15.39	0.77
z37M	**35.232**	**0.080**	35.101	0.664	30.9	43.8	3.74	1.09	3.4	202	0.005469	0.22	0.03517	1.93	0.04666	1.83	0.48	-13.87	1.01
z22M	**35.259**	**0.039**	35.262	0.294	39.2	18.8	5.55	0.65	8.5	435	0.005476	0.10	0.03534	0.85	0.04682	0.79	0.69	10.23	1.39
z4	**35.268**	**0.062**	35.088	0.457	27.3	28.5	2.78	0.32	8.6	469	0.005476	0.17	0.03516	1.33	0.04659	1.19	0.82	-29.16	1.11
z31M	**35.277**	**0.044**	35.167	0.410	32.4	26.5	6.02	1.24	4.9	278	0.005477	0.12	0.03524	1.19	0.04669	1.10	0.71	-8.62	1.01
z8	35.438	0.042	35.245	0.462	27.7	29.8	5.81	1.39	4.2	261	0.005500	0.12	0.03532	1.33	0.04660	1.24	0.79	-27.63	0.67
z3	35.511	0.071	35.297	0.755	25.7	48.6	2.67	0.84	3.2	192	0.005513	0.20	0.03537	2.18	0.04656	2.03	0.77	-38.10	0.94

Table A.3 Results of single crystal U/Pb analyses from volcanic tuffs intercalated in the White River Group sedimentary succession (continued)

	Dates (Ma)						Isotopic Ratios												
Fraction	$^{206}Pb/^{238}U$ (a)	±2σ abs	$^{207}Pb/^{235}U$ (b)	±2σ abs	$^{207}Pb/^{206}Pb$ (b)	±2σ abs	Pb* (pg) (e)	Pbc (pg) (f)	Pb*/Pbc (g)	$^{206}Pb/^{204}Pb$ (h)	$^{206}Pb/^{238}U$ (i)	±2σ %	$^{207}Pb/^{235}U$ (i)	±2σ %	$^{207}Pb/^{206}Pb$ (i)	±2σ %	Corr. coef.	% disc c	Th/ U d
G (continued)																			
z15	35.045	0.096	34.703	0.394	15.7	24.9	3.66	0.58	6.4	353	0.005441	0.27	0.03477	1.15	0.04637	1.04	0.53	-122.30	1.07
z10	**35.216**	**0.135**	34.468	1.332	-11.9	87.6	2.95	1.25	2.4	152	0.005466	0.38	0.03453	3.93	0.04584	3.63	0.81	395.62	0.77
z1	**35.222**	**0.037**	35.235	0.198	41.5	12.5	8.95	0.53	16.8	965	0.005466	0.10	0.03531	0.57	0.04687	0.52	0.57	15.39	0.77
z37M	**35.232**	**0.080**	35.101	0.664	30.9	43.8	3.74	1.09	3.4	202	0.005469	0.22	0.03517	1.93	0.04666	1.83	0.48	-13.87	1.01
z22M	**35.259**	**0.039**	35.262	0.294	39.2	18.8	5.55	0.65	8.5	435	0.005476	0.10	0.03534	0.85	0.04682	0.79	0.69	10.23	1.39
z4	**35.268**	**0.062**	35.088	0.457	27.3	28.5	2.78	0.32	8.6	469	0.005476	0.17	0.03516	1.33	0.04659	1.19	0.82	-29.16	1.11
z31M	**35.277**	**0.044**	35.167	0.410	32.4	26.5	6.02	1.24	4.9	278	0.005477	0.12	0.03524	1.19	0.04669	1.10	0.71	-8.62	1.01
z8	35.438	0.042	35.245	0.462	27.7	29.8	5.81	1.39	4.2	261	0.005500	0.12	0.03532	1.33	0.04660	1.24	0.79	-27.63	0.67
z3	35.511	0.071	35.297	0.755	25.7	48.6	2.67	0.84	3.2	192	0.005513	0.20	0.03537	2.18	0.04656	2.03	0.77	-38.10	0.94
F																			
z11	**35.301**	**0.045**	35.434	0.194	49.6	9.1	17.77	1.38	12.9	730	0.005479	0.12	0.03551	0.56	0.04703	0.38	1.31	28.93	0.87
z4	**35.321**	**0.059**	35.340	0.324	42.2	19.6	14.25	2.31	6.2	375	0.005481	0.17	0.03542	0.93	0.04688	0.82	0.73	16.45	0.69
z1	**35.340**	**0.091**	35.158	0.506	27.7	32.1	9.28	1.52	6.1	353	0.005486	0.26	0.03523	1.46	0.04660	1.34	0.56	-27.13	0.89
z3	**35.341**	**0.078**	35.219	0.520	33.1	32.9	11.92	3.51	3.4	226	0.005483	0.22	0.03529	1.50	0.04670	1.37	0.64	-6.52	0.46
z13	**35.345**	**0.032**	35.305	0.128	37.9	8.0	19.45	0.85	22.9	1312	0.005486	0.09	0.03538	0.37	0.04680	0.33	0.53	7.04	0.77
z10	**35.351**	**0.036**	35.305	0.149	37.9	9.1	28.13	1.76	16.0	953	0.005486	0.10	0.03538	0.43	0.04680	0.38	0.57	6.88	0.63
z12	35.523	0.032	35.596	0.063	46.5	3.1	71.50	1.31	54.4	3294	0.005512	0.09	0.03568	0.18	0.04697	0.13	0.71	23.77	0.53
z5	35.679	0.029	35.711	0.220	43.8	13.8	20.22	2.34	8.6	539	0.005536	0.08	0.03580	0.63	0.04691	0.58	0.63	18.70	0.52
z11b	35.758	0.050	35.651	0.288	32.6	18.3	3.68	0.37	10.0	525	0.005553	0.13	0.03573	0.82	0.04669	0.76	0.49	-9.59	1.22
z8	35.805	0.096	36.012	1.021	54.7	65.6	2.22	0.95	2.3	146	0.005558	0.27	0.03610	2.89	0.04713	2.75	0.54	34.65	0.94
z10b	35.922	0.027	36.063	0.154	51.9	9.0	52.89	3.03	17.4	1126	0.005573	0.08	0.03616	0.43	0.04707	0.38	0.77	30.98	0.33
z6	36.174	0.164	34.269	2.450	-92.2	169.3	0.83	0.64	1.3	90	0.005616	0.46	0.03433	7.27	0.04435	6.90	0.82	139.15	0.88
z9	36.326	0.053	36.895	0.625	80.1	38.3	4.76	1.67	2.8	194	0.005637	0.15	0.03700	1.73	0.04763	1.61	0.77	54.76	0.44
z7	36.500	0.087	36.621	1.119	49.2	69.8	0.76	0.34	2.2	138	0.005667	0.24	0.03672	3.11	0.04702	2.92	0.80	25.93	1.00
F-7.5																			
z1	**35.379**	**0.069**	35.582	0.356	55.0	20.9	7.20	0.46	15.7	921	0.005490	0.19	0.03566	1.02	0.04713	0.88	0.77	35.81	0.64
z3	**35.410**	**0.047**	35.313	0.215	33.5	13.8	8.15	0.57	14.3	788	0.005497	0.13	0.03539	0.62	0.04671	0.58	0.43	-5.45	0.98
z5	**35.411**	**0.031**	35.385	0.105	39.5	6.2	15.37	0.32	48.6	2916	0.005495	0.09	0.03546	0.30	0.04683	0.26	0.60	10.66	0.56
z7	**35.430**	**0.033**	35.256	0.258	28.8	16.4	7.50	0.88	8.5	504	0.005499	0.09	0.03533	0.74	0.04662	0.68	0.71	-22.56	0.73
z2	**35.435**	**0.068**	35.224	0.391	25.8	25.0	2.53	0.31	8.1	459	0.005501	0.19	0.03530	1.13	0.04656	1.04	0.53	-37.30	0.96
z9	35.570	0.116	38.195	1.773	211.3	103.5	1.43	1.00	1.4	98	0.005521	0.33	0.03833	4.73	0.05038	4.47	0.81	83.20	0.86
z6	35.745	0.081	35.422	1.814	18.2	120.7	3.24	2.40	1.4	90	0.005550	0.23	0.03550	5.21	0.04642	5.02	0.84	-96.44	1.06
F-18																			
z5	35.539	0.131	37.245	1.890	153.2	113.4	0.70	0.59	1.2	82	0.005517	0.37	0.03736	5.17	0.04913	4.84	0.890	77	1.01
z2	35.639	0.053	35.637	0.620	39.7	39.5	1.63	0.42	3.9	215	0.005534	0.14	0.03572	1.77	0.04683	1.65	0.861	10	1.21
z3	35.848	0.037	36.203	0.451	65.5	28.8	2.95	0.62	4.7	297	0.005563	0.10	0.03630	1.27	0.04734	1.21	0.587	45	0.60
z1	36.106	0.094	35.124	1.147	-25.6	75.3	6.85	3.67	1.9	130	0.005603	0.26	0.03520	3.32	0.04558	3.11	0.832	241	0.55
z6	45.303	0.065	45.519	0.791	61.3	40.0	1.98	0.65	3.0	194	0.007040	0.14	0.04585	1.78	0.04726	1.68	0.729	26	0.68
z4	71.965	0.302	73.740	4.321	134.8	135.0	2.84	3.50	0.8	69	0.011211	0.42	0.07532	6.07	0.04875	5.75	0.790	47	0.36

Table A.3 Results of single crystal U/Pb analyses from volcanic tuffs intercalated in the White River Group sedimentary succession (continued)

Fraction	Dates (Ma) $^{206}Pb/^{238}U$ (a)	±2σ abs	$^{207}Pb/^{235}U$ (b)	±2σ abs	$^{207}Pb/^{206}Pb$ (b)	±2σ abs	Pb* (pg) (e)	Pbc (pg) (f)	Pb*/Pbc (g)	Isotopic Ratios $^{206}Pb/^{204}Pb$ (h)	$^{206}Pb/^{238}U$ (i)	±2σ %	$^{207}Pb/^{235}U$ (i)	±2σ %	$^{207}Pb/^{206}Pb$ (i)	±2σ %	Corr. coef.	% disc c	Th/ U d
B+18																			
z3	**35.657**	**0.083**	35.715	0.392	45.0	24.6	0.72	5.16	9.3	549	0.005534	0.23	0.03580	1.12	0.04694	1.03	0.47	20.98	0.56
z8	**35.658**	**0.047**	35.692	0.501	42.8	31.8	0.95	4.72	4.2	243	0.005536	0.13	0.03578	1.43	0.04690	1.33	0.80	16.90	1.14
z12	**35.686**	**0.043**	35.909	0.261	56.6	16.7	0.58	14.84	11.7	714	0.005538	0.12	0.03600	0.74	0.04717	0.70	0.40	37.12	1.26
z7b	**35.687**	**0.038**	35.877	0.395	53.3	24.9	0.99	7.24	4.9	281	0.005540	0.10	0.03596	1.12	0.04710	1.04	0.78	33.20	1.48
z9	**35.687**	**0.036**	35.844	0.363	51.6	23.5	0.77	7.82	5.8	345	0.005539	0.10	0.03593	1.03	0.04707	0.98	0.51	31.05	1.35
z4	35.723	0.031	35.672	0.218	38.2	13.8	0.51	15.00	11.5	714	0.005543	0.08	0.03576	0.62	0.04681	0.57	0.59	6.81	1.30
z7	35.753	0.035	35.804	0.242	45.5	15.0	0.39	12.25	9.5	612	0.005547	0.10	0.03589	0.69	0.04695	0.63	0.68	21.60	1.29
z6	35.834	0.032	35.466	0.154	17.1	9.4	0.31	10.31	20.1	1304	0.005559	0.09	0.03555	0.44	0.04639	0.39	0.63	-108.80	0.51
z9b	37.329	0.034	37.543	0.227	56.5	13.7	0.70	11.80	12.3	724	0.005795	0.09	0.03767	0.62	0.04716	0.57	0.54	34.09	0.96
B+15																			
z8	35.507	0.082	35.482	1.010	39.7	65.1	3.94	2.19	1.8	126	0.005510	0.23	0.03556	2.90	0.04683	2.72	0.77	10.81	0.53
z10	35.526	0.051	35.719	0.618	54.1	39.3	3.02	0.99	3.0	191	0.005514	0.14	0.03580	1.76	0.04712	1.65	0.82	34.44	0.75
z6	**35.686**	**0.041**	35.631	0.435	37.8	27.7	16.41	4.13	4.0	258	0.005537	0.11	0.03571	1.24	0.04680	1.16	0.78	5.93	0.52
z3	**35.736**	**0.026**	35.665	0.173	36.2	10.7	8.69	0.60	14.6	841	0.005547	0.07	0.03575	0.49	0.04677	0.45	0.72	1.59	0.77
z4	**35.756**	**0.036**	35.726	0.219	38.9	13.5	7.14	0.46	15.5	891	0.005550	0.10	0.03581	0.63	0.04682	0.56	0.67	8.26	0.80
z8a	**35.759**	**0.048**	35.724	0.307	39.0	19.3	9.16	1.29	7.1	439	0.005549	0.13	0.03581	0.88	0.04682	0.81	0.57	8.63	0.61
z1	**35.764**	**0.034**	35.658	0.184	34.9	11.4	26.90	1.48	18.2	1162	0.005549	0.10	0.03574	0.52	0.04674	0.48	0.56	-2.33	0.36
z2	**35.781**	**0.036**	35.724	0.154	37.6	9.5	20.44	1.42	14.4	867	0.005553	0.10	0.03581	0.44	0.04679	0.40	0.49	5.05	0.60
z5	**35.797**	**0.036**	35.740	0.224	36.0	14.2	26.86	1.97	13.7	710	0.005559	0.09	0.03583	0.64	0.04676	0.59	0.57	0.81	1.24
z9	35.884	0.044	36.245	0.453	66.3	28.2	4.49	1.12	4.0	263	0.005568	0.12	0.03634	1.27	0.04736	1.18	0.75	45.98	0.46
z9a	35.953	0.047	35.939	0.233	40.9	14.4	18.50	2.15	8.6	538	0.005579	0.13	0.03603	0.66	0.04686	0.60	0.53	12.37	0.50
B																			
z10	35.286	0.034	35.197	0.157	33.6	9.6	13.46	0.63	21.5	1139	0.005479	0.09	0.03527	0.45	0.04671	0.40	0.69	-4.83	1.12
z11	35.342	0.095	34.668	1.027	-5.9	69.2	14.63	4.44	3.3	213	0.005484	0.27	0.03473	3.01	0.04595	2.87	0.56	695.28	0.60
z13	35.371	0.049	35.409	0.313	43.9	19.5	8.67	0.83	10.4	642	0.005488	0.14	0.03549	0.90	0.04692	0.82	0.64	19.65	0.55
z4	35.405	0.544	30.398	8.783	-344.6	727.5	0.92	1.96	0.5	43	0.005497	1.55	0.03039	29.33	0.04012	28.21	0.74	110.25	1.07
z9	35.557	0.043	36.030	0.129	73.6	7.1	45.46	2.14	21.2	1290	0.005517	0.12	0.03612	0.36	0.04750	0.30	0.66	51.79	0.54
z3	**35.730**	**0.165**	35.492	2.116	24.2	137.3	1.77	1.63	1.1	77	0.005547	0.47	0.03557	6.07	0.04653	5.72	0.76	-47.08	0.97
z5	35.746	0.184	35.261	2.944	8.2	193.7	2.32	2.52	0.9	73	0.005547	0.52	0.03534	8.49	0.04622	8.05	0.87	-337.43	0.60
z2	**35.805**	**0.156**	36.168	1.066	65.8	66.1	2.21	0.86	2.6	166	0.005557	0.44	0.03626	3.00	0.04735	2.78	0.56	45.69	0.70
z1	**35.864**	**0.115**	35.780	1.388	34.9	88.7	2.60	1.66	1.6	102	0.005568	0.32	0.03587	3.95	0.04674	3.70	0.78	-2.61	0.98
z12	36.057	0.063	37.027	0.143	106.1	7.7	24.85	0.52	48.0	2874	0.005595	0.17	0.03714	0.39	0.04816	0.32	0.58	66.10	0.57
z6	36.314	0.123	34.688	1.551	-72.2	105.3	2.11	0.74	2.8	165	0.005639	0.34	0.03475	4.55	0.04472	4.31	0.72	150.23	1.18

Table A.3 Results of single crystal U/Pb analyses from volcanic tuffs intercalated in the White River Group sedimentary succession (continued)

Appendix B - Palaeomagnetic data from the Flagstaff Rim and Toadstool Park sections

This appendix lists the results of paleomagnetic analysis of samples from the Flagstaff Rim and Toadstool Park sections (Chapter 4). Paleomagnetic analyses were carried out at the Fort Hoffddijk paleomagnetic laboratory, at the university of Utrecht. Analytical methods and protocols are detailed in Chapter 4, Section 4.3. The data are organised in two tables, B.1 (Flagstaff Rim) and B.2 (Toadstool Park) which give information on the stratigrpahic position of each sample, the demagnetization method, and the low and high temperature components calculated through principal component analysis. Annotations for the two tables are as follows:

- Sample - sample number
- m level - stratigraphic position relative to the base of the respective composite measured sections, at 18.35 m below the B tuff at Flagstaff Rim, and 38.25 m below the Upper Purplish White Layer at Toadstool Park. These scales are identical to those used in Appendix A, Table A.2 for the stratigraphic position of volcanic tuff samples discussed in Chapter 3.
- Section - number of section from which the sample was collected. These numbers correspond to those shown in the maps in Chapter 4, Figure 4.3.
- Dm - demagnetization method, listed as ‘th’ - thermal demagnetization, or ‘af’ - alternating field demagnetization
- Q - quality of the magnetic data: D - samples showing unstable magnetic directions when demagnetized above 240 ^{o}C, excluded from interpretation, C - samples with mean angular deviation of the high temperature component above 20^{o}, excluded from intepretation, B - outliers excluded through variable cut-off algorithm of Vandamme (1994), excluded from interpretation, A - good quality samples used to establish the magnetic polarity pattern of the Flagstaff

Rim and Toadstool Park sections

- I - inclination
- MAD - mean angular deviation
- VGP lon & VGP lat - coordinates of the virtual geomagnetic pole calculated on the basis of the declination and inclination of the high temperature component, and the geographic coordinates of the sample.

Sample	m level	Section	Dm	Q	Low temperature component			High temperature component				
					D	I	MAD	D	I	MAD	VGP lon	VGP lat
FR25	0.57	FR_s2	th	D	342.1	66.2	16.8	-	-	-	-	-
FR23	1.51	FR_s2	af	D	324.5	42.8	8.9	-	-	-	-	-
FR22	2.45	FR_s2	th	C	336.0	58.3	7.8	181.7	81.5	28.7	252.7	26
FR21	3.22	FR_s2	af	A	10.4	36.3	17.2	11.0	72.1	7.6	275.1	73.9
FR19	4.26	FR_s2	th	A	325.5	30.4	12.8	313.4	37.3	18.3	148.9	45.5
FR17	4.99	FR_s1	af	A	18.8	69.2	10.0	346.0	64.0	5.1	185.2	79.5
FR16	5.45	FR_s1	af	A	24.3	60.6	3.9	38.0	63.0	7.8	326.1	62.6
FR12	8.05	FR_s1	th	A	44.9	20.0	4.9	334.6	50.0	12.7	141.3	66.6
FR11	9.37	FR_s1	af	A	18.0	62.7	14.8	358.4	35.0	12.4	77	66.7
FR10	10.18	FR_s1	th	A	10.3	69.9	2.3	35.9	61.6	10.5	330.5	63.8
FR9	10.87	FR_s1	af	A	19.9	70.7	4.1	350.2	82.1	6.2	248.3	57.8
FR8	11.84	FR_s1	th	A	293.2	54.2	4.0	346.8	34.8	17.3	102.7	64
FR7	12.60	FR_s1	af	A	161.9	86.9	12.3	314.4	64.3	8.3	185.4	57.7
FR6	13.26	FR_s1	th	A	15.7	65.9	1.1	357.5	68.9	9.3	244.3	80.1
FR4	14.72	FR_s1	th	A	30.7	63.9	6.8	312.8	71.9	10.3	205.4	57.2
FR3	15.21	FR_s1	af	A	48.2	35.3	1.0	19.4	70.0	4.3	294.9	72.9
FR2	15.83	FR_s1	af	A	16.6	54.4	6.4	44.6	60.3	3.5	330.1	57.2
FR1	16.10	FR_s1	th	D	-	-	-	-	-	-	-	-
FR29	20.56	FR_s3	af	A	25.0	74.8	12.6	353.2	73.8	8.3	241.9	72.3
FR30	21.06	FR_s3	th	D	30.9	61.7	5.4	-	-	-	-	-
FR33	22.80	FR_s3	af	A	302.1	32.6	15.8	33.7	54.2	16.1	348.6	62.7
FR34	23.31	FR_s3	af	A	185.9	77.8	8.9	342.1	16.5	5.3	103.1	52.4
FR36	24.11	FR_s3	th	D	2.8	78.6	4.6	-	-	-	-	-
FR37	24.58	FR_s3	th	A	352.9	70.2	8.6	351.2	77.9	11.4	244.9	65.3
FR38	24.93	FR_s3	af	B	-	-	-	282.8	-27.8	18.0	143.8	-0.9
FR39	25.50	FR_s3	af	A	8.2	74.1	17.5	352.4	33.7	10.0	90.5	65
FR40	25.89	FR_s3	th	D	327.3	63.2	6.2	-	-	-	-	-
FR41	26.52	FR_s3	af	A	28.3	52.2	21.4	319.4	60	7.8	173.9	60
FR42	27.42	FR_s4	th	A	25.0	53.5	7.6	238.6	-24	14.0	175.7	-31.4
FR43	27.73	FR_s4	th	D	33.3	56.8	5.1	-	-	-	-	-
FR44	27.88	FR_s4	th	C	56.3	81.7	11.6	234.1	75	27.3	228.6	23.1
FR45	28.15	FR_s4	th	A	259.8	79.0	26.0	191.5	-24.1	17.9	231.4	-58.4

Table B.1 Results of paleomagnetic analysis of samples from the Flagstaff Rim section (continued on the next page)

Sample	m level	Section	Dm	Q	Low temperature component			High temperature component				
					D	I	MAD	D	I	MAD	VGP lon	VGP lat
FR46	28.30	FR_s4	af	A	211.3	-6.1	13.7	172.4	-73.2	17.4	59.6	-73.1
FR48	29.33	FR_s4	th	A	6.9	76.7	13.8	357.3	73.1	14.8	248.2	73.8
FR52	31.37	FR_s5	af	C	-	-	-	161.2	44.7	37.9	271	-18.9
FR55	32.65	FR_s5	af	A	160.9	-45.7	29.2	183.7	-56.3	10.3	225.6	-83.6
FR56	33.10	FR_s5	th	A	354.9	39.1	9.0	5.7	60.9	8.8	350.2	85.7
FR63	37.87	FR_s6	th	A	13.2	38.4	8.9	152.2	-54.7	19.0	333.6	-67.3
FR64	38.51	FR_s6	af	A	85.5	42.1	29.3	150.8	-29.7	17.2	305.2	-53.5
FR66	40.66	FR_s6	af	D	121.7	-23.6	33.0	-	-	-	-	-
FR67	41.56	FR_s6	th	C	0.4	51.0	17.4	123.4	3.5	21.9	317.9	-22.6
FR68	42.13	FR_s6	th	C	-	-	-	229.8	-18.5	23.9	185.5	-35.5
FR70	43.21	FR_s6	th	C	344.3	64.4	16.3	299.6	49.6	25.0	169.6	41
FR74	47.51	FR_s6	af	A	2.9	52.3	9.8	303.3	24.4	8.6	149.4	32.9
FR76	49.91	FR_s6	af	A	3.6	56.9	3.6	352.9	75.7	8.6	244.1	69.2
FR78	52.73	FR_s6	af	C	339.9	41.8	25.6	5.9	30.8	32.9	60.4	63.5
FR83	56.63	FR_s7	af	A	4.8	61.1	2.2	330.7	65.3	4.1	186.4	68.9
FR90b	60.13	FR_s8	af	D	82.2	69.7	3.9	-	-	-	-	-
FR93	62.28	FR_s8	th	D	114.6	56.2	5.5	-	-	-	-	-
FR95	63.43	FR_s8	af	A	72.7	41.0	5.5	356.3	68.7	12.5	239.7	80.2
FR97	64.15	FR_s8	th	D	23.2	75.1	4.6	-	-	-	-	-
FR99	65.47	FR_s8	af	A	5.2	59.7	23.2	343.7	21.4	12.3	102.2	55.4
FR100	65.87	FR_s8	th	A	359.4	73.4	5.9	331.9	32.7	14.8	125.7	55.6
FR102	67.63	FR_s8	af	A	322.9	55.1	7.0	320.1	40.8	13.5	145.8	51.9
FR104	69.27	FR_s8	th	D	78.7	39.2	18.8	-	-	-	-	-
FR145	70.76	FR_s9	af	A	24.5	71.3	7.4	323.7	59.8	7.2	171.5	63
FR107	71.29	FR_s8	af	A	2.9	46.0	14.4	322.6	66	11.7	188.6	63.4
FR109	72.26	FR_s8	af	A	81.4	74.8	15.0	345.8	22	7.1	99	56.5
FR140	72.27	FR_s9	th	D	355.0	64.2	6.2	-	-	-	-	-
FR112	73.41	FR_s8	af	A	6.5	68.0	1.8	14.6	45.1	14.0	31.8	70.1
FR137	73.49	FR_s9	th	A	15.5	59.8	3.8	341.4	49.3	9.2	129.4	70.6
FR114	74.03	FR_s8	th	D	10.0	58.1	18.4	-	-	-	-	-
FR134	74.34	FR_s9	th	D	-	-	-	-	-	-	-	-
FR133	74.71	FR_s9	af	A	348.1	66.1	5.2	40.3	75.6	6.1	288.4	59.2

Table B.1 Results of paleomagnetic analysis of samples from the Flagstaff Rim section (continued on the next page)

Sample	m	Section	Dm	Q	Low temperature component			High temperature component				
	Level				D	I	MAD	D	I	MAD	VGP lon	VGP lat
FR115	75.02	FR_s8	th	D	352.8	63.4	8.3	-	-	-	-	-
FR132	75.06	FR_s9	th	D	19.3	76.5	0.5	-	-	-	-	-
FR116	75.22	FR_s8	th	A	358.0	55.3	3.6	333.5	68.2	17.7	198.4	70.1
FR130	75.92	FR_s9	th	D	13.5	70.1	6.7	-	-	-	-	-
FR128	76.37	FR_s9	th	D	-	-	-	-	-	-	-	-
FR127	76.88	FR_s9	af	B	308.6	79.7	17.7	86.4	52.7	7.8	319.4	24.2
FR121	77.04	FR_s9	af	A	10.5	57.8	3.6	133.5	-46.5	6.4	337.1	-49.8
FR126	77.41	FR_s9	th	A	351.6	74.3	4.6	196.3	-23.2	7.8	223.5	-56.4
FR117	77.80	FR_s8	th	D	354.3	46.1	9.7	-	-	-	-	-
FR125	77.82	FR_s9	th	C	339.2	70.9	7.8	216.3	-35	25.8	189.1	-51.6
FR123	78.63	FR_s9	th	C	10.2	66.6	5.7	180.8	-38.4	31.1	251.1	-69
FR122	78.73	FR_s9	af	B	12.7	21.7	16.2	112.6	-17.4	15.0	334.3	-22.6
FR147	79.48	FR_s10	af	B	32.5	60.0	23.2	205.8	48.2	9.9	230.1	-14.4
FR149	80.23	FR_s10	af	D	30.8	32.1	12.9	-	-	-	-	-
FR154	82.34	FR_s10	th	B	344.9	72.6	17.6	258.6	-13.1	14.7	166	-12.9
FR157	83.33	FR_s10	af	D	6.0	48.8	12.7	-	-	-	-	-
FR159	84.13	FR_s10	th	D	24.2	74.1	8.7	-	-	-	-	-
FR161	85.00	FR_s10	af	A	12.2	66.8	6.7	145.1	-49.6	14.8	331.1	-59.7
FR162	85.28	FR_s10	af	A	21.4	66.3	5.4	163.6	-62.2	14.4	353	-78
FR168	87.04	FR_s10	af	A	46.6	50.9	12.0	162.5	-80.5	13.9	62.2	-59.8
FR169	87.37	FR_s10	af	A	355.6	56.9	5.4	174.4	-81.5	4.9	70.1	-59.1
FR171	87.99	FR_s10	th	D	29.6	45.5	6.4	-	-	-	-	-
FR172	88.41	FR_s10	af	A	305.7	75.2	12.5	176	-55.2	7.1	278.8	-82.5
FR173	88.81	FR_s10	af	A	332.0	75.0	12.7	183.4	-67.4	8.3	89.1	-82
FR175	89.01	FR_s10	af	B	13.2	37.0	3.4	57.5	-46	11.8	24.6	2.3
FR177	89.73	FR_s10	th	D	334.2	65.2	13.1	-	-	-	-	-
FR178	90.44	FR_s10	af	A	15.1	65.5	5.6	158.7	-53.1	13.6	322.1	-71.1
FR179	90.89	FR_s10	af	A	306.1	62.4	8.4	186.1	-40.6	18.8	236.6	-69.9
FR180	91.36	FR_s10	th	D	11.9	65.0	6.9	-	-	-	-	-
FR183	92.98	FR_s10	af	A	359.6	59.0	6.6	168.7	-61.3	12.9	345.7	-81.7
FR184	93.24	FR_s10	af	A	355.4	53.7	5.7	168.8	-51.7	13.6	297.7	-76.4
FR186	93.88	FR_s10	af	D	2.3	68.2	5.1	-	-	-	-	-

Table B.1 Results of paleomagnetic analysis of samples from the Flagstaff Rim section (continued on the next page)

Sample	m	Section	Dm	Q	Low temperature component			High temperature component				
	Level				D	I	MAD	D	I	MAD	VGP lon	VGP lat
FR187	94.93	FR_s10	th	D	351.4	55.0	3.1	-	-	-	-	-
FR188	95.31	FR_s10	af	B	327.1	53.1	21.6	354.3	-55.5	18.9	77.9	11.2
FR190	96.22	FR_s10	af	D	6.1	55.0	4.7	-	-	-	-	-
FR261	98.33	FR_s12	th	A	155.1	23.0	5.1	166.4	-17.7	9.9	276.7	-54.4
FR263	99.12	FR_s12	th	C	53.0	41.2	1.3	222.2	18	24.7	206	-25.4
FR265	99.87	FR_s12	th	D	333.2	34.5	10.6	-	-	-	-	-
FR267	100.92	FR_s12	th	D	342.1	81.2	6.4	-	-	-	-	-
FR269	101.76	FR_s12	th	A	52.3	46.5	17.0	173.2	-48.3	9.3	277.8	-75.6
FR273	103.85	FR_s12	th	D	310.4	75.0	3.2	-	-	-	-	-
FR275	104.64	FR_s12	th	A	22.6	82.4	11.6	238.6	-24.3	12.9	175.5	-31.5
FR279	106.50	FR_s12	th	A	167.5	44.9	11.9	186.1	-66.3	16.7	105.9	-82.5
FR281	107.46	FR_s12	th	A	334.2	84.8	34.5	203.5	-22.1	16.1	213	-52.8
FR283	108.28	FR_s12	th	A	302.7	66.0	22.2	168.1	-32.9	10.2	279.1	-63.3
FR285	109.19	FR_s12	th	D	26.9	73.0	15.7	-	-	-	-	-
FR287	109.91	FR_s12	th	A	333.1	67.4	5.2	165.7	-28.2	9.6	281.5	-59.8
FR289	110.78	FR_s12	th	D	17.0	73.4	10.1	-	-	-	-	-
FR291	112.13	FR_s12	th	A	37.2	45.1	42.0	183.5	-53.5	5.3	234.3	-81
FR293	112.78	FR_s12	th	A	345.9	69.8	20.8	181	-58.6	6.1	239.9	-86.6
FR295	113.85	FR_s12	th	A	320.7	63.2	3.1	145	-67.4	12.6	13.1	-65
FR297	114.95	FR_s12	th	A	17.9	64.8	9.2	173.2	-44.4	9.9	274	-72.6
FR300	116.31	FR_s12	th	A	353.7	77.5	19.7	127.5	-44.3	10.4	339.4	-44.4
FR303	117.58	FR_s12	th	A	19.7	-6.4	5.4	208.7	-39.2	17.5	194.6	-58.6
FR304	117.95	FR_s12	th	A	6.8	59.4	4.8	158.6	-39.9	17.1	301.7	-63.3
FR305	119.14	FR_s12	th	A	37.2	74.1	10.2	197.3	-65.4	6.1	135.3	-76.9
FR307	119.75	FR_s12	th	A	-	-	-	143.8	-44.3	18.4	325.6	-56.2
FR308	120.17	FR_s12	th	B	59.6	81.3	19.2	228.6	53.5	7.9	214.8	-1.4
FR311	121.72	FR_s12	th	D	58.8	50.7	8.0	-	-	-	-	-
FR312	122.02	FR_s12	th	A	359.6	76.9	7.4	196	-40.4	18.3	214	-66.4
FR315	123.19	FR_s12	th	A	50.5	64.5	12.7	187	-36.8	7.0	236.1	-67.1
FR318	124.21	FR_s12	th	B	14.4	72.7	4.3	100.3	-46.2	14.5	358.2	-25.4
FR321	125.33	FR_s12	th	D	57.6	63.1	7.6	-	-	-	-	-
FR322	125.84	FR_s12	th	D	12.2	48.3	6.5	-	-	-	-	-

Table B.1 Results of paleomagnetic analysis of samples from the Flagstaff Rim section (continued on the next page)

Sample	m	Section	Dm	Q	Low temperature component			High temperature component				
	Level				D	I	MAD	D	I	MAD	VGP lon	VGP lat
FR325	126.96	FR_s12	th	A	27.5	52.0	13.8	153.1	-86.1	10.9	67.8	-49.4
FR327	127.80	FR_s12	th	A	7.5	66.0	5.7	345.8	66.9	15.1	203.3	78
FR329	128.70	FR_s12	th	D	13.5	78.1	14.7	-	-	-	-	-
FR331	129.59	FR_s12	th	A	354.9	98.1	4.5	352.4	67.8	18.4	223.4	80.3
FR333	130.71	FR_s12	th	A	11.5	70.9	9.1	342	49.9	16.5	129.4	71.4
FR336	131.62	FR_s12	th	C	356.2	70.4	1.5	57.8	69.5	27.3	306.8	51
FR338	132.44	FR_s12	th	A	35.2	78.4	6.5	353.5	66.4	8.3	219.5	82.3
FR341	133.59	FR_s12	th	A	2.2	54.1	5.4	357.8	59.5	9.2	109.9	87.2
FR343	135.45	FR_s12	th	A	305.2	26.9	3.6	321	46.7	7.8	151.1	55.3
FR345	136.52	FR_s12	th	A	104.7	68.9	10.1	87.8	74.9	18.1	290	37.5
FR347	137.32	FR_s12	th	A	71.5	83.5	7.7	37	56.5	8.1	341.7	61.3
FR349	138.07	FR_s12	th	A	35.2	57.5	8.2	21.7	72.9	18.6	286.3	69.2
FR351	138.95	FR_s12	th	A	17.9	61.8	3.2	7.4	52.3	7.0	39.8	78.7
FR353	140.59	FR_s12	th	A	37.6	67.4	7.9	359.1	57.5	14.2	82.2	85.5
FR355	141.69	FR_s12	th	D	111.7	-12.7	2.3	-	-	-	-	-
FR357	142.82	FR_s12	th	A	2.8	68.1	3.5	328.2	70.9	18.5	206	65.9
FR359	143.76	FR_s12	th	A	6.9	67.2	5.8	337.3	61.8	19.4	172.3	73.4
FR360	145.14	FR_s12	th	C	288.5	70.4	9.8	2.2	70	24.0	259.7	78.6
FR362	146.17	FR_s12	th	A	52.5	54.2	7.4	13.5	72.5	11.5	277.8	72.6
FR364	147.35	FR_s12	th	D	14.8	74.9	9.3	-	-	-	-	-
FR366	148.25	FR_s12	th	D	17.2	64.9	1.8	-	-	-	-	-
FR368	149.65	FR_s12	th	A	6.3	61.5	3.6	172.4	-42.9	8.7	275.1	-71.2
FR370	151.98	FR_s12	th	A	318.9	75.0	14.3	221.5	-64.8	11.6	140.6	-60.5
FR372	153.25	FR_s12	th	D	27.6	66.8	11.7	-	-	-	-	-
FR376	156.10	FR_s12	th	D	276.1	49.3	3.9	-	-	-	-	-
FR205	157.05	FR_s11	th	D	18.8	55.3	5.6	-	-	-	-	-
FR207	159.70	FR_s11	th	A	7.4	82.4	15.0	159.1	-31.4	15.1	294.4	-58.8
FR208	160.18	FR_s11	af	A	2.9	64.4	14.6	157.4	-39.8	10.9	303.6	-62.6
FR210	161.08	FR_s11	af	A	223.4	73.9	10.4	179.2	-38.6	14.9	255.3	-69.1
FR211	161.39	FR_s11	af	A	115.0	72.1	22.7	192.3	-30.5	12.2	227.6	-61.8
FR215	163.38	FR_s11	af	A	333.3	49.0	5.0	163.3	-44.8	10.3	298.7	-68.8
FR217	164.72	FR_s11	af	A	343.6	57.1	11.3	157.8	-49.6	3.0	316	-68.5

Table B.1 Results of paleomagnetic analysis of samples from the Flagstaff Rim section (continued on the next page)

Sample	m	Section	Dm	Q	Low temperature component			High temperature component				
	Level				D	I	MAD	D	I	MAD	VGP lon	VGP lat
FR218	165.12	FR_s11	th	A	14.0	40.9	2.5	184.8	-42.1	9.1	239.4	-71.3
FR219	165.60	FR_s11	th	D	27.7	52.4	5.5	-	-	-	-	-
FR220	165.80	FR_s11	af	A	22.4	72.6	8.3	154.8	-38.9	7.1	306.7	-60.6
FR222	167.27	FR_s11	th	D	36.5	81.0	2.4	-	-	-	-	-
FR226	168.67	FR_s11	af	A	0.1	60.0	3.7	344.1	73.7	6.1	228.9	70.3
FR227	169.45	FR_s11	th	A	350.2	55.8	2.3	28.9	59.6	10.5	339.1	68.4
FR228	170.08	FR_s11	af	A	341.3	51.5	5.7	358.9	49.9	6.4	77.8	78.1
FR229	170.65	FR_s11	th	D	339.9	68.1	1.5	-	-	-	-	-
FR230	171.43	FR_s11	af	A	337.8	70.8	3.3	356.2	66.2	4.0	230.6	83.5
FR231	171.82	FR_s11	th	C	25.1	65.5	6.4	283.1	56.5	33.5	185.7	32.8
FR233	172.78	FR_s11	th	A	15.3	70.4	2.9	37.2	70.5	5.6	303.6	63
FR235	174.06	FR_s11	af	A	349.2	65.2	2.3	351.5	68.7	8.7	224.9	78.9
FR237	174.81	FR_s11	th	A	349.7	63.1	6.5	45.3	68.1	8.4	311.5	58.4
FR238	175.31	FR_s11	af	A	5.6	66.7	0.9	356.5	74.8	4.8	248.1	71
FR239	175.71	FR_s11	th	A	12.2	47.1	15.8	3.3	67.9	7.6	267.2	81.4
FR242	175.76	FR_s11	af	A	339.1	68.0	5.7	345.4	69.8	5.5	217.1	75.3
FR245	177.10	FR_s11	th	A	335.5	64.1	3.7	328.4	67.3	15.0	193.3	67.1
FR246	177.36	FR_s11	af	A	33.2	63.7	4.2	330.5	73.7	7.3	216.9	65.2
FR250	178.89	FR_s11	af	A	341.8	73.3	2.0	14.8	73.8	3.2	275.8	70.5
FR251	179.38	FR_s11	th	A	345.8	58.8	2.3	304.3	75.7	17.6	215.3	52.3
FR252	179.81	FR_s11	th	D	10.6	52.9	3.0	-	-	-	-	-
FR253	180.37	FR_s11	th	A	2.8	63.5	3.1	7.4	63.7	8.0	313.5	84
FR255	181.45	FR_s11	af	A	12.9	63.9	4.0	322	76.9	3.6	222.8	59.1
FR256	182.24	FR_s11	th	A	357.7	64.2	4.5	359.4	41.8	18.0	74.9	71.5
FR258	182.50	FR_s11	th	A	2.3	60.3	8.1	288.3	65.2	11.1	194.8	40.8

Table B.1 Results of paleomagnetic analysis of samples from the Flagstaff Rim section

Sample	m level	Section	Dm	Q	Low temperature component			High temperature component				
					D	I	MAD	D	I	MAD	VGP lon	VGP lat
TP83	0.00	TP_s7	th	D	-	-	-	-	-	-	-	-
TP82	0.57	TP_s7	th	D	5.0	30.6	14.2	-	-	-	-	-
TP78	2.25	TP_s6	af	B	344.3	31.7	11.7	228.7	-36.6	13.7	179.6	-43.7
TP74b	3.46	TP_s5	af	A	0.5	39.0	10.0	356.5	43.5	1.4	87.4	72.6
TP72	4.00	TP_s5	af	A	322.2	54.1	8.3	133.3	-36.9	9.3	332.3	-45.3
TP68	5.10	TP_s4	af	D	-	-	-	-	-	-	-	-
TP67	5.28	TP_s4	af	B	296.9	61.3	37.5	225.1	-16.4	11.2	194.2	-37.8
TP64	6.37	TP_s4	th	D	56.0	64.1	12.1	-	-	-	-	-
TP59	7.70	TP_s4	af	D	16.0	19.1	10.0	-	-	-	-	-
TP58	8.16	TP_s4	th	D	23.6	55.6	19.6	-	-	-	-	-
TP57	8.39	TP_s4	af	B	14.6	52.6	9.3	45.2	31.7	12.4	6	44.1
TP56	8.69	TP_s4	af	A	17.2	31.9	11.3	347.6	40.1	13.2	108.3	67.8
TP50	8.97	TP_s4	af	D	183.6	-13.0	8.0	-	-	-	-	-
TP54	9.14	TP_s4	af	B	14.5	36.2	8.7	238.3	-26.4	11.6	178.1	-32.6
TP52	9.57	TP_s4	th	D	-	-	-	-	-	-	-	-
TP48	9.60	TP_s3	af	D	22.0	-12.7	13.7	-	-	-	-	-
TP46	9.82	TP_s3	af	D	156.3	34.5	4.1	-	-	-	-	-
TP43	10.01	TP_s2	af	D	-	-	-	-	-	-	-	-
TP42	10.34	TP_s2	th	D	-	-	-	-	-	-	-	-
TP41	10.60	TP_s2	th	D	303.5	45.5	14.1	-	-	-	-	-
TP39	11.19	TP_s2	af	A	357.7	49.2	27.3	351.0	46.5	6.8	106	73.6
TP36	11.79	TP_s2	th	D	-	-	-	-	-	-	-	-
TP35	11.94	TP_s2	af	D	-	-	-	-	-	-	-	-
TP33	12.31	TP_s2	th	D	339.0	56.9	6.0	-	-	-	-	-
TP32	12.81	TP_s2	af	A	347.1	61.9	17.7	304.2	62.2	8.9	187.8	50
TP31	13.10	TP_s2	af	A	-	-	-	335.4	56.3	19.6	158.3	70.3
TP30	13.36	TP_s2	af	D	-	-	-	-	-	-	-	-
TP29	13.63	TP_s2	af	D	15.0	87.9	11.5	-	-	-	-	-
TP28	13.99	TP_s2	af	D	11.2	73.7	16.3	-	-	-	-	-
TP27	14.30	TP_s2	af	D	7.6	50.8	5.5	-	-	-	-	-
TP26	14.74	TP_s2	af	D	-	-	-	-	-	-	-	-
TP25	15.01	TP_s2	af	D	15.0	58.2	4.7	-	-	-	-	-

Table B.1 Results of paleomagnetic analysis of samples from the Toadstool Park section (continued on the next page)

Sample	m level	Section	Dm	Q	Low temperature component			High temperature component				
					D	I	MAD	D	I	MAD	VGP lon	VGP lat
TP24	15.32	TP_s2	th	D	116.3	60.1	16.5	-	-	-	-	-
TP22b	16.36	TP_s1	af	A	304.9	-38.7	15.2	126.5	-37.5	10.2	338.3	-40.7
TP19b	17.25	TP_s1	af	A	321.0	68.5	20.3	205.3	-38.3	12.1	203.5	-60.2
TP16	18.45	TP_s1	af	A	-	-	-	121.1	-36.0	9.9	341.3	-36.1
TP17	18.45	TP_s1	af	B	358.4	57.3	3.5	259.0	-27.1	16.6	163.2	-17.7
TP15	18.76	TP_s1	af	B	47.6	71.7	21.2	243.5	-49.3	8.2	158.6	-38.6
TP14	19.09	TP_s1	th	D	277.2	10.2	20.4	-	-	-	-	-
TP13	19.66	TP_s1	af	D	-	-	-	-	-	-	-	-
TP12	19.98	TP_s1	af	D	14.0	69.2	15.0	-	-	-	-	-
TP11	20.32	TP_s1	af	D	-	-	-	-	-	-	-	-
TP10	20.67	TP_s1	th	D	33.1	55.2	14.5	-	-	-	-	-
TP9	21.02	TP_s1	af	C	351.1	44.2	15.2	336.7	42.6	23.6	131.3	63.8
TP8	21.46	TP_s1	af	C	-	-	-	198.5	-42.3	28.3	210.6	-66.4
TP6	22.06	TP_s1	af	A	6.6	65.4	13.9	179.6	-33.0	10.5	257.6	-65.5
TP5	22.31	TP_s1	af	A	-	-	-	196.5	-48.5	12.0	205.8	-71.4
TP4	22.53	TP_s1	af	D	64.7	57.8	10.8	-	-	-	-	-
TP3	22.71	TP_s1	af	A	330.2	50.8	6.0	176.8	-29.1	18.3	263.5	-62.9
TP2	22.91	TP_s1	af	D	-	-	-	-	-	-	-	-
TP1	22.98	TP_s1	af	A	-	-	-	193.4	-43.6	13.1	219.6	-69.7
TP103	23.13	TP_s8	th	C	24.4	74.2	5.4	112.2	-45.8	25.6	354.3	-33.8
TP102	23.56	TP_s8	af	A	32.2	75.9	5.8	322.1	47.9	16.8	155.2	56.7
TP101	23.91	TP_s8	af	A	-	-	-	319.7	68.7	4.9	200.3	61.5
TP97	25.68	TP_s8	th	C	27.8	73.4	23.0	313.5	71.4	29.3	207.7	57.5
TP95	26.08	TP_s8	th	D	196.9	70.9	35.2	-	-	-	-	-
TP94	26.85	TP_s8	th	C	319.0	48.0	37.6	141.9	-35.8	24.4	323.4	-50.8
TP92	27.45	TP_s8	th	A	343.7	48.3	11.4	144.4	-24.5	13.8	313.5	-47.3
TP90	28.04	TP_s8	th	C	-	-	-	208.1	-58.9	21.0	164.9	-68.7
TP86	29.20	TP_s8	af	D	-	-	-	-	-	-	-	-
TP84	30.15	TP_s8	th	D	9.5	66.6	5.7	-	-	-	-	-
TP126	30.85	TP_s9	th	D	284.3	30.7	17.3	-	-	-	-	-
TP125	31.29	TP_s9	th	A	327.9	64.8	10.0	339.9	16.5	18.8	109.9	51.6
TP122	32.68	TP_s9	af	D	9.2	65.3	3.3	-	-	-	-	-

Table B.1 Results of paleomagnetic analysis of samples from the Toadstool Park section (continued on the next page)

Sample	m	Section	Dm	Q	Low temperature component			High temperature component				
	Level				D	I	MAD	D	I	MAD	VGP lon	VGP lat
TP119	34.03	TP_s9	th	D	43.9	39.4	5.2	-	-	-	-	-
TP117	34.56	TP_s9	th	D	345.6	72.0	22.1	-	-	-	-	-
TP116	34.95	TP_s9	th	D	48.4	33.7	12.2	-	-	-	-	-
TP113	35.75	TP_s9	th	D	346.2	53.4	7.5	-	-	-	-	-
TP110	36.50	TP_s9	af	D	332.7	60.6	6.4	-	-	-	-	-
TP197	38.53	TP_s13	th	D	202.9	50.8	29.5	-	-	-	-	-
TP193	39.66	TP_s13	th	D	158.5	4.3	35.2	-	-	-	-	-
TP190	40.53	TP_s13	th	A	194.7	38.5	8.4	156.4	-54.1	7.9	331.4	-70
TP189	41.09	TP_s13	th	A	220.1	42.1	9.9	181.1	21.9	11.4	255.4	-36.1
TP187	41.44	TP_s13	th	A	47.2	31.6	29.3	190.4	-64.8	7.0	133.3	-81.5
TP186	41.66	TP_s13	th	A	318.5	46.5	5.6	140.8	-50.0	14.4	339.1	-56.8
TP183	42.64	TP_s13	th	D	345.4	60.6	3.7	-	-	-	-	-
TP182	42.89	TP_s13	th	C	230.2	74.1	10.4	335.1	30.4	29.1	123.4	56.3
TP180	43.24	TP_s13	th	A	340.9	51.3	31.7	148.9	-45.4	16.2	325.1	-60.3
TP179	43.44	TP_s13	th	C	341.0	50.9	19.8	69.1	38	20.4	343.8	29.4
TP178	43.69	TP_s13	th	D	17.8	60.5	5.7	-	-	-	-	-
TP170	46.58	TP_s12	th	D	18.9	46.6	5.5	-	-	-	-	-
TP168	46.83	TP_s12	th	B	136.2	-23.7	6.7	104.7	82.4	19.7	274.9	37.2
TP163	48.51	TP_s10	th	A	7.4	51.5	12.7	353.4	35.5	4.4	92.4	66.5
TP162	48.58	TP_s10	af	A	35.9	84.1	9.9	7.4	56.2	7.3	29.5	81.9
TP160	48.93	TP_s10	af	A	301.9	61.5	25.6	316.6	58.2	4.9	175.3	57.3
TP157	49.98	TP_s10	af	A	349.6	70.8	11.9	291.6	46.2	3.0	175	33.6
TP156	50.08	TP_s10	th	A	353.7	70.0	12.1	294	47.2	3.0	174.4	35.8
TP154	50.51	TP_s10	af	A	357.3	70.7	9.7	29.7	60.5	1.9	339.3	68
TP148	52.24	TP_s10	th	A	281.9	48.5	18.1	20.9	54.4	6.7	4.7	72.1
TP144	52.94	TP_s10	af	A	326.2	48.9	23.8	334.2	25.7	4.0	122	53.5
TP141	53.69	TP_s10	th	A	348.8	55.9	6.0	335.7	33.2	12.7	124.4	58.1
TP139	54.64	TP_s10	af	A	306.0	50.3	3.6	308.9	17.4	15.3	145.1	34.2
TP136	55.54	TP_s10	th	B	12.8	39.7	13.5	88.1	71.2	14.7	300	34.9
TP135	55.85	TP_s10	th	A	6.9	50.1	17.7	344.7	37.3	7.6	112.1	64.8
TP132	56.70	TP_s10	af	A	327.1	52.6	19.3	312.5	56.8	5.4	175	53.7
TP129	57.73	TP_s10	th	A	5.1	65.1	10.0	325.3	55.4	5.0	164.6	62.5

Table B.1 Results of paleomagnetic analysis of samples from the Toadstool Park section (continued on the next page)

Sample	m Level	Section	Dm	Q	Low temperature component			High temperature component				
					D	I	MAD	D	I	MAD	VGP lon	VGP lat
TP208	58.86	TP_s14	af	A	344.1	67.5	6.8	320	62.9	5.4	184.2	61.2
TP204	60.01	TP_s14	th	C	27.1	65.8	4.3	339.4	53.5	20.1	145.8	71.8
TP203	60.4	TP_s14	th	A	17.6	63.7	51.5	338.1	57.7	7.4	160	72.9
TP202	60.91	TP_s14	af	A	350.5	76.0	12.6	310.2	31.2	3.4	151.1	40.6
TP218	61.56	TP_s16	th	A	351.4	58.7	10.6	352.7	57.6	7.8	131.6	83
TP217	61.8	TP_s16	af	A	16.4	53.0	8.0	5.8	54.3	4.9	44.3	81.1
TP215	62.53	TP_s16	th	A	23.6	60.5	18.2	312.9	40.2	4.0	155.3	46.5
TP214	62.83	TP_s16	af	A	353.4	65.7	6.2	336.7	49.1	3.5	140.5	67.5
TP213	63.43	TP_s15	th	A	26.2	37.9	19.3	359.3	49.3	5.7	79.5	77.7
TP212	63.81	TP_s15	th	A	4.6	34.1	12.2	2.1	27.2	7.5	72.4	61.9
TP211	64.09	TP_s15	th	A	64.4	43.3	2.3	39.6	46.7	10.3	358.2	54.9
TP209	64.62	TP_s15	th	A	32.4	47.7	0.8	5.4	29.4	3.3	65.3	62.8
TP221	65.32	TP_s17	th	D	34.1	60.7	4.3	-	-	-	-	-
TP228	66.62	TP_s18	th	A	14.9	61.3	9.6	189.2	-52.5	14.8	216.1	-78.1
TP226	67.24	TP_s18	af	A	23.0	68.9	4.6	160.1	-58.7	14.3	341.8	-74.7
TP223a	68.4	TP_s18	af	A	344.0	61.3	8.7	139.1	-63.4	11.1	5.7	-60.7
TP223b	68.4	TP_s18	th	A	347.9	33.3	2.1	176.1	-30	14.5	265.1	-63.4
TP230	69.92	TP_s19	th	A	46.8	52.8	2.9	48.6	63.2	13.4	326	55.3
TP231	70.64	TP_s19	af	A	9.5	67.6	4.6	156.9	-62.2	8.4	357.9	-73.1
TP233	71.62	TP_s19	th	A	19.3	70.9	0.5	129	-49.5	15.3	347.2	-47.9
TP234	71.62	TP_s19	th	A	2.1	62.8	8.0	7.9	23.4	11.5	61.6	58.9
TP238	74.37	TP_s19	th	A	49.8	70.6	1.6	157.9	-63	12.3	1.2	-73.9
TP242	76.52	TP_s19	af	A	25.3	63.9	6.3	165	-64.1	18.0	9.1	-78.8
TP244	77.12	TP_s19	th	A	15.0	79.6	34.2	142.1	-78.9	12.2	52.2	-57.3
TP245	78.02	TP_s19	af	C	7.5	53.0	1.3	144.6	-42	31.3	326	-55.6
TP247	78.92	TP_s20	th	A	345.9	65.5	3.1	161.8	-64.3	16.2	8.4	-76.5
TP248	79.62	TP_s20	th	D	356.2	53.7	11.8	-	-	-	-	-
TP250	81.09	TP_s20	af	A	94.9	78.2	17.4	195.1	-43.4	11.2	216.1	-68.8
TP251	81.49	TP_s20	th	D	354.7	50.1	6.8	-	-	-	-	-
TP252	82.07	TP_s20	th	D	9.8	64.3	1.7	-	-	-	-	-
TP253	82.62	TP_s20	th	A	336.0	55.1	4.2	350.4	46.5	9.3	107.7	73.3
TP254	83.1	TP_s20	af	A	2.6	53.9	2.1	352.8	30.5	13.9	92.2	63.2

Table B.1 Results of paleomagnetic analysis of samples from the Toadstool Park section (continued on the next page)

Sample	m Level	Section	Dm	Q	Low temperature component			High temperature component					
					D	I	MAD						
TP256	84.14	TP_s20	th	D	331.4	48.3	14.4	-	-	-	-	-	-
TP261	84.81	TP_s21	th	D	315.9	51.6	13.5	-	-	-	-	-	-
TP260	85.41	TP_s21	af	A	9.4	68.7	3.4	194	-45.6	9.0	215.8	-70.8	
TP258	86.03	TP_s21	th	A	337.3	51.1	5.3	136.1	-39.2	7.7	331.7	-48.3	
TP257	86.65	TP_s21	th	A	347.2	48.6	4.9	118.9	-43.6	7.8	348.3	-37.7	
TP262	88.62	TP_s22	th	D	5.6	69.7	4.6	-	-	-	-	-	-
TP263	88.72	TP_s22	th	D	7.0	61.9	6.2	-	-	-	-	-	-
TP267	91.3	TP_s22	th	A	18.6	62.3	6.7	165.9	-32.2	10.0	286.6	-62.2	
TP268	91.78	TP_s22	th	A	345.1	75.6	8.4	185.2	-57.4	11.5	213.5	-84	
TP269	92.38	TP_s22	af	A	25.5	69.4	2.0	148.3	-20.2	16.7	306.8	-47.7	
TP270	92.62	TP_s22	th	D	345.8	63.9	15.4	-	-	-	-	-	-
TP273	94.04	TP_s22	th	A	84.4	40.0	4.1	203.1	-41.3	14.8	203.9	-63.2	
TP275	94.94	TP_s22	th	D	43.1	74.6	2.7	-	-	-	-	-	-
TP277	95.94	TP_s23	th	A	6.6	84.7	4.1	124.7	-44.7	16.4	345.3	-42.5	
TP278	96.34	TP_s23	th	A	7.0	54.8	2.5	186.7	-39.4	7.0	239.1	-69.1	
TP280	97.84	TP_s23	th	D	22.5	63.6	0.7	-	-	-	-	-	-
TP281	98.54	TP_s23	af	A	346.2	64.1	2.1	194.2	-67.3	7.8	124	-77.6	
TP283	99.89	TP_s23	th	A	340.6	71.2	5.2	170.4	-36.8	10.1	279.8	-66.6	
TP284	100.59	TP_s23	th	A	11.9	61.6	2.3	173.8	-41.7	9.8	274.2	-70.8	
TP285	101.31	TP_s23	af	A	358.7	75.5	0.9	193	-11.7	14.7	235.6	-51.6	
TP286	102.23	TP_s23	af	A	17.4	66.1	2.6	180.4	-47.7	3.4	255.2	-76.3	
TP288	103.68	TP_s23	th	A	295.5	76.5	8.6	174	-40.8	18.7	273.2	-70.2	
TP289	104.28	TP_s23	th	A	344.5	71.5	3.9	331.9	20.3	12.7	122.4	49.7	
TP290	105.03	TP_s23	th	D	35.4	57.1	7.1	-	-	-	-	-	-
TP291	105.63	TP_s23	th	D	28.2	66.4	2.4	-	-	-	-	-	-
TP293	107.02	TP_s23	af	A	6.1	73.9	1.3	182.9	-75.8	19.9	80.4	-69.3	
TP294	108.06	TP_s23	th	C	310.0	71.1	3.3	217.2	24.9	30.3	216.3	-24.8	
TP295	108.45	TP_s23	th	A	356.9	65.9	5.2	312.3	57.8	12.0	176.7	54	
TP296	108.92	TP_s23	af	D	300.5	74.1	3.2	-	-	-	-	-	-
TP297	109.28	TP_s23	th	C	334.3	71.6	5.4	276.3	51.6	28.8	188.2	25.4	
TP298	110.03	TP_s23	th	A	17.9	69.0	4.4	325.1	29.4	9.0	135.5	49.9	
TP301	112.48	TP_s23	af	C	4.2	68.1	8.4	249.3	59.2	31.8	209.2	13.6	

Table B.1 Results of paleomagnetic analysis of samples from the Toadstool Park section (continued on the next page)

Sample	m level	Section	Dm	Q	Low temperature component			High temperature component				
					D	I	MAD	D	I	MAD	VGP lon	VGP lat
TP302	113.32	TP_s23	th	C	11.7	61.5	7.1	108.2	42.6	28.3	316.6	4.2
TP303	114.67	TP_s23	th	C	30.6	35.5	4.2	118.5	23.9	32.4	317.8	-11.4
TP304	115.38	TP_s23	th	C	37.7	59.1	6.4	124.1	19.8	30.8	315	-16.7
TP308	118.36	TP_s24	th	A	62.3	70.6	2.9	156.3	-38.2	9.7	307.4	-61.1
TP310	119.86	TP_s24	th	A	1.5	68.3	1.4	142.5	-37.1	6.5	323.8	-51.8
TP311	121.06	TP_s24	th	A	329.8	68.6	2.0	150.2	-35.4	11.5	313.6	-56
TP312	122.31	TP_s24	th	A	21.1	73.3	1.0	183.2	-24.8	12.5	250.4	-60.4
TP314	124.06	TP_s24	th	A	23.2	66.3	5.2	171.6	-39.2	6.1	278.4	-68.5
TP316	125.66	TP_s24	th	D	356.9	66.3	1.6	-	-	-	-	-
TP317	126.36	TP_s24	th	A	343.1	78.8	7.7	145.9	-59.2	7.9	352.7	-64.4
TP319	127.56	TP_s24	th	A	0.6	68.0	2.5	221.9	-39.8	17.9	183	-50
TP320	128.46	TP_s24	th	A	5.6	56.5	1.7	164.7	-52.3	6.3	313.2	-74.6
TP321	129.64	TP_s24	th	D	356.0	59.9	5.0	-	-	-	-	-
TP322	130.09	TP_s24	th	A	8.8	54.0	13.4	183.8	-55.5	6.4	231	-82.9
TP323	130.99	TP_s24	th	A	20.2	61.1	7.4	46.5	78.9	6.2	283.9	54.5
TP324	132.24	TP_s24	th	A	331.8	54.0	5.5	295.7	55.1	19.2	181.3	40.8
TP325	133.03	TP_s24	th	A	32.8	75.6	9.3	358.4	65	11.6	243.1	85.4
TP326	134.48	TP_s24	th	A	346.2	68.8	1.1	309.2	59.4	8.5	180.9	52.4
TP328	135.88	TP_s24	th	A	29.9	55.3	4.7	354.1	74.3	13.0	247.6	71.5
TP329	137.03	TP_s24	th	A	1.5	55.1	3.9	1.8	51	6.1	68.6	79.1
TP330	137.83	TP_s24	th	A	9.1	62.8	2.7	7.2	53.5	7.7	40.6	79.8
TP331	138.93	TP_s24	th	A	11.8	65.2	3.2	29.5	68.1	8.9	313	68.2
TP332	140.03	TP_s24	th	A	3.8	67.4	1.6	309.8	61	3.9	183.5	53.4
TP333	140.88	TP_s24	th	A	12.6	37.1	10.5	17.1	41.9	5.6	33.7	66.9
TP334	141.23	TP_s24	th	A	5.7	57.7	4.7	1.6	54.9	6.4	66.2	82.8
TP335	141.53	TP_s24	th	A	18.4	56.3	2.6	21.3	25.7	10.6	37.9	55.7

Table B.1 Results of paleomagnetic analysis of samples from the Toadstool Park section

References cited:

Agrinier, P. G., Y. Lewin, E. (1999). On the age calibration of the geomagnetic polarity timescale. *Geophysical Journal International,* 137, 81-90.

Alegret, L., Cruz, L. E., Fenero, R., Molina, E., Ortiz, S., and Thomas, E. (2008). Effects of the Oligocene climatic events on the foraminiferal record from Fuente Caldera section (Spain, western Tethys). *Palaeogeography Palaeoclimatology Palaeoecology*, 269, 94-102.

Alroy, J. (1998). Diachrony of mammalian appearance events: Implications for biochronology. *Geology*, 26, 23-26.

Alvarez, W., and Montanari, A. (1988). The Scaglia limestones (Late Cretaceous - Oligocene) in the northeastern Apennines carbonate sequence: stratigraphic context and geological significance. In "*The Eocene-Oligocene boundary in the Marche-Umbria basin (Italy)*." (I. Premoli Silva, R. Coccioni, and A. Montanari, Eds.), pp. 13-29. International Subcommission on Paleogene Stratigraphy, Ancona.

Baksi, A. K., Archibald, D. A., and Farrar, E. (1996). Intercalibration of $^{40}Ar/^{39}Ar$ dating standards. *Chemical Geology*, 129, 307-324.

Berggren, W. A., Kent, D. V., Flynn, J. J., and Vancouvering, J. A. (1985). Cenozoic Geochronology. *Geological Society of America Bulletin*, 96, 1407-1418.

Berggren, W. A., and Pearson, P. N. (2005). A revised tropical to subtropical paleogene planktonic foraminiferal zonation. *Journal of Foraminiferal Research*, 35, 279-298.

Bice, D. M., and Montanari, A. (1988). Magnetic stratigraphy of the Massignano section across the Eocene-Oligocene boundary. In "*The Eocene-Oligocene boundary in the Marche-Umbria basin (Italy)*." (I. Premoli Silva, R. Coccioni, and A. Montanari, Eds.), pp. 111-117. International Subcommission on Paleogene Stratigraphy, Ancona.

Billups, K., and Schrag, D. P. (2003). Application of benthic foraminiferal Mg/Ca ratios to questions of Cenozoic climate change. *Earth and Planetary Science Letters*, 209, 181-195.

Blaauw, M., and Christen, J. A. (2005). Radiocarbon peat chronologies and environmental change. *Journal of the Royal Statistical Society Series C-Applied Statistics*, 54, 805-816.

Boardman, G. S., and Secord, R. (2013). Stable isotope paleoecology of White River ungulates during the Eocene-Oligocene climate transition in northwestern Nebraska. *Palaeogeography Palaeoclimatology Palaeoecology*, 375, 38-49.

Bowring, J. F., McLean, N. M., and Bowring, S. A. (2011). Engineering cyber infrastructure for U-Pb geochronology: Tripoli and U-Pb_Redux. *Geochemistry Geophysics Geosystems* 12.

Bronk Ramsey, C. (2008). Deposition models for chronological records. *Quaternary Science Reviews* 27, 42-60.

Brown, R. E., Koeberl, C., Montanari, A., and Bice, D. M. (2009). Evidence for a change in Milankovitch forcing caused by extraterrestrial events at Massignano, Italy, Eocene-Oligocene boundary GSSP. *In* "Late Eocene Earth: Hothouse Icehouse and Impacts." pp. 119-137. Geological Society of America Special Paper.

Cande, S. C., and Kent, D. V. (1992). A New Geomagnetic Polarity Time Scale for the Late

Cretaceous and Cenozoic. *Journal of Geophysical Research-Solid Earth* 97, 13917-13951.

Cande, S. C., and Kent, D. V. (1995). Revised calibration of the geomagnetic polarity timescale for the Late Cretaceous and Cenozoic. *Journal of Geophysical Research-Solid Earth* 100, 6093-6095.

Channell, J. E. T., Hodell, D. A., Singer, B. S., and Xuan, C. (2010). Reconciling astrochronological and $^{40}Ar/^{39}Ar$ ages for the Matuyama-Brunhes boundary and late Matuyama Chron. *Geochemistry, Geophysics, Geosystems* 11, Q0AA12.

Charles, A. J., Condon, D. J., Harding, I. C., Pälike, H., Marshall, J. E. A., Cui, Y., Kump, L., and Croudace, I. W. (2011). Constraints on the numerical age of the Paleocene-Eocene boundary. *Geochemistry Geophysics Geosystems* 12.

Christen, J. A., and Perez, S. (2009). A new robust statistical model for radiocarbon data. *Radiocarbon,* 51, 1047-1059.

Clark, J. (1975). Controls of sedimentation and provenance of sediments in the Oligocene of the central Rocky Mountains. *In* "Cenozoic history of the southern Rocky Mountains." (B. F. Curtis, Ed.), pp. 97-117. Geological Society of America Memoir 144.

Coccioni, R., Basso, D., Brinkhuis, H., Galeotti, S., Gardin, S., Monechi, S., and Spezzaferri, S. (2000). Marine biotic signals across a late Eocene impact layer at Massignano, Italy: evidence for long-term environmental perturbations? *Terra Nova* 12, 258-263.

Coccioni, R., Frontalini, F., and Spezzaferri, S. (2009). Late Eocene impact-induced climate and hydrological changes: Evidence from the Massignano global stratotype section and point (central Italy). *In* "Late Eocene Earth: Hothouse Icehouse and Impacts." pp. 97-118. Geological Society of America Special Paper.

Coccioni, R., and Galeotti, S. (2003). Deep-water benthic foraminiferal events from the Massignano Eocene/Oligocene boundary stratotype section and point (central Italy): biostatigraphic, paleoecologic and paleoeanographic implications. *In* "From Greenhouse to Icehouse: the Marine Eocene-Oligocene Transition." (D. R. Prothero, L. Ivany, and E. A. Nesbitt, Eds.), pp. 438-452. Columbia University Press, New York.

Coccioni, R., Marsili, A., Montanari, A., Bellanca, A., Neri, R., Bice, D. M., Brinkhuis, H., Church, N., Macalady, A., McDaniel, A., Deino, A., Lirer, F., Sprovieri, M., Maiorano, P., Monechi, S., Nini, C., Nocchi, M., Pross, J., Rochette, P., Sagnotti, L., Tateo, F., Touchard, Y., Van Simaeys, S., and Williams, G. L. (2008). Integrated stratigraphy of the Oligocene pelagic sequence in the Umbria-Marche basin (northeastern Apennines, Italy): A potential Global Stratotype Section and Point (GSSP) for the Rupelian/Chattian boundary. *Geological Society of America Bulletin* 120, 487-511.

Coccioni, R., Monaco, P., Monechi, S., Nocchi, M., and Parisi, G. (1988). Biostratigraphy of the Eocene-Oligocene boundary at Massignano (Ancona, Italy). *In* "The Eocene-Oligocene boundary in the Marche-Umbria basin (Italy)." (I. Premoli Silva, R. Coccioni, and A. Montanari, Eds.), pp. 59-80. International Subcommission on Paleogene Stratigraphy, Ancona.

Coccioni, R., Sideri, M., Bancalà , G., Catanzariti, R., Frontalini, F., Jovane, L., Montanari, A., and Savian, J. (2012). Integrated stratigraphy (magneto-, bio- and chronostratigraphy) and geochronology of the Palaeogene pelagic succession of the Umbria-Marche Basin (central Italy). *Geological Society, London, Special Publications* 373.

Condon, D. J., and al, e. (in review). Metrology and Traceability of U-Pb Isotope Dilution Geochronology (EARTHTIME Tracer Calibration Part I). Geochemistry Geophysics Geosystems.

Condon, D. J., Schoene, B., Bowring, S. A., Parrish, R. R., McLean, N., Noble, S. R., and Crowley, Q. (2007). EARTHTIME: isotopic tracers and optimized solutions for high-precision U-Pb ID-TIMS geochronology. American Geophysical Union, Fall Meeting Abstract V41E-06.

Costa, E., Garces, M., Saez, A., Cabrera, L., and Lopez-Blanco, M. (2011). The age of the Grande Coupure mammal turnover: New constraints from the Eocene-Oligocene record of the Eastern Ebro Basin (NE Spain). *Palaeogeography, Palaeoclimatology, Palaeoecology* 301, 97-107.

Coxall, H. K., and Pearson, P. D. (2007). The Eocene-Oligocene transition. *In* "Deep-time perspectives on climate change: marrying the signal from computer models and biological proxies." (M. Williams, A. M. Haywood, F. J. Gregory, and D. N. Schmidt, Eds.), pp. 351-387. The Geological Society, London.

Coxall, H. K., Wilson, P. A., Pälike, H., Lear, C. H., and Backman, J. (2005). Rapid stepwise onset of Antarctic glaciation and deeper calcite compensation in the Pacific Ocean. *Nature* 433, 53-57.

Cramer, B. S., Toggweiler, J. R., Wright, J. D., Katz, M. E., and Miller, K. G. (2009). Ocean overturning since the Late Cretaceous: Inferences from a new benthic foraminiferal isotope compilation. *Paleoceanography* 24, PA4216.

Dall'Antonia, B., Bossio, A., and Guernet, C. (2003). The Eocene/Oligocene boundary and the psychrospheric event in the Tethys as recorded by deep-sea ostracods from the Massignano Global Boundary Stratotype Section and Point, Central Italy. *Marine Micropaleontology* 48, 91-106.

Davydov, V. I., Crowley, J. L., Schmitz, M. D., and Poletaev, V. I. (2010). High-precision U-Pb zircon age calibration of the global Carboniferous time scale and Milankovitch band cyclicity in the Donets Basin, eastern Ukraine. *Geochemistry Geophysics Geosystems* 11.

DeConto, R. M., and Pollard, D. (2003). Rapid Cenozoic glaciation of Antarctica induced by declining atmospheric CO_2. *Nature* 421, 245-249.

DeConto, R. M., Pollard, D., Wilson, P. A., Pälike, H., Lear, C. H., and Pagani, M. (2008). Thresholds for Cenozoic bipolar glaciation. *Nature* 455, 652-U52.

Dunn, R. E., Madden, R. H., Kohn, M. J., Schmitz, M. D., Strömberg, C. A. E., Carlini, A. A., Ré, G. H., and Crowley, J. (2012). A new chronology for middle Eocene - early Miocene South American Land Mammal Ages. *Geological Society of America Bulletin* 125, 539-555.

Dupont-Nivet, G., Krijgsman, W., Langereis, C. G., Abels, H. A., Dai, S., and Fang, X. (2007). Tibetan plateau aridification linked to global cooling at the Eocene-Oligocene transition. *Nature* 445, 635-638.

Elderfield, H., Yu, J., Anand, P., Kiefer, T., and Nyland, B. (2006). Calibrations for benthic foraminiferal Mg/Ca paleothermometry and the carbonate ion hypothesis. *Earth and Planetary Science Letters* 250, 633-649.

Eldrett, J. S., Harding, I. C., Wilson, P. A., Butler, E., and Roberts, A. P. (2007). Continental ice

in Greenland during the Eocene and Oligocene. *Nature* 446, 176-179.

Emry, R. J. (1973). Stratigraphy and Preliminary Biostratigraphy of the Flagstaff Rim Area, Natrona County, Wyoming. *Smithsonian Contributions to Paleobiology* 18, pp. 48.

Emry, R. J. (1992). Mammalian range zones in the Chadronian White River Formation at Flagstaff Rim, Wyoming. Princeton Series in Geology and Paleontology; Eocene-Oligocene climatic and biotic evolution, 106-115.

Emry, R. J., Russell, L. S., and Bjork, P. R. (1987). The Chadronian, Orellan, and Whitneyan North American land mammal ages. *In* "Cenozoic Mammals of North America: Geochronology and Biostratigraphy." (M. O. Woodburne, Ed.), pp. 118-152. University of California Press.

Evanoff, E., Prothero, D. R., and Lander, R. H. (1992). Eocene-Oligocene climatic change in North America: The White River formation near Douglas, east-central Wyoming. *In* "Eocene-Oligocene climatic and biotic evolution." (D. R. Prothero, and V. A. Berggren, Eds.), pp. 116-130. Princeton University Press, Princeton.

Farley, K. A., Montanari, A., Shoemaker, E. M., and Shoemaker, C. S. (1998). Geochemical evidence for a comet shower in the Late Eocene. *Science* 280, 1250-1253.

Fenero, R., Cotton, L., Molina, E., and Monechi, S. (2013). Micropalaeontological evidence for the late Oligocene Oi-2b global glaciation event at the Zarabanda section, Spain. *Palaeogeography Palaeoclimatology Palaeoecology* 369, 1-13.

Fenero, R., Thomas, E., Alegret, L., and Molina, E. (2012). Oligocene Benthic Foraminifera from the Fuente Caldera Section (Spain, Western Tethys): Taxonomy and Paleoenvironmental Inferences. *Journal of Foraminiferal Research* 42, 286-304.

Fischer, R. A. (1953). Dispersion on a sphere. *Proceedings of the Royal Society of London Series A-Mathematical and Physical Sciences* 217, 295-305.

Florindo, F., Wilson, G. S., Roberts, A. P., Sagnotti, L., and Verosub, K. L. (2005). Magnetostratigraphic chronology of a late Eocene to early Miocene glacimarine succession from the Victoria Land Basin, Ross Sea, Antarctica. *Global and Planetary Change* 45, 207-236.

Gerstenberger, H., and Haase, G. (1997). A highly effective emitter substance for mass spectrometric Pb isotope ratio determinations. *Chemical Geology* 136, 309-312.

Griffis, N. P. (2011). "Late Eocene terrestrial paleoclimate record from the White River Formation at Flagstaff Rim, Wyoming, USA." MSc Thesis, Temple University, Philadelphia.

Grimes, S. T., Hooker, J. J., Collinson, M. E., and Mattey, D. P. (2005). Summer temperatures of late Eocene to early Oligocene freshwaters. *Geology* 33, 189-192.

Heegaard, E., Birks, H. J. B., and Telford, R. J. (2005). Relationships between calibrated ages and depth in stratigraphical sequences: an estimation procedure by mixed-effect regression. *Holocene* 15, 612-618.

Heirtzler, J. R., Dickson, G. O., Herron, E. M., Pitman, W. C., and Le Pichon, X. (1968). Marine magnetic anomalies, geomagnetic field reversals, and motions of the ocean floor and continents. *Journal of Geophysical Research* 73, 2119-2136.

Hercman, H., and Pawlak, J. (2012). MOD-AGE: An age-depth model construction algorithm. *Quaternary Geochronology* 12, 1-10.

Hess, J., Stott, L. D., Bender, M. L., Kennett, J. P., and Schilling, J.-G. (1989). The Oligocene

marine microfossil record: Age assessments using strontium isotopes. *Paleoceanography* 4, 655-679.

Hiess, J., Condon, D. J., McLean, N., and Noble, S. R. (2012). $^{238}U/^{235}U$ systematics in terrestrial uranium-bearing minerals. *Science* 335, 1610-1614.

Hilgen, F. J., and Kuiper, K. F. (2009). A critical evaluation of the numerical age of the Eocene-Oligocene boundary. *In* "Late Eocene Earth: Hothouse Icehouse and Impacts." (C. Koeberl, and A. Montanari, Eds.), pp. 139-148. Geological Society of America Special Papers 425.

Hilgen, F. J., Kuiper, K. F., and Lourens, L. J. (2010). Evaluation of the astronomical time scale for the Paleocene and earliest Eocene. *Earth and Planetary Science Letters* 300, 139-151.

Hilgen, F. J., Lourens, L. J., Van Dam, J. A., Beu, A. G., Boyes, A. F., Cooper, R. A., Krijgsman, W., Ogg, J. G., Piller, W. E., and Wilson, D. S. (2012). The Neogene Period. *In* "The Geologic Time Scale 2004." pp. 923-978. Elsevier, Boston.

Hinnov, L. A., and Hilgen, F. J. (2012). Cyclostratigraphy and Astrochronology. *In* "The Geologic Time Scale 2012." (F. M. Gradstein, J. G. Ogg, M. D. Schmitz, and G. Ogg, Eds.), pp. 63-83. Elsevier, Boston.

Hooker, J. J., Grimes, S. T., Mattey, D. P., Collinson, M. E., and Sheldon, N. D. (2009). Refined correlation of the UK Late Eocene - Early Oligocene Solent Group and timing of its climate history. *In* "Late Eocene Earth: Hothouse Icehouse and Impacts." (C. Koeberl, and A. Montanari, Eds.), pp. 179-195. Geological Society of America Special Papers 425.

Hora, J. M., Singer, B. S., Jicha, B. R., Beard, B. L., Johnson, C. M., de Silva, S., and Salisbury, M. (2010). Volcanic biotite-sanidine $^{40}Ar/^{39}Ar$ age discordances reflect Ar partitioning and pre-eruption closure in biotite. *Geology* 38, 923-926.

Hren, M. T., Sheldon, N. D., Grimes, S. T., Collinson, M. E., Hooker, J. J., Bugler, M., and Lohmann, K. C. (2013). Terrestrial cooling in Northern Europe during the Eocene-Oligocene transition. *Proceedings of the National Academy of Sciences of the United States of America* 110, 7562-7567.

Huber, M., and Nof, D. (2006). The ocean circulation in the southern hemisphere and its climatic impacts in the Eocene. *Palaeogeography, Palaeoclimatology, Palaeoecology* 231, 9-28.

Huestis, S. P., and Acton, G. D. (1997). On the construction of geomagnetic timescales from non-prejudicial treatment of magnetic anomaly data from multiple ridges. *Geophysical Journal International* 129, 176-182.

Huesing, S. K., Hilgen, F. J., Aziz, H. A., and Krijgsman, W. (2007). Completing the Neogene geological time scale between 8.5 and 12.5 Ma. *Earth and Planetary Science Letters 253, 340-358.*

Huesing, S. K., Kuiper, K. F., Link, W., Hilgen, F. J., and Krijgsman, W. (2009). The upper Tortonian - lower Messinian at Monte dei Corvi (Northern Apennines, Italy): Completing a Mediterranean reference section for the Tortonian Stage. *Earth and Planetary Science Letters* 282, 140-157.

Hutchinson, J. H. (1992). Western North American reptile and amphibian record across the Eocene/Oligocene boundary and its climatic implications. *In* "Eocene-Oligocene climatic and biotic evolution." (D. R. Prothero, and A. Berggren, Eds.), pp. 451-463.

Princeton University Press.

Hyland, E., Murphy, B., Varela, P., Marks, K., Colwell, L., Tori, F., Monechi, S., Cleaveland, L., Brinkhuis, H., van Mourik, C. A., Coccioni, R., Bice, D., and Montanari, A. (2009). Integrated stratigraphic and astrochronologic calibration of the Eocene-Oligocene transition in the Monte Cagnero section (northeastern Apennines, Italy): A potential parastratotype for the Massignano global stratotype section and point (GSSP). *In* "Late Eocene Earth: Hothouse Icehouse and Impacts." pp. 303-322. Geological Society of America Special Paper.

Ivany, L. C., Van Simaeys, S., Domack, E. W., and Samson, S. D. (2006). Evidence for an earliest Oligocene ice sheet on the Antarctic Peninsula. *Geology* 34, 377-380.

Jaffey, A. H., Flynn, K. F., Glendeni.Le, Bentley, W. C., and Essling, A. M. (1971). Precision Measurement of Half-Lives and Specific Activities of U-235 and U-238. *Physical Review C* 4, 1889-&.

Jovane, L., Florindo, F., Dinares-Turell, J., and Turell, S. (2004). Environmental magnetic record of paleoclimate change from the Eocene-Oligocene stratotype section, Massignano, Italy. *Geophysical Research Letters* 31.

Jovane, L., Florindo, F., Sprovieri, M., and Pälike, H. (2006). Astronomic calibration of the late Eocene/early Oligocene Massignano section (central Italy). *Geochemistry Geophysics Geosystems* 7.

Jovane, L., Savian, J. F., Coccioni, R., Frontalini, F., Bancalà, G., Catanzariti, R., Luciani, V., Bohaty, S. M., Wilson, P. A., and Florindo, F. (2013). Integrated magnetobiostratigraphy of the middle Eocene - lower Oligocene interval from the Monte Cagnero section, central Italy. *Geological Society, London, Special Publications* 373.

Jovane, L., Sprovieri, M., Coccioni, R., Florindo, F., Marsili, A., and Laskar, J. (2010). Astronomical calibration of the middle Eocene Contessa Highway section (Gubbio, Italy). *Earth and Planetary Science Letters* 298, 77-88.

Jovane, L., Sprovieri, M., Florindo, F., Acton, G., Coccioni, R., Dall'Antonia, B., and Dinares-Turell, J. (2007). Eocene-Oligocene paleoceanographic changes in the stratotype section, Massignano, Italy: Clues from rock magnetism and stable isotopes. *Journal of Geophysical Research-Solid Earth* 112.

Katz, M. E., Cramer, B. S., Toggweiler, J. R., Esmay, G., Liu, C. J., Miller, K. G., Rosenthal, Y., Wade, B. S., and Wright, J. D. (2011). Impact of Antarctic circumpolar current development on Late Paleogene ocean structure. *Science* 332, 1076-1079.

Katz, M. E., Miller, K. G., Wright, J. D., Wade, B. S., Browning, J. V., Cramer, B. S., and Rosenthal, Y. (2008). Stepwise transition from the Eocene greenhouse to the Oligocene icehouse. *Nature Geoscience* 1, 329-334.

Kirschvink, J. L. (1980). The least-squares line and plane and the analysis of paleomagnetic data: examples from Siberia and Morocco. *Geophisical Journal of the Royal Astronomical Society*, 699-718.

Kohn, M. J., Josef, J. A., Madden, R., Kay, R., Vucetich, G., and Carlini, A. A. (2004). Climate stability across the Eocene-Oligocene transition, southern Argentina. *Geology* 32, 621-624.

Kuiper, K. F., Deino, A., Hilgen, F. J., Krijgsman, W., Renne, P. R., and Wijbrans, J. R. (2008). Synchronizing rock clocks of Earth history. *Science* 320, 500-504.

LaGarry, H. E. (1998). Lithostratigraphic revision and redescription of the Brule Formation (White River Group) of northwestern Nebraska. *In* "Depositional Environments, Lithostratigraphy and Biostratigraphy of the White River and Arikaree Groups (Late Eocene to Early Miocene, North America)." (D. O. Terry, H. E. LaGarry, and R. M. Hunt, Eds.), pp. 63-91. Geological Society of America Special Papers, Boulder, CO.

Langenhorst, F., and Clymer, A. K. (1996). Characteristics of shocked quartz in late Eocene impact ejecta from Massignano (Ancona, Italy): Clues to shock conditions and source crater. *Geology* 24, 487-490.

Larson, E. E., and Evanoff, E. (1998). Tephrostratigraphy and source of the tuffs of the White River sequence. *In* "Depositional Environments, Lithostratigraphy, and Biostratigraphy of the White River and Arikaree Groups (Late Eocene to Early Miocene, North America)." (D.O. Terry, H. E. LaGarry, and R. M. Hunt, Eds.), pp. 1-14. Geological Society of America Special Papers, Boulder, CO.

Laskar, J., Fienga, A., Gastineau, M., and Manche, H. (2011). La2010: a new orbital solution for the long-term motion of the Earth. *Astronomy and Astrophysics* 532, A89.

Laskar, J., Joutel, F., and Boudin, F. (1993). Orbital, Precessional, and Insolation Quantities for the Earth from -20 Myr to +10 Myr. *Astronomy & Astrophysics* 270, 522-533.

Laskar, J., Robutel, P., Joutel, F., Gastineau, M., Correia, A. C. M., and Levrard, B. (2004). A long-term numerical solution for the insolation quantities of the Earth. *Astronomy & Astrophysics* 428, 261-285.

Lear, C. H., Bailey, T. R., Pearson, P. N., Coxall, H. K., and Rosenthal, Y. (2008). Cooling and ice growth across the Eocene-Oligocene transition. *Geology* 36, 251-254.

Lear, C. H., Elderfield, H., and Wilson, P. A. (2000). Cenozoic Deep-Sea Temperatures and Global Ice Volumes from Mg/Ca in Benthic Foraminiferal Calcite. *Scienc*e 287, 269-272.

Lear, C. H., Rosenthal, Y., Coxall, H. K., and Wilson, P. A. (2004). Late Eocene to early Miocene ice sheet dynamics and the global carbon cycle. *Paleoceanography* 19, PA4015.

Leckie, R. M., Farnham, C., and Schmidt, M. G. (1993). Oligocene planktonic foraminifer biostratigraphy of Hole 803D (Ontong Java Plateau) and Hole 628A (Little Bahama Bank) and comparison with the southern high latitudes. *In* "Proceedings of the Ocean Drilling Programme, Scientific Results." (W. H. Berger, L. W. Kroenke, L. A. Mayer, and e. al, Eds.).

Liu, Z. H., Pagani, M., Zinniker, D., DeConto, R., Huber, M., Brinkhuis, H., Shah, S. R., Leckie, R. M., and Pearson, A. (2009). Global Cooling During the Eocene-Oligocene Climate Transition. *Science* 323, 1187-1190.

Livermore, R., Nankivell, A., Eagles, G., and Morris, P. (2005). Paleogene opening of Drake Passage. *Earth and Planetary Science Letters* 236, 459-470.

Lourens, L., Hilgen, F., Shackleton, N. J., Laskar, J., and Wilson, D. (2004). The Neogene period. *In* "A Geologic Time Scale 2004." (F. M. Gradstein, J. G. Ogg, and A. Smith, Eds.), pp. 409-440. Cambridge University Press.

Lourens, L. J., Wehausen, R., and Brumsack, H. J. (2001). Geological constraints on tidal dissipation and dynamical ellipticity of the Earth over the past three million years. *Nature* 409, 1029-1033.

Lowrie, W., and Lanci, L. (1994). Magnetostratigraphy of the Eocene-Oligocene boundary sections in Italy - no evidence for short subchrons within 12r and 13r. *Earth and*

Planetary Science Letters 126, 247-258.

Ludwig, K. (2003). User's manual for Isoplot 3.75, a geochronological toolkit for Microsoft Excel. Berkeley Geochronology Center Special Publication 5, pp. 75.

Luterbacher, H. P., Ali, J. R., Brinkhuis, H., Gradstein, F. M., Hooker, J. J., Monechi, S., Ogg, J. G., Powell, J., Roehl, U., Sanfilippo, A., and Schmitz, B. (2004). The Paleogene period. *In* "A Geologic Time Scale 2004." (F. M. Gradstein, J. G. Ogg, and A. Smith, Eds.), pp. 384-408. Cambridge University Press.

Machlus, M., Hemming, S. R., Olsen, P. E., and Christie-Blick, N. (2004). Eocene calibration of geomagnetic polarity time scale reevaluated: Evidence from the Green River Formation of Wyoming. *Geology* 32, 137-140.

Macho, A. S., Singer, B., Jicha, B. R., Condon, D. J., Hoffman, K. A., Dierkhising, J., Brown, M. C., Feinberg, J. M., and Kidane, T. (in review). On the age of the Réunion and Huckleberry Ridge excursions and geodynamo instabilities during the Matuyama Chron, *Earth and Planetary Science Letters*.

Marchegiani, L., Bertotti, G., Cello, G., Deiana, G., Mazzoli, S., and Tondi, E. (1999). Pre-orogenic tectonics in the Umbria-Marche sector of the Afro-Adriatic continental margin. *Tectonophysics* 315, 123-143.

Martini, E. (1971). Standard Tertiary and Quaternary calcareous nannoplankton zonation. *In* "Proceedings of the Second Planktonic Conference Roma 1970." (A. Farinacci, Ed.), pp. 739-785. Edizioni Tecnoscienza, Rome.

Mattinson, J. M. (2005). Zircon U-Pb chemical abrasion ("CA-TIMS") method: Combined annealing and multi-step partial dissolution analysis for improved precision and accuracy of zircon ages. *Chemical Geology* 220, 47-66.

Mattinson, J. M. (2010). Analysis of the relative decay constants of ^{235}U and ^{238}U by multi-step CA-TIMS measurements of closed-system natural zircon samples. *Chemical Geology* 275, 186-198.

McLean, N., and others. (in review). Evaluating Uncertainties in the Calibration of Isotopic Reference Materials and Multi-Element Isotopic Tracers (EARTHTIME Tracer Calibration Part II). *Geochemistry Geophysics Geosystems*.

McLean, N. M., Bowring, J. F., and Bowring, S. A. (2011). An algorithm for U-Pb isotope dilution data reduction and uncertainty propagation. *Geochemistry Geophysics Geosystems* 12.

Meng, J., and McKenna, M. C. (1998). Faunal turnovers of Palaeogene mammals from the Mongolian plateau. *Nature* 394, 364-367.

Merrihue, C., and Turner, G. (1966). Potassium-argon dating by activation with fast neutrons. *Journal of Geophysical Research* 71, 2852-2857.

Meyers, S. R., Siewert, S. E., Singer, B. S., Sageman, B. B., Condon, D. J., Obradovich, J. D., Jicha, B. R., and Sawyer, D. A. (2012). Intercalibration of radioisotopic and astrochronologic time scales for the Cenomanian-Turonian boundary interval, Western Interior Basin, USA. *Geology* 40, 7-10.

Miller, K. G., Aubry, M.-P., Khan, M. J., Melillo, A. J., Kent, D. V., and Berggren, W. A. (1985). Oligocene-Miocene biostratigraphy, magnetostratigraphy, and isotopic stratigraphy of the western North Atlantic. *Geology* 13, 257-261.

Miller, K. G., Wright, J. D., and Fairbanks, R. G. (1991). Unlocking the Ice House: Oligocene-

Miocene Oxygen Isotopes, Eustasy, and Margin Erosion. *Journal of Geophysical Research* 96, 6829-6848.

Miller, K. G., Wright, J. D., Katz, M. E., Wade, B. S., Browning, J. V., Cramer, B. S., and Rosenthal, Y. (2009). Climate threshold at the Eocene-Oligocene transition: Antarctic ice sheet influence on ocean circulation. Late Eocene Earth: Hothouse Icehouse, and Impacts 452, 169-178.

Min, K. W., Mundil, R., Renne, P. R., and Ludwig, K. R. (2000). A test for systematic errors in $^{40}Ar/^{39}Ar$ geochronology through comparison with U/Pb analysis of a 1.1-Ga rhyolite. *Geochimica Et Cosmochimica Acta* 64, 73-98.

Molina, E., Gonzalvo, C. n., and Keller, G. (1993). The Eocene-Oligocene planktic foraminiferal transition: extinctions, impacts and hiatuses. *Geological Magazine* 130, 483-499.

Montanari, A., Asaro, F., Michel, H. V., and Kennett, J. P. (1993). Iridium anomalies of Late Eocene age at Massignano (Italy), and ODP Site 689B (Maud Rise, Antarctic). *Palaios* 8, 420-437.

Montanari, A., Deino, A. L., Drake, R. E., Turrin, B. D., DePaolo, D. J., Odin, G. S., Curtis, G. H., Alvarez, W., and Bice, D. M. (1988). Radioisotopic dating of the Eocene-Oligocene boundary in the pelagic sequence of the northeastern Appenines. *In* "The Eocene-Oligocene boundary in the Marche-Umbria basin (Italy)." (I. Premoli Silva, R. Coccioni, and A. Montanari, Eds.), pp. 195-208. International Subcommission on Paleogene Stratigraphy, Ancona.

Montanari, A., Drake, R., Bice, D. M., Alvarez, W., Curtis, G. H., Turrin, B. D., and Depaolo, D. J. (1985). Radiometric time scale for the Upper Eocene and Oligocene based on K/Ar and Rb/Sr dating of volcanic biotites from the pelagic sequence of Gubbio, Italy. *Geology* 13, 596-599.

Mullender, T. A. T., Vanvelzen, A. J., and Dekkers, M. J. (1993). Continuous Drift Correction and Separate Identification of Ferrimagnetic and Paramagnetic Contributions in Thermomagnetic Runs. *Geophysical Journal International* 114, 663-672.

Mundil, R., Ludwig, K. R., Metcalfe, I., and Renne, P. R. (2004). Age and timing of the Permian mass extinctions: U/Pb dating of closed-system zircons. *Science* 305, 1760-1763.

Nocchi, M., Monechi, S., Coccioni, R., Madile, M., Monaco, P., Orlando, M., Parisi, G., and Premoli Silva, I. (1988). The extinction of Hantkeninidae as a marker for recognizing the Eocene-Oligocene boundary: A proposal. *In* "The Eocene-Oligocene boundary in the Marche-Umbria basin (Italy)." (I. Premoli Silva, R. Coccioni, and A. Montanari, Eds.), pp. 249-252. International Subcommission on Paleogene Stratigraphy, Ancona.

Oberli, F., and Meier, M. (1991). Age of the Eocene-Oligocene boundary in the Marche-Umbria basin, Italy, by high resolution U-Th-Pb dating. *Terra* 3, 286.

Obradovich, J. D. (1993). A Cretaceous time scale. *In* "Evolution of the Western Interior Basin, Geological Association of Canada Special Paper." (W. G. E. Caldwell, and E. G. Kauffman, Eds.), pp. 379-396. Geological Association of Canada, Ottawa.

Obradovich, J. D., Evanoff, E., and Larson, E. E. (1995). Revised single crystal laser fusion $^{40}Ar/^{39}Ar$ ages of Chadronian tuffs in the White River Formation of Wyoming. *GSA Abstract with Programs*, North Central/South Central sections 27, A77.

Odin, G. S., Barbin, V., Hurford, A. J., Baadsgaard, H., Galbrun, B., and Gillot, P. Y. (1991a). Multimethod radiometric dating of volcano-sedimentary layers from Northern Italy -

Age and duration of the Priabonian stage. *Earth and Planetary Science Letters* 106, 151-168.

Odin, G. S., Montanari, A., Deino, A., Drake, R., Guise, P. G., Kreuzer, H., and Rex, D. C. (1991b). Reliability of volcano-sedimentary biotite ages across the Eocene-Oligocene boundary. *Chemical Geology* 86, 203-224.

Ogg, J. G. (2012). Geomagnetic Polarity Time Scale. *In* "The Geologic Time Scale 2012." pp. 85-113. Elsevier, Boston.

Ogg, J. G., and Smith, A. G. (2004). The geomagnetic polarity time scale. *In* "A Geologic Time Scale 2004." (F. M. Gradstein, J. G. Ogg, and A. G. Smith, Eds.), pp. 63-86. Cambridge University Press.

Pagani, M., Zachos, J. C., Freeman, K. H., Tipple, B., and Bohaty, S. (2005). Marked decline in atmospheric carbon dioxide concentrations during the Paleogene. *Science* 309, 600-603.

Pälike, H., Lyle, M. W., Nishi, H., Raffi, I., Ridgwell, A., Gamage, K., Klaus, A., Acton, G., Anderson, L., Backman, J., Baldauf, J., Beltran, C., Bohaty, S. M., Bown, P., Busch, W., Channell, J. E. T., Chun, C. O. J., Delaney, M., Dewangan, P., Jones, T. D., Edgar, K. M., Evans, H., Fitch, P., Foster, G. L., Gussone, N., Hasegawa, H., Hathorne, E. C., Hayashi, H., Herrle, J. O., Holbourn, A., Hovan, S., Hyeong, K., Iijima, K., Ito, T., Kamikuri, S., Kimoto, K., Kuroda, J., Leon-Rodriguez, L., Malinverno, A., Moore, T. C., Murphy, B. H., Murphy, D. P., Nakamura, H., Ogane, K., Ohneiser, C., Richter, C., Robinson, R., Rohling, E. J., Romero, O., Sawada, K., Scher, H., Schneider, L., Sluijs, A., Takata, H., Tian, J., Tsujimoto, A., Wade, B. S., Westerhold, T., Wilkens, R., Williams, T., Wilson, P. A., Yamamoto, Y., Yamamoto, S., Yamazaki, T., and Zeebe, R. E. (2012). A Cenozoic record of the equatorial Pacific carbonate compensation depth. *Nature* 488, 609-613.

Pälike, H., Norris, R. D., Herrle, J. O., Wilson, P. A., Coxall, H. K., Lear, C. H., Shackleton, N. J., Tripati, A. K., and Wade, B. S. (2006). The heartbeat of the oligocene climate system. *Science* 314, 1894-1898.

Pälike, H., Shackleton, N. J., and Röhl, U. (2001). Astronomical forcing in Late Eocene marine sediments. *Earth and Planetary Science Letters* 193, 589-602.

Parisi, G., Guerrera, F., Madile, M., Magnoni, G., Monaco, P., Monechi, S., and Nocchi, M. (1988). Middle Eocene to Early Oligocene calcareous nannofossil and foraminiferal biostratigraphy in the Monte Cagnero section, Piobbico (Italy). *In* "The Eocene-Oligocene boundary in the Marche-Umbria basin (Italy)." (I. Premoli Silva, R. Coccioni, and A. Montanari, Eds.), pp. 119-136. International Subcommission on Paleogene Stratigraphy, Ancona.

Pearson, P. N., McMillan, I. K., Wade, B. S., Dunkley Jones, T., Coxall, H. K., Bown, P. R., and Lear, C. H. (2008). Extinction and environmental change across the Eocene-Oligocene boundary in Tanzania. *Geology* 36, 179-182.

Phillips, D., and Matchan, E. L. (2013). Ultra-high precision $^{40}Ar/^{39}Ar$ ages for Fish Canyon Tuff and Alder Creek Rhyolite sanidine: new dating standards required? *Geochimica Et Cosmochimica Acta.*

Pierrard, O., Robin, E., Rocchia, R., and Montanari, A. (1998). Extraterrestrial Ni-rich spinel in upper Eocene sediments from Massignano, Italy. *Geology* 26, 307-310.

Poore, R. Z., Tauxe, L., Percival Jr, S. F., L. Labrecque, J., Wright, R., Petersen, N. P., Smith, C. C., Tucker, P., and Hsu, K. J. (1983). Late Cretaceous-Cenozoic magnetostratigraphic

and biostratigraphic correlations of the South Atlantic Ocean: DSDP Leg 73. *Palaeogeography, Palaeoclimatology, Palaeoecology* 42, 127-149.

Premoli Silva, I., and Jenkins, D. G. (1993). Decision on the Eocene-Oligocene boundary stratotype. *Episodes* 16, 379-382.

Prothero, D. R. (1985). Chadronian (Early Oligocene) magnetostratigraphy of eastern Wyoming - Implications for the age of the Eocene-Oligocene boundary. *Journal of Geology* 93, 555-565.

Prothero, D. R. (1996). Magnetostratigraphy of the White River Group in the High Plains *In* "The Terrestrial Eocene-Oligocene Transition in North America." (D. R. Prothero, and R. J. Emry, Eds.), pp. 247-262. Cambridge University Press, Cambridge.

Prothero, D. R., Denham, C. R., and Farmer, H. G. (1982). Oligocene calibration of the magnetic polarity time scale. *Geology* 10, 650-653.

Prothero, D. R., Denham, C. R., and Farmer, H. G. (1983). Magnetostratigraphy of the White River Group and its implications for Oligocene geochronology. *Palaeogeography Palaeoclimatology Palaeoecology* 42, 151-166.

Prothero, D. R., and Emry, R. J. (1996). Summary. *In* "The terrestrial Eocene - Oligocene transition in North America." (D. R. Prothero, and R. J. Emry, Eds.), pp. 646-664. Cambridge University Press.

Prothero, D. R., and Heaton, T. H. (1996). Faunal stability during the Early Oligocene climatic crash. *Palaeogeography Palaeoclimatology Palaeoecology* 127.

Prothero, D. R., and Swisher, C. C. (1992). Magnetostratigraphy and geochronology of the terrestrial Eocene-Oligocene transition in North America. *In* "Eocene-Oligocene climatic and biotic evolution." (D. R. Prothero, and V. A. Berggren, Eds.), pp. 49-73. Princeton University Press.

Prothero, D. R., and Whittlesey, K. E. (1998). Magnetostratigraphy and biostratigraphy of the Orellan and Whitneyan land mammal "ages" in the White River Group *In* "Depositional Environments, Lithostratigraphy and Biostratigraphy of the White River and Arikaree Groups (Late Eocene to Early Miocene, North America)." (D. O. Terry, H. E. LaGarry, and R. M. Hunt, Eds.), pp. 39-62. Geological Society of America Special Paper 325.

Pujol, C. (1983). Cenozoic Planktonic Foraminiferal Biostratigraphy of the Southwestern Atlantic (Rio-Grande Rise) - Deep-Sea Drilling Project Leg-72. *Initial Reports of the Deep Sea Drilling Project 72,* 623-673.

Rea, D. K., and Lyle, M. W. (2005). Paleogene calcite compensation depth in the eastern subtropical Pacific: Answers and questions. *Paleoceanography* 20.

Renne, P. R., Deino, A. L., Hilgen, F. J., Kuiper, K. F., Mark, D. F., Mitchell, W. S., Morgan, L. E., Mundil, R., and Smit, J. (2013). Time scales of critical events around the Cretaceous-Paleogene boundary. *Science* 339, 684-687.

Renne, P. R., Deino, A. L., Walter, R. C., Turrin, B. D., Swisher , C. C., Becker, T. A., Curtis, G. H., Sharp, W. D., and Jaouni, A.-R. (1994). Intercalibration of astronomical and radioisotopic time. *Geology* 22, 783-786.

Renne, P. R., Mundil, R., Balco, G., Min, K., and Ludwig, K. R. (2010). Joint determination of ^{40}K decay constants and ^{40}Ar*/^{40}K for the Fish Canyon sanidine standard, and improved accuracy for ^{40}Ar/^{39}Ar geochronology. *Geochimica et Cosmochimica Acta* 74, 5349-5367.

Renne, P. R., Swisher, C. C., Deino, A. L., Karner, D. B., Owens, T. L., and DePaolo, D. J. (1998). Intercalibration of standards, absolute ages and uncertainties in $^{40}Ar/^{39}Ar$ dating. *Chemical Geology* 145, 117-152.

Retallack, G. J. (1992). Paleosols and changes in climate and vegetation across the Eocene-Oligocene boundary. *In* "Eocene-Oligocene climatic and biotic evolution." (D. R. Prothero, and A. Berggren, Eds.), pp. 383-398. Princeton University Press.

Retallack, G. J. (2007). Cenozoic paleoclimate on land in North America. *Journal of Geology* 115, 271-294.

Retallack, G. J., Orr, W. N., Prothero, D. R., Duncan, R. A., Kester, P. R., and Ambers, C. P. (2004). Eocene-Oligocene extinction and paleoclimatic change near Eugene, Oregon. *Geological Society of America Bulletin* 116, 817-839.

Rivera, T. A., Storey, M., Schmitz, M. D., and Crowley, J. L. (2013). Age intercalibration of $^{40}Ar/^{39}Ar$ sanidine and chemically distinct U/Pb zircon populations from the Alder Creek Rhyolite Quaternary geochronology standard. *Chemical Geology* 345, 87-98.

Rivera, T. A., Storey, M., Zeeden, C., Hilgen, F. J., and Kuiper, K. (2011). A refined astronomically calibrated $^{40}Ar/^{39}Ar$ age for Fish Canyon sanidine. *Earth and Planetary Science Letters* 311, 420-426.

Sadler, P. M. (2004). Quantitative biostratigraphy - Achieving finer resolution in global correlation. *Annual Review of Earth and Planetary Sciences* 32, 187-213.

Sageman, B.B., Singer, B.S., Meyers, S.R., Siewert, S.E., Walaszczyk, I., Condon, D.J., Jicha, B.R., Obradovich, J.D., and Sawyer, D.A. (in press). Integrating 40Ar/39Ar, U-Pb, and astronomical clocks in the Cretaceous Niobrara Formation, Western Interior Basin, USA. *Geological Society of America Bulletin*.

Sagnotti, L., Florindo, F., Verosub, K. L., Wilson, G. S., and Roberts, A. P. (1998). Environmental magnetic record of Antarctic palaeoclimate from Eocene/Oligocene glaciomarine sediments, Victoria Land Basin. *Geophysical Journal International* 134, 653-662.

Schmitz, M. D. (2012). Radiogenic Isotope Geochronology. *In* "The Geologic Time Scale 2012." pp. 115-126. Elsevier, Boston.

Schmitz, M. D., and Kuiper, K. F. (2013). High-Precision Geochronology. *Elements* 9, 25-30.

Scholz, D., and Hoffmann, D. L. (2011). StalAge - An algorithm designed for construction of speleothem age models. *Quaternary Geochronology* 6, 369-382.

Schultz, C. B., and Stout, T. M. (1955). Classification of Oligocene sediments of Nebraska. *Bulletin of the University of Nebraska State Museum* 4, 17-52.

Scott, J. W., Sundell, K. A., Thompson, M. D., and Bowring, S. A. (1999). High precision U-Pb geochronology of Oligocene tuffs from the White River Formation, Douglas, Wyoming. *Geological Society of America Abstracts with Programs* 31, A66.

Shackleton, N. J., Hall, M. A., Raffi, I., Tauxe, L., and Zachos, J. (2000). Astronomical calibration age for the Oligocene-Miocene boundary. *Geology* 28, 447-450.

Shackleton, N. J., and Kennett, P. (1975). Paleotemperature history of the Cenozoic and the initiation of Antarctic glaciation: oxygen and carbon analyses in DSDP Sites 277, 279, and 281. *Deep Sea Drilling Project Initial Reports* 29, 743-755.

Sheldon, N. D. (2009). Nonmarine records of climatic change across the Eocene-Oligocene transition. *In* "Late Eocene Earth: Hothouse Icehouse and Impacts." (C. Koeberl, and A.

Montanari, Eds.), pp. 241-248. Geological Society of America Special Papers.

Sheldon, N. D., and Retallack, G. J. (2004). Regional paleoprecipitation records from the late eocene and oligocene of North America. *Journal of Geology* 112, 487-494.

Sijp, W. P., and England, M. H. (2004). Effect of the Drake Passage throughflow on global climate. *Journal of Physical Oceanography* 34, 1254-1266.

Simon, J. I., Renne, P. R., and Mundil, R. (2008). Implications of pre-eruptive magmatic histories of zircons for U-Pb geochronology of silicic extrusions. *Earth and Planetary Science Letters* 266, 182-194.

Smith, M. E., Chamberlain, K. R., Singer, B. S., and Carroll, A. R. (2010). Eocene clocks agree: Coeval $^{40}Ar/^{39}Ar$, U-Pb, and astronomical ages from the Green River Formation. Geology 38, 527-530.

Spezzaferri, S., Basso, D., and Coccioni, R. (2002). Late Eocene planktonic foraminiferal response to an extraterrestrial impact at Massignano GSSP (northeastern Appennines, Italy). *Journal of Foraminiferal Research* 32, 188-199.

Stanley, K. O., and Benson, L. V. (1979). Early diagenesis of High Plains Tertiary vitric and arkosic sandstone, Wyoming and Nebraska. *In* "Aspects of diagenesis: Society of Economica Geologists and Paleontologists Special Publication 26." (P. A. Scholle, and P. R. Schluger, Eds.), pp. 401-423.

Steiger, R. H., and Jäger, E. (1977). Subcommission on geochronology: Convention on the use of decay constants in geo- and cosmochronology. *Earth and Planetary Science Letters* 36, 359-362.

Swisher, C. C., Dingus, L., and Butler, R. F. (1993). $^{40}Ar/^{39}Ar$ dating and magnetostratigraphic correlation of the terrestrial Cretaceous-Paleogene boundary and Puercan Mammal Age, Hell Creek - Tullock Formations, Eastern Montana. *Canadian Journal of Earth Sciences* 30, 1981-1996.

Swisher, C. C., and Prothero, D. R. (1990). Single-crystal $^{40}Ar/^{39}Ar$ dating of the Eocene-Oligocene transition in North America. *Science* 249, 760-762.

Tauxe, L. (2010). "Essentials of Paleomagnetism." University of California Press.

Terry, D. O. (1998). Lithostratigraphic revision and correlation of the lower part of the White River Group: South Dakota to Nebraska. *In* "Depositional Environments, Lithostratigraphy and Biostratigraphy of the White River and Arikaree Groups (Late Eocene to Early Miocene, North America)." (D. O. Terry, H. E. LaGarry, and R. M. Hunt, Eds.). Geological Society of America Special Paper 325.

Terry, D. O. (2001). Paleopedology of the Chadron Formation of Northwestern Nebraska: implications for paleoclimatic change in the North American midcontinent across the Eocene-Oligocene boundary. *Palaeogeography Palaeoclimatology Palaeoecology* 168, 1-38.

Terry, D. O., and LaGarry, H. E. (1998). The Big Cottonwood Creek Member: A new member of the Chadron Formation in northwestern Nebraska. *In* "Depositional Environments, Lithostratigraphy and Biostratigraphy of the White River and Arikaree Groups (Late Eocene to Early Miocene, North America)." (D. O. Terry, H. E. LaGarry, and R. M. Hunt, Eds.). Geological Society of America Special Paper 325.

Torsvik, T. H., Muller, R. D., Van der Voo, R., Steinberger, B., and Gaina, C. (2008). Global plate motion frames: Toward a unified model. *Reviews of Geophysics* 46.

Tripati, A. K., Eagle, R. A., Morton, A., Dowdeswell, J. A., Atkinson, K. L., Bahe, Y., Dawber, C. F., Khadun, E., Shaw, R. M. H., Shorttle, O., and Thanabalasundaram, L. (2008). Evidence for glaciation in the Northern Hemisphere back to 44 Ma from ice-rafted debris in the Greenland Sea. *Earth and Planetary Science Letters* 265, 112-122.

Van Mourik, C. A., and Brinkhuis, H. (2005). The Massignano Eocene-Oligocene golden spike revisited. *Stratigraphy* 2, 13-30.

Van Simaeys, S., Man, E. D., Vandenberghe, N. l., Brinkhuis, H., and Steurbaut, E. (2004). Stratigraphic and palaeoenvironmental analysis of the Rupelian-Chattian transition in the type region: evidence from dinoflagellate cysts, foraminifera and calcareous nannofossils. *Palaeogeography, Palaeoclimatology, Palaeoecology* 208, 31-58.

Vandamme, D. (1994). A new method to determine paleosecular variation. *Physics of the Earth and Planetary Interiors* 85, 131-142.

Vandenberghe, N., Hilgen, F. J., Speijer, R. P., Ogg, J. G., Gradstein, F. M., Hammer, O., Hollis, C. J., and Hooker, J. J. (2012). The Paleogene Period. *In* "The Geologic Time Scale 2012." (F. M. Gradstein, J. G. Ogg, M. D. Schmitz, and G. M. Ogg, Eds.), pp. 855-921. Elsevier, Boston.

Wade, B. S., Berggren, W. A., and Olsson, R. K. (2007). The biostratigraphy and paleobiology of Oligocene planktonic foraminifera from the equatorial Pacific Ocean (ODP Site 1218). *Marine Micropaleontology* 62, 167-179.

Wade, B. S., and Palike, H. (2004). Oligocene climate dynamics. *Paleoceanography* 19, PA4019.

Wade, B. S., Pearson, P. N., Berggren, W. A., and Pälike, H. (2011). Review and revision of Cenozoic tropical planktonic foraminiferal biostratigraphy and calibration to the geomagnetic polarity and astronomical time scale. *Earth-Science Reviews* 104, 111-142.

Wei, W. (1995). Revised age calibration points for the geomagnetic polarity time scale. *Geophysical Research Letters* 22, 957-960.

Wendt, I., and Carl, C. (1991). The statistical distribution of the mean squared weighted deviation. *Chemical Geology* 86, 275-285.

Westerhold, T., and Röhl, U. (2009). High resolution cyclostratigraphy of the early Eocene - new insights into the origin of the Cenozoic cooling trend. *Climate of the Past* 5, 309-327.

Westerhold, T., Röhl, U., Laskar, J., Raffi, I., Bowles, J., Lourens, L. J., and Zachos, J. C. (2007). On the duration of magnetochrons C24r and C25n and the timing of early Eocene global warming events: Implications from the Ocean Drilling Program Leg 208 Walvis Ridge depth transect. *Paleoceanography* 22, PA2201.

Westerhold, T., Röhl, U., Raffi, I., Fornaciari, E., Monechi, S., Reale, V., Bowles, J., and Evans, H. F. (2008). Astronomical calibration of the Paleocene time. *Palaeogeography Palaeoclimatology Palaeoecology* 257, 377-403.

Wolfe, J. A. (1994). Tertiary climatic changes at middle latitudes of western North America. *Palaeogeography, Palaeoclimatology, Palaeoecology* 108, 195-205.

Wood, H. E., Chaney, R. W., Clark, J., Colbert, E. H., Jepsen, G. L., Reeside, J. B., and Stock, C. (1941). Nomenclature and correlation of the North American continental Tertiary. *Geological Society of America Bulletin* 52, 1-48.

Wotzlaw, J.-F., Schaltegger, U., Frick, D. A., Dungan, M. A., Gerdes, A., and Günther, D. (2013). Tracking the evolution of large-volume silicic magma reservoirs from assembly to

supereruption. *Geology* 41, 867-870.

Xiao, G. Q., Abels, H. A., Yao, Z. Q., Dupont-Nivet, G., and Hilgen, F. J. (2010). Asian aridification linked to the first step of the Eocene-Oligocene climate Transition (EOT) in obliquity-dominated terrestrial records (Xining Basin, China). *Climate of the Past* 6, 501-513.

Zachos, J., Pagani, M., Sloan, L., Thomas, E., and Billups, K. (2001). Trends, rhythms, and aberrations in global climate 65 Ma to present. *Science* 292, 686-693.

Zachos, J. C., Quinn, T. M., and Salamy, K. A. (1996). High-Resolution (10^4 Years) Deep-Sea Foraminiferal Stable Isotope Records of the Eocene-Oligocene Climate Transition. *Paleoceanography* 11, 251-266.

Zanazzi, A., Kohn, M. J., MacFadden, B. J., and Terry, D. O. (2007). Large temperature drop across the Eocene-Oligocene transition in central North America. *Nature* 445, 639-642.

Zanazzi, A., Kohn, M. J., and Terry, D. O. (2009). Biostratigraphy and paleoclimatology of the Eocene-Oligocene boundary section at Toadstool Park, northwestern Nebraska, USA. *Geological Society of America Special Papers* 452, 197-214.

Zijderveld, J. D. A. (1967). A.C. demagnetization of rocks: analysis of results. *In* "Methods in paleomagnetism." (D. W. Collinson, K. M. Creer, and S. K. Runcorn, Eds.), pp. 254-286. Elsevier.